JOHANNES GUTENBERG UNIVERSITÄT MAINZ

JG|U

Electronic structure and spin-dependent transport of altermagnets and odd-parity-wave magnets

Dissertation submitted for the award of the title

"Doctor of Natural Sciences"

at the Faculty of Physics, Mathematics, and Computer Science
at the Johannes Gutenberg University Mainz
in Mainz

Anna Birk Hellenes

Mainz, date: 19th December, 2024

Advisor: Jairo Sinova

Date of examination: 19th May, 2025

Abstract

Spintronics is a field of research and technology employing electron spin in electronic devices. Conventionally, generating a spin degree of freedom has been achieved using ferromagnets and systems with large spin-orbit coupling. More recently, antiferromagnetic spintronics has explored the principle ability of compensated magnets to be highly densified in devices, their ultrafast dynamics, and the possibility of high switching energy efficiency. However, functionalizing conventional collinear antiferromagnets for spin-dependent effects is nontrivial. Their antiferromagnetic electronic band structure is either spin degenerate, or it is spin-split due to relativistic spin-orbit coupling, which is weak for common elements and more significant only in heavy, rare elements.

This thesis concerns a different emerging mechanism for generating a spin degree of freedom based on unconventional, magnetically compensated magnets. Among these are the recently identified even-parity (e.g., d- or g-wave) altermagnets and odd-parity (e.g., p- or f-wave) magnets—the latter we theoretically predict in this thesis [publication1, publication2]. Generating a spin polarization in the electronic structure in these unconventional magnets does not require net magnetization or heavy relativistic elements but instead forms due to distributions of nonrelativistic exchange fields in the crystal. We discuss and formulate the spin group symmetry criteria for these unconventional magnets. Unlike the commonly studied magnetic symmetries, which consider a single operation acting on the spin and lattice degree of freedom, spin symmetries consider pairs of operations that can act differently on these two degrees of freedom, opening new possibilities for studying and identifying magnetic phases.

We also contribute to the first experimental confirmations of the altermagnetic electronic structure with our *ab initio* calculations and symmetry analysis [publication3, publication4, publication5].

Moreover, we propose concepts for spintronics effects based on altermagnets and p-wave magnets. We develop new concepts for giant and tunneling magnetoresistance effects in altermagnets which originate from their spin-polarized, exchange-split band structure in the nonrelativistic limit, which is unprecedented for collinear compensated magnets [publication6]. We have also proposed spin-dependent effects in our p-wave magnets with a special focus on the coplanar class, including nonrelativistic transport anisotropy [publication1] and Edelstein effects [publication2], which is however beyond the scope of this thesis.

Our findings can have broad implications, ranging from fundamental research, such as topology and charge-to-spin conversion with lighter-element materials, to the more applied, such as memory and sensing applications.

Key words: *Spintronics, altermagnetism, odd-parity-wave magnetism, p-wave magnetism, giant magnetoresistance, tunneling magnetoresistance, spin-dependent transport*

Acknowledgements

I want to express my deepest gratitude to everyone who has supported me throughout my PhD journey. Special thanks to my supervisor, Jairo Sinova, for invaluable guidance and connecting me with researchers worldwide. My deep appreciation to Libor Šmejkal for insightful discussions, advice, and support. The work of Libor Šmejkal, Jairo Sinova, and Tomaš Jungwirth on altermagnetism and antiferromagnetism has been a significant inspiration for my research.

I extend my appreciation to my experimental collaborators for their immense expertise. Thank you to the extended INSPIRE team, including Rafael González-Hernández, Venkata Krishna Bharadwaj, Rodrigo Jaeschke Ubiergo, Nayra A. Álvarez Pari, Bennet Karetta, and Atasi Chakraborty, for their fruitful collaboration and stimulating discussions. My gratitude extends to my Spin+X mentors, Jürgen Halt and Tiffany Santos, for their fresh perspectives and guidance.

I am grateful to Johannes Gutenberg University, the collaborative research centers Spin+X and TopDyn, and the MOGON high-performance computing cluster for their resources. I also appreciate the support of the administrative and technical staff at INSPIRE. Furthermore, I am grateful for the training and events organized by Young Entrepreneurs in Science, Spin+X, INSPIRE, SPICE, and FZU, which have significantly enriched my research experience.

Lastly, I am profoundly thankful to my family and friends for their unwavering support.

Contents

Introduction

Magnetism is one of the most fundamental, largest, and technologically relevant fields in condensed matter research [1]. Conventionally, collinear magnets have been considered to fall into two main categories: ferromagnets and antiferromagnets. Ferromagnets have a net magnetization, which gives them a spin-polarized electronic structure that breaks time-reversal symmetry, enabling a range of phenomena including *spin-dependent transport*, such as spin-polarized currents and tunneling and giant magnetoresistance. Collinear antiferromagnets have a vanishing net magnetization. Their electronic band structures preserve time-reversal symmetry and are *Kramers spin-degenerate* in the nonrelativistic limit, thus largely removing any spin polarization in the electronic band structure, rendering spin-dependent transport of either weak relativistic origin or completely absent [1].

Anomalous phenomena in compensated, collinear magnets. Recently, anomalous transport phenomena have been observed in collinear magnets that have seemingly combined the properties of both ferromagnets and antiferromagnets. These magnets displaying such anomalous phenomena are magnetically compensated, typical for antiferromagnets, but were shown to host time-reversal symmetry-breaking responses [publication7, publication8, publication9][2, 3, 4, 5, 6, 7, 8, 9, 10, 11, 12, 13, 14] and spin-split [2, 3, 4, 5, 6, 7, 8, 1, 15, 16, 17, 18, 19, 20, 21, 22, 23, 24], time-reversal symmetry breaking [3][publication5] electronic band structures, typical for ferromagnets [1]. This has posed an apparent contradiction between the convention that there are only two main collinear magnetic phases, ferromagnets and antiferromagnets, and the fact that particular collinear magnets exhibit properties of both these phases.

A resolution: a third collinear class of magnets. A resolution to this apparent contradiction came with a complete symmetry classification of all collinear magnets in the nonrelativistic limit, which delineated ferromagnets, antiferromagnets, and yet another, third collinear phase, dubbed altermagnets [25]. The classification used an unorthodox, but generalized symmetry toolbox, crystallographic *spin symmetry groups*. What rigorously distinguishes the third collinear phase of altermagnets from collinear ferromagnets and antiferromagnets from this group theory can be boiled down to the following [25]: Firstly, the magnetic sublattices (sites with opposite mag-

netic moments) of altermagnets can be treated separately in the nonrelativistic limit. Secondly, each sublattice in altermagnets obeys only half the symmetries of the underlying nonmagnetic crystal (contrary to ferromagnets and collinear antiferromagnets, where they obey all symmetries of the nonmagnetic crystal). Lastly, the sublattices are related by rotation symmetries, symmorphic or nonsymmorpic, possibly combined with translations (contrary to ferromagnets, which have no *sublattice-transposing symmetries*, and collinear antiferromagnets, where inversions and translations relate the sublattices) [25]. As a result, the spin symmetry groups of ferromagnets, antiferromagnets, and altermagnets take three distinct forms, see Eqs. (1.27)-(1.29), making them distinct phases of collinear magnets [25], as phases of matter are in general distinguished by their symmetries (the Landau paradigm) and topology [26].

The distinct spin symmetries of collinear ferromagets, antiferromagnets, and altermagnets manifests in their electronic structures. In real space, the spin-polarized electronic structure takes the form of *spin*, or, *magnetization densities*; in reciprocal space, as *electronic band structures*. Interestingly, all altermagnets, even though they are magnetically compensated, have spin-split energy bands that lift Kramers spin degeneracy due to their particular spin symmetry [25].

Altermagnetic lifting of Kramers spin degeneracy. Conventionally, two internal mechanisms have been considered to enable *lifting of Kramers spin degeneracy* (LKSD) in magnets. The first is ferromagnetism, or net magnetization, which is typically strong. It originates from *magnetic exchange*, a robust interaction in these electronic systems that lowers the total energy by forming local magnetic moments due to the combination of Pauli's exclusion principle and Coulumb interaction [27, 28]. The second mechanism is enabled in systems that break inversion symmetry, and it is typically weaker because it originates from *relativistic spin-orbit coupling*, which is a perturbative correction in common elements such as Fe or Si [29]. In altermagnets, LKSD is allowed, even without net magnetization and inversion symmetry breaking in real space or relativistic spin-orbit coupling [25].

In our work, we have contributed to a confirmation of altermagnetic LKSD via first-principles calculations of the electronic structure in collaboration with first photoemission spectroscopy experiments on the topic [30, 31]. We find two distinct LKSD mechanisms in the semiconducting altermagnetic candidate MnTe: *strong* and *weak* altermagnetic LKSD [30]. The strong LKSD arises from the altermagnetism itself (it is observed away from the planes that would be nodal in the nonrelativistic limit). The weak LKSD combines altermagnetism with spin-orbit coupling (lifting the Kramers spin degeneracy along the planes). The computational prediction of the weak LKSD is shown in Fig. 1(left) and is in excellent agreement with the experimental spectroscopically obtained spectra in Fig. 1(right) [30].

The weak LKSD mechanism is distinct from the abovementioned ferromagnetic

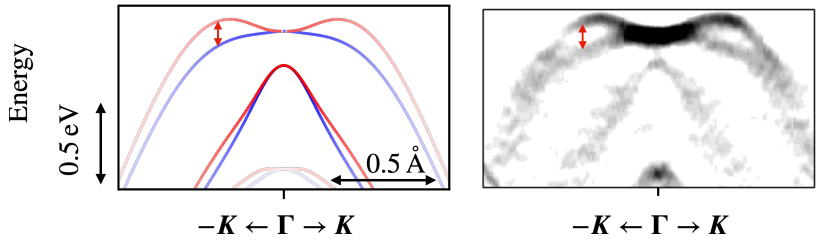

Figure 1: Weak altermagnetic LKSD in MnTe. Left: our first principles calculation of the weak altermagnetism in the electronic band structure (the red/blue coloring marks the spin polarization). Right: our collaborative experimental signature of the altermagnetic LKSD with photoemission. For details, see Ch. 3. Figure adapted from [30], CC BY 4.0.

and inversion-symmetry-breaking LKSD mechanisms, and it lifts in *the altermagnetic form* [25, 3], as we can see from Fig. 1:

Remark 1. ***The altermagnetic form of spin degeneracy lifting.*** *(i) The bands meet at the* $\mathbf{\Gamma}$*-point (or nodal surfaces in general) and spin-split away from it. It does not split at the* $\mathbf{\Gamma}$*-point, which would otherwise be a signature of ferromagnetism or net magnetization (a constant Zeeman term* $\sim k^0$ *around* $\mathbf{\Gamma}$*, where* k *is the wavevector). (ii) The bands break time-reversal symmetry, i.e.,* $\epsilon_n(k,s) \neq \epsilon_n(-k,-s)$ *where* s *is the spin index, and are (iii) centrosymmetric in the nonrelativistic limit, i.e.,* $\epsilon_n(k,s) = \epsilon_n(-k,s)$*, as well as in the relativistic limit in the presence of crystal inversion symmetry (this makes them distinct from relativistic spin-orbit split bands in noncentrosymmetric crystals). The bands thus disperse quadratically (*$\sim k^2$*), concurrent with the inversion symmetry of the system (in general, crystal inversion symmetry, but notably also collinear magnetism impose inversion symmetry of the band structure, limiting the Hamiltonian around* $\mathbf{\Gamma}$ *to only contain even terms in* k *[25]).*

These, *(i)-(iii)*, are hallmarks of the altermagnetic LKSD in MnTe and altermagnets generally, which we observe in both our density functional theory (DFT) calculations and the collaborative experimental spectra from Fig. 1 [publication3]. Additionally, three other works on MnTe appeared that also shows LKSD [32, 33, 34], thus further strengthening the experimental evidence for LKSD in MnTe and the band structure of MnTe being altermagnetic.

We also confirm the strong altermagnetic LKSD in the altermagnetic candidate, CrSb [31]. Notably, it belongs to the same spin symmetry group as MnTe, and thus, its magnetic crystal and band structure exhibit the same spin symmetries. It has a higher critical temperature of $705\,K$ [35] than MnTe (that of MnTe is $323\,K$ [36]) and unlike MnTe, CrSb is metallic [37]. Moreover, our collaborative work with the first spectroscopy experiment on a candidate heavily discussed for the possibility of altermagnetism, RuO_2, indicates that the band structure breaks time-reversal symmetry [38].

A natural question to ask now is: Are there further types of unconventional magnetic orders? For instance, altermagnets and ferromagnets are even-parity-wave on the nonrelativistic level, as their electronic structures preserve inversion symmetry [25]. Can there also exist magnetically compensated *odd-parity-wave* magnets whose nonrelativistic electronic structures break inversion symmetry, i.e., $\epsilon_n(k,s) \neq \epsilon_n(-k,s)$, and preserve time-reversal symmetry, i.e., $\epsilon_n(k,s) = \epsilon_n(-k,-s)$, opposite to altermagnets?

Odd-parity-wave magnets. Over several decades, the possibility of realizing odd-parity-wave, *p-wave* magnetism (p-wave magnets being odd-parity-wave magnets with a single nodal surface) from correlations and instabilities around the Fermi surface has been explored [39, 40, 41, 42]. However, these approaches are limited to metals, and there have been conceptual hurdles to realizing p-wave magnetism in this way [39, 40, 43, 41, 42]. In the footsteps of altermagnetism research, we focus instead on magnetic exchange to realize p-wave and odd-parity-wave magnetism in general (e.g., p-, f-wave, and so on). Magnetic exchange is typically associated with large energy scales and thus often dominates the overall form of the electronic structure. If we could identify odd-parity-wave magnetism arising from magnetic exchange, we thus would not rely on materials with large relativistic spin-orbit coupling [40], which would limit us to heavy elements which are often rare and toxic.

Magnetic exchange and the magnetic crystal structure naturally occurring in a potential material candidate could also symmetry-protect the p-wave and odd-parity-wave magnetism, making the phase robust. Here [publication1], we identify the spin symmetries required for p-wave magnetism and odd-parity-wave magnetism in general. We demonstrate it in a realistic material candidate CeNiAsO using first-principles calculations as shown in Fig. 2. We emphasize that we also demonstrate by our spin symmetry arguments that we can obtain a collinear p-wave spin-polarization of the electronic band structure in momentum space, even though the spin order of the magnetic crystal of all p-wave and odd-parity-wave magnets has to be noncollinear in real space.

Symmetry guidelines for p-wave and odd-parity-wave magnetism. The symmetry guidelines for the p-wave magnetism we have identified can be summarized as follows, see Ch. 3.2.2 [publication1]:

- Noncollinear magnetic order in the magnetic crystal.
- Break inversion symmetry in the magnetic crystal.
- Preserve $\mathcal{T}\mathbf{t}$ symmetry in the magnetic crystal ($\mathbf{t}$ is a translation).
- Have a single, symmetry-enforced nodal surface.

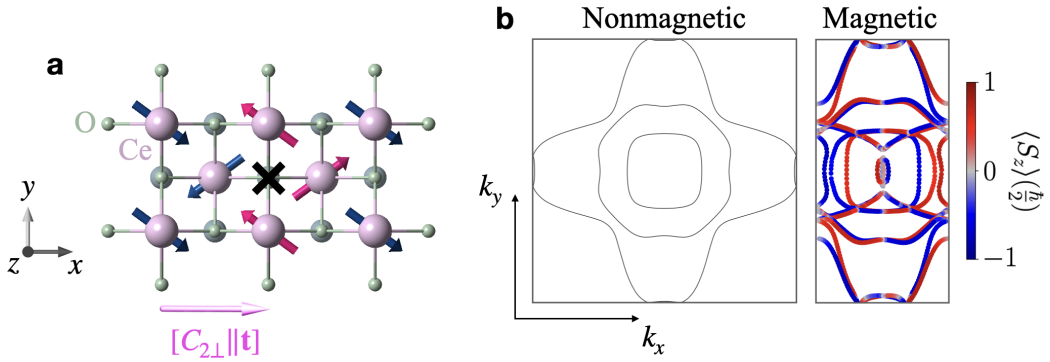

Figure 2: P-wave magnetism in candidate material CeNiAsO. (a) The magnetic crystal structure projected in the $x-y$ plane shows the symmetry conditions for p-wave magnetism, detailed in the main text. The red/blue arrows indicate the coplanar magnetization vectors in the Ce atoms measured experimentally [44]. The cross denotes the inversion symmetry breaking resulting from the magnetic order (by comparison, the nonmagnetic crystal would otherwise have an inversion center at this cross). The bottom magenta arrow shows the $[C_{2\perp}||\mathbf{t}]$ symmetry relating the blue to the red magnetizations. This symmetry doubles the unit cell (and halves the Brillouin zone) compared to the nonmagnetic unit cell along $\mathbf{t}$. (b) Fermi surfaces for nonmagnetic and magnetic CeNiAsO, calculated using density functional theory (for details regarding it and the calculation, see Chs. 2.3.6 and 3.2). Due to the particular magnetic order and corresponding spin symmetries (outlined under "symmetry guidelines" in the main text), the magnetic Fermi surface is p-wave with an anisotropic, odd-parity, collinear spin polarization with a single symmetry-enforced nodal surface (which intersects the k_y-axis here). The p-wave Fermi surface band sheets are distorted and mutually shifted away from the origin in opposite directions for opposite spin polarizations. It breaks the symmetries of the underlying nonmagnetic lattice and the corresponding nonmagnetic Fermi surface. Figure adapted from [publication1], CC BY-NC-SA 4.0.

The first two points ensure the energy bands are inversion symmetric, the $\mathcal{T}\mathbf{t}$ symmetry that they are time-reversal symmetric. Furthermore, in coplanar systems, we can preserve $[C_{2\perp}||\mathbf{t}]$ spin symmetry in the magnetic crystal ($C_{2\perp}$ is a two-fold spin-space rotation around an axis oriented perpendicular to the coplanar spins in the crystal), yielding a collinear spin-polarization in reciprocal space. We illustrate these symmetries on the coplanar magnetic CeNiAsO crystal in Fig. 2(a). Using our spin symmetry criteria, we collaboratively identify more than 40 realistic material candidates for collinear, p-wave spin-polarization [publication1]. If we lift the last requirements of a single nodal line and coplanar spin order, we obtain rules for generic odd-party wave magnets that can host noncollinear spin polarizations in momentum space and higher-partial wave channels (e.g., f-wave).

Symmetry-lowering in the electronic structure. We note that the electronic structure of altermagnets and odd-parity-wave magnets—in real and reciprocal space—obeys fewer symmetries than the electronic structure of the underlying nonmagnetic crystal [publication1][25, 45]. For example, the p-wave Fermi surface breaks the four-

fold rotation symmetry of the nonmagnetic Fermi surface in Fig. 2 [publication1], and each spin channel in altermagnets typically obeys half of the symmetries of the nonmagnetic crystal (see Ch. 1.3.2) [25]. Altermagnets and odd-parity-wave magnets thus differ from, for example, ferromagnets and collinear antiferromagnets on the nonrelativistic level, whose separate spin channels obey all symmetries of the nonmagnetic crystal [25]. The symmetry-lowering of the energy bands in altermagnets and odd-parity-wave magnets can be viewed as an analogy to the symmetry-lowering in unconventional d-wave superconductors [1, 25], where the order parameter breaks symmetries of the crystal [46]. Interestingly, in altermagnets and p-wave magnets, the symmetry-lowering makes their electronic structure anisotropic, which can explain spin-dependent transport in these magnets [publication1, publication6, publication2][25, 7].

Spin-dependent transport in p-wave magnets and altermagnets. We predict anisotropic transport as an effect related to p-wave magnetism. It is a charge transport signal, which is *spin-dependent*. The anisotropic transport is allowed as a result of the anisotropic, low-symmetry, spin-polarized electronic structure of the p-wave order shown in Fig. 2(b), and it is absent in the nonmagnetic case [publication1]. We have simulated the effect with minimal models and collaboratively demonstrated the effect with first-principle simulations of CeNiAsO [publication1]. Moreover, we have collaboratively shown that p-wave magnets host a nonrelativistic counterpart of the Edelstein effect, i.e., a spin density accumulation due to an applied electric field [publication2].

In our collaborative work, we have furthermore studied unconventional transport in Mn_5Si_3 [publication7, publication8, publication9]. It has a complex phase diagram with numerous proposed magnetic orderings at different temperatures and pressures.

We note that the proposed AF1 phases below $60\,K$ [47, 48] obey our symmetry guidelines for odd-parity-wave magnetism, and thus, odd-parity-wave magnetism may contribute to unconventional transport in this phase [publication9, publication1].

We collaboratively also show experimentally that thin-film Mn_5Si_3 hosts large anomalous Hall effect and Nernst effects that do not originate from net magnetization [publication7, publication8]. It is consistent with a collinear, altermagnetic phase where the electronic structure breaks time-reversal symmetry [publication7, publication8], where we take the magnetic moments to be concentrated on the four our of ten Mn sites similarly to the collinear AF2 phase for $60\,K < T < 100\,K$ [publication9][49, 50] of bulk Mn_5Si_3 [publication7].

Spin-dependent transport in altermagnets. Given that, similarly to ferromagnets, the electronic structure of altermagnets breaks time-reversal symmetry and can have robust spin-polarizations with large spin-splittings, we now ask [publication6] if altermagnets, in analogy to ferromagnets, can host spin-polarized currents and giant

magnetoresistance effects?

In ferromagnets, magnetic exchange spin-splits the electronic band structure, producing spin states with different occupations and majority and minority spin channels. The majority and minority spin channels give rise to different resistivities of the two spin channels, and hence *giant magnetoresistance* (GMR) in ferromagnet-metal-ferromagnet devices, and the different occupations allow for *tunneling magnetoresistance* (TMR) in ferromagnet-insulator-ferromagnet devices [51, 52, 53]. Read-out via spin transfer torque (STT) is allowed due to spin-polarized currents [54, 55, 56].

Conventional antiferromagnets with Kramers spin degenerate electronic structures have been proposed to host tunneling magnetoresistance, but their mechanisms are more fragile and fundamentally different from the ferromagnetic mechanism. One antiferromagnetic TMR mechanism in collinear antiferromagnets is based on coherently interfering, staggered currents [57]. This mechanism is, however, subtle, as it requires the multilayers to be epitaxial with pristine interfaces [58]. Another proposed mechanism is TMR arising from a net ferromagnetic moment at the ferromagnet-insulator interface due to the specific termination of the antiferromagnet [59]. Both are delicate effects, which may explain why they have not been experimentally viable so far [58].

Instead, the antiferromagnetic spintronics field has turned to spin-orbit-coupling-induced effects to circumvent the challenge of functionalizing antiferromagnets. Leveraging spin-orbit coupling effects, the field has sucsessfully demonstrated numerous functionalities in antiferromagnets, including reading and writing [60, 61, 62, 63, 64, 65, 66, 67, 68, 69, 70], and ultrafast dynamics [71, 72], but TMR, GMR, and STT based on robust spin-dependent currents, in analogy to ferromagnets, has remained elusive.

Here [publication6], we instead develop TMR and GMR concepts based on altermagnets.

Spin-polarized currents and giant magnetoresistance in altermagnets. Using spin symmetry analysis and minimal bulk models, we show that altermagnets host robust, spin-polarized, longitudinal currents and GMR as illustrated in Fig. 3 [publication6]. GMR in altermagnets is enhanced by *anisotropic spin polarization* features in their electronic structure. These features gives rise to spin-polarized currents, illustrated Fig. 3(a), and thus GMR, illustrated in Fig. 3(b) in analogy to ferromagnets [publication6]. Based on spin symmetries and linear response, we collaboratively find that d-wave altermagnets host these spin-polarized currents [publication6]. At the same time, they are disallowed, at least for the symmetric part of the conductivity tensor, expected to be the largest contribution [7], for linear response in g- and i-wave magnets[publication6]. We collaboratively verify the concept in the altermagnetic candidate RuO_2 and note that the spin-polarized currents can give rise to STT [publication6].

Notably, we predict that the more anisotropic the spin polarization is, the larger

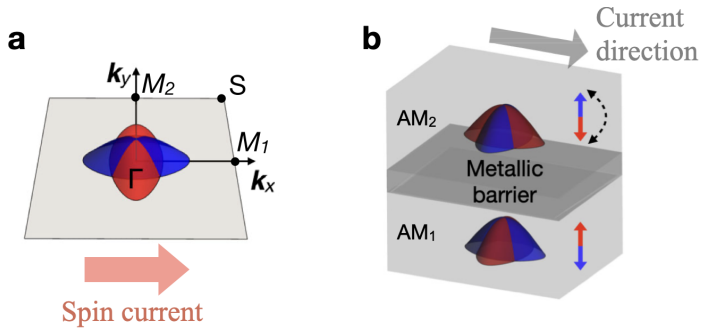

Figure 3: Archetype mechanism for GMR in altermagnets. (a) Anisotropic spin polarization and spin current in the electronic band structure of a d-wave altermagnet. The red and blue colors signify the opposite spin expectation values of the bands, and the gray square and annotations show the Brillouin zone. This type of spin polarization gives rise to a spin-polarized current because the spin current contributed from one spin channel is greater than that of the other. (b) GMR stack in a current-in-plane geometry. Here, we show the antiparallel configuration where the Néel vectors of the two altermagnets, the red-blue double arrows, are antiparallel in the two altermagnetic electrodes, AM_2 and AM_2. For details, see Chs. 4.1, 4.1.2, and 4.3, and [publication6]. Figure adapted from [publication6], CC BY 4.0.

the spin current and corresponding GMR, which we also verify in the RuO_2 calculations. Moreover, we discuss that the spin-splitter effect, predicted [7] and indicated experimentally via the torque it excerts on a ferromagnet [9, 10, 11], also increases with this increasing nonrelativistic altermagnetic anisotropy, and corroborate it in our collaborative RuO_2 calculations.

Tunneling magnetoresistance in altermagnets. TMR in altermagnets can arise from—and be enhanced by—*valley spin polarization* features of the altermagnetic spin-momentum locking in the electronic band structure [publication6], as illustrated in Fig. 4. This type of spin polarization gives rise to spin-dependent tunneling for the parallel and antiparallel geometries, shown in Fig. 4(a,b), and valley-dependent spin-polarized densities of states, and hence TMR.

We verify our TMR concept via minimal models and transport simulations of altermagnet-insulator-altermagnet heterostructures [publication6]. The TMR persists for various system sizes and orientations [publication6]. For example, the alternating spin polarization shown in Fig. 4 lies in a plane perpendicular to the interface. But we can equally well orient it such that it is in-plane with the interface, and have TMR [publication6]. We have also verified with our models that we can equally well use a ferromagnet for the second electrode and produce TMR due to the analogous mechanism.

By symmetry, all altermagnets—d-, g-, and i-wave—can host our TMR mechanism as they all possess spin-polarized, spin-momentum-locked energy bands and valley spin polarization character in their electronic structure [publication6]. We also discuss

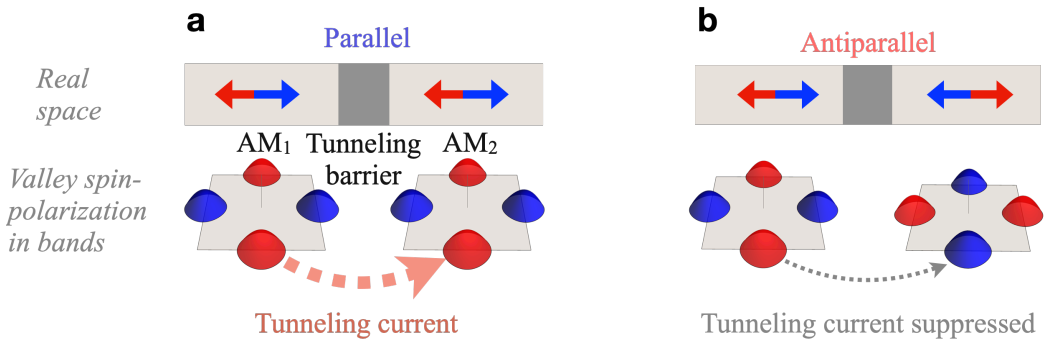

Figure 4: Our TMR mechanism in altermagnets. Here, we highlight the valley spin polarization features in the electronic band structure. They enhance the TMR effect. (a) The upper panel shows the set-up in real space, with two altermagnetic electrodes separated by a tunneling barrier. The double red and blue arrows indicate the Néel vector orientations in the two altermagnets, which are identical and thus *parallel*. The lower panel shows the corresponding valley-spin polarization in the band structure for these parallel Néel vectors. When the spin and wavevector in the band structure of the two altermagnets match, it promotes tunneling current indicated by the red dashed arrow between two same-spin valleys. In (b), the Néel vector in the right electrode is antiparallel to the Néel vector in the left electrode. Therefore, the corresponding spin polarization of the valleys changes sign. This sign-change suppresses the tunneling current because there are fewer available states to tunnel into with the same spin. Inter-valley scattering can alter the tunneling current, but in analogy to conventional valleytronics [73], inter-valley scattering can be suppressed due to the here symmetry-enforced, large distance between the valleys in reciprocal space. In our work, we also find that the more valley-like the band structure is (the valley character) at a given energy of incident electrons in an electrode, the larger the TMR [publication6] Figure adapted from [publication6][1], CC BY 4.0.

the correspondence between our models and altermagnetic candidates, RuO_2 and Mn_5Si_3, and the criteria for identifying materials with large spin-polarized currents and TMR.

Our mechanism for TMR and GMR in altermagnets is analogous to that in ferromagnets. It arises from magnetic exchange, allowing the bulk electronic band structure to spin-split, producing spin-dependent transport. It is not a subtle quantum interference effect, nor is it due to a net ferromagnetic moment at the magnet-spacer interface from the studies mentioned above [57, 58, 59] on collinear antiferromagnets.

Independent work on TMR, where the alternating spin-polarization was considered in-plane with the interface in $RuO_2/TiO_2/RuO_2$, has shown that with a different orientation (current applied out-of-the d-wave plane) can also lead to TMR via a distinct, so-called spin neutral current mechanism [13]. Furthermore, other works have also demonstrated TMR with different magnetically compensated systems, namely noncollinear and time-reversal symmetry breaking Mn_3X systems (X=Sn [74], Pt [75]), reaching 2% [74] and 100% experimentally [75]. However, altermagnets may

be promising for high TMR values due to the collinear spin polarization of their band structure, which, in principle, could be associated with higher spin coherence than noncollinear spin textures in the band structure, because electrons scattering and changing their wavevector may generally be less likely to suffer an additional change in their spin polarization.

Outlook. Our evidenced LKSD in metal and semiconducting altermagnets may have broad consequences for magnetism research. It motivates to explore and exploit unconventional phenomena in a wide variety of altermagnets, ranging from insulators to superconductors [25, 1], in materials newly identified as altermagnets, or materials that for decades have been regarded as conventional antiferromagnets [1, 76, 36, 35, 77, 78]. Our work opens up the possibility to identify and exploit altermagnets and odd-parity-wave magnets for spin-dependent transport and superior spintronics concepts based on compensated magnets and light elements, such as giant magnetoresistance effects [publication6], but also nonrelativistic anisotropic transport and charge-to-spin conversion traditionally reserved for systems comprising heavy relativistic elements [publication1, publication2].

Structure of thesis. This thesis is structured as follows.

In Ch. 1, we show how we can use general symmetry arguments to predict the symmetries of electronic structures. We introduce symmetries, crystals, and groups (Ch. 1.1), and explain the basic premise of spin symmetries in the crystallographic spin symmetry formalism (Ch. 1.2.1). We review how spin symmetries can systematically delineate, first, collinear, coplanar, and noncoplanar magnets (Ch. 1.2.2), and then, all collinear magnets (ferromagnets, antiferromagnets, and altermagnets in Ch. 1.3). We review the three distinct and mutually exclusive types of spin Laue groups for collinear magnets and how to understand the subtle and conventionally overlooked consequences of the third group that describes altermagnets (Chs. 1.3,1.8). We also review Kramers theorems for magnetic crystals (Ch. 1.6), which eludes to its lifting in odd-parity-wave magnets and altermagnets (Chs. 3,1.8). We review how to derive symmetry-enforced nodal surfaces in altermagnets (Ch. 1.8), which is a pre-requisite for studying LKSD in MnTe, CrSb, and RuO_3 in Ch. 3.

In Ch. 2, we review electronic structure theory. We explain band formation in tight-binding models (Ch. 2.1) and show a derivation of our altermagnetic models (Ch. 2.2) which we use to simulate TMR in Ch. 4 and which captures parts of the band structure of certain altermagnetic candidate materials (e.g., RuO_3 in Ch. 3.1.8). We also review spin-full density functional theory (Ch. 2.3), which we use to calculate the electronic structure of altermagnets for the collaborative theory-experiment verification of LKSD and for predicting p-wave magnetism in Ch. 3.

In Ch. 3, we describe our symmetry analysis (Chs. 3.1.1-3.1.3,3.1.5,3.2.1-3.2.6) and DFT calculations (Ch. 3.1,3.1.4-3.1.8), leading to the electronic structure of strong

and weak altermagnetism and its agreement with collaborative experimental results (Chs. 3.1.4-3.1.8), and our prediction of p-wave and odd-parity magnetism (Ch. 3.2).

In Ch. 4, we predict longitudinal spin-currents and GMR (Chs. 4.1,4.1.1-4.1.2,4.3), and spin-dependent tunneling and TMR (Chs. 4.1.3,4.2) in altermagnets. We elucidate their general symmetry criteria and origin and enhancement via the anisotropic and valley spin polarization character in the electronic band structure (Chs. 4.1.1-4.1.3,4.4,4.5). We explicitly demonstrate our GMR and TMR concepts in simulations, with models (from Ch. 2.2) simulation of trilayers using the Landauer-Büttiker formalism (Chs. 4.1.4, 4.2), and collaboratively using DFT (Ch. 4.3). We discuss material design based on our TMR and GMR concepts (Chs. 4.4-4.5).

In the conclusion chapter, we summarize and compare altermagnetism and odd-parity-wave magnetism studied here and provide an outlook on its potential for superior spintronics concepts.

Publications

[publication1] Anna Birk Hellenes, Tomáš Jungwirth, Rodrigo Jaeschke-Ubiergo, Atasi Chakraborty, Jairo Sinova, and Libor Šmejkal. P-wave magnets. *ArXiv 2309.01607v3*, sep 2023.

[publication2] Atasi Chakraborty, Anna Birk Hellenes, Rodrigo Jaeschke-Ubiergo, Tomas Jungwirth, Libor Šmejkal, and Jairo Sinova. Highly Efficient Non-relativistic Edelstein effect in p-wave magnets. *ArXiv 2411.16378*, nov 2024.

[publication3] J Krempaský, L Šmejkal, S. W. D'Souza, M Hajlaoui, G Springholz, K Uhlířová, F Alarab, P C Constantinou, V. Strocov, D Usanov, W R Pudelko, R González-Hernández, A. Birk Hellenes, Z Jansa, H Reichlová, Z Šobáň, R. D. Gonzalez Betancourt, P Wadley, Jairo Sinova, D Kriegner, J Minár, J H Dil, and T Jungwirth. Altermagnetic lifting of Kramers spin degeneracy. *Nature*, 626(7999):517–522, feb 2024.

[publication4] Sonka Reimers, Lukas Odenbreit, Libor Šmejkal, Vladimir N. Strocov, Procopios Constantinou, Anna B. Hellenes, Rodrigo Jaeschke Ubiergo, Warlley H. Campos, Venkata K. Bharadwaj, Atasi Chakraborty, Thibaud Denneulin, Wen Shi, Rafal E. Dunin-Borkowski, Suvadip Das, Mathias Kläui, Jairo Sinova, and Martin Jourdan. Direct observation of altermagnetic band splitting in CrSb thin films. *Nature Communications*, 15(1):2116, mar 2024.

[publication5] Olena Fedchenko, J. Minar, Akashdeep Akashdeep, S. W. D'Souza, Dmitry Vasilyev, Olena Tkach, Lukas Odenbreit, Q. L. Nguyen, Dmytro Kutnyakhov, Nils Wind, Lukas Wenthaus, Markus Scholz, Kai Rossnagel, Moritz Hoesch, Martin Aeschlimann, B. Stadtmueller, M. Klaeui, G. Schoenhense, Gerhard Jakob, Tomas Jungwirth, L. Smejkal, Jairo Sinova, and H. J. Elmers. Observation of time-reversal symmetry breaking in the band structure of altermagnetic RuO_2. *Science Advances*, 10(5):31, feb 2024.

[publication6] Libor Šmejkal, Anna Birk Hellenes, Rafael González-Hernández, Jairo Sinova, and Tomas Jungwirth. Giant and Tunneling Magnetoresistance in Unconventional Collinear Antiferromagnets with Nonrelativistic Spin-Momentum Coupling. *Physical Review X*, 12(1):011028, feb 2022.

[publication7] Helena Reichlova, Rafael Lopes Seeger, Rafael González-Hernández, Ismaila Kounta, Richard Schlitz, Dominik Kriegner, Philipp Ritzinger, Michaela Lammel, Miina Leiviskä, Anna Birk Hellenes, Kamil Olejník, Vaclav Petříček, Petr Doležal, Lukas Horak, Eva Schmoranzerova, Antonín Badura, Sylvain Bertaina, Andy Thomas, Vincent Baltz, Lisa Michez, Jairo Sinova, Sebastian T. B. Goennenwein, Tomáš Jungwirth, and Libor Šmejkal. Observation of a spontaneous anomalous Hall response in the Mn_5Si_3 d-wave altermagnet candidate. *Nature Communications*, 15(1):4961, jun 2024.

[publication8] Antonin Badura, Warlley H. Campos, Venkata K. Bharadwaj, Ismaïla Kounta, Lisa Michez, Matthieu Petit, Javier Rial, Miina Leiviskä, Vincent Baltz, Filip Krizek, Dominik Kriegner, Jan Zemen, Sjoerd Telkamp, Sebastian Sailler, Michaela Lammel, Rodrigo Jaeschke Ubiergo, Anna Birk Hellenes, Rafael González-Hernández, Jairo Sinova, Tomáš Jungwirth, Sebastian T. B. Goennenwein, Libor Šmejkal, and Helena Reichlova. Observation of the anomalous Nernst effect in altermagnetic candidate Mn_5Si_3. *ArXiv 2403.12929*, mar 2024.

[publication9] Christoph Sürgers, Gerda Fischer, Warlley H. Campos, Anna Birk Hellenes, Libor Šmejkal, Jairo Sinova, Michael Merz, Thomas Wolf, and Wolfgang Wernsdorfer. Anomalous Nernst effect in the noncollinear antiferromagnet Mn_5Si_3. *Communications Materials*, 5(1):176, aug 2024.

Chapter 1

Symmetries of magnetic crystals

Symmetry is fundamental in physics, serving as a tool to understand the laws of nature in fields ranging from general relativity to condensed matter physics. The predictive power of symmetry analysis is exemplified by its comprehensive predictions throughout decades of research in magnetism and nanoelectronics, ranging from characterizing relativistic symmetries of magnets to dissipation-less electronic transport phenomena and topological quasiparticles [79, 2, 80, 81]. In general, phases of matter are distinguished by their symmetries (the Landau paradigm) and topology [26]. In the emerging field of altermagnetism, an unorthodox symmetry toolbox, *spin symmetries* [1, 82, 83, 23, 84, 85, 86], have allowed delineating collinear magnetic orders into three distinct phases [1].

We employ the unorthodox crystallographic spin symmetry framework to fully describe the emergence of altermagnetism and odd-parity-wave magnetism, as the conventional magnetic symmetry framework does not allow disentangling magnetic and spin-orbit coupling related symmetry-breakings [83, 25, 84]. This chapter introduces and reviews symmetry frameworks instrumental to our work.

First, we describe group theory and symmetries specific to crystals, followed by the crystallographic spin group theory framework and its delineation of collinear, coplanar, and noncoplanar magnets. We then review the crystallographic spin symmetries of altermagnets and their consequences for altermagnetic spin splittings and *lifting of Kramers spin degeneracy* (LKSD).

The crystallographic spin symmetry framework we present here provides crucial insight for our work into which symmetries of magnetic crystals enable the LKSD in altermagnets and odd-parity-wave magnets and how transport can be spin-dependent and spin-polarized, even when these magnets are overall magnetically compensated. The framework has provided new insight into magnetism research that has enabled the identification of more altermagnets than there are known ferromagnets, ranging from insulators to superconductors, and which has already provided an expanded play-

ground throughout condensed matter physics research areas [25, 87, 88, 89, 90, 91, 92].

We then explain why magnets with $\mathcal{T}\mathbf{t}$ symmetry (type-IV magnets, $\mathcal{T}$ is time-reversal and $\mathbf{t}$ a real space translation) can be spin-split in noncollinear noncentrosymmetric magnets [93]. Remarkably, this observation has, hitherto, been largely overlooked in existing literature. This degeneracy lifting is a vital piece of the symmetry guidelines that have enabled us to identify odd-parity-wave and p-wave magnetism [93], which we will discuss in detail in Ch. 3.2.

1.1 Introduction to symmetry and groups

1.1.1 Symmetry operations in quantum mechanics

Before we describe symmetry and group theory, we recap how rotations, translations, inversion (parity), and time reversal operations act in quantum mechanics. This will clarify the differences between acting, for example, with time reversal on eigenstates and expectation values; the former is associated with a phase factor, the latter with being either even or odd under time reversal. This difference arises from time reversal being an antiunitary operator [94]. We now define antiunitary operators and show that time reversal is one. Time reversal being antiunitary is part of the reason why some magnets are Kramers spin degenerate (see Ch. 1.6) [95, 96].

Transforming quantum states. Consider a transformation of two different eigenstates of a system, $|\alpha\rangle$ and $|\beta\rangle$ into their transformed eigenstates $|\tilde{\alpha}\rangle$ and $|\tilde{\beta}\rangle$:

$$|\alpha\rangle \to |\tilde{\alpha}\rangle, \quad |\beta\rangle \to |\tilde{\beta}\rangle. \tag{1.1}$$

For unitary symmetries, such as rotations, translations, and even parity[1], the original and transformed eigenstates obey

$$\langle\tilde{\beta}|\tilde{\alpha}\rangle = \langle\beta|\alpha\rangle\,. \tag{1.2}$$

Eq. (1.2) holds for all unitary operators (the unitary operator U obeys $U^\dagger U = 1$ and $UU^\dagger = 1$) [94] In contrast, the time-reversal symmetry operator $\mathcal{T}$ is antiunitary, and therefore, the following holds for the original and transformed eigenstates [94]:

$$\langle\tilde{\beta}|\tilde{\alpha}\rangle = \langle\beta|\alpha\rangle^*\,. \tag{1.3}$$

We note that, per definition, an antiunitary operator obeys Eq. (1.3) and

$$\Theta(c_1|\alpha\rangle + c_2|\beta\rangle) = c_1^*\Theta|\alpha\rangle + c_2^*\Theta|\beta\rangle. \tag{1.4}$$

Here, c_1 and c_2 are complex numbers. An operator that obeys Eq. (1.4) alone is *antilinear*. We show that $\mathcal{T}$ is *antiunitary* in Appendix A.

[1] In quantum mechanics, even parity refers to inversion symmetry that is even and thus does not change the overall sign of the eigenstate [94].

Basis and spin quantization axis for spin-half systems. Throughout this thesis, we will consider both collinear and noncollinear magnetic systems. We now show that whether spin can be a *good quantum number* generally depends on whether a magnetic system comprises collinear or noncollinear spins, which is one aspect contrasting these two types of systems.

Fig. 1.1 illustrates collinear spins (found in collinear magnetic systems) and a corresponding *spin-quantization axis*. We can always choose the basis kets to equal the eigenkets for systems with collinear spins. Therefore, there is always a *spin-quantization axis* (the axis of the spin basis kets), which aligns with the axis of the spin eigenkets. For example, suppose all the collinear spins lie along the z-axis in real space with corresponding $\pm S_z$ eigenkets (as illustrated by the red and blue arrows in Fig. 1.1). In that case, we can align the basis with it by choosing the basis also to be $\pm S_z$ (yellow arrow in Fig. 1.1). When the spin basis kets and eigenkets are the same, we say that spin is a *good quantum number*. The spins are associated with either a 100% or a 0% probability, as, for example projecting $|\uparrow\rangle$ onto a spin up or down with $|\sigma\rangle\langle\sigma|$ (here, σ is the spin index), always yields either spin up or down.

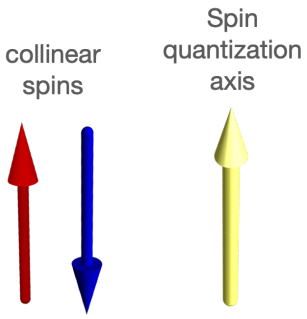

Figure 1.1: Spin quantization axis (yellow arrow) for a collinear spin configuration (red, blue arrows). It can always be aligned with the collinear spins.

However, for systems with noncollinear spins, e.g., two spins S_y and S_z, spin is not a *good quantum number*. For example, if we choose the *spin-quantization axis* to be along S_z (choosing the S_z basis), then the S_y eigenkets are a linear combination of S_z eigenkets as in Eq. (50) in Appendix B. Projecting this onto spin up yields spin up with a 50% probability. In other words, if this spin was measured by a detector represented by the projection operator $|\uparrow\rangle\langle\uparrow|$, it would measure no spin half of the time. Similarly, if we choose the spin quantization axis to be along S_y (the S_y basis), then the S_z eigenkets are associated with a 50% probability. There is no way to project all the spins in the system onto the spin quantization axis with either 100% or 0% probability, so spin is not a *good quantum number* in noncollinear systems.

Acting with $\mathcal{T}$ on spin expectation values, positions, and wavevectors. In addition to keeping track of the spin quantization axis, we will also distinguish between whether an antiunitary operator acts on a ket (a wavefunction) or an expectation value. In describing the symmetries of a system, we will choose in this thesis to focus on symmetry operations acting on the expectation values of the spins, e.g., as commonly

done in the crystallographic spin group framework [82, 83, 25].

Spin expectation values, given by

$$s_i = \langle\alpha|S_i|\alpha\rangle, \tag{1.5}$$

only aquire an overall sign under time-reversal $\mathcal{T}$,

$$\langle\alpha|S_i|\alpha\rangle = -\langle\tilde{\alpha}|S_i|\tilde{\alpha}\rangle \tag{1.6}$$

i.e., it is *odd in* $\mathcal{T}$. It does not acquire a phase under time-reversal (contrary to a ket, which would) [94]. Other *odd-in-*$\mathcal{T}$ observables include wavevectors (reciprocal space k-vectors) and quantum angular momentum. Other *even-in-*$\mathcal{T}$ observables include real space position. In summary, time-reversal acting on a spin expectation value s and wavevector k inverts both:

$$\mathcal{T}: \ (s,k) \to (-s,-k). \tag{1.7}$$

When acting on a spin expectation value and a position in real space, it only inverts the spin [83]:

$$\mathcal{T}: \ (s,x) \to (-s,x). \tag{1.8}$$

1.1.2 Crystals and Bloch's theorem

Symmetry analysis of spin-full systems can be applied to spins alone, or to spins in crystals. Crystals are translationally invariant, periodic systems. Therefore, the system is composed of patterns of atomic sites that compose a *unit cell* which repeats according to the periodicity of the particular system. In general, we can define the unit cell as a cell spanned by lattice vectors $\mathbf{a}_1, \mathbf{a}_2$, and $\mathbf{a}_3$ in three-dimensional real-space. The periodicity of the crystal is then given in terms of the lattice vector [97],

$$\boldsymbol{R} = n_1\mathbf{a}_1 + n_2\mathbf{a}_2 + n_3\mathbf{a}_3 \quad (n_i \text{ are integers}), \tag{1.9}$$

and the corresponding reciprocal lattice vector,

$$\boldsymbol{G} = n_1\mathbf{b}_1 + n_2\mathbf{b}_2 + n_3\mathbf{b}_3 \quad (n_i \text{ are integers, } \mathbf{b}_i \text{ are reciprocal lattice vectors}). \tag{1.10}$$

The reciprocal lattice vectors $\mathbf{b}_i$ are given by [97]

$$\mathbf{b}_1 = 2\pi\frac{\mathbf{a}_2 \times \mathbf{a}_3}{V}, \quad \mathbf{b}_2 = 2\pi\frac{\mathbf{a}_3 \times \mathbf{a}_1}{V}, \quad \mathbf{b}_3 = 2\pi\frac{\mathbf{a}_1 \times \mathbf{a}_2}{V} \tag{1.11}$$

where $V = |\mathbf{a}_1 \cdot \mathbf{a}_2 \times \mathbf{a}_3|$ is the volume of the unit cell. As a result, the energy eigenstates of a crystal are Bloch states periodic in $\boldsymbol{R}$, and are labeled by the wavevector $\mathbf{k}$ and band index n.

Bloch states are given by Bloch's theorem where plane-waves $e^{i\mathbf{k}\cdot\mathbf{r}}$ are modulated by a crystal periodic function $u_{n\mathbf{k}}(\mathbf{r})$ [94, 98, 97]:

$$\psi_{n\mathbf{k}} = e^{i\mathbf{k}\cdot\mathbf{r}} u_{n\mathbf{k}}(\mathbf{r}) \tag{1.12}$$

as we will prove in Ch. 2.1. The crystal periodicity can be expressed as

$$u_{n\mathbf{k}}(\mathbf{r}) = u_{n\mathbf{k}}(\mathbf{r} + \boldsymbol{R}) \tag{1.13}$$

where $\boldsymbol{R}$ is the above-described lattice vector defining the unit cell and the periodicity of the crystal.

When there is a finite overlap between wavefunctions on neighbouring sites in a crystal, electrons are allowed to have a finite wavevector and thus form energy bands, $\epsilon_n(\sigma, \mathbf{k})$, as described in more detail in Ch. 2.1.

Before describing spin group theory and Kramers theorem in magnetic crystals, we now introduce the concept of groups.

1.1.3 Introduction to groups

We first recall the defining properties of groups.

Definition 1. *The elements $\tilde{A}, \tilde{B}, \tilde{C}, ...$ form a group if they satisfy the following four conditions [99]:*

1. Closure. The multiplication of two group elements is also an element of the group. For instance, relations like $\tilde{A} \cdot \tilde{B} = \tilde{C}$ hold for all elements in the group.

2. Associativity. $(\tilde{A}\tilde{B})\tilde{C} = \tilde{A}(\tilde{B}\tilde{C})$ is valid for all elements.

3. Identity element. The identity, E, is an element of the group.

4. Inverse elements. There exists an inverse element $\tilde{A}^{-1}$ for every element $\tilde{A}$, satisfying $\tilde{A}^{-1}\tilde{A} = E$.

In crystallography, the symmetries of crystals are described by crystallographic point groups and space groups. Space groups contain the following symmetry operations that leave the crystal invariant [99].

Definition 2. *A space group contains the operations: identity, translations, inversion, rotations, and mirrors. Mirrors are improper rotations, i.e., rotations combined with inversion.*

Point groups contain the same symmetries as space groups, but without the translations [99]. A simple example of a point group is

$$2/m = \{E,\, \mathcal{P},\, C_{2y},\, M_y\} \tag{1.14}$$

Here, $\mathcal{P}$ denotes inversion, C_{2y} is a two-fold rotation around the y-axis, and M_y is a mirror in the plane perpendicular to the y-axis. We can denote this group as $2/m$ in the Hermann–Mauguin notation, where the two-fold rotation C_{2y} ("2") is perpendicular ("/") to the mirror M_y ("m").

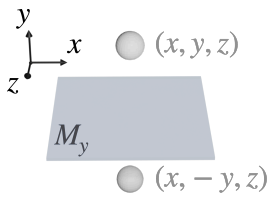

Figure 1.2: A mirror in the plane perpendicular to the y-axis (M_y) transforms between the two points shown.

We now show that this group satisfies the conditions 1-4 in Def. 1. Firstly, it obeys closure, as seen from its multiplication table with the product between every element. To evaluate the products, we can represent every element by a matrix that transforms three-dimensional Euclidian space [99]. For example, the M_y mirror transforms the coordinates (x, y, z) to $(x, -y, z)$ as shown in Fig. 1.2, and therefore takes the form of a diagonal matrix $\mathrm{diag}(1, -1, 1)$. Similarly, $C_{2y} = \mathrm{diag}(-1, 1, -1)$, $\mathcal{P} = \mathrm{diag}(-1, -1, -1)$, and $E = \mathrm{diag}(1, 1, 1)$. The resulting *multiplication table* [99] is:

	$\mathcal{P}$	C_{2y}	M_y
$\mathcal{P}$	E	M_y	C_{2y}
C_{2y}	M_y	E	$\mathcal{P}$
M_y	C_{2y}	$\mathcal{P}$	E

(1.15)

This table shows the product between the elements in the leftmost column and the top row. Every product is itself an element of the group, and thus the group obeys closure. We omit products with the identity element here, as it trivially obeys closure with all other elements.

Secondly, inspecting this multiplication table shows that the associativity rule holds. For instance, $(\mathcal{P}C_{2y})M_y = M_yM_y = E$ and $\mathcal{P}(C_{2y}M_y) = \mathcal{P}\mathcal{P} = E$, and, therefore, $(\mathcal{P}C_{2y})M_y = \mathcal{P}(C_{2y}M_y)$. Thirdly, the group contains the identity element. Fourthly, there is an inverse for every operation. In sum, the elements of $2/m$ satisfy the four conditions of a group in Def. 1.

1.2 Crystallographic spin group theory

1.2.1 General construction of crystallographic spin groups

Crystallographic spin groups take the form of a product between a *spin-only group* and a *nontrivial spin group* [83, 100, 25, 23]. Operations in the spin-only group act only in spin space. Operations in the nontrivial spin group are pairs of operations in spin and crystal space which couple the two spaces, but these operations in the two spaces can in principle be different. This starkly contrasts the more commonly used

magnetic groups, which do not have a spin-only part and where elements are single operations acting in both spaces simultaneously [83, 100, 25, 23].

The non-trivial spin group, $\mathbf{R}_s$, contains elements $[R_i||R_j]$ with one component on the left of the two vertical bars (R_i) acting only in spin space, and a component on the right (R_j) acting only in crystal real space. We adopt this notation for individual operations $\hat{O}_i$,

$$[\ \overset{\text{(spin)}}{\hat{O}_1}\ ||\ \overset{\text{(crystal)}}{\hat{O}_2}\ ], \tag{1.16}$$

in the following.

Time-reversal in the spin group formalism. Note that in the following, we refer to *spin* as its expectation value, Eq. (1.5), of local magnetic moments at atomic sites [82, 83]. Thus, we will treat *time-reversal* in spin space as an inversion [83] which is not associated with additional complex phases [94], only the sign-reversal shown in Eq. (1.6).

1.2.2 Spin-only symmetries of collinear, coplanar, and noncoplanar spin arrangements in the nonrelativistic limit

Collinear, coplanar, and noncoplanar magnetic orderings can be distinguished by their spin-only groups [83, 23, 85, 86], as illustrated in the following. This symmetry distinction is essential for understanding the distinct symmetries of altermagnets and odd-parity-wave magnets leading to their even- versus odd-parity-wave, anisotropic spin-polarized electronic structures, and spin-dependent transport [25, 93, 12].

Collinear magnets

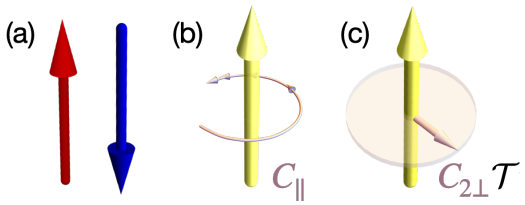

Figure 1.3: Components of the spin-only group for collinear systems. The collinear spins in (a) are symmetric under (b), an arbitrary rotation around the yellow spin quantization axis ($C_{\parallel}$), and (c), a two-fold spin rotation around any axis in the plane perpendicular to the yellow axis, followed by spin inversion ($C_{2\perp}\mathcal{T}$).

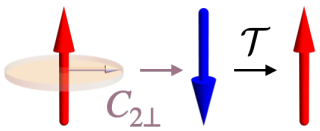

Figure 1.4: $C_{2\perp}\mathcal{T}$ acting on a spin leaves the spin invariant.

Collinear spin arrangements always obey the spin-only symmetries illustrated in Fig. 1.3. Collinear spins are parallel or antiparallel to one another, as exemplified by the two antiparallel spins in Fig. 1.3(a). The spins are aligned with one common axis shown by the yellow arrow in Fig. 1.3(b,c). In collinear systems, this yellow axis defines the *spin quantization axis*, which is the axis along which we choose to specify the spins (the spin basis kets from Sec. 1.1.1). Along this axis, the spins are either up or down with a 100% probability, i.e., spin is a *good quantum number* as described in Sec. 1.1.1.

Around this spin quantization axis, a rotation by any angle $C_\parallel$, shown in Fig. 1.3(b), is a symmetry leaving the collinear spins invariant.

Around any axis perpendicular to the spin quantization axis, i.e., any axis lying in the plane shown in Fig. 1.3(c), the operation $C_{2\perp}\mathcal{T}$ is a symmetry. As we explicitly show in Fig. 1.4, $C_{2\perp}$ rotates the spins to their antiparallel orientation, and time-reversal $\mathcal{T}$ inverts them, as in Eq. (1.6), back to their original orientation[2].

These two operations form the spin-only group of collinear systems [82, 83, 25, 23, 85],

$$\mathbf{r}_s^{\text{coll}} = \{E, C_{2\perp}\mathcal{T}\} \times \text{SO}(2), \tag{1.17}$$

where SO(2) is a group composed of all $C_\parallel$ rotations (an infinite number of rotations with rotation angles in $(0, 2\pi]$) and is commonly used in the literature on spin groups in crystals. The multiplication combines all elements of the subgroups $\{E, C_{2\perp}\mathcal{T}\}$ and SO(2) with each other. For example, the identity-element of SO(2) combined with $\{E, C_{2\perp}\mathcal{T}\}$ yields $\{E, C_{2\perp}\mathcal{T}\} \in \mathbf{r}_s^{\text{coll}}$, and similarly, $\text{SO}(2) \in \mathbf{r}_s^{\text{coll}}$.

Inversion symmetry of energy bands in collinear magnets and applicability of spin Laue groups. We now show that electronic band structures of collinear magnets are inversion symmetric in the nonrelativistic limit due to their SO(2) and $C_{2\perp}\mathcal{T}$ spin-only symmetries.

Without loss of generality, let $\parallel = z$ and $\perp$ be an axis perpendicular to the z-axis. Then, from the symmetries $C_{2\perp}\mathcal{T} \times \text{SO}(2) \in \mathbf{r}_s^{\text{coll}}$,

$$C_{2\perp}\mathcal{T} \times \text{SO}(2)\,(s_x, s_y, s_z, \mathbf{k}) = C_{2\perp}\mathcal{T}\,(0, 0, s_z, \mathbf{k}) = (0, 0, s_z, -\mathbf{k}), \tag{1.18}$$

where s_x- and s_y-components are zero due to the infinite-fold $C_\parallel$ rotations of the SO(2) group (second expression), $C_{2\perp}\mathcal{T}$ effectively inverts the wavevector (last expression),

[2]We note that one can also view this symmetry as a mirror that lies in-plane with the collinear or coplanar spins, mirroring the spins as a polar vector and leaving the spins invariant [85] (see, e.g., Fig. 3.6, illustrating how a mirror acts on a polar vector).

and analogously for any other $\parallel$ and $\perp$. Being symmetries of the system, Eq. (1.18) implies that $(0,0,s_z,-\mathbf{k}) = (0,0,s_z,\mathbf{k})$. As a result, the energy bands are symmetric in the wavevector $\mathbf{k}$, as we can express by

$$\mathbf{r}_s^{\text{coll}} = [E||\mathcal{P}] \quad \text{when acting on energy bands.} \tag{1.19}$$

Thus, acting with $\mathbf{r}_s^{\text{coll}}$ on the nonrelativistic band structure $\epsilon(\sigma,\mathbf{k})$, where σ is the spin index and $\mathbf{k}$ is the wavevector, yields

$$\epsilon(\sigma,\mathbf{k}) = \epsilon(\sigma,-\mathbf{k}) \quad \forall\,\mathbf{k} \quad \text{for collinear spin arrangements.} \tag{1.20}$$

$C_{2\perp}\mathcal{T}$ symmetry alone does not enforce inversion-symmetric energy bands.

We emphasize that this effective inversion symmetry of the nonrelativistic energy bands holds for all collinear magnetic crystals. Notably, these band structures are thus inversion symmetric even if the magnetic crystal is not—breaking crystal inversion would simply not enforce inversion symmetry on the band structure, while the collinear magnetism would.

Consequently, we can describe the symmetries of nonrelativistic energy bands of collinear systems with the system's corresponding *spin Laue group*. A *Laue group* is a point group that contains the inversion operation as an element [101]. If a point group does not contain inversion as an element (a noncentrosymmetric point group), it always has a corresponding Laue group [101]. Since inversion is a symmetry in *Laue groups*[3], and the nonrelativistic energy bands are always inversion symmetric in collinear magnetic crystals from Eq. (1.20), *spin Laue groups* capture all possible symmetries of energy bands of collinear magnetic crystals in the nonrelativistic limit [25].

Notably, Eq. (1.20) tells us that to break the inversion symmetry in the energy bands in the nonrelativistic limit, we would have to break the collinear spin-only symmetry and thus consider noncollinear spin arrangements. We can further categorize noncollinear spin arrangements into coplanar and noncoplanar ones [83].

Coplanar magnets

In coplanar spin arrangements, the spins all lie in a single plane, as illustrated by the three purple arrows in Fig. 1.5(a). The coplanar spins break the $C_\parallel$ rotation symmetries in SO(2) (contrary to collinear spin arrangements, cf. Fig. 1.3(a,b)) because

[3]We can obtain the corresponding spin Laue group by adding the inversion operation as an element as follows:

$$\{f_1,f_2,\dots\} = \{f_1,f_2,\dots,[E||\mathcal{P}]g_1,[E||\mathcal{P}]g_2,\dots\} \tag{1.21}$$

Here, $\{f_1,f_2,\dots\}$ is the spin Laue groups with elements $f_1,f_2,\dots$, and $\{g_1,g_2,\dots\}$ the original noncentrosymmetric spin point group with elements $g_1,g_2,\dots$

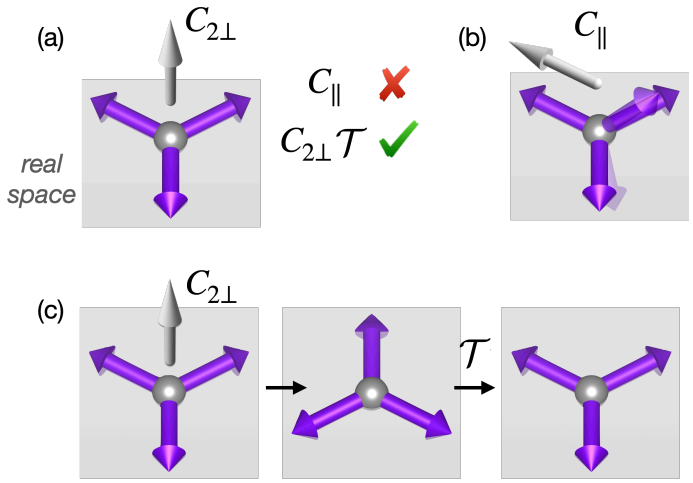

Figure 1.5: Symmetries of coplanar spin arrangements. (a) The purple arrows denote the spins, which all lie in a single plane, making them coplanar. All coplanar spin arrangements obey $C_{2\perp}\mathcal{T}$ symmetry (where $C_{2\perp}$ is perpendicular to the coplanar spins), but break the $C_\parallel \in \mathrm{SO}(2)$ symmetries present in collinear spin arrangements. (b) Coplanar (and any noncollinear) spin arrangements break $C_\parallel$ spin-only symmetries otherwise present in collinear systems. There is no single axis we can rotate around by an arbitrary rotation to leave the spins invariant because there is no axis parallel to all spins. For example, if we fix the rotation axis (white arrow) to be parallel to one of the spins, an arbitrary rotation will change the two other spins. (c) $C_{2\perp}\mathcal{T}$ acting on a coplanar spin arrangement. The $C_{2\perp}$ rotation effectively inverts the spins, resulting in the spin arrangement in the middle. Then, $\mathcal{T}$ inverts them back, resulting in the spin arrangement on the right.

there is no single rotation axis that is parallel to all the spins. For example, fixing the $C_\parallel$ axis along one of the spins shown in Fig. 1.5(b) and rotating by an arbitrary rotation will change the other spins. $C_\parallel$ is broken for all noncollinear systems.

However, coplanar spin arrangements are $C_{2\perp}\mathcal{T}$ symmetric [102, 23, 93]. Here, $C_{2\perp}$ (white arrow in Figs. 1.5(a,c)) is still perpendicular to all the spins, which in a coplanar system means it has to point normal to the plane of the spins. It effectively inverts all the spins, as shown in Fig. 1.5(c), because it is perpendicular to all the spins. Next, $\mathcal{T}$ inverts the spins back to their original arrangement as shown in Fig. 1.5(c, right), and thus $C_{2\perp}\mathcal{T}$ is a symmetry. The spin-only group of coplanar spin arrangements is $\mathbf{r}_s^{\text{coplanar}} = \{E, C_{2\perp}\mathcal{T}\}$ [83].

Noncoplanar magnets

Noncoplanar spin arrangements have spins that do not lie in a single plane. The simplest noncoplanar spin arrangement comprises three spins, for example, as in Fig. 1.6, where any two of the spins form a plane, but the third spin is tilted away from the plane.

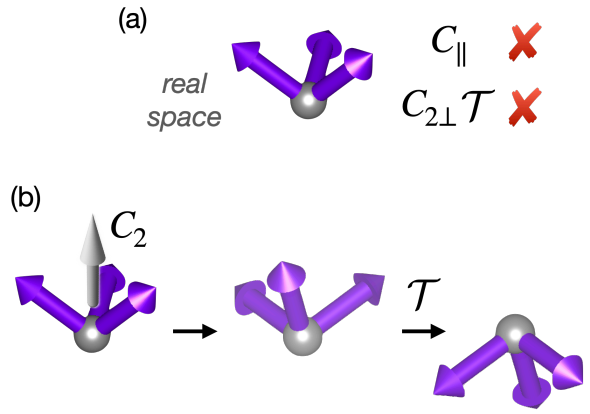

Figure 1.6: Symmetries of noncoplanar spin arrangements. (a) A noncoplanar spin arrangement comprises spins that do not lie in a single plane. There is no single axis parallel to all spins. Thus, it breaks $C_{\parallel}$ symmetries. Additionally, there is no axis perpendicular to all spins. Thus, it breaks $C_{2\perp}\mathcal{T}$ symmetry. We illustrate this symmetry breaking in (b): the spins are not invariant under a two-fold rotation and $\mathcal{T}$ because the two-fold notation does not effectively invert the spins (cf. the collinear and coplanar systems in Figs. 1.4 and 1.5, where $C_{2\perp}$ effectively inverts them.)

Similarly to coplanar spin arrangements, noncoplanar spin arrangements break $C_{\parallel}$ symmetries in SO(2) because they are noncollinear and thus have no single axis that aligns with all spins. Contrary to coplanar spin arrangements, they break $C_{2\perp}\mathcal{T}$ symmetry because there is no single axis for a rotation $C_{2\perp}$ that is perpendicular to all spins (cf. Fig. 1.5(c)). For example, suppose we try an axis shown by the white arrow in Fig. 1.6(b) and perform a two-fold rotation around it. In that case, the spins are not the inverse of the original spin arrangement because the rotation axis is not perpendicular to all spins. Then, inverting the spins with $\mathcal{T}$ as shown in Fig. 1.6(b) yields a spin arrangement that is different from the original one and, thus, $C_{2\perp}\mathcal{T}$ is not a symmetry. Since no non-trivial spin-only symmetries are left, the spin-only group of noncoplanar spin arrangements is the trivial group $\mathbf{r}_s^{\text{noncoplanar}} = \{E\}$ [83].

1.3 Crystallographic spin group classification of all collinear magnets in the nonrelativistic limit

We now describe the three distinct nontrivial spin Laue groups for collinear systems in the nonrelativistic limit derived in [25] using crystallographic spin group theory. To do this, we will use the fact that the two spin channels can be considered separately on the nonrelativistic level.

1.3.1 De-coupled spin channels

On the nonrelativistic level, the two spin-channels are de-coupled and the Hamiltonian H is block-diagonal, which we can express as

$$H = H_\uparrow + H_\downarrow \tag{1.22}$$

where $H_\uparrow$ and $H_\downarrow$ are the two blocks living in the two de-coupled spin-channels. Hence, the spin up and down eigen-wavefunctions take the corresponding forms

$$\Psi_\uparrow = (\psi_\uparrow, 0) \tag{1.23}$$
$$\Psi_\downarrow = (0, \psi_\downarrow) \tag{1.24}$$

where $\psi_\uparrow$ and $\psi_\downarrow$ are eigenstates in the two different spin channels, i.e., eigenstates of $H_\uparrow$ and $H_\downarrow$, respectively. From Eq. (1.24), we explicitly see that $\Psi_\uparrow$ and $\Psi_\downarrow$ are orthogonal states, i.e., $\langle\Psi_\uparrow|\Psi_\downarrow\rangle = 0$. We can therefore consider the two spin-channels separately in the nonrelativistic limit.

1.3.2 The spin Laue group classification for collinear systems

Since we consider collinear systems, we have only two options for operations in spin space: either we can leave every spin unchanged—with identity E—or turn every spin into its antiparallel—with a two-fold rotation in spin space C_2. The rotation axis of this two-fold rotation lies perpendicular to the spin quantization axis, and thus $C_2 = C_{2\perp}$, where we recall that $C_{2\perp}$ is as illustrated Fig. 1.4(left). Also, recall from Sec. 1.2.2 that a *Laue group* $\mathbf{G}$ is a point group that contains inversion as an element [101].

There are three ways to combine these two spin operations with crystal space operations [25]. The first way is to combine identity in spin space with the entire group $\mathbf{G}$ in crystal space. The second way is to combine identity and a two-fold rotation in spin space with the entire group $\mathbf{G}$. The third way is to combine identity in spin space with half the elements of $\mathbf{G}$ and a two-fold spin rotation with the second half of the elements of $\mathbf{G}$ [25]. The first half of the elements is the *halving group* $\mathbf{H}$, and the second half of the elements is the second coset $\mathbf{G} - \mathbf{H}$, which we can also write as

$$\mathbf{G} = \mathbf{H} + (\mathbf{G} - \mathbf{H}). \tag{1.25}$$

As shown in Appendix C, we can alternatively write $\mathbf{G} - \mathbf{H}$ as $A\mathbf{H}$ where A is any element of $\mathbf{G} - \mathbf{H}$, which yields the alternative expression:

$$\mathbf{G} = \mathbf{H} + A\mathbf{H}. \tag{1.26}$$

We write the three ways of combining spin-space and crystal-space operations as three different nontrivial spin Laue groups [25],

$$\mathbf{R}_s^{\mathrm{I}} = [E||\mathbf{G}], \tag{1.27}$$

$$\mathbf{R}_s^{\mathrm{II}} = [E||\mathbf{G}] + [C_2||\mathbf{G}], \tag{1.28}$$

$$\mathbf{R}_s^{\mathrm{III}} = [E||\mathbf{H}] + [C_2||A\mathbf{H}]. \tag{1.29}$$

These three nontrivial spin groups correspond to ferromagnetism, antiferromagnetism, and altermagnetism, respectively, as illustrated in Fig. 1.7. Panel (a) of the figure depicts the Laue group $\mathbf{G}$ for a nonmagnetic crystal and a corresponding nonmagnetic electronic band structure. Panels (b) and (c) show the three nontrivial spin Laue groups applied to representative magnetic crystals and nonrelativistic spin densities: ferromagnetism and antiferromagnetism in panel (b), and altermagnetism in panel (c). We now explain these nontrivial spin groups in more detail.

Ferromagnets. The type-I spin Laue group $\mathbf{R}_s^{\mathrm{I}}$ describes ferromagnets (and ferrimagnets), illustrated on a magnetic crystal Fig. 1.7(b), where all spins align parallel to each other (or all symmetry-connected spins are parallel). With this parallel spin alignment, there is only one spin sublattice, shown in blue in the figure, and it obeys all symmetries of $\mathbf{G}$. The corresponding band structure also obeys the same symmetries. The group does not contain any combinations of crystallographic operations with spin rotations. For example, for $\mathbf{G} = 2/m$ from Eq. (1.14), the type-I spin Laue group is

$$\mathbf{R}_s^{\mathrm{I}} = [E||\{E,\, \mathcal{P},\, C_{2y},\, M_y\}]. \tag{1.30}$$

We can also express it as $\{[E||E],\, [E||\mathcal{P}],\, [E||C_{2y}],\, [E||M_y]\}$, where we adopt the spin group notation in each element, or we can write ${}^{1}2/{}^{1}m$, where the "1" superscript is the identity operation E in spin space, which combines with crystal space operations shown by baseline symbols in the Hermann–Mauguin notation.

Antiferromagnets. The type-II spin Laue group $\mathbf{R}_s^{\mathrm{II}}$ describes antiferromagnets, illustrated in Fig. 1.7(b). Type-II spin Laue groups have two terms, one for each spin channel, and each spin channel obeying all symmetries of $\mathbf{G}$. The second term contains a two-fold spin rotation that combines with all elements of $\mathbf{G}$, transposing one sublattice onto the other called *sublattice-transposing symmetries*, or transposing symmetries for short. This sublattice-transposing second term is never present in type-I spin Laue groups; thus, type-II and type-I spin Laue groups are always distinct. Since the sublattice-transposing symmetries involve all operations in $\mathbf{G}$, they always include crystal inversion, $[E||\mathcal{P}]$, or translation $[E||\mathbf{t}]$, or both, which force the energy bands to be spin-degenerate on the nonrelativistic level. For $\mathbf{G} = 2/m$, the

type-II spin Laue group is

$$\mathbf{R}_s^{\mathrm{II}} = [E||\{E,\, \mathcal{P},\, C_{2y},\, M_y\}] + [C_2||\{E,\, \mathcal{P},\, C_{2y},\, M_y\}] \tag{1.31}$$

where the second term contains a transposing symmetry $[C_2||\mathcal{P}]$ with crystal inversion.

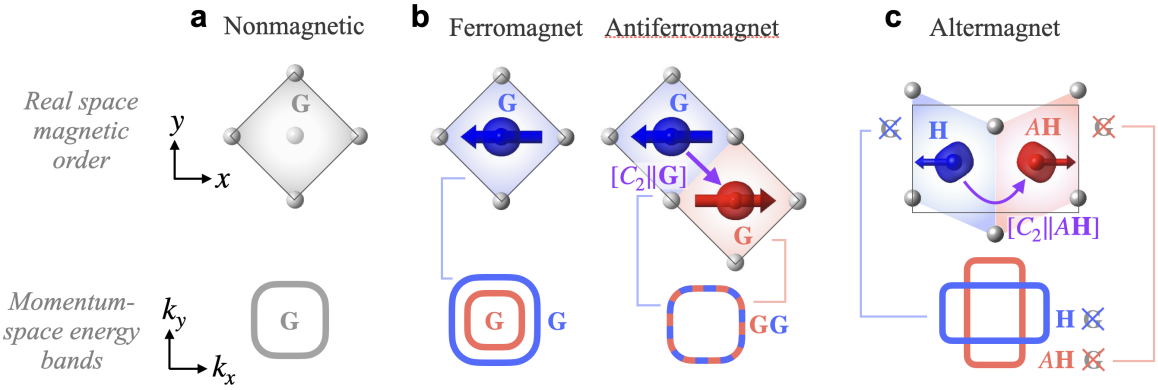

Figure 1.7: Illustration of nontrivial spin Laue group symmetries delineating collinear magnets, ferromagnets, antiferromagnets, and altermagnets on the nonrelativistic level, Eqs. (1.27)-(1.29) [25]. (a) Corresponding nonmagnetic lattice described by the Laue group **G**. (b) Ferromagnets and antiferromagnets: each spin channel (red- and blue-colored regions and spin densities for each magnetic subpattice in real space and bands reciprocal space) obeys all symmetries of **G**. The net magnetic moment in ferromagnets lifts the energy degeneracy of the nonmagnetic energy bands illustrated in (a inset; gray iso-energy cut) by Zeeman-splitting (b, left inset; red and blue spin-polarized bands). Antiferromagnets have two magnetic sublattices related by $[C_2||\mathbf{G}]$ (purple arrow), which contains crystal inversion or translation or both, thus enforcing double spin degeneracy of the energy bands (b, right inset). (c) Altermagnets: each spin channel obeys **H**, i.e., half the symmetries of **G**. Opposite spin channels are related by $[C_2||A\mathbf{H}]$, which are exclusively mirrors or rotations, possibly combined with translations.

Altermagnets. The type-III spin Laue group $\mathbf{R}_s^{\mathrm{III}}$ describes altermagnets, illustrated in Fig. 1.7(c) [25].

Type-III spin Laue groups, Eq. (1.29), have a first term where identity in spin space is combined with a halving subgroup **H**, which typically contains half of the symmetry elements in **G** of the underlying nonmagnetic crystal. The symmetries of **H** apply to each of the two spin channels separately—we can consider the spin channels separately because they are de-coupled in the nonrelativistic limit, as described in Sec. 1.3.1. In each separate spin channel, altermagnets thus break half of the crystallographic Laue group symmetries of the underlying nonmagnetic lattice, **G**, on the nonrelativistic level. The corresponding spin densities and energy bands are thus deformed, with each spin channel obeying only the symmetries of **H**, i.e., half the symmetries of **G**.

The second term in Eq. (1.29) combines the two-fold spin rotation with the rest of the elements of **G**, namely $A\mathbf{H}$, which relates the two separate spin channels to

each other as indicated by the purple arrow in Fig. 1.7(c). Here, the sublattice-transposing symmetry A is restricted to be a crystal rotation or a mirror operation [25]. (If A would be a translation or an inversion, the spin Laue group will reduce to a type-II spin Laue group, e.g., the one in Eq. (1.31), and thus not be type-III). We note that rotations or mirrors in the corresponding spin space group can be symmorphic or nonsymmorphic, the latter combining the operation with a partial unit cell translation.

We now provide an example. For $\mathbf{G} = 2/m$, we have $\mathbf{H} = \{E, P\}$ and $\mathbf{G} - \mathbf{H} = \{C_{2y}, M_y\}$. Then, A, which is an element of $\mathbf{G} - \mathbf{H}$, is either a rotation C_{2y} or a mirror M_y [4]. The corresponding type-III spin Laue group is

$$\mathbf{R}_s^{\mathrm{III}} = [E||\{E, \mathcal{P}\}] + [C_2||\{C_{2y},\, M_y\}]. \tag{1.32}$$

We can rewrite Eq. (1.32) as

$$\mathbf{R}_s^{\mathrm{III}} = [E||\{E, \mathcal{P}\}] + [C_2||C_{2y}\{E,\, \mathcal{P}\}] \tag{1.33}$$

where the seond term arises from the multiplication $C_{2y}\mathcal{P} = M_y$ [5]. We thus recover the form in Eq. (1.29), where $A = C_{2y}$ and $\mathbf{H} = \{E,\, \mathcal{P}\}$.

In summary, in addition to the collinear spin-only group, we have seen in this section that the nontrivial type-III spin Laue group describes the symmetries of altermagnets on the nonrelativistic level. Arriving at this was enabled by realizing the following three points: *(i)* in the nonrelativistic limit, the two spin channels are de-coupled and can thus be treated separately. *(ii)* Each spin channel only obeys half the symmetries of the underlying nonmagnetic crystal, i.e., they each obey the symmetries of the halving subgroup $\mathbf{H}$. *(iii)* The two magnetic sublattices are related by rotations or mirrors, symmorphic or nonsymmorphic. We will see in Sec. 1.6 and Ch. 3 that these very symmetries enable altermagnets to lift Kramers spin degeneracy nonrelativistically in *the altermagnetic form* from Remark 1, forming altermagnetic d-, g-, and i-wave electronic structures.

[4] Note that if we had tried $\mathbf{H} = \{E, C_{2y}\}$ or $\{E, M_y\}$, then A would be P. If we inserted this into $\mathbf{R}_s^{\mathrm{III}}$, the result would not be a Laue group as it would miss the inversion element $[E||P]$.

It is known from crystallography that we can always add inversion to a point group to obtain a corresponding Laue group [101]. The same holds for crystallographic spin groups: We can add inversion to a spin point group to obtain the corresponding spin Laue group and, hence, see if it is of type I, II, or III in Eqs. (1.27)-(1.29).

To obtain the corresponding spin Laue group, we would add the inversion symmetry as in Eq. (1.21). With $A = P$, we would see that the resulting spin Laue group equals the spin Laue group in Eq. (1.31) and is thus type-II, which illustrates that when A is inversion P, the spin Laue group will be of type-II.

[5] Equivalently, we can write $\mathbf{R}_s^{\mathrm{III}} = [E||\{E, P\}] + [C_2||M_y\{E,\, \mathcal{P}\}]$ with $A = M_y$, using $M_y\mathcal{P} = C_{2y}$, and the spin Laue group is identical.

1.4 Magnetic groups

In contrast to crystallographic spin groups, where operations in spin and crystal space can be different or the same, in magnetic groups, the operations are always the same [79]:

$$[\ \overset{(\text{spin})}{\hat{O}}\ ||\ \overset{(\text{crystal})}{\hat{O}}\ ] = \hat{O}. \tag{1.34}$$

Let us explain the distinction between magnetic and crystallographic spin groups with an example of a magnetic structure in real space, shown in Fig. 1.8(a), where oppositely magnetized atoms, in red and blue, are surrounded by nonmagnetic atoms that form diamond-shaped environments in gray. Similar orders of magnetic and nonmagnetic atoms are present in numerous altermagnetic candidates, such as RuO_2, KRu_4O_8, and CoF_2 [25]. In Fig. 1.8(a), we show an example of a sublattice-transposing symmetry $[C_2||C_4]$ (magenta arrow), which is a combination of a four-fold rotation in crystal space (gray dotted arrow), and a two-fold rotation in spin space (black dashed arrow). No magnetic group operation can describe this symmetry. For example, in

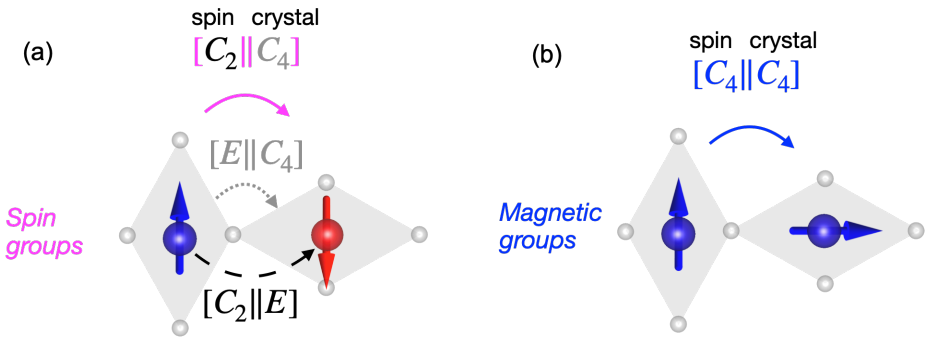

Figure 1.8: Spin and magnetic symmetry operations. (a) A crystallographic spin symmetry operation acts in spin and crystal space separately. The spin and crystal space operations are two different rotations in this example ($[C_2||C_4]$). (b) A magnetic symmetry operation acts with the same operation in both spin and crystal space. For instance, a four-fold rotation in crystal space is accompanied by the same rotation in spin space ($[C_4||C_4]$). It is not a symmetry of the crystal in (a), and thus, this example shows that magnetic groups do not describe all possible spin symmetries.

Fig. 1.8(b), we can attempt to reproduce the nonmagnetic diamond environments with a four-fold crystal rotation. However, in the magnetic symmetry framework, it is accompanied by a four-fold rotation in spin space. This operation does not reproduce the red antiparallel spin. Therefore, the magnetic symmetry operation is not a symmetry of the crystal in 1.8(a).

On the other hand, magnetic symmetries describe physics where spin and crystal space are transformed by the same operation. For example, relativistic spin-orbit coupling couples spin and crystal space, and thus, it is common to consider magnetic

symmetries when describing effects involving relativistic spin-orbit-coupling phenomena, such as magnetocrystalline anisotropies which allow for the stability of magnetic bits in magnetic memories [103]. This approach has been successful in predicting and experimentally demonstrating, for example, spectroscopic evidence of topological insulators [104, 105], the anomalous Hall effect in ferromagnets [106] and noncollinear magnets [67, 69, 70, 2], and parity-violation in antiferromagnets with $\mathcal{PT}$ symmetry [107].

1.5 Spin splittings

In, for instance, altermagnets, the energy bands with opposite spin polarizations meet at specific symmetry-enforced points of the Brillouin zone, for example, at the $\mathbf{\Gamma}$-point in the nonrelativistic limit [25, 93]. Away from such a point, the bands in the two spin channels can disperse differently, lifting the spin degeneracy and forming an energy difference between them, or a *spin splitting*. Ferromagnets also have spin splittings, but contrary to altermagnets and our odd-parity-wave magnets, which are magnetically compensated, ferromagnets will split at the $\mathbf{\Gamma}$ point in the nonrelativistic limit due to their net magnetization [25].

In magnetic crystals, the energy scale of the spin splittings associated with the magnetic exchange, E_{J}, and Coulomb interaction, E_{C} is typically large ($\sim$ eV scale). Spin-orbit coupling, E_{SOC}, is typically significantly smaller (up to a $\sim 100\,\mathrm{meV}$ scale with heavy elements, but typically $\lesssim 10\,\mathrm{meV}$ [108]). We can summarize these typical energy scales as follows:

$$E_{\mathrm{J}}, E_{\mathrm{C}} \gg E_{\mathrm{SOC}} \tag{1.35}$$

In the nonrelativistic limit without spin-orbit coupling, $E_{\mathrm{SOC}} \to 0$ and the Coulomb and exchange interactions perfectly govern the electronic band structure. We note that the exchange and Coulomb-induced spin splittings have been confirmed to induce large energy scale spin splittings in the nonrelativistic limit in altermagnets and our odd-parity-wave magnets in first-principles calculations across several studies: in altermagnets, [3, 25, 1] and our database of over 200 d-, g-, and i-wave altermagnetic candidates [109], in a study of over 60 altermagnetic candidates [110], and in our p-wave magnetic candidates [93]. Crystallographic spin groups perfectly describe the symmetries of magnets in the nonrelativistic limit.

For this typical energy scale in Eq. (1.35), adding spin-orbit coupling modifies the band structure perturbatively. Thus, the symmetries from crystallographic spin groups typically describe the gross features of the band structure, even when spin-orbit coupling is added, making these spin groups particularly predictive in several ways.

Firstly, crystallographic spin symmetries describe the symmetry-enforced location of nodal surfaces in, for instance, altermagnets in the nonrelativistic limit. Once adding spin-orbit coupling, the energy bands may additionally lift Kramers spin degeneracy along these nodal surfaces [6]. If they do lift, the electronic structure forms avoided crossings, which were shown to be associated with Berry curvature hotspots located along the nonrelativistic, previously nodal surfaces predicted by the spin symmetries [3, 2] (and not at accidental locations as is commonly seen in, e.g., ferromagnets).

Secondly, even when strong spin-orbit coupling lifts degeneracies along nonrelativistic nodal surfaces, the band structure is virtually identical to the nonrelativistic band structure away from the symmetry-imposed avoided crossings [25, 3, 38, 30, 31].

Thirdly, crystallographic spin groups predict whether the energy bands break or preserve symmetries such as inversion or time-reversal symmetries, as well as the spin winding number around the $\mathbf{\Gamma}$ point [25, 93]. It was necessary, for example, to realize that the band structure of altermagnets breaks time-reversal symmetry [3] to predict and experimentally verify the crystal (anomalous) Hall effect in the altermagnetic candidates RuO_2 [3, 5], Mn_5Si_3 [111, 112], and MnTe [113, 2]. (Here, *crystal* refers to the strong dependence of the Hall conductivity on the mutual orientation of the crystal environments and spin axes [3].)

If we want to describe the detailed symmetry of the modified, gapped band structure along the nonrelativistic nodal surfaces, it is instructive to consider both spin and magnetic groups [25, 23]. Interestingly, in MnTe, we will see in Ch. 3 that when altermagnetism combines with spin-orbit coupling, it induces a spin-splitting along some of the nonrelativistic nodal surfaces. The magnitude of the spin splitting is significant, of the order of 100 meV, thanks to the large spin-orbit coupling from Te (atomic number 52) [30]. Thus, this spin splitting in MnTe is of a similar order of magnitude as the other energy scales:

$$E_{\mathrm{J}}, E_{\mathrm{C}} \gtrsim E_{\mathrm{SOC}}. \tag{1.36}$$

This E_{SOC} spin-splitting energy in MnTe is comparatively large. For comparison, a spin-splitting value considered to be large for relativistic spin-orbit coupling is for instance ~ 300 meV (corresponding to a Rashba energy [108] ~ 100 meV) found in nonmagnetic BiTeI, where the Bi atom has the atomic number 83 [114].

1.6 Kramers theorems

Kramers degeneracy refers to the situation when two distinct (orthogonal) eigenstates of a system are energy-degenerate due to time-reversal symmetry [94]. If those two states have opposite spins, we will refer to them as *Kramers spin degenerate*. In

crystals, the energy states are not levels but instead depend on the wavector. In reciprocal space, then, an eigenstate with a corresponding eigenenergy, wavevector $\mathbf{k}$, and spin index σ, we will refer to as *Kramers spin degenerate* if it has the same energy as an orthogonal state with wavevector $\mathbf{k}$ and opposite spin $-\sigma$. The *Kramers spin degeneracy is lifted* if the same-wavevector-opposite-spin states have different energies.

We now summarize the general symmetries of magnets and how they relate to Kramers theorem, and will then show that $\mathcal{PT}$ antiferromagnets are Kramers spin degenerate in Sec. 1.6.2. Moreover, we show that magnets with $\mathcal{T}\mathbf{t}$ symmetry, where $\mathbf{t}$ is a translation, are Kramers spin degenerate *only in the case when the crystal is inversion symmetric and the magnetic order collinear*. This realization has served as a key symmetry guideline in our description of p-wave and odd-parity-wave magnets in Ch. 3. Finally, we describe the methods for determining spin-degenerate nodal surfaces in altermagnets in Sec. 1.8 which we will use in Ch. 3 to understand the electronic structure and *lifting of Kramers spin degeneracy* (LKSD) in altermagnetic candidates.

1.6.1 Spin-polarized electronic structure and Kramers spin degeneracy of collinear magnets

Collinear magnets in general obey the symmetries of the $\mathbf{r}_s^{\text{coll}}$ spin-only group from Eq. (1.17) and, thus, the energy bands are inversion symmetric as we showed in Eq. (1.19).

Ferromagnets. Ferromagnets have a uniform magnetization on every magnetic atom in real space (no sublattice-transposing symmetry, see Eq. (1.27)). The net magnetization is associated with an s-wave-like spin polarization in the reciprocal space energy band structure as in Fig. 1.7(b), left inset) [25], lifting Kramers spin degeneracy. Here, s-wave refers to the isotropic spin splitting in momentum space and the isotropic shape of the Fermi surfaces allowed in ferromagnets.

Antiferromagnets. Among the sublattice-transposing symmetries of collinear antiferromagnets are translations or inversion, as we see from Eq. (1.28). These crystal operations are augmented in spin space by a two-fold rotation. Suppose the sublattice-transposing symmetry is a translation $\mathbf{t}$ and the antiferromagnet is collinear, obeying $\mathbf{r}_s^{\text{coll}}$. In that case, Kramers spin degeneracy is enforced in the entire Brillouin zone (Fig. 1.7(b), right inset) in the nonrelativistic limit, as we will see in Sec. 1.7. Alternatively, if the transposing symmetry is inversion, then $\mathcal{PT}$ symmetry enforces Kramers spin degeneracy in both the relativistic and nonrelativistic case, as we will discuss in Sec. 1.6.2.

Altermagnets. Altermagnets are magnetically compensated in real space. Its nonrelativistic *spin densities* (also called *magnetization densities*) are given by

$$\langle\psi|\sigma_z|\psi\rangle = |\psi_\uparrow|^2 - |\psi_\downarrow|^2, \quad |\psi\rangle = (\psi_\uparrow, \psi_\downarrow). \tag{1.37}$$

In each spin channel, the spin densities obey only the symmetries of the halving subgroup **H**, thus breaking symmetries in **G** of the underlying crystal as we saw in Fig. 1.7(c). The spin densities in the two spin channels (and, analogously, the two opposite magnetic sublattices) are related by the sublattice-transposing symmetry A [25].

Obeying only the symmetries of **H** allows the spin densities to be anisotropic [25]. The emergence of lattice symmetry-breaking spin densities can have various origins. In the original altermagnets, this symmetry-breaking anisotropy arises due to the opposite spin sublattices' mutually rotated local crystallographic environments. However, proposals exist on achieving such local anisotropies without the crystal environments, with electronic correlations producing mutually rotated orbital ordering on opposite spin sublattices instead [115]. The even partial-wave magnetization in direct space represents the order parameter of an altermagnet [1].

The corresponding band structure also follows the spin symmetries. Each separate spin channel in the band structure obeys **H** and is related by the sublattice-transposing symmetry A (Fig. 1.7(c), inset). Other bulk properties can also obey the spin symmetries [25, 1, 116], but this is beyond our scope.

As a result of analyzing type-III spin Laue groups for all possible Bravais lattices with their corresponding Laue groups **G**, the electronic band structures of altermagnets take a d-, g-, or i-wave form with, respectively, 2, 4, or 6 nodal surfaces crossing the **Γ**-point on the nonrelativistic level [25].

Fig. 1.9 shows schematics of these d-, g-, and i-wave spin polarizations allowed in altermagnets on the nonrelativistic level [25]. The spin expectation value of the energy bands (e.g., a "blue" spin for a wavevector **k** in a blue area) are enforced by sublattice-transposing symmetries $[C_2||A\mathbf{H}]$ to alternate according to the coloring of these volumes, yielding energy bands with opposite ("red") or same ("blue") spin polarization in adjacent volumes. The planar spin polarizations (first row) are characterized by its nodal surfaces traversing from one side of the Brillouin zone to the other in the k_z direction, i.e., from $k_z = -\frac{\pi}{c}$ to $k_z = \frac{\pi}{c}$ where c is a lattice constant for the z-direction. Thus, in planar systems, one can connect points at $k_z = \pm\frac{\pi}{c}$ without crossing a nodal surface. The bulk spin polarizations (second row) have nodal surfaces that traverse from one side to the other also in directions perpendicular to $\mathbf{k}_z$, e.g., from $k_x = -\frac{\pi}{a}$ to $k_x = \frac{\pi}{a}$ side, with a a lattice constant along the x-direction. Thus, in bulk systems, one can not connect points at $k_z = \pm\frac{\pi}{c}$ without crossing a nodal surface. Of the candidate altermagnets we will study here, MnTe and CrSb are bulk g-wave and RuO_2 is planar d-wave.

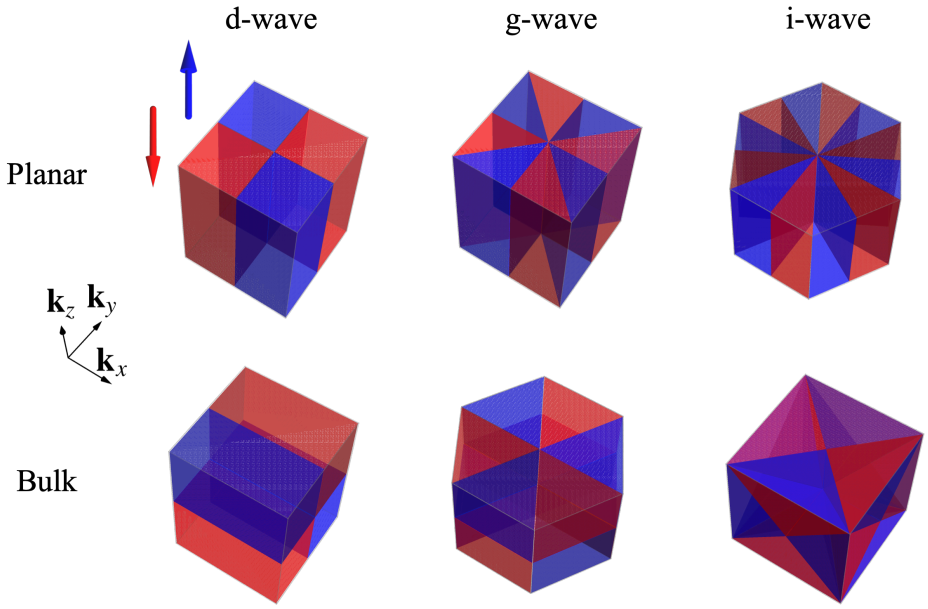

Figure 1.9: Summary of the types of altermagnetic spin polarizations in the nonrelativistic electronic band structure. The classification altermagnets into, firstly, d-, g-, and i-wave systems with respectively 2, 4, and 6 spin-degenerate nodal surfaces (columns), and secondly, planar vs. bulk systems (rows) [25]. The spin-degenerate nodal surfaces separate regions with opposite spin-polarizations, indicated by red and blue volumes and arrows. The number and orientation of spin-degenerate nodal surfaces, and whether they are planes or not, are determined by the sublattice-transposing symmetries in R_s^{III}.

Note on Kramers spin degeneracy in altermagnets. We note that the spin-degeneracy of spin up and down states in surfaces in altermagnets is analogous to Kramers spin degeneracy. However, in altermagnets, the states are not related by $\mathcal{T}$ symmetry, but rather by sublattice-transposing symmetry elements $[C_2||AH]$ in the nonrelativistic limit.

If we couple spin and crystal space by including spin-orbit coupling, then the spin degeneracy can lift along some of the surfaces, while others may remain spin degenerate. Such degeneracies and liftings have been demonstrated in altermagnetic Cr and Co-doped $FeSb_2$ by analyzing the magnetic groups for different Néel vector orientations, where symmetry-elements containing $\mathcal{T}$ can enforce Kramers spin degeneracy [6].

Summary. In Tab. 1.1 and 1.2, we summarize the symmetries and lifting of Kramers spin degeneracy for collinear magnets and for systems with $\mathcal{PT}$ symmetry.

Steps to prove Kramers spin degeneracy. To prove Kramers spin degeneracy requires two steps.

Spin-only group	Nontrivial spin group	System	Nonrel. reciprocal space spin order	Kramers degeneracy
$C_{\parallel}+C_{2\perp}\mathcal{T}$ (collinear)	$\mathbf{R}_s^{\mathrm{I}}$	FM	s-wave	lifted
	$\mathbf{R}_s^{\mathrm{III}}$	AM	d-, g- , i-wave	lifted nonrel., may be enforced rel. along planes
	$\mathbf{R}_s^{\mathrm{II}}$	AF	—	nonrel.

Table 1.1: Summary of Kramers theorems in collinear magnets. The spin-only symmetries (first column) and nontrivial spin Laue groups (second column) determine the type of reciprocal space spin order in the nonrelativistic level (third column). The fourth column summarizes the types of Kramers spin degeneracy possible in the non-relativistic limit (nonrel.) and with relativistic spin-orbit coupling (rel.).

Symmetry	System	Nonrel. reciprocal space spin order	Kramers degeneracy
$\mathcal{PT}$	AF coll./noncoll.	—	nonrel.+rel.

Table 1.2: Summary of Kramers theorem in systems with $\mathcal{PT}$ symmetry, such as $\mathcal{PT}$ antiferromagnets. Notably, $\mathcal{PT}$ symmetric systems are always Kramers spin degenerate, even with spin-orbit coupling [95, 96, 107].

Step 1. is to show that same-wavevector eigenstates with spin up and spin down have the same energy.

Step 2. is to show that these two states are orthogonal.

If we can show both *Step 1.* and *Step 2.*, then the same-wavevector eigenstates are Kramers spin degenerate.

We now prove Kramers spin degeneracy for systems with $\mathcal{PT}$ symmetry, which can be collinear magnets or otherwise, and then for magnetic systems with $\mathcal{T}\mathbf{t}$ symmetry, and how to lift the spin degeneracy in the latter.

1.6.2 Kramers theorem for $\mathcal{PT}$-symmetric systems

$\mathcal{PT}$ Kramers theorem

Acting with $\mathcal{T}$ on the energy bands, we reverse both the spin and wavevector index as we saw in Eq. (1.7):

$$\mathcal{T}\epsilon_n(\sigma, \mathbf{k}) = \epsilon_n(-\sigma, -\mathbf{k}) \tag{1.38}$$

Crystal-inversion $\mathcal{P}$ only inverts the wavevector,

$$\mathcal{P}\epsilon_n(\sigma, \mathbf{k}) = \epsilon_n(\sigma, -\mathbf{k}) \tag{1.39}$$

With these prerequisites, we are in a position to prove Kramers theorem for systems with $\mathcal{PT}$ symmetry:

Theorem 1. *Systems with $\mathcal{PT}$ symmetry are Kramers spin degenerate for all wavevectors [95, 117].*

Proof.

Step 1. Since $\mathcal{PT}$ is a symmetry, if we apply it to the energy eigenstate (Bloch wavefunction) $\psi_{\mathbf{k}}$, the resulting wavefunction $\phi_{\mathbf{k}} = \mathcal{PT}\psi_{\mathbf{k}}$ is also an eigenstate (here, we suppress the band index n). To show this, we use the fact that $\mathcal{PT}$ commutes with the Hamiltonian, $H_{\mathbf{k}}$, and hence we can apply $H_{\mathbf{k}}$ to the wavefunction in the following [95]:

$$H_{\mathbf{k}}\phi_{\mathbf{k}} = H_{\mathbf{k}}\mathcal{PT}\psi_{\mathbf{k}} \overset{\text{commute}}{=} \mathcal{PT}H_{\mathbf{k}}\psi_{\mathbf{k}} = \epsilon_{\mathbf{k}}\mathcal{PT}\psi_{\mathbf{k}} = \epsilon_{\mathbf{k}}\phi_{\mathbf{k}} \tag{1.40}$$

Thus, comparing the left and right sides, we see that $\phi_{\mathbf{k}}$ is an eigenstate. Also note that $\phi_{\mathbf{k}}$ and $\psi_{\mathbf{k}}$ are same-energy-opposite-spin partners due to the $\mathcal{PT}$ symmtry relating them by

$$\mathcal{PT}\epsilon_n(\sigma, \mathbf{k}) = \epsilon_n(-\sigma, \mathbf{k}). \tag{1.41}$$

Thus, *Step 1.* of the proof is done.

Step 2. We need to show that $\phi_{\mathbf{k}}$ and $\psi_{\mathbf{k}}$ are orthogonal, i.e., the inner product between them is zero. To show this, we note that $\mathcal{PT}$ is antiunitary[6]and thus satisfies Eq. (1.3), which yields [95]:

$$\langle\phi_{\mathbf{k}}|\psi_{\mathbf{k}}\rangle = \langle\mathcal{PT}\psi_{\mathbf{k}}|\mathcal{PT}\phi_{\mathbf{k}}\rangle = \langle\phi_{\mathbf{k}}|(\mathcal{PT})^2|\psi_{\mathbf{k}}\rangle = -\langle\phi_{\mathbf{k}}|\psi_{\mathbf{k}}\rangle \tag{1.42}$$

Here, we used the antiunitary property in Eq. (1.3) (first equality), then inserted $\mathcal{PT}\psi_{\mathbf{k}} = \phi_{\mathbf{k}}$ in the bra and $\phi_{\mathbf{k}} = \mathcal{PT}\psi_{\mathbf{k}}$ in the ket (second equality), and finally used that electrons are fermions, $\mathcal{T}^2 = -1$, and that $\mathcal{P}^2 = 1$ (last equality). The only way this equality holds is if the states are orthogonal, $\langle\phi_{\mathbf{k}}|\psi_{\mathbf{k}}\rangle = 0$. Thus, *Step 2.* is done.

[6] $\mathcal{PT}$ is a product of a unitary ($\mathcal{P}$) and an antiunitary operator ($\mathcal{T}$). In general, the product of a unitary operator, U_1, and an antiunitary operator is also an antiunitary operator. To show this, we first recall that the product of a unitary operator and complex conjugation, U_2K, is an antiunitary operator (see, e.g., Eq. 44). Thus, to show that U_1U_2K is antiunitary, we only need to show that the product of two unitary operators, U_1U_2, is unitary.

If the product U_1U_2 is unitary, then it, per definition, obeys $(U_1U_2)(U_1U_2)^\dagger = 1$. Using the identity $(U_1U_2)^\dagger = U_2^\dagger U_1^\dagger$ and the definition $U_iU_i^\dagger = 1$ $(i = 1, 2)$, we have

$$(U_1U_2)(U_1U_2)^\dagger = U_1U_2U_2^\dagger U_1^\dagger = U_1U_1^\dagger = 1.$$

Thus, U_1U_2 is unitary. Hence, the product of a unitary operator U_1 and an antiunitary operator U_2K is antiunitary.

We have therefore shown that $\phi_{\mathbf{k}}$ and $\psi_{\mathbf{k}}$ are energy-degenerate orthogonal eigenstates with opposite spins, i.e., *Kramers spin degenerate*, for all wavevectors $\mathbf{k}$, q.e.d.

We note that collinear antiferromagnets with inversion as a sublattice-transposing symmetry in the type-II spin Laue group always have the magnetic $\mathcal{PT}$ symmetry. Therefore, these collinear antiferromagnets fall into this category of $\mathcal{PT}$-symmetric Kramers spin degenerate systems.

$\mathcal{PT}$ universally enforces Kramers spin degeneracy by Theorem 1, even with spin-orbit coupling (which can make the system noncollinear thus breaking symmetries in $\mathbf{r}_s^{\text{coll}}$), and even when breaking of the individual symmetries $\mathcal{P}$ [107] or $\mathcal{T}$ while preserving $\mathcal{PT}$. Several antiferromagnets, both collinear and noncollinear, can have $\mathcal{PT}$ symmetry and thus have spin degenerate band structures.

We also note that an analogous proof is possible to show for systems with the individual $\mathcal{P}$ and $\mathcal{T}$ symmetries in real space [117]. However, such systems are nonmagnetic because $\mathcal{T}$ symmetry in real space prohibits magnetism.

1.7 Spin degeneracy and its lifting in $\mathcal{T}\mathbf{t}$-symmetric systems

We now discuss spin degeneracy in systems with $\mathcal{T}\mathbf{t}$ symmetry and how to lift it. Here, $\mathbf{t}$ is a lattice vector translation with respect to the nonmagnetic unit cell, and thus, the $\mathcal{T}\mathbf{t}$ symmetry notably doubles the size of the unit cell.

We will show that systems with $\mathcal{T}\mathbf{t}$ symmetry that are collinear—which belong to the collinear spin-only group $\mathbf{r}_s^{\text{coll}}$ in Eq. (1.17)—are spin degenerate in the nonrelativistic limit. However, if the system is noncollinear ($\mathbf{r}_s^{\text{coll}}$ symmetry breaking) and noncentrosymmetric ($\mathcal{P}$ breaking), or if we add spin-orbit coupling (which can break $\mathbf{r}_s^{\text{coll}}$ and $\mathcal{P}$), we can lift the spin degeneracy, in contrast to $\mathcal{PT}$ magnets which would stay spin degenerate.

1.7.1 Proof of the spin degeneracy, and how to lift it

We now prove that systems with $\mathbf{r}_s^{\text{coll}}$ symmetry—applicable to collinear systems in the nonrelativistic limit—combined with $\mathcal{T}\mathbf{t}$ symmetry are spin degenerate. By an analogous proof, also systems with $\mathcal{T}\mathbf{t}$ symmetry combined with $\mathcal{P}$ symmetry—centrosymmetric systems—are spin degenerate. From these two proofs, we can therefore answer the question of *how to lift spin degeneracy in systems with $\mathcal{T}\mathbf{t}$ symmetry in the nonrelativistic limit: we need to break both $\mathbf{r}_s^{\text{coll}}$ symmetry and $\mathcal{P}$ symmetry, i.e., we need noncollinear, noncentrosymmetric systems.*

The takeaway is, therefore, that noncollinear, noncentrosymmetric systems with $\mathcal{T}\mathbf{t}$ symmetry can lift spin degeneracy from the magnetic order itself without requiring

relativistic spin-orbit coupling. Realizing this has allowed us to identify p-wave and odd-parity-wave magnetism, which we will discuss in detail in Ch. 3.2 [93].

Proof

In proving spin degeneracy for these systems, we follow the general *Step 1* and *Step 2*.

Step 1. Let $\Psi_{\mathbf{k}}$ be an eigenstate of the Hamiltonian. Consider a system with $C_{2\perp}\mathcal{T} \times \mathrm{SO}(2) \in \mathbf{r}_s^{\mathrm{coll}}$ and $\mathcal{T}\mathbf{t}$ symmetries, and thus also the combined symmetries $C_{2\perp}\mathcal{T} \times \mathrm{SO}(2) \times \mathcal{T}\mathbf{t}$. Let $\Phi_{\mathbf{k}}$ be a state related to $\Psi_{\mathbf{k}}$ by $C_{2\perp}\mathcal{T}\, C_{\parallel}\, \mathcal{T}\mathbf{t}$ symmetry as $\Phi_{\mathbf{k}} = C_{2\perp}\mathcal{T}\, C_{\parallel}\, \mathcal{T}\mathbf{t}\, \Psi_{\mathbf{k}}$, where $C_{\parallel}$ is an arbitrary element of SO(2). $\Phi_{\mathbf{k}}$ is an eigenstate because $C_{2\perp}\mathcal{T}\, C_{\parallel}\, \mathcal{T}\mathbf{t}$, being a symmetry, commutes with the Hamiltonian, similarly to Eq. (1.40). Thus, *Step 1* is complete.

Step 2. We need to show that $\Phi_{\mathbf{k}}$ and $\Psi_{\mathbf{k}}$ are orthogonal. As a prerequisite for the proof, we first show that the action of $C_{2\perp}\mathcal{T} \times \mathrm{SO}(2)$ on an eigenstate is effectively $[E||\mathcal{P}]$, similarly to when acting on energy bands in Eq. (1.19).

Prerequisites. Consider the eigenstate written in terms of Bloch's theorem from Eq. (1.12) as $|\Psi_{\mathbf{k}}\rangle \equiv |\Psi(\mathbf{k}, s_x, s_y, s_z)\rangle = e^{i\mathbf{k}\cdot\mathbf{r}} u_{\mathbf{k}}(\mathbf{r}, s_x, s_y, s_z)$. Here, we have explicitly included the dependence on the wavevector, $\mathbf{k}$, and spin, (s_x, s_y, s_z), and suppressed the band index. The system is collinear and obeys $C_{2\perp}\mathcal{T} \times \mathrm{SO}(2) \in \mathbf{r}_s^{\mathrm{coll}}$, which acts on this eigenstate as follows:

$$\begin{aligned} &C_{2\perp}\mathcal{T} \times \mathrm{SO}(2)|\Psi(\mathbf{k}, s_x, s_y, s_z)\rangle = C_{2\perp}\mathcal{T}|\Psi(\mathbf{k}, 0, 0, s_z)\rangle \\ &\quad = C_{2\perp}\mathcal{T} e^{i\mathbf{k}\cdot\mathbf{r}} u_{\mathbf{k}}(\mathbf{r}, 0, 0, s_z) = C_{2\perp} e^{-i\mathbf{k}\cdot\mathbf{r}} u_{-\mathbf{k}}(\mathbf{r}, 0, 0, -s_z) = e^{-i\mathbf{k}\cdot\mathbf{r}} u_{-\mathbf{k}}(\mathbf{r}, 0, 0, s_z) \\ &\quad = |\Psi(-\mathbf{k}, 0, 0, s_z)\rangle. \end{aligned} \tag{1.43}$$

In the first line, we applied SO(2) analogously to in Eq. (1.18) with $\parallel = z$ without loss of generality. In the first and second equality, we used that $\mathcal{T} e^{i\mathbf{k}\cdot\mathbf{r}} u_{\mathbf{k}}(\mathbf{r}, 0, 0, s_z) = e^{-i\mathbf{k}\cdot\mathbf{r}} u_{-\mathbf{k}}(\mathbf{r}, 0, 0, -s_z)$ because $\mathcal{T}$ is antilinear from Eq. (1.4) and reverses the spin and wavevector. In the third equality, we applied $C_{2\perp}$, and in the last equality, we inserted the definition of $|\Psi(-\mathbf{k}, 0, 0, s_z)\rangle$. Eq. (1.43) shows that $C_{2\perp}\mathcal{T} \times \mathrm{SO}(2)$ effectively inverts the wavevector of the wavefunction for collinear systems. Therefore, it acts as inversion $[E||\mathcal{P}]$ on the eigenstate $\Psi_{\mathbf{k}}$ for collinear systems. We thus have $\Phi_{\mathbf{k}} = [E||P]\mathcal{T}\mathbf{t}\, \Psi_{\mathbf{k}}$, which we will use in *Step 2*.

We also note that $[E||\mathcal{P}]$ is a unitary operator, which combined with $\mathcal{T}\mathbf{t}$—$[E||\mathcal{P}]\mathcal{T}\mathbf{t}$—is also antiunitary, see Footnote 6.

Orthogonality (Step 2). With these prerequisites in mind, we now show the orthogonality relation. The inner product is:

$$\begin{aligned} \langle \Phi_{\mathbf{k}}|\Psi_{\mathbf{k}}\rangle &= \langle [E||\mathcal{P}]\mathcal{T}\mathbf{t}\, \Psi_{\mathbf{k}}|[E||\mathcal{P}]\mathcal{T}\mathbf{t}\, \Phi_{\mathbf{k}}\rangle = \langle \Phi_{\mathbf{k}}|([E||\mathcal{P}]\mathcal{T}\mathbf{t})^2|\Psi_{\mathbf{k}}\rangle \\ &= \langle \Phi_{\mathbf{k}}|([E||\mathcal{P}]\mathcal{T})^2|\mathbf{t}^2\Psi_{\mathbf{k}}\rangle = \langle \Phi_{\mathbf{k}}|([E||\mathcal{P}]\mathcal{T})^2|\Psi_{\mathbf{k}}\rangle = -\langle \Phi_{\mathbf{k}}|\Psi_{\mathbf{k}}\rangle \end{aligned} \tag{1.44}$$

Here, we have used that $[E||\mathcal{P}]\mathcal{T}\mathbf{t}$ is antiunitary (first equality), inserted $[E||\mathcal{P}]\mathcal{T}\mathbf{t}\,\Psi_{\mathbf{k}} = \Phi_{\mathbf{k}}$ in the bra and $\Phi_{\mathbf{k}} = [E||\mathcal{P}]\mathcal{T}\mathbf{t}\,\Psi_{\mathbf{k}}$ in the ket (second equality), moved $\mathbf{t}^2$ (third equality), used $\mathbf{t}^2\Psi_{\mathbf{k}} = \Psi_{\mathbf{k}}$ because $\mathbf{t}^2$ is a symmetry (it is a translation by a lattice vector of the magnetic unit cell, $2\boldsymbol{t}$; fourth equality), and finally used $\mathcal{T}^2 = -1$ and $\mathcal{P}^2 = 1$ (last equality). Thus, we have shown that $\Phi_{\mathbf{k}}$ and $\Psi_{\mathbf{k}}$ are orthogonal, and *Step 2* is complete.

Since we have shown both *Step 1* and *Step 2*, we have proven that

Theorem 2. *Systems with $C_{2\perp}\mathcal{T} \times \mathrm{SO}(2) \in \mathbf{r}_s^{\mathrm{coll}}$ symmetry (applicable to collinear systems in the nonrelativistic limit) combined with $\mathcal{T}\boldsymbol{t}$ symmetry are spin degenerate.*

We note that the algebraic steps in Eq. (1.44) are analogous for systems with crystal inversion symmetry $\mathcal{P}$ instead of the collinear $C_{2\perp}\mathcal{T}\times\mathrm{SO}(2)$ symmetry. Thus, both $C_{2\perp}\mathcal{T} \times \mathrm{SO}(2)$ symmetry and $\mathcal{P}$ symmetry enforce spin degeneracy when combined with $\mathcal{T}\mathbf{t}$ symmetry. Therefore, if we look to noncollinear $\mathcal{T}\mathbf{t}$-symmetric systems to lift Kramers spin degeneracy, we must also ensure the system breaks crystal inversion symmetry.

In summary, to lift spin degeneracy in systems with $\mathcal{T}\mathbf{t}$ symmetry in the nonrelativistic limit, we need to break two types of symmetries: we need to break $C_{2\perp}\mathcal{T} \times \mathrm{SO}(2) \in \mathbf{r}_s^{\mathrm{coll}}$ symmetry with noncollinear magnetism, and we need to break crystal inversion symmetry $\mathcal{P}$.

1.8 Spin-degenerate nodal surfaces by spin symmetry analysis

We now describe the method to derive symmetry-imposed nodal surfaces on the nonrelativistic level. One can use this method to derive nodal surfaces in even-parity (e.g., d-, g-, and i-wave) types of spin polarizations as in Fig. 1.9, allowed in altermagnetic electronic band structures [25, 6], and nodal surfaces in odd-parity (e.g., p- and f-wave) magnets [93].

Orthogonal states. Let $\Psi_\uparrow$ and $\Psi_\downarrow$ be the sublattice-transposing symmetry-related wavefunctions in opposite spin channels on the nonrelativistic level. They have the same eigenenergy (*Step 1*) because the symmetry relating them (e.g., AH) commutes with the Hamiltonian, analogously to in Eq. (1.40). Similarly to in Kramers theorem proofs, $\Psi_\uparrow$ and $\Psi_\downarrow$ are orthogonal (*Step 2*), but here, it is because the spin channels are de-coupled in the nonrelativistic limit and thus $\langle\Psi_\uparrow|\Psi_\downarrow\rangle = 0$ as we saw in Sec. 1.3.1.

1.8.1 Spin-degenerate nodal surfaces

Per definition, nodal surfaces for the band structure form where bands with opposite spin expectation values overlap. We can use this definition to derive nodal surfaces in the non-relativistic limit with spin symmetries.

Since nodal surfaces are where opposite spins overlap, the symmetry operations to consider when deriving the nodal surfaces need to involve a spin rotation operator. Further simplifying the matter, the spins are either up or down, and the only spin rotation operator is the two-fold spin rotation in collinear systems. Therefore, the types of equations to solve are:

$$\epsilon(\mathbf{k}, s) = [C_2||AH]\epsilon(\mathbf{k}, s) = \epsilon(\mathbf{k}' \overset{!}{=} \mathbf{k}, -s). \tag{1.45}$$

Here, $[C_2||AH]$ is a transposing symmetry of the altermagnetic crystal with AH being a crystal space operation in $A\mathbf{H}$ (as in Eq. (1.29)), $\mathbf{k}$ is a wavevector, s is the spin expectation value of, e.g., an energy band, and $\mathbf{k}'$ and $-s$ are the wavevector and spin operated on by the transposing symmetry operator. On the right hand side in Eq. (1.45), we can demand that $\mathbf{k}' \overset{!}{=} \mathbf{k}$, because $[C_2||AH]$ is a symmetry and, thus, $\mathbf{k} = [C_2||AH]\mathbf{k} = \mathbf{k}'$. (Alternatively, up to a reciprocal lattice vector $\boldsymbol{G}$, Eq. (1.10), we have $\mathbf{k}' \overset{!}{=} \mathbf{k} + \boldsymbol{G}$ in Eq. (1.45), but we focus our further discussion here on nodal surfaces around the $\mathbf{\Gamma}$-point).

It is simple to solve Eq. (1.45) in the non-relativistic limit, as the two spin channels are de-coupled and, thus, eigenstates in the two spin channels are orthogonal as we saw above. Hence, it suffices to find the algebraic solution of Eq. (1.45).

Spin-degenerate nodal planes from mirror sublattice-transposing symmetries. For example, consider a mirror transposing symmetry, e.g., $[C_2||M_z]$. The mirror inverts k_z, and thus Eq. (1.45) becomes

$$\epsilon(k_x, k_y, k_z, s) = [C_2||M_z]\epsilon(k_x, k_y, k_z, s) = \epsilon(k_x, k_y, -k_z, -s) \tag{1.46}$$

This equation implies that $s = 0$ for $k_z = 0$. Thus, the system has a spin-degenerate nodal plane for $k_z = 0$. Analogously, replacing M_z in this example with an arbitrary mirror sublattice-transposing symmetry will symmetry-enforce a spin-degenerate nodal plane inside the mirror symmetry plane.

Spin-degenerate nodal surfaces from rotation sublattice-transposing symmetries. Consider a rotation transposing symmetry, e.g., $[C_2||C_{2y}]$. The crystal rotation rotates k_x and k_z, and thus Eq. (1.45) becomes

$$\epsilon(k_x, k_y, k_z, s) = [C_2||C_{2y}]\epsilon(k_x, k_y, k_z, s) = \epsilon(-k_x, k_y, -k_z, -s) \tag{1.47}$$

Thus, $\epsilon(k_x, k_y, k_z, s) = \epsilon(-k_x, k_y, -k_z, -s)$, which is spin-degenerate for $k_x = 0 = k_z$. This corresponds to a spin-degenerate nodal line along the k_y-axis, $\epsilon(0, k_y, 0, s) = \epsilon(0, k_y, 0, -s)$.

Note that if a spin Laue group enforces nodal lines by rotation sublattice-transposing symmetries instead of mirrors, these nodal lines are part nodal surfaces because said rotation symmetries connect states with opposite spin at $\mathbf{k}$ and $\mathbf{k}'$. Therefore, there must be a nodal surface between $\mathbf{k}$ and $\mathbf{k}'$ where the spin changes. Rotation sublattice-transposing symmetries do not enforce the shape of the surface, except that it intersects the rotation axis (e.g., the k_y-axis in Eq. (1.47)) of the crystal rotation operation (e.g., C_{2y}).

Such nodal surfaces have been verified in, e.g., KRu_4O_8 belonging to the spin Laue group ${}^{2}4/{}^{1}m$ [25], and one is present that crosses the k_y-axis in our coplanar p-wave material candidate CeNiAsO, see Ch. 3.2.7 and Eq. (3.18).

In summary, we have illustrated that mirror and rotation sublattice-transposing symmetries enforce spin-degenerate nodal planes and surfaces, respectively, in the nonrelativistic limit.

Chapter 2

Electronic structure theory

In recent years, the fields of magnetism and spintronics have made significant advancements in understanding and exploiting compensated magnets whose *electronic band structures* break time-reversal symmetry. Examples include altermagnets [3, 25, 1, 2, 118, 119] and particular noncollinear magnets [67, 69, 70, 120, 2, 119]. The *electronic structure* describes how electrons order and move in crystals [94]. In real space, the spin-polarized electronic structure takes the form of *magnetization densities*; in reciprocal space, of electronic band structures. Altermagnets break time-reversal symmetry of the energy bands [3], and each spin channel in the electronic structure (magnetization densities and energy bands) is anisotropic due to breaking half the symmetries of the underlying nonmagnetic crystal. Simultaneously, the opposite spin channels are related by rotations and mirrors [3, 25].

Our understanding of the electronic structure of altermagnets has been instrumental in predicting and experimentally verifying a myriad of unconventional physics in them. Electronic structure theory has served as a powerful tool to understand altermagnets conceptually and in predicting candidate materials for experiments and spin-dependent transport in them [3, 25, 1, 2, 118, 119]. Here, we, therefore, need electronic structure theory in our toolbox to understand altermagnets and odd-parity-wave magnets on a fundamental level and predict material candidates [25, 93]; to show by symmetry analysis and *ab initio* calculations how some of the first experimental signatures of the altermagnetic electronic structure delineates it from other, conventional magnetic phases [30, 31, 38]; and to predict spin-dependent electronic transport in altermagnets and p-wave magnets [12, 93].

Electronic band structure theory. Here, we will first revisit the band theory of crystals to understand electronic structure theory. Crystals are characterized by having spatial translational symmetry. Plane waves can describe the wavefunction of free electrons. However, in a crystal structure, periodic potentials originating from the atoms perturb the electrons, which Bloch encoded in a periodic modulation of

the plane-wave wavefunction (Eq. (1.12)) [97]. This periodicity corresponds to the translational symmetry. This translational symmetry has important consequences for solid-state physics, as it leads to the concept of electronic energy bands, i.e., the electronic structure in reciprocal space [94].

Several approaches are used to study electronic structures. One approach, commonly used in the condensed matter community, is *tight-binding models* [121]. These models describe noninteracting electrons in a periodic potential that are allowed to delocalize by tunneling between nearest-neighbor potential wells that model atomic sites [94]. Tight-binding models thus describe how electrons delocalize and form electronic band structures in crystals. They can illustrate specific symmetries and energy dispersions of interest and enhance our conceptual understanding of key physics [121], which is also valuable for studying altermagnets and odd-parity-wave magnets. Moreover, we note that energy bands from more sophisticated simulation methods can be mapped onto these tight-binding models, which can be used as illustrative effective models [122, 123, 121, 124], also for altermagnets and odd-parity-wave magnets [25, 1, 12, 93, 125, 126]. Details of such mappings are beyond our scope.

Density functional theory. In real materials, electrons interact and form complex many-body wavefunctions so complex that today's computers cannot handle them. That is where a second approach is suitable, namely *density-funcional-theory* (DFT), which has caused a revolution in what is possible to do in material simulation [127, 128]. DFT maps the complex many-body problem onto a much simpler problem where we can treat the *electronic density* and *spin density* instead of the full wavefunctions, which makes it possible to solve on today's computers [127, 128, 121]. We will use DFT to study altermagnets and odd-parity-wave magnets with real material candidates [93, 12, 30, 31, 38, 112, 129, 130].

Organization of this chapter. In this chapter, we first review the emergence of energy bands in crystals and how we can use this to construct our altermagnetic tight-binding models [12, 25, 1]. Here, we will use these models to illustrate the specific altermagnetic symmetries (inversion and sublattice-transposing symmetries in several distinct d-wave models) and energy dispersions (quadratic around the $\mathbf{\Gamma}$-point and with different periodicities and nodal line orientations). These models can apply to real altermagnetic materials [25, 1]. We will use these models later to demonstrate tunneling magnetoresistance with altermagnetic electrodes in Ch. 4. We will also use the tight-binding method to construct odd-parity-wave models in Ch. 3.

Then, we review the complex many-body problem and its solution with DFT. We will use DFT to corroborate our recent collaborative experiment-theory work on altermagnetic candidate materials, MnTe [30], CrSb [31], and RuO_2 [38] in Ch. 2. Since we will study in Ch. 2 p-wave and odd-parity wave magnets, which are noncollinear in real space, we also describe noncollinear spin-polarized DFT. Particularly, we will

focus on simulations with constraining the magnetic moments to satisfy necessary symmetries by employing the *Vienna Ab initio Simulation Package* (VASP). With this method, we show here that we obtain the magnetic order that perfectly obeys the symmetries needed to realize p-wave magnetism in a real candidate material [93] whose magnetic order is known from experiment [44].

2.1 Translational symmetry and the tight-binding method

Translational symmetry combined with tunneling between neighboring sites in a crystal are the ingredients in constructing tight-binding models [94]. These models can capture symmetries and provide simple models to qualitatively understand leading effects by modeling non-interacting electrons in crystals [121].

Translational symmetry. For example, consider a periodic potential with periodicity a in one dimension as shown in Fig. 2.1. In crystals, electrons move in a periodic

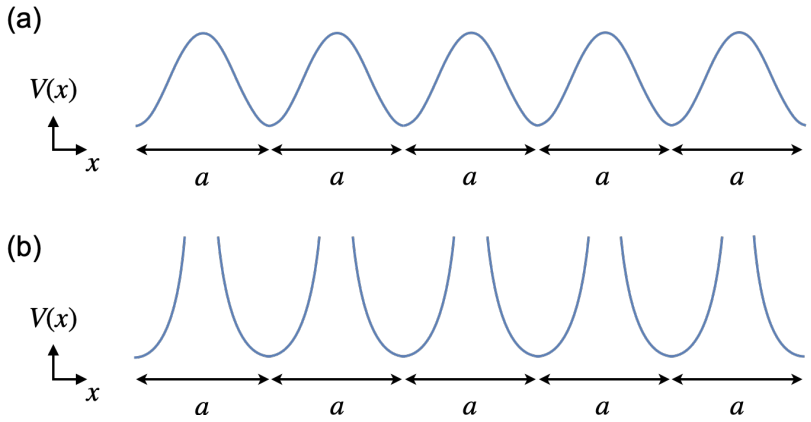

Figure 2.1: Periodic potentials: (a) with periodicity a, and (b) when the height of the barrier between neighboring sites is infinite[94]. Both potentials are in one dimension.

potential from positive ions. In general, the translation operator $\tau(l)$, which acts on the position x and a ket indexed by x, $|x\rangle$, as follows

$$\tau^\dagger(l)\, x\, \tau(l) = x + l, \quad \tau(l)\, |x'\rangle = |x' + l\rangle\,, \tag{2.1}$$

is not a symmetry for an arbitrary l. However, when l coincides with the lattice spacing a, we have the relation $\tau(a)\,|x\rangle = |x + a\rangle$ for the ket $|x\rangle$ and translational symmetry of the potential, as illustrated in Fig. 2.1(a). This translational symmetry

can be expressed as:

$$\tau(a)^\dagger V(x)\tau(a) = V(x+a) = V(x). \tag{2.2}$$

Forming a Hamiltonian from the potential and a kinetic term, $\hbar^2k^2/2m$, where the latter is independent of the real-space position x, we see that the Hamiltonian is symmetric under $\tau(a)$ and thereby satisfies $\tau^\dagger(a)H\tau(a) = H$. Furthermore, $\tau(a)$ is unitary, $\tau^\dagger(a) = \tau^{-1}(a)$, which implies $\tau^\dagger(a)\tau(a) = \tau^{-1}(a)\tau(a) = \mathbf{1}$. Hence, we can write the commutation relation as

$$[H, \tau(a)] = 0 \tag{2.3}$$

Therefore, certain eigenstates exist that simultaneously diagonalize H and $\tau(a)$ for any translationally invariant system [94].

Infinite periodic potential. Before discussing energy band formation, we consider the instructive situation where the potential at each site is infinite, as shown in Fig. 2.1(b). Since the height of the potential is infinite at each site, a ground state of the system can be a wavefunction fully localized at a single site [94]. We denote this fully localized state as $|n\rangle$ where n is the site index. This localized state is an eigenstate of H with an eigenenergy E_0,

$$H\,|n\rangle = E_0\,|n\rangle\,, \tag{2.4}$$

but it is not eigenstates of $\tau(a)$, because

$$\tau(a)\,|n\rangle = |n+1\rangle \neq |n\rangle\,. \tag{2.5}$$

However, the linear combination of the states at each atomic site, expressed by

$$|\theta\rangle \equiv \sum_{n=-\infty}^{\infty} e^{in\theta}\,|n\rangle\,, \quad \text{with } \theta \in \text{Re},\ -\pi < \theta < \pi, \tag{2.6}$$

is a simultaneous eigenstate of H and $\tau(a)$. Here we chose $-\pi < \theta < \pi$, but we could equally well use $-\pi < \theta < \pi$ modulus 2π, i.e., add or subtract 2π.

We can show that this is an eigenstate of H by applying Eq. (2.4), which immediately yields $H\,|\theta\rangle = E_0\,|\theta\rangle$. As for $\tau(a)$, we re-index the sum over n as follows:

$$\tau(a)|\theta\rangle = \sum_{n=-\infty}^{\infty} e^{in\theta}|n+1\rangle = \sum_{n'=-\infty}^{\infty} e^{i(n'-1)\theta}|n'\rangle = e^{-i\theta}|\theta\rangle. \tag{2.7}$$

Here, the eigenenergy is $e^{-i\theta}$. Note that the linear combination in Eq. (2.6) is parametrized by the continuous parameter θ, in contrast to the eigenenergies of $|n\rangle$ in Eq. (2.4) which are all energy degenerate with the energy E_0.

Finite periodic potential. Next, we consider the more realistic case for crystals, where the potential has a finite height at each lattice site as illustrated in Fig. 2.1(a), enabling electrons to delocalize (their wavefunctions spread out). This spread allows for a finite overlap between their wavefunctions, allowing electrons to tunnel to neighboring sites.

In this situation, we can still construct the localized energy eigenstates $|n\rangle$ that obey $\tau(a)\,|n\rangle = |n+1\rangle$ (Eq. (2.5)). From Eq. (2.4), the diagonal elements of the Hamiltonian are

$$\langle n|\, H\, |n\rangle = E_0. \tag{2.8}$$

All these diagonal elements are identical for every site index n because the system is translationally invariant.

However, the finite barrier allows quantum mechanical tunneling between neighboring lattice sites because the spread wavefunctions have a tail extending to other sites. We model this in terms of the off-diagonal matrix elements of the Hamiltonian as

$$\langle n|\, H\, |n'\rangle \neq 0 \quad \text{when} \quad n \neq n'. \tag{2.9}$$

In the context of tight-binding models, we refer to off-diagonal terms of the Hamiltonian as *hopping terms* or *hoppings*.

Tight-binding approxmation. If the tunneling barrier to the neighboring sites is high, only tunneling between a few nearest neighbors corresponds to non-negligible off-diagonal elements in the Hamiltonian. Keeping these terms while neglecting further neighbor terms is *the tight-binding approximation* [94]. For example, if only nearest-neighbor terms contribute, then

$$\langle n'|H|n\rangle \neq 0 \quad \text{if } n' = n \quad \text{or} \quad n' = n \pm 1. \tag{2.10}$$

We will denote the off-diagonal elements as

$$\langle n \pm 1|\, H\, |n\rangle = -t \tag{2.11}$$

This expression is also independent of n due to the translational symmetry, similar to in Eq. (2.8). If $|n\rangle$ and $|n'\rangle$ are orthogonal when $n \neq n'$, then we have an orthogonal basis in which we can write the Hamiltonian as

$$H|n\rangle = E_0|n\rangle - t|n+1\rangle - t|n-1\rangle. \tag{2.12}$$

Observe that $|n\rangle$ is no longer an eigenstate of H now that there are additional finite off-diagonal elements in the Hamiltonian compared to the infinite-potential case (Eq. (2.4)).

Energy bands. We now show how this tight-binding model leads to the concept of energy bands. We construct $|\theta\rangle$ as before in Eq. (2.6). $|\theta\rangle$ is an eigenstate of $\tau(a)$ because Eq. (2.7) still holds due to translational symmetry. $|\theta\rangle$ is also an eigenstate of H with the eigenenergy $E_0 - 2t\cos\theta$, expressed as

$$H\,|\theta\rangle = (E_0 - 2t\cos\theta)\,|\theta\rangle\,. \tag{2.13}$$

We can show this by inserting for Eq. (2.6) in Eq. (2.12) (suppressing the n-index in the sums) [94]:

$$\begin{aligned} H\sum e^{in\theta}|n\rangle &= E_0\sum e^{in\theta}|n\rangle - t\sum e^{in\theta}|n+1\rangle - t\sum e^{in\theta}|n-1\rangle \\ &= E_0\sum e^{in\theta}|n\rangle - t\sum \left(e^{in\theta-i\theta} + e^{in\theta+i\theta}\right)|n\rangle \\ &= (E_0 - 2t\cos\theta)\sum e^{in\theta}|n\rangle. \end{aligned} \tag{2.14}$$

We used the identity $\cos\theta = (e^{i\theta} + e^{-i\theta})/2$ in the last line.

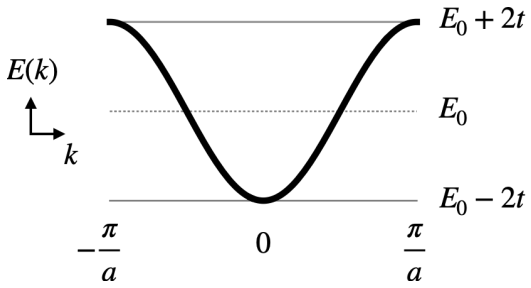

Figure 2.2: Energy bands formation. When the ground state wavefunctions around each site have no overlap, as in the infinite barrier potential in Fig. 2.1(b), the only possible energy is E_0 (dotted horizontal line). When tunneling is finite between sites, as is possible with the finite barrier potential in Fig. 2.1(a), the allowed energies form a band dispersion in the Brillouin zone $|k| \leq \pi/a$ (thick line) [94].

Notably, allowing tunneling between neighboring sites has introduced finite off-diagonal elements of the Hamiltonian, t, which together with the continuous parameter, θ, lifts the energy degeneracy of the original energy eigenstates $|n\rangle$ (which all had the same energy E_0 in Eq. (2.4)). We will now show that this degeneracy lifting results in the system forming *energy bands*, which disperse in the Brillouin zone as shown in Fig. 2.2.

Bloch's theorem and the Brillouin zone. The physical significance of the degeneracy lifting in Eq. (2.14) and the formation of energy bands originates from the fact that the wavefunction of $|\theta\rangle$ are Bloch states. Bloch states obey *Bloch's theorem*, which takes the following form as we recall from Ch. 1:

$$\psi_k(x) = \langle x|\theta\rangle = u_k(x)\,e^{ikx} \quad \text{with} \quad \theta = ka \tag{2.15}$$

Here, e^{ikx} is a plane-wave with the propagation wave-vector k, and $u_k(x)$ is the periodic function modulating the wavefunction and has the periodicity a which matches the periodicity of the potential $V(x)$.

Bloch's theorem follows directly from periodicity and the fact that $|\theta\rangle$ is an eigenstate of the translation operator with eigenvalues $e^{-i\theta}$ (see Eq. (2.7)). We can derive it by applying $\tau(a)$ to the left and the right in $\langle x|\tau(a)|\theta\rangle$, which yields

$$\langle x-a|\theta\rangle = e^{-i\theta}\langle x|\theta\rangle. \tag{2.16}$$

This equality is solved by Eq. (2.15) by inserting $\langle x|\theta\rangle = u_k(x)$ and setting $\theta = ka$, or,

$$k = \frac{\theta}{a}, \tag{2.17}$$

as follows:

$$\begin{aligned} \langle x-a|\theta\rangle &\overset{\text{Eq. (2.15)}}{=} u_k(x-a)\, e^{i\frac{\theta}{a}(x-a)} = u_k(x)\, e^{i\frac{ka}{a}(x-a)} = u_k(x)\, e^{ik(x-a)} \\ e^{-i\theta}\langle x|\theta\rangle &\overset{\text{Eq. (2.15)}}{=} e^{-i\theta}\left(u_k(x)\, e^{ikx}\right) = u_k(x)\, e^{ikx-i\theta} = u_k(x)\, e^{ik(x-a)} \end{aligned} \tag{2.18}$$

Therefore, Bloch's theorem solves Eq. (2.16), which completes our proof [94].

Since $-\pi < \theta < \pi$, as per Eq. (2.6), the corresponding values of the wavevector from Eq. (2.17) lie in the range

$$-\frac{\pi}{a} < k < \frac{\pi}{a} \tag{2.19}$$

This wavevector cut-off represents *the first Brillouin zone* in one dimension, which uniquely defines a primitive unit cell in reciprocal space (see also the wavevectors defining the three-dimensional Brillouin zone in Eq. (1.11)). With $\theta = ka$, the energies from Eq. (2.13) are

$$E(k) = E_0 - 2t\cos ka \tag{2.20}$$

and form the dispersion curve in Fig. 2.2.

Summary. In summary, when we allow for electron tunneling between lattice sites, the previous infinite-fold degeneracy of the energy levels lifts. The energy levels form a continuous band in the Brillouin zone, a *band structure*. For a one-dimensional model with a normal, spin-independent onsite energy E_0 and a nearest-neighbor hopping energy t, the band takes energy values between $E_0 - 2t$ and $E_0 + 2t$ as we can see in Fig. 2.2 [94].

2.2 Altermagnetic tight-binding models

We now describe altermagnetic tight-binding models. The symmetries of altermagnets guide the construction of these models (see Ch. 1), where each spin channel breaks the symmetry of the underlying nonmagnetic crystal and are related by rotation and mirror sublattice-transposing symmetries (Eq. 1.29) [25]. These models illustrate how exchange in altermagnets follow the sublattice-transposing symmetries, that collinearity enforces inversion symmetry with an allowed quadratic dispersion in the electronic band structure, and that there are different versions of d-wave altermagnetism, where nodal lines can be differently oriented and the Brillouin zone edge may or may not be spin degenerate, which is also reflected in the variation in d-wave electronic structures in candidate materials [25, 1]. We will use these models to simulate tunneling magnetoresistance in Ch. 4 [12].

Altermagnetic models with nearest and next-nearest neighbor hoppings

Fig. 2.3(a) shows an altermagnetic tight-binding model in real space. It has two nearest-neighbor hopping terms with alternating signs that respect the d-wave altermagnetic symmetry; for example, a 90-degree rotation flips the spin polarisation. Microscopically, the sign dependence of the hoppings can originate from alternating exchange fields along the x- and y-directions. For instance, these alternating exchange fields can originate from magnetic atoms with opposite spins located at midpoints along the x- and y-bonds of a square lattice. This situation was identified in real material candidates with Lieb-lattice-derived structures composed of transition metals and oxygen [12, 111, 131, 132].

Hopping in the y-direction, the hopping term is $+t_J\,\mathbf{d}\cdot\boldsymbol{\sigma}$, while in the x-direction, it is $-t_J\,\mathbf{d}\cdot\boldsymbol{\sigma}$, where $\boldsymbol{\sigma} = (\sigma_x, \sigma_y, \sigma_z)$ is the vector of spin Pauli matrices, and $\mathbf{d}$ is a unit vector pointing along the Néel vector. We can write these hoppings as a real-space Hamiltonian

$$H_{\mathrm{AM}}^{\mathrm{NN}} = t_J \left[\sum_{\langle ij \rangle_+} - \sum_{\langle ij \rangle_-} \right] \mathbf{d}\cdot\boldsymbol{\sigma}\, c_i^\dagger c_j, \tag{2.21}$$

where $c_i^\dagger$ and c_j are electronic creation and annihilation operators of sites i and j. $\langle ij \rangle_+$ are nearest neighbor sites indexed by i and j where the overall sign of the hopping is positive. Here, the NN notation marks that the term is between nearest neighbors, and AM that it models altermagnetism. In Fig. 2.3(a), $\langle ij \rangle_+$ corresponds to all hoppings along the y-direction. Similarly, $\langle ij \rangle_-$ corresponds to hoppings along which the overall sign is negative, which is in the x-direction in this case. This model is altermagnetic because of this directionally dependent sign-difference of the spin. For

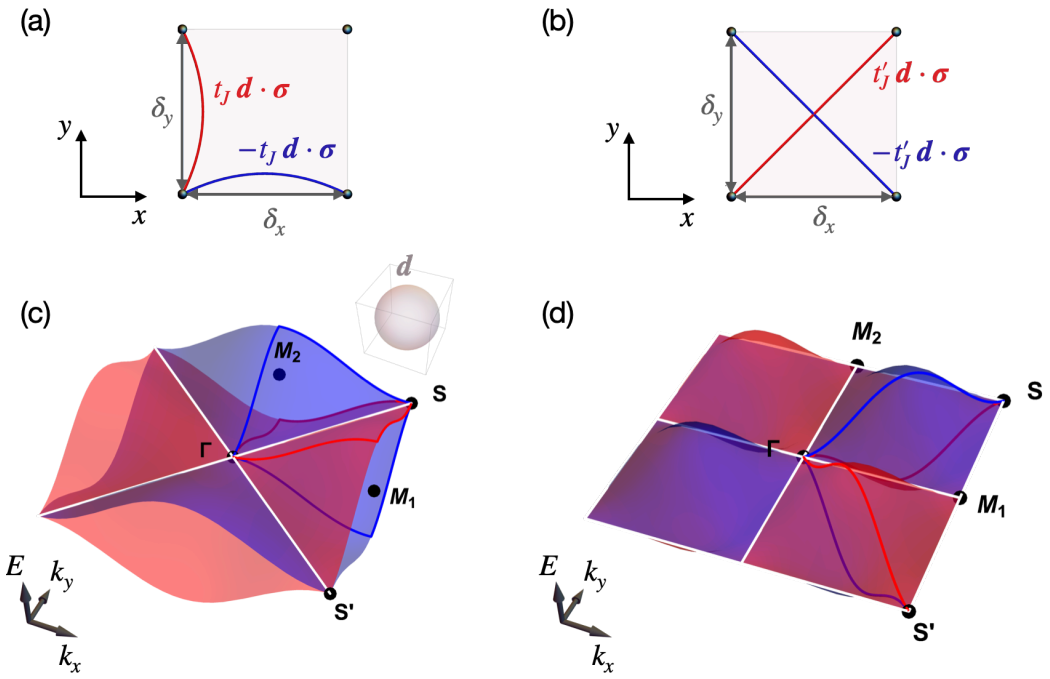

Figure 2.3: Altermagnetic tight-binding models. Real-space models with (a) nearest-neighbor and (b) next-nearest neighbor hoppings that are spin-dependent and whose sign alternates depending on the hopping direction (see Eqs. (2.21) and (2.22)). The corresponding energy bands (c,d) have an alternating spin splitting, which disperse and reach a maximum spin splitting along the paths indicated with red and blue lines. The Néel vector $\mathbf{d}$ can be in any direction (c, indicated by the inset), as rotating it by an arbitrary angle leaves the band structure unchanged. Here, we denote $\boldsymbol{M}_1 = \frac{\pi}{a}\hat{\mathbf{k}}_x$, $\boldsymbol{M}_2 = \frac{\pi}{b}\hat{\mathbf{k}}_y$, $\boldsymbol{S} = \frac{\pi}{a}\hat{\mathbf{k}}_x + \frac{\pi}{b}\hat{\mathbf{k}}_y$, and $\boldsymbol{S}' = \frac{\pi}{a}\hat{\mathbf{k}}_x - \frac{\pi}{b}\hat{\mathbf{k}}_y$, with $\hat{\mathbf{k}}_x$ and $\hat{\mathbf{k}}_y$ being unit vectors along the $\mathbf{k}_x$ and $\mathbf{k}_y$ vectors.

example, the hoppings in both models are related by the altermagnetic spin symmetry $[C_2||C_{4z}]$, where C_2 is a two-fold rotation in spin space and C_{4z} a four-fold rotation in crystal space (recall the crystallographic spin symmetry notation from Eq. (1.16)).

We can also construct an altermagnetic model with next-nearest neighbor hoppings. Fig. 2.3(b) shows an example. This time, the hoppings are along the diagonals. The real-space Hamiltonian reads:

$$H_{\mathrm{AM}}^{\mathrm{NNN}} = t'_J \left[\sum_{\langle\langle ij\rangle\rangle_+} - \sum_{\langle\langle ij\rangle\rangle_-} \right] \boldsymbol{d}\cdot\boldsymbol{\sigma}\, c_i^\dagger c_j. \tag{2.22}$$

Here, the NNN notation marks that it is a next-nearest neighbor term. The only difference from the nearest-neighbor model expression is $\langle\langle ij\rangle\rangle_{+/-}$ denoting the next-nearest neighbor sites, and that here we represent the next-nearest hopping strength by t'_J.

Exchange interaction. Fundamentally, the magnetic exchange interaction in altermagnets differs from ferromagnetic and antiferromagnetic exchange interactions. In altermagnets, the exchange parameter acquires a particular directional dependence, which respects the altermagnetic spin symmetries, as shown, for example, in Fig. 2.3(a,b). The directional dependence is governed by the sublattice-transposing symmetry of the altermagnet [25], e.g., symmetries like $[C_2||C_{4z}]$ in our model examples here [12]. In ferromagnets and antiferromagnets, the symmetry of exchange interactions is different [28].

Wavevector space. To obtain a momentum-space expression, we use a standard Fourier transformation, which we show below.

Fourier transform

For both the nearest and nest-nearest neighbor models, we can write part of the real-space Hamiltonian as follows:

$$\left[\sum_{\langle ij\rangle_+} - \sum_{\langle ij\rangle_-}\right] c_i^\dagger c_j = \sum_j \left[c^\dagger_{\mathbf{r}_j+\boldsymbol{\delta}_+} c_{\mathbf{r}_j} - c^\dagger_{\mathbf{r}_j+\boldsymbol{\delta}_-} c_{\mathbf{r}_j}\right] + \text{h.c.} \tag{2.23}$$

Here, $\mathbf{r}_j$ is the position of site j. $\boldsymbol{\delta}_{+/-}$ is the inter-site vector between the nearest or nest-nearest neighbors, shown in Fig. 2.3(a,b), and is associated with a positive ($\boldsymbol{\delta}_+$) and negative ($\boldsymbol{\delta}_-$) overall sign in the altermagnetic hopping term. The Fourier transformation is given by

$$\begin{aligned} c^\dagger_{\mathbf{r}_j+\boldsymbol{\delta}_{+/-}} &= \frac{1}{\sqrt{\mathcal{V}}}\sum_{\mathbf{k}} e^{-i\mathbf{k}\cdot\left(\mathbf{r}_j+\boldsymbol{\delta}_{+/-}\right)} c^\dagger_{\mathbf{k}} \\ c_{\mathbf{r}_j} &= \frac{1}{\sqrt{\mathcal{V}}}\sum_{\mathbf{k}'} e^{i\mathbf{k}'\cdot\mathbf{r}_j} c_{\mathbf{k}'} \end{aligned} \tag{2.24}$$

where the pre-factor is a normalization constant. Inserting for this Fourier transform, Eq. (2.23) becomes

$$\begin{aligned} &\frac{1}{\mathcal{V}}\sum_j\sum_{\mathbf{k}\mathbf{k}'}\left[e^{-i\mathbf{k}\cdot\left(\mathbf{r}_j+\boldsymbol{\delta}_+\right)} c^\dagger_{\mathbf{k}} e^{i\mathbf{k}'\cdot\mathbf{r}_j} c_{\mathbf{k}} - e^{-i\mathbf{k}\cdot\left(\mathbf{r}_j+\boldsymbol{\delta}_-\right)} c^\dagger_{\mathbf{k}} e^{i\mathbf{k}'\cdot\mathbf{r}_j} c_{\mathbf{k}}\right] + \text{h.c.} \\ &= e^{-i\mathbf{k}\cdot\boldsymbol{\delta}_+} - e^{-i\mathbf{k}\cdot\boldsymbol{\delta}_-} + \text{h.c.} \\ &= 2\cos\left(\mathbf{k}\cdot\boldsymbol{\delta}_+\right) - 2\cos\left(\mathbf{k}\cdot\boldsymbol{\delta}_-\right) \end{aligned} \tag{2.25}$$

In the first equality, we use the definition of the delta-function $\delta_{\mathbf{k}\mathbf{k}'} = \frac{1}{\mathcal{V}}\sum_j e^{-i\mathbf{k}\cdot\mathbf{r}_j} e^{i\mathbf{k}'\cdot\mathbf{r}_j}$ and employ Bloch Hamiltonian notation. In the second equality, we insert for the hermitian conjugate and use the identity $e^{-i\mathbf{k}\cdot\boldsymbol{\delta}_{+/-}} + e^{i\mathbf{k}\cdot\boldsymbol{\delta}_{+/-}} = 2\cos\left(\mathbf{k}\cdot\boldsymbol{\delta}_{+/-}\right)$.

Momentum-space Hamiltonians. We obtain the two momentum-space Hamiltonians by inserting for their relevant expressions for $\mathbf{k}\cdot\boldsymbol{\delta}_{+/-}$ above (in Eqs. (2.21), (2.22), and (2.25)). For example, for the nearest-neighbor model, $\mathbf{k}\cdot\boldsymbol{\delta}_+ = k_y\delta_y$ and $\mathbf{k}\cdot\boldsymbol{\delta}_- = k_x\delta_x$ (see Fig. 2.3(a)). Similarly for the next-nearest neighbor model, $\mathbf{k}\cdot\boldsymbol{\delta}_+ = k_x\delta_x + k_y\delta_y$

and $\mathbf{k}\cdot\boldsymbol{\delta}_- = k_x\delta_x - k_y\delta_y$ (see Fig. 2.3(b)). For simplicity, we let $\delta_x = \delta_y = 1$, and the nearest-neighbor and next-nearest neighbor models then take the forms

$$H_{\mathrm{AM}}^{\mathrm{NN}}(k_x, k_y) = 2t_J\left[\cos k_y - \cos k_x\right]\boldsymbol{d}\cdot\boldsymbol{\sigma} \tag{2.26}$$

and

$$\begin{aligned} H_{\mathrm{AM}}^{\mathrm{NNN}}(k_x, k_y) &= 2t_J\left[\cos(k_x + k_y) - \cos(k_x - k_y)\right]\boldsymbol{d}\cdot\boldsymbol{\sigma} \\ &= -4t_J \sin k_x \sin k_y\, \boldsymbol{d}\cdot\boldsymbol{\sigma}. \end{aligned} \tag{2.27}$$

Energy bands. The corresponding energy bands are found by diagonalizing these expressions, yielding $\pm 2t_J\left[\cos k_x - \cos k_y\right]|\boldsymbol{d}|$ and $\pm 4t_J \sin k_x \sin k_y |\boldsymbol{d}|$ for the two models. Since $\boldsymbol{d}$ is a unit vector, these expressions simplify to

$$E_{\mathrm{AM},\pm}^{\mathrm{NN}}(k_x, k_y) = \pm 2t_J\left[\cos k_x - \cos k_y\right] \tag{2.28}$$

$$E_{\mathrm{AM},\pm}^{\mathrm{NNN}}(k_x, k_y) = \pm 4t_J \sin k_x \sin k_y \tag{2.29}$$

We note that these expressions are independent of the direction of the Néel vector $\boldsymbol{d}$. Thus, the Néel vector can take any direction in three dimensions (indicated by the sphere in Fig. 2.3(c, inset)) without changing the energy bands.

The bands are shown in Fig. 2.3(c) for Eq. (2.28) and 2.3(d) for Eq. (2.29). The "+" and "−" bands have opposite spin expectation values shown by the red and blue coloring. Each of the two bands is perfectly spin-polarized as either spin up or down along the spin quantization axis, which is conserved and parallel to $\boldsymbol{d}$.

D-wave symmetry with different periodicities. The band structures in Fig. 2.3 are of the d-wave type. Like the real space models, the bands obey the $[C_2||C_{4z}]$ symmetry and are magnetically compensated overall.

Mirror sublattice-transposing symmetries enforce the bands have two nodal lines marked by white lines in Fig. 2.3(c,d), the two nodal lines crossing the $\boldsymbol{\Gamma}$-point being a signature of d-wave altermagnetism (recall Fig. 1.9). The nodal lines are oriented differently in the two models due to the distinct mirror sublattice-transposing symmetries of the two models; in the nearest-neighbor model, the mirrors are along the xy diagonals ($[C_2||M_{1\bar{1}}]$ and $[C_2||M_{\bar{1}1}]$), in the next-nearest neighbor model, along the x and y axes ($[C_2||M_x]$ and $[C_2||M_y]$). This difference is reflected in the different sinusoidal forms of the energy bands, where the $\sin k_x \sin k_y$ sinusoidal (next-nearest neighbor model, Fig. 2.3(d) and Eq. (2.29)) has half the periodicity of $\cos k_x - \cos k_y$ (nearest-neighbor, Fig. 2.3(b) and Eq. 2.28).

The bands are degenerate at the edge of the Brillouin zone for the next-nearest neighbor model in Fig. 2.3(d), and reach a maximal spin splitting in between $\boldsymbol{\Gamma}$ and $\boldsymbol{S}$ as highlighted by the red and blue lines. In the nearest-neighbor model in Fig. 2.3(c), the bands reach their maximum splitting at the Brillouin zone edge, similarly highlighted.

The different symmetry and periodicity in the d-wave models here have also been seen in material candidates depending on their particular spin Laue groups. For example, the d-wave altermagnetic candidate RuO_2 is spin degenerate at $\boldsymbol{S}$ and $\boldsymbol{S}'$ and maximally split along the $\boldsymbol{\Gamma}$-$\boldsymbol{S}$ and $\boldsymbol{\Gamma}$-$\boldsymbol{S}'$ paths [3], as we will see in Ch. 3, similarly to the next-nearest neighbor model in Fig. 2.3(d). A further example is the d-wave candidate KRu_4O_8, which is maximally spin-split at the edges of the Brillouin zone, similar to the nearest-neighbor model in Fig. 2.3(c). Its effective Hamiltonian has the symmetry of a sum of the nearest- and next-nearest neighbor Hamiltonians (breaking the mirror transposing symmetries and leaving the transposing four-fold rotation in its spin Laue group ${}^{2}4/{}^{1}m$) [25].

Inversion symmetry and quadratic dispersion. The exchange terms in this model are collinear ($\pm t_J^{(\prime)} \boldsymbol{d} \cdot \boldsymbol{\sigma}$, e.g., $\pm t_J \sigma_z$ with $\boldsymbol{d} = \boldsymbol{z}$) obeying the collinear spin-only group $\mathbf{r}_s^{\text{coll}} = \{E, C_{2\perp}\mathcal{T}\} \times \text{SO}(2)$ (see Eq. (1.17)) and thus the electronic band structure is enforced to be inversion symmetric (Eq. (1.20)). This inversion symmetry is evident in the electronic band structure in Fig. 2.3(c,d) by inverting the electronic structure around $\boldsymbol{\Gamma}$, i.e., $E_{ns}(k_x, k_y) = E_{ns}(-k_x, -k_y)$.

Due to inversion symmetry, the k.p Hamiltonian around $\boldsymbol{\Gamma}$ can only contain even terms in the wavevectors. For example, an even in wavevector term $k_x k_y$, when inverted, yields $(-k_x)(-k_y) = k_x k_y$ and thus obeys the inversion symmetry. In Fig. 2.3(c,d), we see that the energy bands disperse quadratically (i.e., even) in the wavevectors around $\boldsymbol{\Gamma}$ (see red and blue lines), in concurrence with inversion symmetry (here, $\cos k_x - \cos k_y \sim (1 - k_x^2/2) - (1 - k_y^2/2) \sim k_y^2 - k_x^2$ and $\sin k_x \sin k_y \sim k_x k_y$). Note that this inversion symmetry of the energy bands will still be there as long as the magnetic order (exchange term here) is collinear, even if the crystal would break inversion symmetry. In other words, collinear magnetism enforces inversion symmetric bands even in noncentrosymmetric crystals.

Altermagnetic models with additional normal hoppings

The models in Fig. 2.3 are purely altermagnetic exchange terms hosting d-wave spin polarizations. We can add further terms to alter their dispersions while the nodal planes and symmetries remain. Here, we will add normal hopping terms for nearest neighbors to alter the dispersions. In Ch. 4, we will see how it can affect tunneling magnetoresistance. We note that adding these terms does not change the d-wave and inversion symmetries of the bands. The models will still obey the same mirror sublattice-transposing symmetries (enforcing the nodal planes), and the magnetic order is still collinear (enforcing inversion symmetry of the band structures and an even dispersion around the $\boldsymbol{\Gamma}$-point).

For example, Fig. 2.4(a) shows an adapted model for the nearest-neighbor altermagnetic model. The gray lines connecting the nearest-neighbor sites are the normal

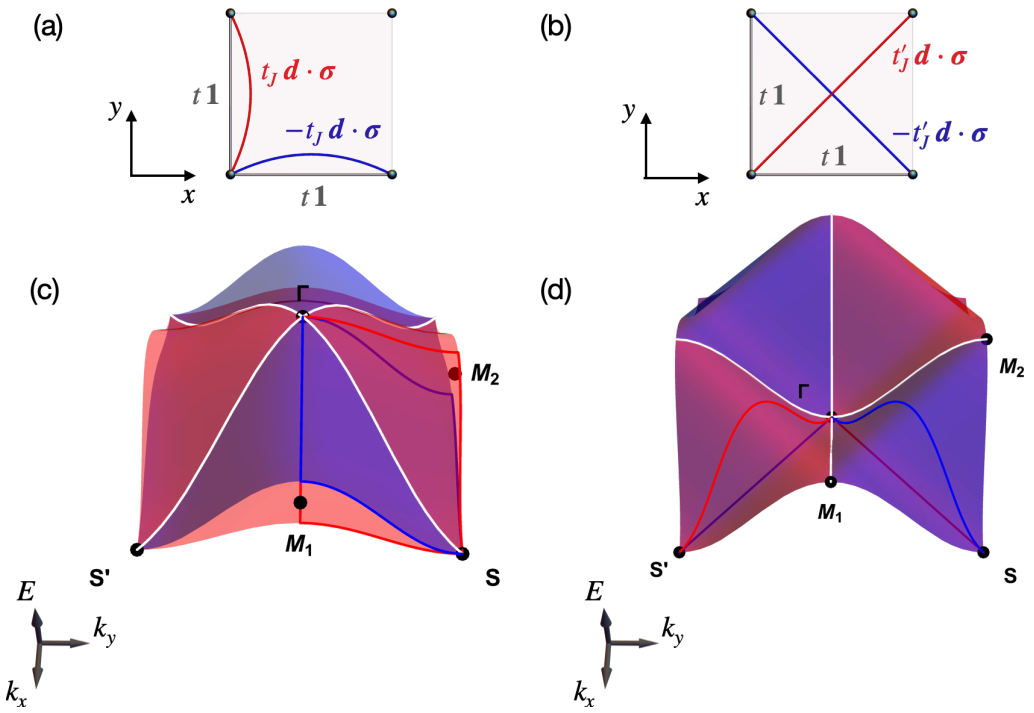

Figure 2.4: D-wave tight-binding models as in Fig. 2.3, now with an additional nearest-neighbor normal hopping term given by Eq. (2.30). In (a), $t_J = 0.4\,t$; in (b), $t_J = t$.

hopping term t, corresponding to the Hamiltonian

$$H_{\mathrm{N}}^{\mathrm{NN}}(k_x, k_y) = 2t\,(\cos k_x + \cos k_y)\,\mathbf{1}, \tag{2.30}$$

where $\mathbf{1}$ is the identity matrix in spin space, and t is a normal hopping parameter which is spin-independent. This Hamiltonian is the two-dimensional version of the tight-binding model from Sec. 2.1. The alternating red and blue hoppings in Fig. 2.4(a) are the same spin-dependent alternating hoppings as before, given by $H_{\mathrm{AM}}^{\mathrm{NN}}$ in Eq. (2.21). The full Hamiltonian is therefore $H_{\mathrm{N}}^{\mathrm{NN}} + H_{\mathrm{AM}}^{\mathrm{NN}}$, which reads

$$\mathcal{H}(\mathbf{k}) = 2t\,(\cos k_x + \cos k_y)\,\mathbf{1} + 2t_J\,(\cos k_x - \cos k_y)\,\boldsymbol{\sigma}\cdot\mathbf{d}. \tag{2.31}$$

The energy bands are

$$E_{\pm}(\mathbf{k}) = 2t\,(\cos k_x + \cos k_y) \pm 2t_J\,(\cos k_x - \cos k_y) \tag{2.32}$$

for spin up (+) and down (−), shown in red and blue in Fig. 2.4(c). The bands in 2.4(c) is a two-band version of the four-band model used to fit the *ab-initio* calculated bands of KRu_4O_8 in [25].

Similarly, Fig. 2.4(b,d) shows the the model corresponding to $H_{\mathrm{N}}^{\mathrm{NN}}+H_{\mathrm{AM}}^{\mathrm{NNN}}$ with the spin-up and down dispersions $E_{\pm}(\mathbf{k}) = 2t\,(\cos k_x + \cos k_y) \pm 4t_J \sin k_x \sin k_y$. As shown in [25, 1], is a two-band model that can fit the altermagnetic *ab-initio*-calculated bands of RuO_2 [3].

Three-dimensional models

With three-dimensional versions of altermagnetic models, we can additionally choose the *plane with the d-wave spin-momentum locking*, or, *d-wave plane* (i.e., the plane where the two nodal lines cross $\mathbf{\Gamma}$, and planes parallel to it) [12]. We illustrate this by examples in Fig. 2.5. We have used this to demonstrate tunneling magnetoresistance in three dimensions with different orientations of the d-wave magnetism (Ch. 4) [12].

Here, we add nearest-neighbor normal hoppings shown by the gray straight lines between the sites in Fig. 2.5 to obtain three-dimensional models. These hoppings correspond to the wavevector-space Hamiltonian given by

$$H_{\mathrm{N}}^{\mathrm{NN,3D}}(k_x, k_y, k_z) = 2\,(t_x \cos k_x + t_y \cos k_y + t_z \cos k_z)\,. \tag{2.33}$$

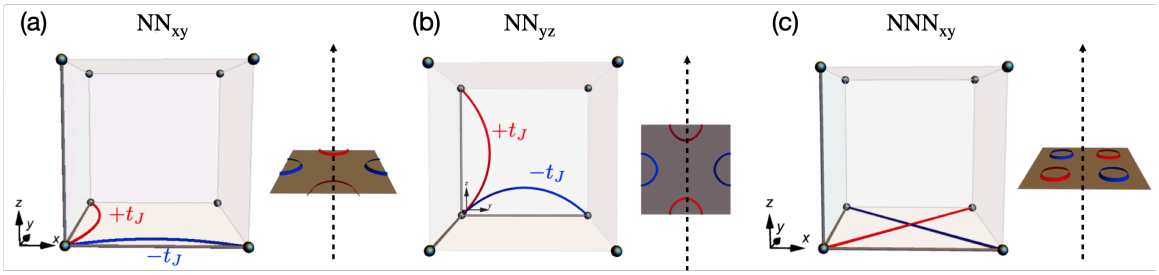

Figure 2.5: D-wave altermagnetic tight-binding models in three dimensions. The alternating spin-dependent hopping in real space (red and blue lines) can lie in different planes, for instance, in the xy-plane (a,c, left) or the zy-plane (b, left), yielding the momentum-space d-wave spin polarization in these respective planes (a-c, right). Figure adapted from [12], CC BY 4.0.

In the first example in Fig. 2.5(a, left, labeled $\mathrm{NN}_{\mathrm{xy}}$), the d-wave-symmetric alternating hopping terms lie in the xy-plane. The Hamiltonian is therefore one where the $H_{\mathrm{AM}}^{\mathrm{NN}}$ term is in the k_xk_y-plane, i.e., $H_{\mathrm{AM}}^{\mathrm{NN_{xy}}}(k_x, k_y, k_z) = H_{\mathrm{AM}}^{\mathrm{NN}}(k_x, k_y) + H_{\mathrm{N}}^{\mathrm{NN,3D}}(k_x, k_y, k_z)$. In momentum space (Fig. 2.5(a), right), the d-wave plane is also in the xy-plane, due to the $[C_2||C_{4z}]$ spin symmetry of the model, where the crystal rotation is around the z-axis [1].

[1]This symmetry is enough to tell us the d-wave plane must be in the xy-plane. Analogous to the two-dimensional model, to determine the nodal planes, we would also need to realize that it has $[C_2||M_{[1\bar{1}0]}]$ and $[C_2||M_{[\bar{1}10]}]$ symmetries.

If, instead, the d-wave-symmetric hoppings is placed in the yz-plane (2.5(b, left, labeled $\mathrm{NN_{yz}}$)), the hamiltonian is $H_{\mathrm{AM}}^{\mathrm{NN_{yz}}}(k_x, k_y, k_z) = H_{\mathrm{AM}}^{\mathrm{NN}}(k_y, k_z) + H_{\mathrm{N}}^{\mathrm{NN,3D}}(k_x, k_y, k_z)$. The corresponding momentum-space d-wave plane is also in the yz-plane, due to the $[C_2||C_{4x}]$ spin symmetry.

Analogously, we can construct the next-nearest neighbor model in three dimensions, illustrated in 2.5(c, left, labeled $\mathrm{NNN_{xy}}$) with $H_{\mathrm{AM}}^{\mathrm{NNN_{xy}}}(k_x, k_y, k_z) = H_{\mathrm{AM}}^{\mathrm{NNN}}(k_x, k_y) + H_{\mathrm{N}}^{\mathrm{NN,3D}}(k_x, k_y, k_z)$ and $[C_2||C_{4z}]$ spin symmetry.

These examples illustrate that by constructing three-dimensional models in this way, we can decide how to orient the d-wave plane. They are not an exhaustive set of examples, as, e.g., g- and i-wave altermagnetic models can be constructed whose symmetries are different [25].

2.2.1 Effect of adding spin-orbit coupling

The perfectly collinear spin polarization of altermagnetic band structures acquires a spin texture if we add spin-orbit coupling. For example, we may add to our model an inversion-breaking Rashba spin-orbit coupling [133, 134] term, given by

$$H_{\mathrm{SOC}}(k_x, k_y) = \lambda \left(\cos k_x \sigma_y - \cos k_y \sigma_x\right). \tag{2.34}$$

The SOC label denotes it being a spin-orbit coupling term. It is illustrated in Fig. 2.6(a) by white and black hoppings in the two-dimensional nearest-neighbor model. We use $t = 1$ and $\lambda = 0.4\,t$ in this example. The resulting components of the

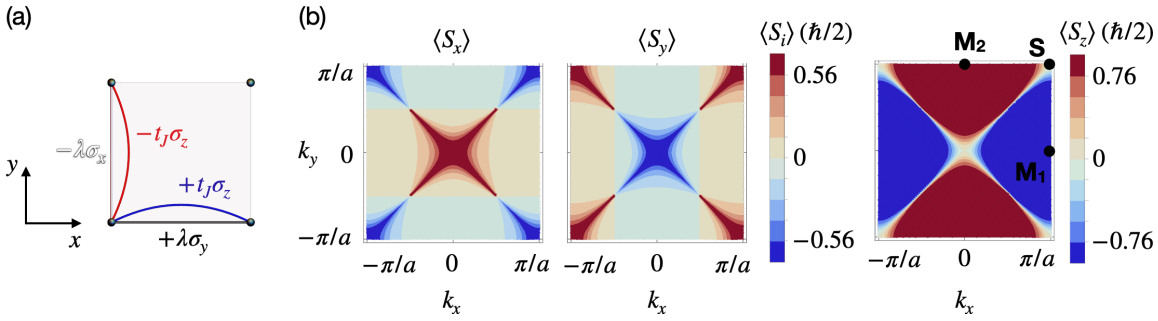

Figure 2.6: Altermagnetic model with spin-orbit coupling. (a) Real-space representation of the hoppings in the tight-binding model, where we add the spin-orbit coupling terms (black and white lines) to the altermagnetic nearest-neighbor terms (red and blue lines). (b) Spin expectation values $\langle\sigma_i\rangle$ for the upper band in the two-band model in units of $\hbar/2$. The lattice vector length in the y-direction, b, equals the one in the x-direction, a.

spin expectation values, $\langle S_i\rangle$ $(i = x, y, z)$, are shown in Fig. 2.6(b) for the upper band. The band structure acquires an additional spin texture compared to the nonrelativistic limit (Fig. 2.3(c)), localized around the nodal lines. Away from the nodal lines,

the spin expectation values stay largely identical to those in the nonrelativistic limit. The spin expectation values for the lower band are identical except for an overall sign change.

We note that altermagnetic crystals are not restricted to be inversion symmetric. Thus, it can be reasonable to add this phenomenological Rashba spin-orbit coupling term for altermagnets that break inversion symmetry [12]. Moreover, if inversion-symmetric altermagnets are interfaced with a different material, the system breaks inversion symmetry due to the interface, and Rashba spin-orbit coupling may model this breaking of inversion symmetry.

The altermagnetic material candidates we will discuss in subsequent chapters (MnTe [30], CrSb [31], RuO_2 [12, 38], and Mn_5Si_3 [12, 112]) all preserve inversion symmetry. Notably, in MnTe, we verify in collaboration with experiment the inversion-symmetric electronic structure in the presence of spin-orbit coupling (Ch. 3.1.4) [30].

2.3 Density functional theory

Quantum theory of magnetic crystals has been instrumental for the study of altermagnetism in real materials [3, 25, 1, 2, 118]. We will combine this theory with symmetry analysis to predict p-wave and odd-parity-wave magnetism in real material candidates and the band structures of altermagnetic MnTe, CrSb, and RuO_2. Our DFT calculations and symmetry analysis guided experimental confirmations of the altermagnetic spin splitting in MnTe and CrSb and time-reversal symmetry breaking in RuO_2, which was done by our experimental colleagues [30, 31, 38].

In principle, this quantum theory relies on solving a complex many-body problem of N spin-full electrons. This problem is known as an *N-body problem*, and solving it is a formidable task [128, 127, 135, 94, 136].

In quantum theory, the probability of finding an electron at a position $\mathbf{r}_1$ with a spin σ_1 within an infinitesimal volume $d\mathbf{r}_1$ centered around $\mathbf{r}_1$, and similarly for the rest of the electrons, is given by [94]

$$\Psi^* \left(\mathbf{r}_1\sigma_1, \ldots, \mathbf{r}_N\sigma_N\right) \Psi \left(\mathbf{r}_1\sigma_1, \ldots, \mathbf{r}_N\sigma_N\right) d\mathbf{r}_1 \ldots d\mathbf{r}_N, \tag{2.35}$$

where Ψ is the wavefunction for all the electrons. If we neglect spin, the wavefunction has $3N$ variables — N electrons, each with three spatial coordinates.

Before even trying to solve the N-body problem, the first step of storing this wavefunction can be difficult, even for small systems. Take, for instance, the Nitrogen atom which has $N = 7$ electrons. If we neglect spin, each of the seven electrons is specified by three spatial coordinates. Thus, there are $3N = 21$ electron position coordinates to represent on a grid of, say, a very coarse 10 points in real space. In

order to represent the wavefunction on this grid using quantum theory, we need to represent the linear combination of all possible combinations of electrons in points on the grid [94]. This number of combinations, or entries we need to save on a memory, is given by (number of grid points)$^{\text{number of coordinates}} = 10^{3N} = 10^{21}$. Assuming that each entry requires one byte, we would need 1.56×10^4 tons of micro SD cards with 64 GB memory each to store the wavefunction for a single Nitrogen atom [128]. Handling such data is practically impossible if we want to simulate realistic materials. Additionally, it is not desirable to know so much information, which would be very difficult to analyze.

While the wavefunction contains information that could be useful, for instance, for quantum computers [137], it actually contains information that is redundant for us [117]. After all, a wavefunction is not an observable, and we are interested in observable manifestations of altermagnetism and odd-parity-wave magnetism and the resulting spin-dependent transport.

One way to try remedying the problem is with mean-field theories, which treat the N-body problem as a single-particle problem where each single particle interacts only with the mean (or mean-field) of the rest of the particles [136]. One is the Hartree mean-field theory (1928), approximating the wavefunction by a product of single-particle wavefunctions [138], and another is the extended Hartree-Fock theory (1930) which additionally accounts for the antisymmetric exchange of electrons [127, 94, 136]. Hartree-Fock theory alone is, however, limited to systems of tens of atoms, and therefore is not feasible to use for describing systems with many atoms in real materials [127].

A breakthrough for material science came with a tremendous simplification of the problem, namely *density functional theory* (DFT), celebrated with the 1998 Nobel Prize in chemistry. In essence, it maps the many-body interacting problem (with $3N$ variables) onto an effective single-particle noninteracting problem by using *electron densities* $n(\mathbf{r})$ (with just three variables, $\mathbf{r} = (x, y, z)$) [139, 117, 127, 128, 135]. For the Nitrogen example, it lowers the number of entries for the memory from $10^{3N} = 10^{21}$ to 10^3, or 18 orders of magnitude, and the change is even more drastic for larger systems and denser grids.

2.3.1 Spin density functional theory

Since we are interested in magnetic systems, we will be using *spin density functional theory*, a spin-full version of normal density functional theory. In this section, we briefly review the two Hohenberg-Kohn theorems, which establish that *(i)*, we can describe the N-body problem (uniquely) using electron densities instead of wavefunctions and, *(ii)*, that there exists a (unique) electron density of the ground-state [139]. Then, we describe the *Kohn-Sham approach* to obtaining the ground state electron

density, based on minimizing the total energy using the *variational principle* [140]. With this, we will have the necessary foundation to calculate, for example, the *magnetization densities*, or *spin densities* of magnets, the total energy of the system, and spin-polarized electronic band structures [135, 128, 127], which are key to understanding the unique electronic structure of altermagnets and odd-parity-wave magnets.

Hamiltonian of N-body spin-full electronic systems

We begin by considering the Hamiltonian of an N-body spin-full electronic system, e.g., a magnetic crystal, which is given by [135]

$$\mathcal{H}_{\alpha\beta} = T_{\alpha\beta} + U_{\alpha\beta} + V_{\alpha\beta} \tag{2.36}$$

where α and β are spin indices. Here, $T_{\alpha\beta}$ is the kinetic energy of the electrons, $U_{\alpha\beta}$ is the Coulomb interaction between electrons, and $V_{\alpha\beta}$ is the external potential electrons experience from nuclei and possibly external magnetic and electric fields. These three terms can be expressed as [135]

$$\begin{aligned} T_{\alpha\beta} &= -\delta_{\alpha\beta} \sum_{i=1}^{N} \nabla_i^2 \\ V_{\alpha\beta} &= \sum_{i=1}^{N} v_{\alpha\beta}^{\text{ext}}\left(\mathbf{r}_i\right) \\ U_{\alpha\beta} &= \sum_{\substack{i=1,j=1 \\ i\neq j}}^{N} \frac{\delta_{\alpha\beta}}{|\mathbf{r}_i - \mathbf{r}_j|} \end{aligned} \tag{2.37}$$

Note that these expressions are written in atomic units[2]. We also note that in the Born-Oppenheimer approximation[3], $v_{\alpha\beta}^{\text{ext}}$ consists of electrons interacting with the atomic nuclei (positive ions) at static positions, $\mathbf{R}_\mu$, plus other possible fields, i.e., $v_{\alpha\beta}^{\text{ext}}(\mathbf{r}) = \sum_\mu v_{\alpha\beta}^{\text{ion}}\left(\mathbf{r} - \mathbf{R}_\mu\right) + v_{\alpha\beta}^{\text{field}}(\mathbf{r})$ [135]. $\delta_{\alpha\beta}$ is the Kronecker-Delta and $\mathbf{r}_i$ the position of a given electron indexed by i.

[2]To convert between normal and atomic units, we can use the following recipe: $m = 1/2, \hbar = 1, e^2 = 2$ [135].

[3]We note that the N-body problem is usually solved assuming the Born-Oppenheimer approximation, i.e., the nuclei are assumed to be at rest while only the electrons are moving [128]. This assumption is a good approximation because electrons are much lighter than atomic nuclei. Thus, we can focus on the electrons, which interact with nuclei and themselves (and possible external magnetic or electric fields) [128].

Hohenberg-Kohn theorems (1964)

DFT is based on the abovementioned Hohenberg-Kohn [139] and Kohn-Sham [140] theorems. We state the theorems without proofs here, as detailed demonstrations are available in most DFT textbooks (e.g., [135] and [128]). We note that the theorems were originally formulated in terms of the electron density n [139, 140], but they apply equally well to the spin density matrix $\tilde{n}$ [141, 135].

Hohenberg-Kohn theorem 1. *The total energy of a system can be uniquely expressed in terms of a functional $E[n]$ of the electron density n [139].*

This theorem means that there exists an energy functional,

$$E[\tilde{n}(\mathbf{r})] = T[\tilde{n}(\mathbf{r})] + U[\tilde{n}(\mathbf{r})] + V[\tilde{n}(\mathbf{r})], \tag{2.38}$$

where the spin density matrix, $\tilde{n}$, determines the energy functional uniquely, thus establishing the density as a primary variable [139]. For example, another density, say $\tilde{n}'$, will always give rise to a different energy potential [128, 135]. (Here, analogously to in Eq. (2.37), T, U, and V are the kinetic energy, electron-electron, and external potentials, now as functionals of the spin density matrix.)

Hohenberg-Kohn theorem 2. *The energy functional $E[n]$ has a minimum that equals the ground-state energy when the electron density n is the ground state density [139].*

Here, if we try to conjecture that there is another energy functional, say $E'[\tilde{n}]$, that also describes the ground state, then our conjecture will always fail because its energy will always be greater than the ground state energy corresponding to $E[\tilde{n}]$ [139, 128].

We can now obtain the ground-state energy by minimizing $E[\tilde{n}]$ while keeping the total number of electrons, N, constant [127, 135, 128]. The N Kohn-Sham equations describe this.

Kohn-Sham equations (1965)

In the Kohn-Sham equations, to make the interacting N-body problem easier to solve, the system is described in terms of noninteracting single-particle electron (and spin) densities [140, 135]. One constructs N Schrödinger equations in terms of the corresponding single-particle wavefunctions $\phi_{i\beta}$ as follows [140, 135]:

$$\sum_{\beta} \left(-\delta_{\alpha\beta}\nabla^2 + v'_{\alpha\beta}(\mathbf{r}) - \varepsilon_i \delta_{\alpha\beta}\right) \phi_{i\beta}(\mathbf{r}) = 0. \tag{2.39}$$

Here, the first term is the single-particle kinetic energy, the last term is the eigenenergy, and the second term contains all the remaining terms in the Hamiltonian in Eq. (2.37). By minimizing $E[\tilde{n}]$, the expression for $v'_{\alpha\beta}(\mathbf{r})$ is an effective potential that describes all electron interactions, given by [140, 135, 127]

$$v'_{\alpha\beta}(\mathbf{r}) \equiv v^{\text{eff}}_{\alpha\beta}(\mathbf{r}) = v^{\text{ext}}_{\alpha\beta}(\mathbf{r}) + 2\delta_{\alpha\beta}\int \frac{n\,(\mathbf{r}')}{|\mathbf{r}-\mathbf{r}'|}\mathrm{d}\mathbf{r}' + v^{xc}_{\alpha\beta}(\mathbf{r}), \tag{2.40}$$

where

$$v^{xc}_{\alpha\beta}(\mathbf{r}) = \frac{\delta}{\delta\tilde{n}_{\beta\alpha}(\mathbf{r})}\left(E_{xc}[\tilde{n}]\right) + T_{xc}[\tilde{n}]). \tag{2.41}$$

Here, the electron-electron interaction $U_{\alpha\beta}$ has been decomposed into a Hartree term, corresponding to the second term in Eq. (2.40), and a remaining, unknown *exchange-correlation* term $E_{xc}[\tilde{n}]$, which describes remaining electron-electron interactions and, unlike the Hartree term, accounts for Pauli's exclusion principle [140, 127]. Similarly, the kinetic energy $T_{\alpha\beta}$ has been decomposed into that of single particles (first term in Eq. (2.39)) and an unknown term $T_{xc}[\tilde{n}]$ [135].

Now, the many-body problem is not only mapped onto densities with fewer dimensions, but we also use simpler noninteracting single-particle wavefunctions and mean-field theory while moving the remaining interactions into *exchange-correlation* terms [127]. If the exchange correlations were known exactly, this theory would reproduce the exact charge and spin densities of the system [127].

Now that we have the Kohn-Sham equations with single-particle wavefunctions, we will define the *spin density matrix* (or *magnetization density matrix*), $\tilde{n}$, used in spin density functional theory.

Spin density. In spin density functional theory, the electronic charge and spin densities are respectively given by [135, 128]:

$$n(\mathbf{r}) = \sum_{i=1}^{N} \phi_i^\dagger(\mathbf{r})\phi_i(\mathbf{r}), \tag{2.42}$$

$$\mathbf{m}(\mathbf{r}) = \mu_{\text{B}} \sum_{i=1}^{N} \phi_i^\dagger(\mathbf{r})\,\boldsymbol{\sigma}\,\phi_i(\mathbf{r}). \tag{2.43}$$

Here, $\phi_i(\mathbf{r})$ are the single-particle Kohn-Sham wavefunctions in their spinor form, $\phi_i(\mathbf{r}) = (\phi_{i\uparrow}(\mathbf{r}), \phi_{i\downarrow}(\mathbf{r}))$, and $\boldsymbol{\sigma} = (\sigma_x, \sigma_y, \sigma_z)$ contains the three spin Pauli matrices. The *spin density matrix* can be expressed in terms of the electronic charge and spin densities as follows [135, 128]:

$$\tilde{n} = \frac{1}{2}(n\mathbf{1} + \boldsymbol{\sigma}\cdot\mathbf{m}) = \frac{1}{2}\begin{pmatrix} n+m_z & m_x - im_y \\ m_x + im_y & n - m_z \end{pmatrix}. \tag{2.44}$$

For example, for a collinear system expressed in the σ_z-basis on the nonrelativistic level, we can express the spin density matrix as $\tilde{n} = \mathrm{diag}(n + m_z, n - m_z)/2 \equiv \mathrm{diag}(n_\uparrow, n_\downarrow)$ (the corresponding *spin density* is then $\mathbf{m} = \mu_\mathrm{B}(n_\uparrow - n_\downarrow) = m_z$), that is, it is block-diagonal in the two spin channels, analogously to how the Hamiltonian is block-diagonal (see Sec. 1.3.1).

This block-diagonality has profound implications for altermagnets. In altermagnets, each block (or spin density in separate spin channels) can be treated separately and obey half the symmetries of the underlying crystal (the halving subgroup **H** in Eq. (1.29)) [25]. This lower symmetry, described exactly by the symmetries in **H** on the nonrelativistic level, makes the spin densities conform to their anisotropic shapes [3, 25].

For noncollinear systems, the off-diagonal elements of the spin density can, in general, be finite, and the spin quantization axis (or basis) we choose will not align with all spins in the magnetic crystal (see Sec. 1.1.1). In this thesis, we always use a spin-quantization axis pointing along the z-axis for DFT calculations with noncollinear magnetism or spin-orbit coupling.

2.3.2 Exchange correlation approximations

Exchange-correlations are typically divided into two types of interactions, exchange and correlations [127]. Exchange arises from the antisymmetric exchange of electrons and the Pauli exclusion principle, where same-state electrons repulse each other, increasing the distance between these electrons and thus lowering the total energy. Correlations arise, e.g., when electrons of opposite spin occupy the same atomic orbital but repulse each other since they have the same negative charge [127]. The exchange-correlation term typically accounts for only about 10% of the total energy; however, it can still influence crucial material properties, such as whether the system is insulating or metallic, nonmagnetic or magnetic [127]. For example, changing correlations on localized d-orbitals in RuO_2 changes whether it is nonmagnetic, altermagnetic, or insulating [3].

The problem now becomes describing the unknown exchange-correlation. Approximations, apart from the commonly adopted Born-Oppenheimer approximation, come into play here. There is a rich literature on exchange-correlations [127]. Here, we will show the idea behind three such widely used methods, the *local spin density approximation* (LSDA), the *generalized gradient approximation* (GGA), which builds on LSDA, and adding electronic correlations with a Hubbard term.

Local spin density approximation. In this approach, we divide the inhomogeneous electron gas that is our system into a grid of infinitesimal regions. Each region is approximated by a homogeneous electron gas of the local density [141, 128, 135]. The

corresponding energy functional is determined by integrating over the infinitesimal regions, each centered around a position $\mathbf{r}$, as follows [141, 128, 135]:

$$E_{\mathrm{xc}}\left[n_{\uparrow}, n_{\downarrow}\right] = \int d\mathbf{r}\, n(\mathbf{r}) \varepsilon_{\mathrm{xc}}\left(n_{\uparrow}(\mathbf{r}), n_{\downarrow}(\mathbf{r})\right). \tag{2.45}$$

Here, $n_{\uparrow}(\mathbf{r})$ and $n_{\downarrow}(\mathbf{r})$ are the charge densities for the spin up and spin down channels (the diagonal elements in Eq. (2.44)). The corresponding exchange-correlation function is given by [128]:

$$v_{\mathrm{xc}}^{\mathrm{LSDA},\sigma}\left[n_{\uparrow}, n_{\downarrow}\right](\mathbf{r}) = \frac{\delta E_{\mathrm{xc}}^{\mathrm{LSDA}}\left[n_{\uparrow}, n_{\downarrow}\right](\mathbf{r})}{\delta n_{\sigma}(\mathbf{r})}. \tag{2.46}$$

LSDA is known to underestimate exchange and overestimate correlations [127]. The following approximation, GGA, improves this.

Generalized gradient approximation. Real materials are evidently not homogeneous, and the density landscape varies across the system [127]. The GGA approach better accounts for this variation by describing both local and semi-local information around each point $\mathbf{r}$ – the local density, like in the LSDA, but also semi-local gradients, $\boldsymbol{\nabla} n_{\sigma}(\mathbf{r})$ [127]. Thus, the spin-polarized GGA can be expressed as [142]

$$E_{\mathrm{xc}}\left[n_{\uparrow}, n_{\downarrow}\right] = \int d\mathbf{r}\, n(\mathbf{r}) \varepsilon_{\mathrm{xc}}\left(n_{\uparrow}(\mathbf{r}), n_{\downarrow}(\mathbf{r}), \nabla n_{\uparrow}(\mathbf{r}), \nabla n_{\downarrow}(\mathbf{r})\right) \tag{2.47}$$

An implementation of GGA, namely Perdew Burke Erzenhorf (PBE), is what we will use for our DFT calculations. It implements additional second-order gradients in a way that was shown to be accurate [127] (e.g., compared to LSDA [142] and experimental lattice constants and band gap data [143, 144] for archetypical solid state systems) and computationally efficient [127].

Improving LSDA/GGA with electronic correlation using the Hubbard potential. DFT is known to describe well-localized s and p orbitals accurately, but it can fail with more localized d and f orbitals [128]. When electrons are strongly localized, they become prone to a repulsive interaction between them, which can be approximated by a Hubbard repulsion energy [145, 146, 127]. Thus, to alleviate the localization problem in DFT, we can add a Hubbard repulsion (*Hubbard U*) term on the electrons in the localized orbitals [128], which can be understood as the energy cost of placing two electrons in the same orbital [147]. We refer to this approach as *DFT+U*.

To describe this, we can single out a sub-space of localized, e.g., d orbital states. Here, there will be a Coulomb interaction between same-orbital electrons (a d orbital in our example), given by the Hubbard Hamiltonian [128],

$$\frac{U}{2} \sum_{i} n_{i\uparrow} n_{i\downarrow}. \tag{2.48}$$

Here, $n_{i\sigma} = c^{\dagger}_{i\sigma} c_{i\sigma}$ are electron occupancies, where $c^{\dagger}_{i\sigma}$ and $c_{i\sigma}$ are creation and annihilation operators of spin σ localized on the d orbital ($\sigma = \uparrow, \downarrow$). These occupancies have different spin indices to capture Pauli's exclusion principle because same-spin electrons cannot occupy the same spatial orbital [136]. U is an energy parametrizing the interaction strength, typically in the order of eVs [127].

Adding Hubbard repulsion can improve concurrence with the insulating nature of materials, magnetizations, crystal structures, etc. [127]. For example, ferromagnetism can arise in mean-field theories when adding the Hubbard term [136], and DFT with altermagnetic candidates might require a Hubbard U repulsion to stabilize the magnetic order [3].

Within the DFT+U method, the total energy is then [128]:

$$E\left[n_{\uparrow}, n_{\downarrow}, \{n_{i\sigma}\}\right] = E_{\mathrm{DFT}}[n_{\uparrow}, n_{\downarrow}] + \frac{U}{2} \sum_{i} n_{i\uparrow} n_{i\downarrow} - E_{\mathrm{dc}} \tag{2.49}$$

The first term can be an LSDA or a GGA term. The second term is the Hubbard term [145]. The third term is a double-counting term that subtracts the onsite terms in the Hubbard term that are already accounted for [145] in the LSDA or GGA term, and it can be modeled in different ways [128].

There are several commonly used approaches to DFT+U, for example, the fully localized [148], the around-mean-field [149], and the spherically symmetric Dudarev [146] approaches. We will use the latter, which is given by [146, 150]

$$E_{\mathrm{DFT+U}} = E_{\mathrm{DFT}} + \frac{(U-J)}{2} \sum_{\sigma} \left[\left(\sum_{i} n^{\sigma}_{ii} \right) - \left(\sum_{i,j} n^{\sigma}_{ij} n^{\sigma}_{ji} \right) \right]. \tag{2.50}$$

Here, n^{σ}_{ij} is the spin density matrix within the localized orbital sub-space. The Hubbard term, U, and the exchange term, J (which corrects for the Pauli exclusion principle, where same-spin electrons cannot occupy the same state on the same orbital), are spherically averaged and, thus, isotropic and rotationally invariant. Note that this correction depends only on the difference $(U - J)$.

2.3.3 Augmenting the wavefunctions

Wavefunctions can display different degrees of complexity in different regions of space around atoms [151]. Far from the nucleus, the wavefunction is relatively smooth. Close to the nucleus, the wavefunction oscillates rapidly in space due to the large attractive potential from the nucleus [151, 127]. These rapid oscillations are numerically expensive to handle; for example, we would need a large number of plane waves if we use a plane-wave basis [151], as is commonly done in DFT calculations.

Several ways of approximating the wavefunction have been developed. They divide the space around the nucleus into two regions: far from and close to the nucleus [127]. We now introduce two common approaches in DFT. First, the frozen-core approximation and ultrasoft pseudopotentials [152], and then the projector-augmented-wave approximation [151]. The latter enables the inclusion of perturbative relativistic spin-orbit coupling that includes core electrons [153, 154] commonly implemented in DFT codes, including VASP.

Frozen core approximation. The electrons closer to the nucleus, *core electrons*, are tightly bound in the deep potential well. Therefore, they tend to remain relatively unchanged in different conditions, such as when placed in a crystal, and contribute less to bonding than valence electrons. Valence electrons are far from the nucleus and high above the potential well. It enables them to, e.g., delocalize throughout metallic crystals, form bonds, conduct electricity, and form energy bands [127]. This picture justifies using the *frozen-core approximation*, where one effectively removes the core electrons and nucleus and only treats the valence electrons [127]. In this approximation, the valence electrons effectively feel a screened and thus weaker Coulomb interaction from the core [127].

Soft pseudopotentials. To apply this in practice, one can approximate the electron wavefunction by smoothening the curve inside the core region. When a valence electron enters the core region, it must remain orthogonal to the core states due to Pauli's exclusion principle, and its wavefunction thus oscillates fast [127]. However, in the frozen-core approximation, there are no core electrons to which the valence electrons must be orthogonal. Thus, it is appropriate to smoothen or "soften" the valence electron wavefunction in the core region [155, 127]. One can also approximate the corresponding potential well with a finite, smoother well in the core region, a *pseudopotential*.

One such approach is the ultrasoft pseudopotential approach developed by Vanderbilt [152]. This method is very efficient numerically as it does not require many plane waves [152], making it around ten times faster than the so-called *norm-conserving* approach [127, 156, 157]. However, these approaches largely eliminate relativistic effects because the core electrons are most prone to them [127].

Projector-augmented-wave approach

Another approach to treating the core and valence regions is the *projector-augmented-wave* (PAW) approach. It was described by Blöchl [151], adopted by Kresse and Joubert [155], and implemented numerically in VASP. The method aims to combine the accuracy of the full, *all-electron* wavefunction that includes core and valence electrons with the efficiency of the ultrasoft approach [127].

Consider a wavefunction $|\Psi\rangle$ that accounts for all electrons throughout space, both valence and core electrons. $|\Psi\rangle$ is the target wavefunction we want to express in a computationally efficient manner. The idea of Blöchl was to transform the Hilbert space of the *all-electron* wavefunction $|\Psi\rangle$ into a pseudo-Hilbert space with smoother pseudo-space *augmented* wavefunctions $|\tilde{\Psi}\rangle$, using a simple, linear transformation operation, $\hat{O}$, as $|\Psi\rangle = \hat{O}|\tilde{\Psi}\rangle$ [151]. If this were possible, one could describe both the core and valence electrons, but with a smooth function that is computationally much more efficient.

Transformation from all-electron to pseudo Hilbert space. Blöchl showed that $\hat{O}$ takes the form of a simple linear operator[4], given by $\hat{O} = 1 + \sum_i (|\phi_i\rangle - |\tilde{\phi}_i\rangle)\langle\tilde{p}_i|$, such that

$$|\Psi\rangle = |\tilde{\Psi}\rangle + \sum_i (|\phi_i\rangle - |\tilde{\phi}_i\rangle)\langle\tilde{p}_i|\tilde{\Psi}\rangle. \tag{2.51}$$

Here, $|\tilde{\phi}_i\rangle$ are partial waves (the wavefunctions scattered off a localized spherical potential [158]) in pseudo-space, and $|\phi_i\rangle$ are those in all-electron space. i is an index $i = \{\mathbf{R}, \mathbf{L}, n\}$ encompassing the atomic site $\mathbf{R}$, quantum angular momentum indices $\mathbf{L} = \{l, m\}$, and a state index n labeling different states at the same site with the same angular momentum, and $\tilde{p}_i$ are some fixed function for each i, called *projector-functions* [151].

Thus, we have in Eq. (2.51) the target, all-electron wavefunction $|\Psi\rangle$ modeling both the core and valence electrons, expressed in terms of the smoother wavefunctions $|\tilde{\Psi}\rangle$ in the pseudo-space that, due to their smoothness, require fewer plane-waves and are more computationally efficient [151]. Outside the augmentation region, $|\Psi\rangle = |\tilde{\Psi}\rangle$, and the second term in Eq. (2.51) is zero. Inside the augmentation region, the second term is non-zero and provides contributions from the all-electron wavefunction via its partial waves. The added all-electron contribution helps to model the core region more accurately compared to other standard approaches such as the ultrasoft pseudopotential approach [127]. It also allows one to consider relativistic effects that affect the core electrons [127].

Spin-orbit coupling in VASP

The spin-orbit coupling Hamiltonian can be implemented as a relativistic correction that predominantly affects electrons closest to the atomic nuclei, using the PAW approach [154]. Under the assumption that spin-orbit-coupling is negligible outside

[4]He showed Eq. (2.51) by writing the all-electron wavefunction as $|\Psi\rangle = |\tilde{\Psi}\rangle + |\Psi\rangle - |\tilde{\Psi}\rangle$ and inserting into it the partial wave expansions within Ω_R ($|\tilde{\Psi}\rangle = \sum_i |\tilde{\phi}_i\rangle c_i$, $|\Psi\rangle = \sum_i |\phi_i\rangle\, c_i$ where $c_i = \langle\tilde{p}_i|\tilde{\Psi}\rangle$) [151].

the augmentation region, the spin-orbit coupling term is given by [154]:

$$\tilde{H}_{\mathrm{SOC}} = \sum_{ij} |p_i\rangle \langle \phi_i | H_{\mathrm{SOC}} | \phi_j \rangle \langle p_j | . \tag{2.52}$$

The Hamiltonian is in a lowest order expansion given by [154, 153]

$$H_{\mathrm{SOC}}^{\alpha\beta} = \frac{\hbar^2}{(2m_e c)^2} \frac{K(r)}{r} \frac{dV(r)}{dr} \boldsymbol{\sigma}^{\alpha\beta} \cdot \mathbf{L}, \tag{2.53}$$

where $\boldsymbol{\sigma}$ are the three spin Pauli matrices, $\mathbf{L} = \mathbf{r} \times \mathbf{p}$ is the angular momentum operator ($\mathbf{r}$ and $\mathbf{p}$ are position and momentum operators), $V(r)$ is the spherical component of the all-electron pseudo-potential within the augmentation region at a radial distance r away form the center of an atom, m_e is the electron mass, c is the speed of light, and $K(r) = (1 - V(r)/2m_e c^2)^{-2}$. The action of $H_{\mathrm{SOC}}^{\alpha\beta}$ on an augmented wavefunction is $|\widetilde{\psi}_n^{\alpha}\rangle = \sum_{\alpha\beta} \widetilde{H}_{\mathrm{SO}}^{\alpha\beta} |\widetilde{\psi}_n^{\beta}\rangle$, where α and β are the spin up and down components of the spinors. Here, we have adopted a two-component noncollinear magnetism notation [154]. In the VASP code, switching spin-orbit coupling on (`LSORBIT` tag) adds this term to the Hamiltonian.

2.3.4 Numerical approximations with crystals

In addition to the approximations associated with pseudopotentials and the exchange-correlation function, additional numerical approximations to DFT simulations of crystals arise from representing wavefunctions with plane waves. They are often chosen in DFT calculations because of several advantages. They are already solutions of free electrons, they represent smooth functions well, they are easy to perform derivatives with, and we can increase the total number of plane waves to improve convergence and accuracy systematically [127]. Moreover, with pseudopotential approaches such as PAWs, one can drastically decrease the number of plane waves needed.

Plane waves and precision. When we use plane waves, the level of precision associated with it is governed by the number of plane waves we use (corresponding to an *energy cut-off*) and the number of k-points we use to represent our system on the computer (*k-point sampling*).

Plane waves are nonlocal waves that span an entire system and propagate perpendicular to the wavefront. A plane wave takes the general form [127]

$$\phi_{\mathrm{PW}}(\mathbf{r}) = C \exp(i\mathbf{k} \cdot \mathbf{r}) \tag{2.54}$$

where C is a complex number, $\mathbf{k}$ is a wavevector and $\mathbf{r}$ a real space position vector.

It is natural to express the plane waves as a Fourier series. After all, the Fourier theorem states that if a function is periodic in real space, it can be expanded in a Fourier series [127]. Recall that Bloch functions are periodic in the lattice vector $\boldsymbol{R} = n_1\mathbf{a}_1 + n_2\mathbf{a}_2 + n_3\mathbf{a}_3$ ($\mathbf{a}_i$ are lattice vectors and n_i are integers, see Eq. (1.9)) and the corresponding reciprocal lattice vector $\mathbf{G} = n_1\mathbf{b}_1 + n_2\mathbf{b}_2 + n_3\mathbf{b}_3$ ($\mathbf{b}_i$ are reciprocal lattice vectors, see Eq. (1.10)) [97]. Combining the Fourier and Bloch theorems, we can thus write the wavefunction as a Fourier expansion given by [127]:

$$\psi_{\mathbf{k}}(\mathbf{r}) = \sum_{|\mathbf{k}+\mathbf{G}|\leq|\mathbf{k}+\mathbf{G}|_{\text{cut}}} c_{\mathbf{k}+\mathbf{G}} \exp^{i(\mathbf{k}+\mathbf{G})\cdot\mathbf{r}} . \tag{2.55}$$

Any crystal-periodic property, such as electron densities and potentials, can be expanded analogously [127, 128, 135]. Numerically, we can only expand up to an upper reciprocal vector $|\mathbf{k}+\mathbf{G}|_{\text{cut}}$, which specifies the number of wavevectors we use and is associated with a corresponding *energy cut-off* [127]. We specify this energy in the input file (the `ENCUT` tag in VASP).

Moreover, we must perform *k-point sampling* to represent the system on a reciprocal-space grid numerically. Recall that the larger the real space unit cell, the smaller the Brillouin zone because the reciprocal space lattice vectors are given by $\mathbf{b}_1 = 2\pi\,\mathbf{a}_2 \times \mathbf{a}_3/|\mathbf{a}_1 \cdot \mathbf{a}_2 \times \mathbf{a}_3|$ and so on (see Eq. (1.11)) [97]. Thus, we need fewer k-points if the unit cell is large for a given direction and vice versa. For example, if the lattice vector lengths obey the ratios $a_1 : a_2 : a_3 = 1 : 2 : 2$, then the optimal choice of the corresponding k-vectors are ratios $2 : 1 : 1$. It is common practice to increase the number of k-points and plane waves until properties such as the total energy and energy bands do not change to determine an appropriate number of k-vectors and plane waves for a given system [127].

Switching symmetrization off. It is common in DFT codes to use a symmetrization scheme to further reduce the k-points that are used [127]. This reduction is done by relating k-points by symmetries the code determines, obtaining an *irreducible Brillouin zone* [127].

Here, we avoid using symmetrization when we study altermagnets and odd-parity-wave magnets because it may over-symmetrize the calculation [3]. For example, VASP currently uses magnetic symmetries for the procedure [159], which may ignore important spin symmetries [25, 1] (as illustrated, e.g., in Fig. 1.8 for an altermagnetic rutile structure), thereby possibly removing them and over-symmetrizing the calculation. We set the tag `ISYM=-1` in VASP to switch symmetrization off.

2.3.5 Constrained magnetic moments

When studying altermagnets and odd-parity-wave magnets, obtaining DFT solutions that preserve specific symmetries is crucial. It is usually straightforward in collinear

magnets without or with spin-orbit coupling turned on. However, this can be more involved for noncollinear magnets. To preserve specific symmetries in noncollinear magnets, e.g., concurrent with experiment and unconventional electronic structures, we can *constrain* the magnetic moments.

We can constrain the magnetic moments by adding an energy penalty if they deviate from the desired, or *constraining*, magnetic moments [160, 161]. In this procedure, the total energy is given by [161, 160]

$$E = E_0 + \sum_{\mathrm{I}} \lambda \left(\mathbf{M}_{\mathrm{I}} - \mathbf{M}_{\mathrm{I}}^0\right)^2. \tag{2.56}$$

The first term (E_0) is the usual total energy from the DFT calculation. The second term is the added energy penalty (which we will denote E_{p}). It sums over every atomic site, I, adding an overall energy penalty given by λ when the actual magnetic moment $\mathbf{M}_{\mathrm{I}}$ is different from the desired, or *constraining* magnetic moment, $\mathbf{M}_{\mathrm{I}}^0$. $\mathbf{M}_{\mathrm{I}}$ is an integrated magnetic moment, which integrates the magnetization density $\mathbf{m}(\mathbf{r})$ of the DFT solution (Eq. 2.43) within a sphere Ω_{I} around the I'th atomic site as:

$$\mathbf{M}_{\mathrm{I}} = \int_{\Omega_{\mathrm{I}}} \mathbf{m}(\mathbf{r}) F_I(|\mathbf{r}|) d\mathbf{r}. \tag{2.57}$$

Here, $F_{\mathrm{I}}(|\mathbf{r}|)$ is a function that goes to zero at the boundary of the sphere given by the radius Ω_{I} and whose norm is 1 inside Ω_{I} [160].

Workflow for constraining magnetic moments

It is helpful to vary specific parameters to obtain the best results using the constraining procedure in practice [161]. Firstly, the best results should usually be attainable when the integration radii Ω_I for the magnetic atoms are as large as possible, without them overlapping (but there are several ways to choose these radii, particularly in systems with more than one atomic species) [161, 160]. Secondly, the artificially added energy penalty from the procedure, E_{p}, should be made as small as possible [161, 160].

Workflow for $[C_{2\perp}||\mathbf{t}]$ symmetric p-wave candidate material. In Ch. 3.2, we will study in detail the noncollinear, coplanar magnet CeNiAsO, a p-wave material candidate [93]. To study its p-wave magnetism, we need to preserve the $[C_{2\perp}||\mathbf{t}]$ spin symmetry (see, e.g., Fig. 2(a)), where $\mathbf{t}$ is a partial translation, as it is one of the necessary symmetries for its p-wave electronic structure to emerge. We combine this symmetry criterion with the above-described guidelines in our workflow shown in Fig. 2.7. We note that we can apply this workflow to any symmetry of interest, and here, we focus on $[C_{2\perp}||\mathbf{t}]$ as an example.

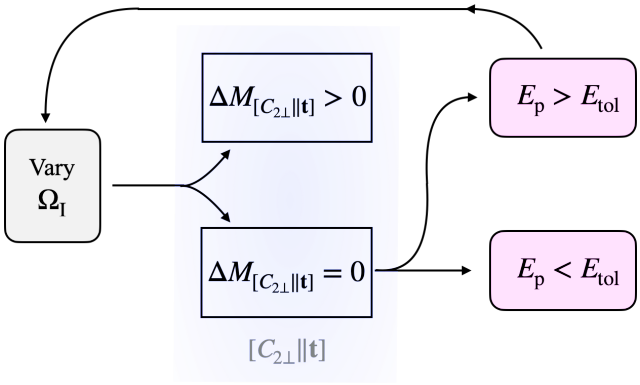

Figure 2.7: Workflow for constraining magnetic moments and ensuring they have a desired (here $[C_{2\perp}||\mathbf{t}]$) symmetry. We first converge several self-consistency calculations with different integration radii, Ω_I, on each site I ("vary Ω_I"). Then, we choose the solution that obeys the desired $[C_{2\perp}||\mathbf{t}]$ symmetry (blue region). Lastly, we choose the solution where the penalty energy E_p is smaller than the energy tolerance E_tol (magenta boxes). Generally, this workflow is not guaranteed to produce the desired symmetry or a sufficiently small penalty energy. If that is the case, we can vary other parameters [161] in the first step (gray box) and repeat the workflow (see main text for details).

First, we do several self-consistency calculations where we vary the integration radii ("vary Ω_I" in Fig. 2.7) and ensure each calculation converges fully (within an energy tolerance, e.g., `ENCUT` in VASP).

Then, we check if the spin configuration of the solution obeys the symmetry of interest, for example, the $[C_{2\perp}||\mathbf{t}]$ spin symmetry (blue shaded region in Fig. 2.7). To check whether the $[C_{2\perp}||\mathbf{t}]$ symmetry is conserved, we can calculate

$$\Delta M_{[C_{2\perp}||\mathbf{t}]} \equiv M_\mathrm{I}^{x_i} + M_{\mathrm{I}_{[C_{2\perp}||\mathbf{t}]}}^{x_i} \quad \text{for all } [C_{2\perp}||\mathbf{t}] \text{ symmetry pair sites } (\mathrm{I}, \mathrm{I}_{[C_{2\perp}||\mathbf{t}]}) \text{ and components } x_i = x, y, z. \tag{2.58}$$

Here, the pairs of sites related by $[C_{2\perp}||\mathbf{t}]$ symmetry are the sites with indices $(\mathrm{I}, \mathrm{I}_{[C_{2\perp}||\mathbf{t}]})$. When $\Delta M_{[C_{2\perp}||\mathbf{t}]} = 0$, these sites have opposite magnetizations ($M_\mathrm{I}^{x_i} = -M_{\mathrm{I}_{[C_{2\perp}||\mathbf{t}]}}^{x_i}$). If these magnetizations are equal and opposite for each spin component (indexed by x_i here) for each pair of sites related by $[C_{2\perp}||\mathbf{t}]$ symmetry, then the system preserves $[C_{2\perp}||\mathbf{t}]$ symmetry. If not, $\Delta M_{[C_{2\perp}||\mathbf{t}]} > 0$. If we find solutions obeying $[C_{2\perp}||\mathbf{t}]$ symmetry, we move to the next step.

In the next step, we check if the penalty energy, E_p, is smaller than a tolerance, E_tol (magenta marked boxes). This tolerance is user-defined and could, for instance, be the convergence criterion of the self-consistency calculation (`ENCUT` in VASP) or an energy below which the quantities of interest do not change (such as the electronic band structure). Suppose the artificially added penalty energy is small enough. In that case, we have a solution where it is effectively removed, and we can be sure it does

not produce artificial numerical features in our simulations. As we will see shortly, this workflow was sufficient to produce the desired symmetry and small enough penalty energy in our simulation on CeNiAsO.

Note on general workflow. We note that, in general, this workflow alone does not guarantee to produce the desired results, as it depends on the particular material. Suppose the symmetry is not satisfied after varying the integration radii Ω_I. In that case, we can vary further parameters in the first step (gray box in Fig. 2.7) and repeat the workflow for these parameters. For example, suppose the solution is close to having the correct symmetry and penalty energy. In that case, we can vary the initial or constraining magnetic moments ($\mathbf{M}_\mathrm{I}$ or $\mathbf{M}_\mathrm{I}^0$) or increase the k-grid resolution or energy cut-off and repeat the workflow in Fig. 2.7. If this does not work, we can step-wise increase λ as described in [161]. For each time we would increase λ, we would ideally have the values of $\Delta M_{[C_{2\perp}||\mathbf{t}]}$ and the overall magnetic order improve, and E_p and the total energy decrease [161].

In theory, it should be possible to decrease E_p to become arbitrarily small when step-wise increasing λ, rendering the total energy independent of the integration radii Ω_I after many continuation runs [161]. However, in practice, the process can be time-consuming, and it may be more straightforward if the seed calculation is already as close as possible to the desired result. Thus, we could also use our workflow to optimize the charge and spin densities for a seed calculation, should we need to step-wise increase λ as described in [161].

Simulations using the workflow with CeNiAsO

Here, we show the results of applying the workflow from Fig. 2.7 to VASP calculations with CeNiAsO.

Numerical parameters. We used the constraining magnetic moments $(\pm 0.3, \pm 0.22, 0)\,\mu_\mathrm{B}$ (corresponding to the experimental values [44]), initial magnetic moments the same but twice as large, and a relatively small [160] energy penalty term of $\lambda = 2\,\mathrm{eV}/\mu_\mathrm{B}^2$. The k-grid was $4\times8\times4$, and we used a 460 eV energy cut-off (ensuring it is larger than the recommended values for the PAW pseudopotentials [155, 151] for each atomic species). For all the calculations, we converged the solution within $5 \times 10^{-8}\,\mathrm{eV}$, a relatively strict convergence criterion. With these parameters, we obtained perfect $[C_{2\perp}||\mathbf{t}]$ symmetry and a penalty energy of $2.77 \times 10^{-8}\,\mathrm{eV}$ with a one-shot self-consistency calculation. This suggests CeNiAsO is a relatively straightforward material to calculate using constrained magnetism, as we did not have to step-wise increase λ [161] to obtain negligible penalty energy and could use the comparatively simple workflow of Fig. 2.7.

We now show how we determined these parameters using the workflow from Fig. 2.7.

Determining parameters for constrained calculation of CeNiAsO. We varied the integration radii as summarized in Tab. 2.1. First, we performed calculations for a wide

	$\Omega_{\mathrm{I}}^{\mathrm{ion}}$ (Å)	'×': X (%)	'+': Ω_{I} (Å)
Ce	1.323	50	1.98
Ni	1.286	−50	1.21
As	1.217	−50	1.09
O	0.820	−60	0.24

Table 2.1: Integration radii used for the constraining magnetic moments workflow with CeNiAsO. The first column shows the individual atomic species. The second column shows the ionic radii for the species, $\Omega_{\mathrm{I}}^{\mathrm{ion}}$, tabulated in VASP PAW pseudopotential files (`POTCAR_Ce`, `POTCAR_Ni`, `POTCAR_As`, and `POTCAR_O` [155, 151] in VASP version 6.3.2). We performed calculations where we increased and decreased these values by X% according to Eq. (2.59) (see main text). The third column shows X-values for a data point where we decreased the radius by a larger amount on the O atom (by −60%) to prevent overlap between O and Ce integration radii. The last column shows integration radii where we kept Ω_{Ce} as large as possible without overlapping with each other, then increased the Ni and As radii to be as large as possible, and lastly, the O radius to be as large as possible, without any integration spheres overlapping.

range of integration radii to estimate which sets of radii would give the best results. To this end, we started with the tabulated ionic radii, $\Omega_{\mathrm{I}}^{\mathrm{ion}}$, from the pseudopotential files for each atomic species, `POTCAR` [155, 151], which are part of the VASP package. The first column in Tab. 2.1 shows these values. We then increased or decreased the integration radii from these values by a percentage, X, which we can also express as

$$\Omega_{\mathrm{I}} = \Omega_{\mathrm{I}}^{\mathrm{ion}}(1 + X\%), \quad X = \frac{\Omega_{\mathrm{I}} - \Omega_{\mathrm{I}}^{\mathrm{ion}}}{\Omega_{\mathrm{I}}^{\mathrm{ion}}}. \tag{2.59}$$

For example, in our first set of calculations with the wide range of radii, we increased the integration radii on the magnetic Ce atoms (and decreased it by the same percentage on the nonmagnetic Ni, As, and O atoms), with a 10% interval ($X = +\{0, 10, 20, \ldots, 90\}$% on Ce and $-X$ on Ni, As, and O).

The resulting total energy, E_0, and energy penalty, E_{p}, are shown by the round, colored data points in Fig. 2.8(a) and 2.8(b), respectively. On the horizontal axis, we show the value of X for the Ce atom. The gray, shaded region is where the integration radii of the Ce atoms are so large that they start to overlap with each other. When they overlap, it means that the overlapping regions are integrated twice.

All these solutions are $[C_{2\perp}||\mathbf{t}]$ symmetric and thus satisfy the criterion $\Delta M_{[C_{2\perp}||\mathbf{t}]} = 0$ in our work-flow (Fig. 2.7 and Eq. (2.58)). Next, we focus on obtaining a small penalty energy E_{p}.

In Fig. 2.8, we see that the total energy and penalty energy decreases when we increase the Ce integration radii (Ω_{Ce}, or X). However, the penalty energy reaches

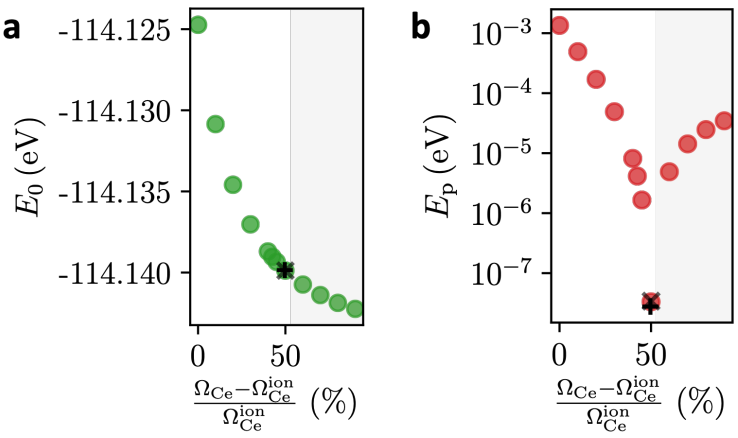

Figure 2.8: Total energy and penalty energy as a function of the % increase in integration radius of the magnetic Ce atoms compared to the tabulated ionic radius. (a) The total energy, E_0, decreases monotolically as the magnetic integration radius increases. (b) The penalty energy, E_p, decreases until the magnetic Ω_{Ce} integration radius is increased by about 50%, and then increases for higher radii. The gray, shaded region shows radii where the integration spheres between Ce atoms overlap. Here, the start of this region coincides with the increase in E_p.

a minimum right below the radius where the Ce integration spheres start to overlap, and then it starts to increase. Therefore, the best calculation in terms of low penalty energy is the data point at 50%. Here, the penalty energy is smaller than our convergence criterion or 5×10^{-8} eV, which is in itself a strict criterion below which we typically would not expect any change in the calculated total energy or the band structure.

In principle, we could stop the workflow at this point. However, the Ce and O integration radii slightly overlap for the $X = 50\%$ data point. We, therefore, perform a calculation where we decrease the integration radii of the oxygen atom (Ω_O) by -60% instead of -50%, preventing the overlap. This data point is given in the second column in Tab. 2.1. The '×' data point in Fig. 2.8 shows the simulation result. It does not change the resulting total energy or penalty energy significantly.

We also performed another calculation, where we set Ω_{Ce} as large as possible without overlapping other spheres, then set Ω_{Ni} and Ω_{As} as large as possible without overlapping (filling larger regions that were in previous runs not covered by their integration spheres), and lastly set Ω_O as large as possible without overlapping. The integration radii are in the last column in Tab. 2.1. These radii cover 98% of the smallest distance between Ni and another atom (As) and 94% between O and another atom (Ce). The '+' data point in Fig. 2.8 shows the simulation result.

While these two more optimized sets of integration radii do not change the simulation results significantly, the '+' data point has a slightly lower penalty energy.

Corresponding magnetic moments of the calculations. In addition to the basic workflow, we also checked two more properties of the magnetic moments, shown in Fig. 2.9.

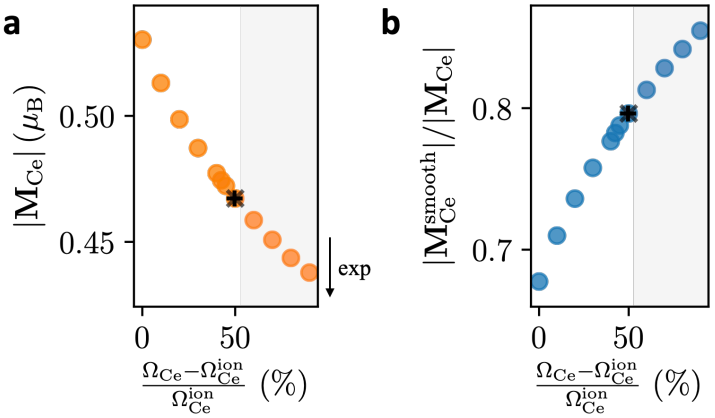

Figure 2.9: Magnetization sizes (vertical axes) as a function of the relative magnetic integration radius (horizontal axes). Each data point corresponds to the simulations in Fig. 2.8. (a) Size of the integrated, local magnetic moment on Ce sites ($|\mathbf{M}_{\mathrm{Ce}}|$). It is preferably smaller here (indicated by the downward black arrow; smaller values are closer to the experimental value). (b) The ratio of the magnetization with its smoothened version, $|\mathbf{M}_{\mathrm{Ce}}^{\mathrm{smooth}}|/|\mathbf{M}_{\mathrm{Ce}}|$. Generally, this ratio is preferably as large as possible (as close as possible to 1). Here, both (a) and (b) show more favorable values for larger magnetic integration radii.

First, we check the size of the magnetic moments in Fig. 2.9(a), here shown by the size for the Ce atoms. Here, the magnetic moment is the integrated magnetic moment from Eq. (2.57), without any smoothening towards the boundary of the integration sphere [160]). We note that all the individual x, y, and z components of the magnetic moments of the Ce atoms were identical in our calculations ($|M_{\mathrm{Ce}_1}^{x_i}| = |M_{\mathrm{Ce}_2}^{x_i}|$ etc.). Thus, the magnetic moment sizes in Fig. 2.9(a) apply to every Ce atom in the unit cell. We observe that the magnetization size decreases and becomes closer to the experimentally measured [44] size of $|(\pm 0.3, \pm 0.22, 0)|\,\mu_{\mathrm{B}} = 0.37\,\mu_{\mathrm{B}}$ when we increase the magnetic integration radii (indicated by downward black arrow marked "exp").

Second, we look in Fig. 2.9(b) at the ratio of this magnetization and its smoothened counterpart, $\mathbf{M}_{\mathrm{Ce}}^{\mathrm{smooth}}$. In $\mathbf{M}_{\mathrm{Ce}}^{\mathrm{smooth}}$, $F_{\mathrm{Ce}}(|\mathbf{r}|)$ from Eq. (2.57) is a function of $\mathbf{r}$ that goes to zero at the integration boundary. This smoothened magnetization is the input for the constraining energy penalty term in Eq. (2.56). Therefore, the VASP manual recomments having this ratio, $|\mathbf{M}_{\mathrm{Ce}}^{\mathrm{smooth}}|/|\mathbf{M}_{\mathrm{Ce}}|$, as large as possible for the best results [160]. We see that the ratio increases with increasing magnetic integration radii.

In summary, we have seen that increasing the magnetic integration radii in CeNiAsO improves both the size of the integrated magnetization and its ratio with the smoothened integrated magnetization.

Conclusion and parameter choice. Comparing all our simulations shown in Figs. 2.8 and 2.9, we conclude that we obtain the best results when the integration radii are as large as possible without causing the magnetic integration spheres to overlap, in concurrence with the recommendation in the VASP manual [160]. When we let the Ce integration spheres overlap, we could further decrease the total energy and improve the integrated magnetization values. However, the penalty energy increases significantly for these values, and the VASP manual generally recommends avoiding integration sphere overlap. Therefore, we choose the integration radii with the lowest

Ω_I, Å (`RWIGS`)	1.98 (Ce), 1.21 (Ni), 1.09 (As), 0.24 (O)
$\mathbf{M}_\mathrm{I}^0$, μ_B (`I_CONSTRAINED_M`)	$(\pm 0.3, \pm 0.22, 0)$
Initial $\mathbf{M}_\mathrm{I}$, μ_B (`MAGMOM`)	$2\mathbf{M}_\mathrm{I}^0$
λ, eV/μ_B^2 (`LAMBDA`)	2
k-grid, $k_x \times k_y \times k_z$ (`KPOINTS`)	$4 \times 8 \times 4$
`ENCUT`, eV	460
E_p, eV (`E_p`)	2.77×10^{-8}
Ce `magnetization`, μ_B	$(\pm 0.353, \pm 0.258, 0)$

Table 2.2: Summary of final parameter choice for our constrained calculation of CeNiAsO. We name the corresponding tags and names in VASP files in brackets. The first three rows are input parameters specifying the constraining energy penalty from Eq. (2.56). The following two are the k-grid and energy cut-off we used, affecting the plane-wave basis as described in Sec. 2.3.4. The last row shows the negligible total energy penalty from constraining the magnetic moments (data point '+' from Fig. 2.8), and the magnetization summed over the Ce orbitals for the DFT solution (found in `OUTCAR` file in VASP).

penalty energy ('+' in Tab. 2.1 and Figs. 2.8 and 2.9), and no overlap between integration spheres, which is still associated with some of the better magnetization sizes and ratios of all the calculations. We summarize these parameters in Tab. 2.2.

2.3.6 DFT method for CeNiAsO, MnTe, CrSb, RuO_2, and Mn_5Si_3

Here, we summarize the method and parameters we used for our DFT calculations on the p-wave material candidate CeNiAsO and altermagnetic candidate materials. We used VASPKIT [162] and VESTA [163] to plot spin densities. We have also used VESTA to visualize crystals. We used PyProcar version 6.1.7 [164] to plot the iso-energy cuts and energy bands in CeNiAsO, and version 5.6.6 for MnTe and CrSb.

CeNiAsO. For the DFT calculations on CeNiAsO in Ch. 3.2.7, we used VASP with symmetrization switched off and constrained magnetism, where an energy penalty term guides the magnetic moment toward the desired spin order. For more details about this method and how we applied it to CeNiAsO, see Ch. 2.3.5. Tab. 2.2 and the associated paragraph summarize the specific parameters we used for the calculation, for which we obtained the best results in terms of lowest total energy and penalty energies and the magnetic moment size being closer to the experimentally reported ones.

We calculated iso-energy cuts using a 27×27 and 29×29 ($k_x \times k_y$) grid for the nonmagnetic and magnetic calculations, respectively. The iso-energy cuts did not visibly change above this resolution.

MnTe. The calculations for MnTe in Ch. 3.1 and Ch. 3.1.4-3.1.6 were performed in VASP [165] using Perdew-Burke-Ernserhof (PBE)+U [155, 151, 142] with and without spin-orbit coupling, with the Hubbard parameter $U = 3.03\,\mu_\mathrm{B}$, a 520 eV energy cut-off, and a $8 \times 8 \times 5$ k-point grid. We converged the self-consistency calculations within $\sim 2 \times 10^{-5}$ eV and the electronic band structure calculations within 10^{-8} eV. The lattice parameters were $a = b = 4.134\,\text{Å}$ and $c = 6.652\,\text{Å}$, corresponding to experimental values determined from X-ray diffraction at $\sim 15\,K$ for MnTe grown on a $SrF_2(111)$ substrate [166]. We calculated iso-energy cuts on a 31×31 ($k_x \times k_y$) grid.

CrSb. The calculations for CrSb in Ch. 3.1.7 were performed similarly to MnTe, but without spin-orbit coupling, without Hubbard U, with a 400 eV energy cut-off, and a $6 \times 6 \times 5$ k-grid, with a self-consistency calculation converged within 10^{-5} eV.

RuO_2. We performed the calculations for RuO_2 in Ch. 3.1.8 using VASP within DFT+PBE+U [155, 151, 142], with and without spin-orbit coupling. We used the relaxed lattice parameters $a = b = 4.53\,\text{Å}$ and $c = 3.12\,\text{Å}$ that were obtained for the PBE+U+SOC calculation with the Néel vector along the [100] crystallographic axis in [3], a $8 \times 8 \times 10$ k-grid, a 460 eV energy cut-off, and a Hubbard $U = 1.3\,\mu_\mathrm{B}$ on the Ru sites which ensures that the solution is magnetic [77, 3], and converged the solution within 10^{-8} eV in the self-consistency and the energy band structure calculations.

In our collaborative work [12] in Ch. 4.3, we calculated the electronic band structure of RuO_2 in the same way without spin-orbit coupling, but using a 500 eV energy cut-off and Hubbard U of 1.6 eV. We obtained maximally localized Wannier functions using the Wannier90 code. The longitudinal conductivity was calculated for each spin channel using the Boltzmann equation with a $160 \times 160 \times 160$ k-mesh. The scattering rate we used, 6.6 meV, corresponds to the experimentally measured conductivity. It was obtained from computing the conductivity as a function of the scattering rate and comparing it to the experimental value [7].

Mn_5Si_3. We performed self-consistent DFT calculations for Mn_5Si_3 in Ch. 4.4 with collinear VASP without SOC or U and with symmetrization switched off [112, 12]. We

used a $5 \times 7 \times 11$ k-grid, a 500 eV energy cut-off, and converged the solution within 10^{-8} eV. We used lattice parameters for the bulk collinear antiferromagnetic AF2 phase at the temperature 70 K [50] and relaxed them to $a = 6.89$ Å, $c = 4.79$ Å. Using thin-film parameters from experiment [112] did not change our results significantly.

Chapter 3

Electronic structure of altermagnets and odd-parity-wave magnets

Recently, even-parity-wave altermagnetism was theorized as a third class of collinear magnets—in addition to conventional ferromagnets and antiferromagnets—based on symmetry analysis and *ab-initio* density functional theory calculations [25]. It was motivated by the earlier predictions of the unconventional time-reversal symmetry broken electronic structure in compensated magnets [3]. The crystallographic spin group theory analysis of all collinear magnets revealed altermagnetic order parameters and corresponding momentum space spin splittings taking even-parity d-, g-, and i-wave forms enforced by the nontrivial $\mathbf{R}_s^{\mathrm{III}}$ spin Laue group [25]. The discovery was enabled by the unorthodox crystallographic spin group formalism [25, 83], where, as opposed to magnetic groups, operations acting on spin and crystal degrees of freedom are allowed to be different [25, 82], thus opening up for describing more complex symmetries in magnets. Spin symmetries can describe the symmetries associated with large energy scales, i.e., magnetic exchange, predicted to give rise to eV scale electronic, momentum-dependent *spin splittings* in altermagnets [25]. For more details, see our discussion of altermagnetism and spin symmetries in Ch. 1.

Numerous spintronics effects resulting from altermagnetism have been predicted and experimentally confirmed. Our calculations contributed to guiding more recent direct experimental observation of the predicted altermagnetic electronic structure in photoemission experiments [30, 31, 38]. In this chapter, we will discuss the altermagnetic electronic structure and its confirmation in experiments.

Direct verification of altermagnetism. In collaboration with three experimental groups, we contribute to confirmations of the existence of altermagnetism for the first time by showing with symmetry analysis and *ab initio* density functional theory calcu-

lations how its experimental signature, in agreement with our theory, delineates it from the other magnetic phases [30, 31, 38]. We will see that the altermagnetic electronic structure spin-splits in the *altermagnetic form* [25, 3], which we explained in Remark 1, and which we define here in general, now also including terminology from Ch. 1:

Definition 3. ***Spin-splitting in the altermagnetic form****. The altermagnetic electronic energy bands meet at symmetry-imposed, spin-degenerate nodal surfaces (corresponding to d-, g- and i-wave altermagnetism) and spin-split away from them [25].*

The dispersion of the altermagnetic spin splittings is inversion symmetric due to collinear magnetism (due to the collinear spin-only group symmetries $\mathbf{r}_s^{\mathrm{coll}}$*, see Eq. (1.20)) on the nonrelativistic level and, if relevant, due to crystal inversion symmetry allowed due to inversion symmetry also on the relativistic level. Only even-in-momentum terms are inversion symmetric (e.g., inverting* k *in an even term* k^2 *yields* $(-k)^2 = k^2$*, so* k^2 *is inversion symmetric). In contrast, odd-in-momentum terms break inversion symmetry and are thus not allowed for inversion symmetric energy bands (e.g., inverting an odd term* k *yields* $-k \neq k$*). Therefore, the inversion symmetric bands disperse even-in-momentum around* $\mathbf{\Gamma}$ *[25]. The nonrelativistic Hamiltonian around* $\mathbf{\Gamma}$ *takes the form [25]:*

$$H^{\alpha\beta\gamma}_{\mathbf{k}\sim\mathbf{\Gamma}}(k_x,k_y,k_z) \sim \Delta\mathbf{d}\cdot\boldsymbol{\sigma}\, k_l^\alpha k_m^\beta k_n^\gamma, \quad \begin{array}{l}\alpha+\beta+\gamma = 2, 4, \textit{ or } 6;\\ l,m,n = x,y,z,\end{array} \tag{3.1}$$

Here, Δ *parametrizes the size and sign of the spin-splitting,* $\mathbf{d}$ *is a unit vector along the spin-quantization axis,* $\boldsymbol{\sigma}$ *is a vector with the spin Pauli matrices,* $k_l^\alpha k_m^\beta k_n^\gamma$ *is even-in-wavevector with* $\alpha+\beta+\gamma$ *being even integers* 2*,* 4*, or* 6 *on the nonrelativistic level, and a summation over the indices is implied. The number of nodal surfaces corresponds to the power of the* k*-polynomial, i.e., d-, g-, and i-wave altermagnetism corresponds to the powers of* 2*,* 4*, and* 6 *allowed in this nonrelativistic Hamiltonian [25]. On the nonrelativistic level,* $\Delta\mathbf{d}\cdot\boldsymbol{\sigma} = \Delta\sigma_z$ *where the spin quantization axis* σ_z *points along the Néel vector [25, 6].*

The altermagnetic spin polarization in the electronic band structure breaks time-reversal symmetry, $\mathcal{T}$*, as* $\epsilon(\sigma,\mathbf{k}) = \epsilon(\sigma,-\mathbf{k})$ *in altermagnets, which violates the condition imposed by time-reversal symmetry,* $\epsilon(\sigma,\mathbf{k}) = \mathcal{T}\epsilon(\sigma,\mathbf{k}) = \epsilon(-\sigma,-\mathbf{k})$ *[3].*

These altermagnetic spin splittings are therefore distinct from ferromagnets (constant and even-in-momentum Zeeman splitting $\propto k^0$ at $\mathbf{\Gamma}$), and relativistic noncentrosymmetric spin-orbit coupling (odd and linear-in-momentum spin splitting $\sim k$ around $\mathbf{\Gamma}$).

In the g-wave candidates MnTe and CrSb, we decipher different energy scales of altermagnetism with and without spin-orbit coupling. Our candidate materials

host $\sim$ eV scale, time-reversal symmetry broken nonrelativistic spin splittings [30, 31, 38], as well as an inversion-symmetric $\sim 100\,\mathrm{meV}$ spin splitting emerging when altermagnetism and spin-orbit-coupling combines (*weak altermagnetism*) in MnTe [30]. Remarkably, the latter splitting is of the scale of large value spin-splittings induced by spin-orbit-coupling using heavy elements, such as in BiTeI [114].

With the predictions and evidence of even-parity-wave altermagnetism (d-, g-, and i-wave) arising from magnetic ordering in crystals, a natural question is whether odd-parity-wave magnetism (p-, f-wave, and so on) can also be derived by spin symmetries. In our work [93], we have demonstrated the possibility of p-wave magnets by spin symmetry analysis and first-principle calculations.

P-wave magnetism. The realization of p-wave magnetism has been an open problem for decades [39, 40, 43]. From the 1990s, correlated Pomeranhuck instabilities in metallic Fermi fluids were considered as a possible route toward the realization of p-wave spin splittings in reciprocal space [39, 40, 43]. This mechanism relies on strong correlations and does not require magnetic long-range order in real space. However, this route has not yelded realistic material realizations, and certain conceptual limitations were discussed [41, 42].

The successful identification of altermagnets from magnetic crystal order by use of unorthodox spin symmetry analysis and density functional theory [25, 1, 3] prompts the question of whether a similar analysis can elucidate p-wave magnetism and odd-parity-wave magnetism in general. Here, we answer this question in the affirmative.

In fig. 3.1 we illustrate our realization of p-wave magnetism and contrast it to ferromagnetism and d-wave altermagnetism in terms of electronic band structure iso-energy cuts. As Fig. 3.1 illustrates, a *p-wave* nonrelativistic electronic band structure is *odd-parity-wave* (breaking inversion symmetry), it preserves $\mathcal{T}$ symmetry, and it has a single nodal surface [39, 43] (contrary to even-parity and $\mathcal{T}$-breaking magnets—altermagnets and ferromagnets illustrated here, but also extensively studied non-collinear compensated magnets such as Mn_3Sn [2, 119]).

While antisymmetric spin splitting commonly arises from relativistic spin-orbit coupling in noncentrosymmetric crystals [167], it is typically isotropic (e.g., momentum independent, such as Rashba spin-orbit coupling), it does not exhibit a nodal anisotropic structure, and its strength is limited to a relativistic energy scale. Our identification of p-wave magnetism from magnetic crystal order enables its electronic band structure to *(i)* be symmetry-protected by the magnetic crystal itself (rather than relying on fine-tuning spin-orbit coupling parameters [167]), and *(ii)* host orders of magnitude larger spin splittings, even in materials comprised of light elements (see, e.g., Sec. 1.5).

Prediction of odd-parity-wave magnetism. We use spin symmetry analysis to elucidate symmetry guidelines for identifying odd-parity wave magnetism and focus specif-

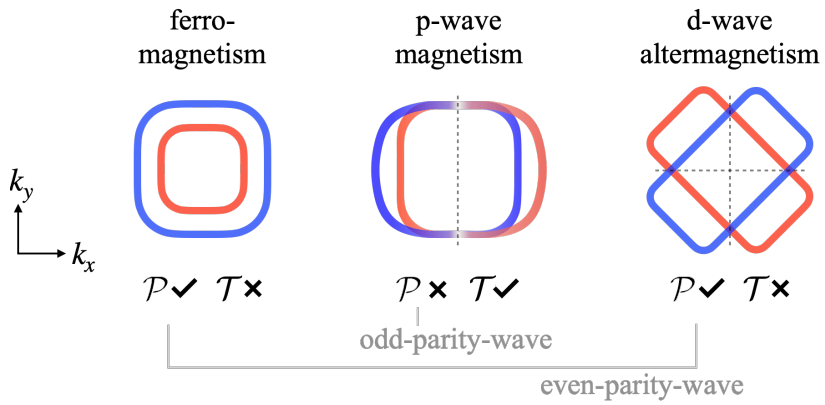

Figure 3.1: Illustration of the electronic structure order of ferromagnetism, p-wave magnetism, and d-wave altermagnetism. We illustrate it here by iso-energy cuts of the electronic band structure. The red and blue color indicate the spin expectation value along a spin-quantization axis. The p-wave electronic band structure breaks inversion symmetry $\mathcal{P}$ and preserves time-reversal symmetry $\mathcal{T}$. The ferromagnetic and altermagnetic ones preserve $\mathcal{P}$ and break $\mathcal{T}$. Ferromagnets and altermagnets are even-parity-wave as they preserve $\mathcal{P}$; p-wave magnets are odd-parity-wave, as they break $\mathcal{P}$. The dashed lines indicate the number of symmetry-enforced nodal surfaces (none for ferromagnets, one for p-wave magnets, two for d-wave altermagnets).

ically on p-wave magnets with a single nodal surface. With our symmetry guidelines, we show that to spin-split the odd-parity way, the magnets have to be noncollinear (and thus break the collinear spin-only symmetries in $\mathbf{r}_s^{\text{coll}}$, Eq. (1.17)), and the magnetic crystal has to break inversion symmetry and preserve $\mathcal{T}\mathbf{t}$ symmetry, where $\mathbf{t}$ is a half unit cell translation. To obtain our p-wave magnets, the crystallographic spin group has to support a single nodal surface. Interestingly, we further find that when the spin order in real space is *coplanar*, these systems have a $[C_{2\perp}||\mathbf{t}]$ spin symmetry that enforces the spin polarized electronic band structure to be *collinear*.

Combining our symmetry guidelines with *ab initio* calculations, we universally find the bands of material candidates and models are odd-parity-wave and nonrelativistically spin split with $\mathcal{T}$ symmetry as expected from our spin symmetry analysis. With a particular focus on the coplanar p-wave candidate CeNiAsO, we verify that it hosts a p-wave Fermi surface with collinear spin polarization, much similar to the one in Fig. 3.1, thus explicitly showing it is a candidate for p-wave magnetism. We also show that the p-wave electronic structure of CeNiAsO breaks symmetries of the underlying (nonmagnetic) crystal.

Notably, it might not seem intuitive that magnets, which all break $\mathcal{T}$ symmetry in real space, can preserve $\mathcal{T}$ symmetry in reciprocal space like our odd-parity-wave magnets do. We explicitly show the flaw in a commonly believed argument aligned with such an intuition [93], which states systems with $\mathcal{T}\mathbf{t}$ symmetry (type-IV magnetic

groups) prohibit nonrelativistic spin splittings [21].

3.1 Strong and weak altermagnetism

Traditionally, collinear *compensated magnets* (without a net magnetic moment) have been thought to be Kramers spin degenerate in the nonrelativistic limit. The spin group symmetry analysis confirms that conventional collinear antiferromagnets are Kramers spin degenerate because they belong to type-II spin Laue groups in Eq. (1.28), where inversion or translation relates their magnetic sublattices [25], see e.g. Ch.1.6.1. An internal mechanism to achieve lifting of Kramers spin degeneracy (LKSD) in antiferromagnets has been to add spin-orbit coupling in inversion symmetry-breaking crystals. However, the size of the resulting spin-splitting would be limited as spin-orbit coupling is typically relatively weak and generally leads to spin decoherence [167]. Spin symmetries have allowed disentangling the types of collinear compensated magnets, predicting that altermagnetic materials belonging to the type-III spin Laue groups (Eq. (1.29)) which lift Kramers spin degeneracy without requiring relativistic spin-orbit coupling [25].

We now illustrate examples of strong and weak altermagnetism in MnTe. Then, we describe its magnetic crystal structure, spin symmetries, and magnetic symmetries, and decipher in detail how these symmetries enforce the energy bands to spin-split in *the altermagnetic form* (Def. 3), thus distinguishing its *ab initio* calculated electronic band structure and collaborative experimental spectroscopic signature from other magnetic phases [30]. Lastly, we conduct similar analyses for CrSb and RuO_2, providing evidence of altermagnetism in these materials in collaboration with experiment [31, 38].

Strong altermagnetism. In the nonrelativistic limit, a strong altermagnetic LKSD of the electronic band structure emerges in altermagnets away from the symmetry-imposed nodal planes (see Fig. 1.9). This *strong altermagnetis*m has vanishing net magnetization, is present without relativistic spin-orbit coupling, and is insensitive to inversion symmetry breaking of the crystal.

Weak altermagnetism. When adding spin-orbit coupling, the Kramers spin degeneracy can additionally lift along the *nonrelativistic nodal surfaces* (which are spin degenerate in the nonrelativistic limit, see, e.g., Fig. 1.9) [6, 30]. This LKSD emerges when combining altermagnetism with relativistic spin-orbit coupling, forming relativistic altermagnetism. The size of the resulting spin splitting in the band structure is typically smaller than the strong altermagnetism because the splitting requires spin-orbit coupling to lift the Kramers spin degeneracy. Being typically smaller, and in analogy to relativistic spin-orbit coupling-induced weak ferromagnetism, we will thus refer to it as *weak altermagnetism*.

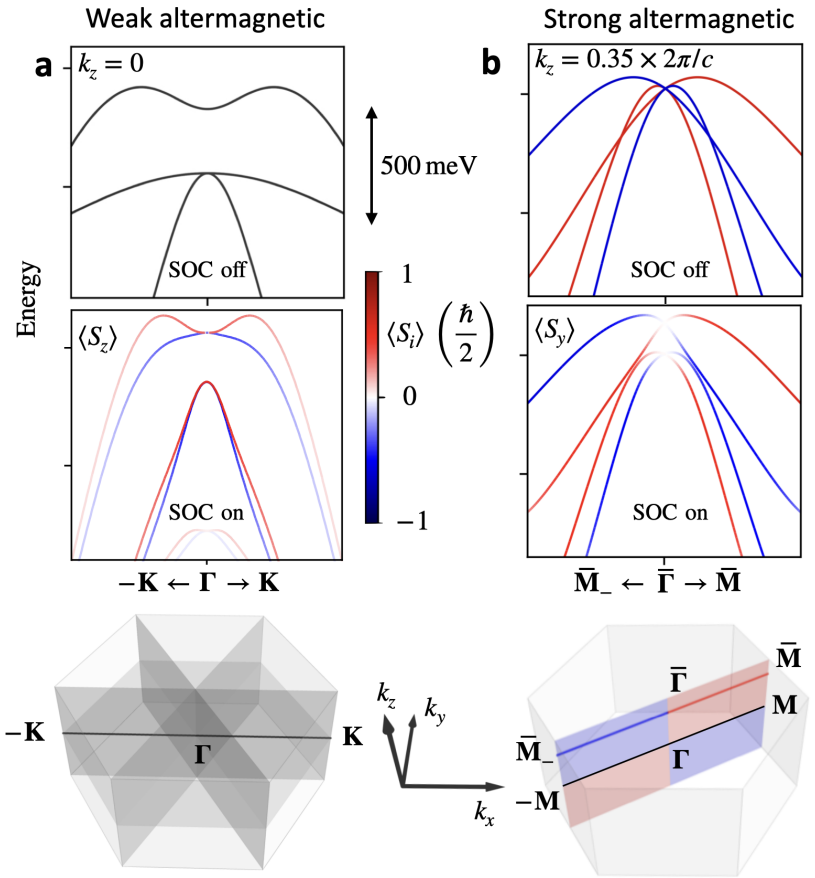

Figure 3.2: Strong and weak altermagnetic LKSD illustrated by *ab initio* band structures in MnTe. Here, the red and blue coloring indicates the spin expectation value. (a) Weak altermagnetic band structure showing LKSD along $\mathbf{\Gamma} - \mathbf{K}$ (path shown on the bottom) only when spin-orbit coupling is switched on (top and middle band structures). (b) Strong altermagnetic band structure showing LKSD. It emerges without spin-orbit coupling (top) due to nonrelativistic g-wave altermagnetism, for which spin symmetries relate spin polarizations of the electronic structure (similarly to Fig. 1.9) as highlighted in the Brillouin zone by the colored plane and the $\bar{\mathbf{\Gamma}} - \bar{\mathbf{M}}$ path (bottom). Switching on spin-orbit coupling only modifies the band structure (middle). Here, $\mathbf{M} = \frac{\mathbf{b_1}}{2} + \frac{\mathbf{b_2}}{2}$, and the $\bar{\mathbf{\Gamma}} - \bar{\mathbf{M}}$ path is shifted vertically to $k_z = 0.35 \times 2\pi/c \sim 0.35\,\text{Å}^{-1}$ as shown in the bottom panel. Figure adapted from [30], CC BY 4.0.

Fig. 3.2 shows examples of strong and weak altermagnetism in MnTe [168]. We calculated it *ab initio* with the density functional theory (DFT) code VASP, as described in Ch. 2.3.6.

Fig. 3.2(a) shows the weak altermagnetism, which lifts Kramers spin degeneracy only when spin-orbit coupling is switched on. When spin-orbit coupling is switched off (top panel), the bands are Kramers spin degenerate along wavevectors in the

nodal planes (bottom panel showing the Brillouin zone), such as the $\mathbf{\Gamma} - \mathbf{K}$ path calculated here and highlighted by the black line in the Brillouin zone. When spin-orbit coupling is switched on (middle panel), the bands lift Kramers spin degeneracy, and weak altermagnetism emerges. The weak altermagnetism is inversion symmetric due to the inversion symmetry of the MnTe crystal.

Fig. 3.2(b) shows the strong altermagnetism, which lifts Kramers spin degeneracy without spin-orbit coupling. Without spin-orbit coupling (top panel), the bands show LKSD along the $\bar{\mathbf{\Gamma}} - \bar{\mathbf{M}}$ path (blue-red line in the Brillouin zone, bottom panel) due to the g-wave altermagnetism. The even-parity character of the g-wave altermagnetism, $\epsilon(\sigma, \mathbf{k}) = \epsilon(\sigma, -\mathbf{k})$, is highlighted in the vertical plane (bottom panel), similarly to in Fig. 1.9. Switching spin-orbit coupling on, shown in Fig. 3.2(b, middle), only modifies the band structure.

3.1.1 The altermagnetic MnTe crystal structure and its sublattice-transposing symmetries

Fig. 3.3(a) shows a schematic of the MnTe crystal structure below the transition temperature of $310\,K$ [36]. The Mn atoms (red and blue) comprise two magnetic sublattices with opposite magnetic moments. In the following, we will consider the case when the Néel vector points along the easy-axis direction 30 degrees away from the $x(a)$-axis, as shown in Fig. 3.3(b), consistent with earlier magnetotransport and magnetic measurements of the Néel vector in epitaxial MnTe thin films [166, 113]. In reciprocal space, this direction corresponds to the $\mathbf{\Gamma} - \mathbf{M}$ direction (see Fig. 3.2(b)). The corresponding nonrelativistic nontrivial spin Laue group is

$$^{2}6/^{2}m^{2}m^{1}m \tag{3.2}$$

in the usual crystallographic spin group notation [25] indicating the generators using international notation. We now illustrate the sublattice-transposing symmetries in this group, which we will use to derive the exact orientation of its nonrelativistic nodal planes along which we evidence its weak altermagnetism and LKSD in the altermagnetic form. The nontrivial spin Laue group is identical for CrSb. Thus, the nonrelativistic electronic structure of CrSb has the same g-wave symmetry.

The rotation sublattice-transposing symmetry. Starting from the left ("$^{2}6$"), the first sublattice-transposing symmetry is the non-symmorphic screw rotation, $[C_2||C_{6z}\mathbf{t}]$. It is shown in Fig. 3.3(a) and as a 2D projection for ease of visualization in Fig. 3.3(b). Here, $\mathbf{t}$ is a half unit cell-translation along the z axis. It can be both along $+z$ or $-z$ due to the periodicity of the crystal.

First, $[E||C_{6z}]$ rotates the crystal by a six-fold rotation around the z-axis as indicated by the magenta arrow (Fig. 3.3). Then, $[E||\mathbf{t}]$ translates by the non-symmorphic, half a unit cell translation in the z-direction (Fig. 3.3(a), gray dashed

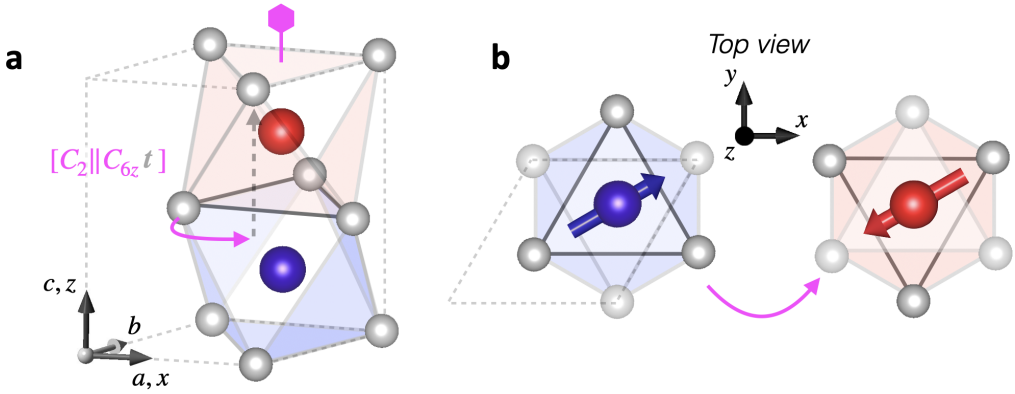

Figure 3.3: The MnTe magnetic crystal below 310 K and its sublattice-transposing (proper) rotation symmetry. (a) The two magnetic Mn atoms order with opposite magnetizations, indicated by the red and blue colored sites. They are surrounded by nonmagnetic Te atoms (gray colored), forming two rotated octahedra. These octahedra are related by a six-fold rotation $[E||C_{6z}]$ (magenta arrow around magenta six-fold rotation axis penetrating the magnetic sites) followed by a half-unit-cell translation $[E||\mathbf{t}]$ (gray dashed line). Lastly, the two-fold spin-space rotation $[C_2||E]$ converts one spin to its opposite (e.g., blue to red), thus recovering the original crystal and showing $[C_2||C_{6z}\mathbf{t}]$ is a symmetry. (b) The spin group operation $[C_2||C_{6z}\mathbf{t}]$ viewed from above. The red and blue arrows show the easy-axis direction for the magnetic moments [166, 113]. The corresponding nonmagnetic crystal structure belongs to the crystallographic space group #194.

arrow). These two operations bring the lowest nonmagnetic octahedra-shaped environment up to the top one. Last, $[C_2||E]$ rotates the spin by a two-fold rotation, converting the blue-colored spin to a red-colored spin and vice versa. Thus, we obtain the original magnetic crystal, and $[C_2||C_{6z}\mathbf{t}]$ is a symmetry.

Mirror sublattice-transposing symmetries. The second sublattice-transposing symmetry ("$/^2m$") is $[C_2||M_z]$, a mirror in the plane perpendicular to the z rotation axis, indicated by the magenta plane in Fig. 3.4(a). The magenta arrows show how every site in the blue-shaded region below the $[E||M_z]$ mirror is related to sites in the red-shaded region above the mirror. The magnetic atoms additionally change magnetization due to the two-fold spin rotation $[C_2||E]$.

The last sublattice-transposing symmetry ('^2m') is $[C_2||M_y\mathbf{t}]$, which is a nonsymmorphic mirror, shown by the magenta plane in Fig. 3.4(b). First, $[E||M_y]$ mirrors the sites as shown by the magenta arrows. As before, combining the mirror with the additional translation (dashed gray arrows) ensures that the position of the atoms matches that of the original crystal. Lastly, the red-colored spin becomes blue via the two-fold spin rotation.

For completeness, we also indicate the last mirror ("^1m"), $[E||M_{1\bar{1}0}]$, by the thick gray line in Fig. 3.4(b) (the line indicates the intersection of the $1\bar{1}0$ plane with the $\mathbf{a}-\mathbf{b}$ plane at $z = c$). It is not sublattice-transposing, as it does not involve a two-fold

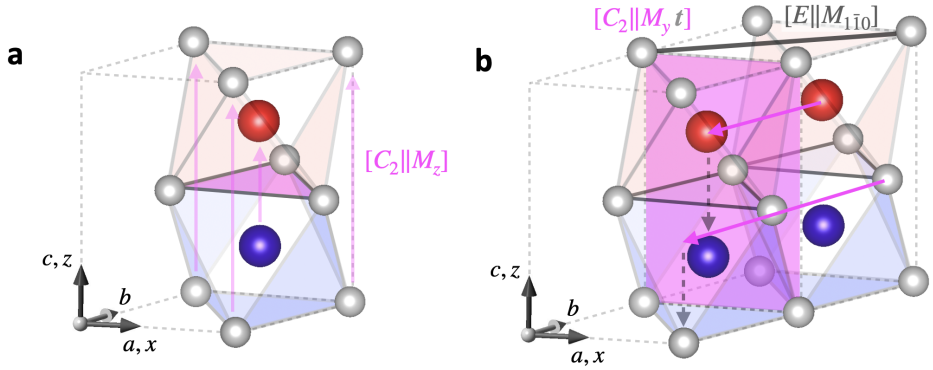

Figure 3.4: Sublattice-transposing mirror symmetries in MnTe. (a) $[C_2||M_z]$, an M_z mirror combined with a two-fold spin rotation. The magenta arrows indicate how the mirror transforms the sites. (b) $[C_2||M_y\mathbf{t}]$, a mirror in the $x-z$ plane combined with a two-fold spin rotation. The magenta arrows show how the M_y mirror acts. A half-unit-cell translation finally shifts the sites, shown by gray dashed arrows. The thick gray line indicates where the non-sublattice-transposing mirror symmetry $[E||M_{1\bar{1}0}]$ intersects the $z = c$ plane.

spin rotation.

With the sublattice-transposing symmetries shown here (Figs. 3.3 and 3.4), we can now derive the nonrelativistic nodal planes.

3.1.2 Spin-degenerate nodal planes in MnTe on the nonrelativistic level

The nonrelativistic band structure resulting from the spin group of MnTe is g-wave, with four nodal planes crossing the $\mathbf{\Gamma}$-point [25] as shown in Fig. 3.2(a) (bottom panel). Three nodal planes are parallel to the k_z-axis and a fourth one perpendicular to it with $k_z = 0$, and they separate spin-polarized regions in the Brillouin zone hosting strong altermagnetism (see, e.g., Fig. 1.9). Next, we derive these nodal planes using the methodology shown in Ch. 1.8 based on [6, 25]. Our analysis applies to any material in the spin Laue group in Eq. (3.2), including CrSb which we study later in this chapter.

Nodal planes from mirror sublattice-transposing symmetries. The first mirror sublattice-transposing symmetry, $[C_2||M_z]$, enforces a spin-degenerate $k_z = 0$ nodal plane, as we saw in Eq. (1.46). We show this nodal plane in Fig. 3.5, which horizontally cuts through the middle of the Brillouin zone (white horizontal plane marked $k_z = 0$). The straight magenta arrow (lower right) marks the vector normal to the plane.

The second mirror symmetry, $[C_2||M_y\mathbf{t}]$ analogously enforces the spin-degenerate nodal plane, now along the M_y mirror plane marked by $\mathbf{k}''$ in Fig. 3.5 ($k_y = 0$). Here, we define $\mathbf{k}''$ as a vector in this plane. The normal vector of this plane is indicated

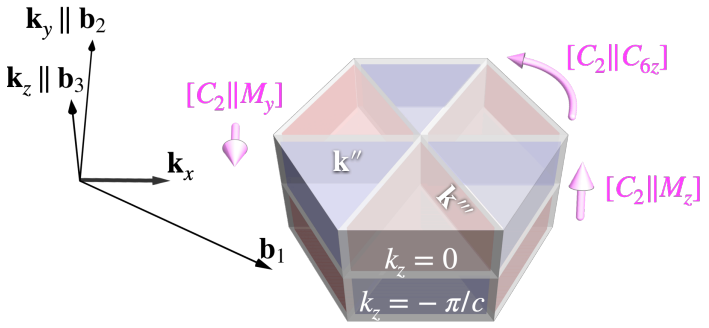

Figure 3.5: Nodal planes in reciprocal space of MnTe. The nodal planes are shown in white, separating regions of alternating red and blue spin polarization. Four planes cross the **Γ**-point (the center of the Brillouin zone), and eight encase the Brillouin zone edges (fainter white planes). The magenta arrows indicate the sublattice-transposing symmetries used to derive the equations describing the nodal planes (straight arrows the normal to the mirrors, the curved arrow the six-fold rotation). We have annotated the wavevectors of the constant-k_z nodal planes by $k_z = 0, -\pi/c$. We annotate the wavevectors of the parallel-to-$\mathbf{k}_z$ planes by $\mathbf{k}''$ ($k_y = 0$ plane) and $\mathbf{k}'''$ (the plane rotated by a three-fold rotation from the latter). The last parallel-to-$\mathbf{k}_z$ plane is obtained by rotating the $\mathbf{k}''$ plane by $[C_2||C_{6z}]$. The planes encasing the Brillouin zone edges are obtained by combining the transposing symmetries (e.g., mirroring wavevectors from $k_z = -\pi/c$ to $k_z = \pi/c$) and then applying Bloch's theorem (bringing the wavevectors back to, e.g., $k_z = -\pi/c$).

by the leftmost magenta arrow in Fig. 3.5 and is parallel to $\mathbf{b}_2$ ($\mathbf{k}_y$). The nodal plane is parallel to the k_x and k_z axes.

Nodal planes by combining with rotation symmetry. We can obtain the other two planes parallel to the k_z axis by acting via $[C_2||C_{6z}\mathbf{t}]$, illustrated in Fig. 3.5 by the curved magenta arrow, and $[E||C_{3z}\mathbf{t}]$ $(= [C_2||C_{6z}\mathbf{t}]^2)$. Let us illustrate, for instance, $[E||C_{3z}\mathbf{t}]$ acting on the wavevectors $\mathbf{k}''$ in the $k_y = 0$ nodal plane in either spin channel $\sigma = \uparrow, \downarrow$:

$$\epsilon(\mathbf{k}'', \sigma) = [E||C_{3z}]\epsilon(\mathbf{k}'', \sigma) = \epsilon(C_{3z}\mathbf{k}'', \sigma) \equiv \epsilon(\mathbf{k}''', \sigma). \tag{3.3}$$

Here, the resulting wavevectors, shown in Fig. 3.5, are $\mathbf{k}''' = C_{3z}\mathbf{k}''$. Since $\mathbf{k}''$ forms a nodal plane $\epsilon(\mathbf{k}'', \uparrow) = \epsilon(\mathbf{k}'', \downarrow)$, then by Eq. (3.3), $\mathbf{k}'''$ also forms a nodal plane $\epsilon(\mathbf{k}''', \uparrow) = \epsilon(\mathbf{k}''', \downarrow)$.

Finding nodal planes at the edges of the Brillouin zone. Analogously, we can find additional spin-degenerate nodal planes that do not cross the **Γ**-point.

It turns out that the opposite spin channels in these planes are related by a sublattice-transposing symmetry combined with the periodicity of the Brillouin zone [6]. For example, consider the bottom plane of the Brillouin zone ($k_z = -\frac{\pi}{c}$). First, we apply the sublattice-transposing symmetry $[C_2||M_z]$ to a spin channel (e.g., $\uparrow$), bringing us to the top plane ($k_z = \frac{\pi}{c}$) in the opposite spin channel ($\downarrow$); then, we use the $\frac{2\pi}{c}$

periodicity along the $\mathbf{k}_z$ direction to bring us back to the original plane:

$$[C_2||M_z]\epsilon\left(k_x, k_y, -\frac{\pi}{c}, \uparrow\right) = \epsilon\left(k_x, k_y, \frac{\pi}{c}, \downarrow\right) = \epsilon\left(k_x, k_y, -\frac{\pi}{c}, \downarrow\right) \tag{3.4}$$

In other words, these two steps correspond to the equation for the nodal planes, Eq. (1.45), with $\boldsymbol{G} = (0, 0, -\frac{2\pi}{c})$ added to the sublattice-transposing symmetry-transformed wavevector. Comparing the first and the last expression in Eq. (3.4), we see that the bottom plane of the Brillouin zone, $(k_x, k_y, -\frac{\pi}{c})$, is another spin-degenerate nodal plane because it also solves Eq. (3.4). We denote this plane by $k_z = -\frac{\pi}{c}$ in Fig. 3.5. By periodicity of the Brillouin zone, $k_z = \frac{\pi}{c}$ is the same nodal plane. We now have all constant-k_z nodal planes.

Analogously, from the remaining sublattice-transposing symmetries, the vertical edges of the Brillouin zone (planes parallel to the k_z axis) are also nodal planes. Thus, in addition to the four nodal planes crossing the $\mathbf{\Gamma}$-point, the entire Brillouin zone is encased in a nodal box in the nonrelativistic limit.

Summary. With nonrelativistic spin symmetry analysis, we have thus derived the form of the strong g-wave altermagnetism for the spin Laue group of MnTe (and CrSb, Eq. (3.2)) shown in Fig. 3.5 and hightlighted in Figs. 3.2(b) and 1.9.

3.1.3 Symmetries of weak altermagnetism in the $k_z = 0$ plane

Collinear s_z spin-polarization of the weak altermagnetism

We now consider the case when the Néel vector points along the easy-axis direction [166, 113] as shown in Fig. 3.3(b). The corresponding magnetic point group is

$$m'm'm = \{E, \mathcal{P}, M'_x, M'_y, M_z, C'_{2x}, C'_{2y}, C_{2z}\}, \tag{3.5}$$

where $M'_x = \mathcal{T}M_x$ and $M'_y = \mathcal{T}M_y$. We generally only need to consider the generators of the group to analyze all symmetry constraints it imposes. For example, we can consider $\mathcal{P}$ and the mirrors because all other elements of the group (identity E and rotations) can be obtained by multiplying the mirros and $\mathcal{P}$, see, e.g., Tab. 1.15.

We will apply the generators to the momentum-resolved spin operators, $S_i(k_x, k_y, k_z)$, where $i = x, y, z$ is the spin direction. Recall that the spin operators transform as *pseudovectors*, while the wavevectors transform as *polar vectors*.

Pseudovectors are invariant under inversion, while polar vectors do become inverted. As a consequence, when mirroring a pseudovector, the components of the pseudovector that are in-plane with the mirror change sign, and the out-of-plane component is invariant, as illustrated in Fig. 3.6(left). For the spin operators, for example, applying the mirror $M_z(S_x, S_y, S_z) = (-S_x, -S_y, S_z)$, inverts S_x and S_y, but not S_z.

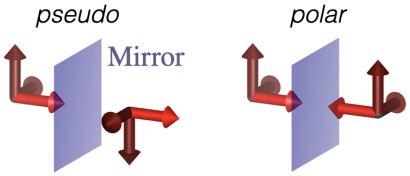

Figure 3.6: When mirroring a pseudovector, the components lying in the plane (dark red arrows) get inverted, while the out-of-plane component (light red arrow) is unchanged. The opposite is the case for a polar vector.

Applying this mirror symmetry, we therefore have for the $k_z = 0$ plane (including the $\mathbf{\Gamma} - \mathbf{M}$ and $\mathbf{\Gamma} - \mathbf{K}$ paths):

$$\begin{aligned} M_z S_x(k_x, k_y, 0) &= -S_x(k_x, k_y, 0) \\ M_z S_y(k_x, k_y, 0) &= -S_y(k_x, k_y, 0) \\ M_z S_z(k_x, k_y, 0) &= S_z(k_x, k_y, 0) \end{aligned} \tag{3.6}$$

The only solution for the first equation is $S_x(k_x, k_y, 0) = 0$, and similarly for the second equation, $S_y(k_x, k_y, 0) = 0$. The third equation, $S_z(k_x, k_y, 0) = S_z(k_x, k_y, 0)$, imposes no restrictions on the S_z-component, and thus a momentum-dependent spin expectation value $s_z = \langle S_z \rangle$ is allowed.

By an analogous analysis and using that time-reversal inverts spin and wavevectors, Eq. (1.7), M_x' alone imposes a spin polarization ($S_x = 0, S_y \neq 0, S_z \neq 0$) along the k_x-axis ($k_y = k_z = 0$), and M_y' alone imposes ($S_x \neq 0, S_y = 0, S_z \neq 0$) along the k_y-axis ($k_x = k_z = 0$). However, due to Eq. (3.6), M_z enforces these spin polarizations to be collinear and along S_z because they lie in the $k_z = 0$ plane.

Inversion symmetry of the weak altermagnetism

The crystal inversion symmetry $\mathcal{P}$ in $m'm'm$ enforces the spin-polarized band structure to be inversion symmetric as follows,

$$\mathcal{P} s_z(k_x, k_y, k_z) = s_z(-k_x, -k_y, -k_z), \tag{3.7}$$

similar to strong altermagnetism on the nonrelativistic level.

Let us expand the Hamiltonian around the $\mathbf{\Gamma}$-point. Then, only even-in-momentum terms are allowed (similarly to Eq. (3.1)) due to inversion symmetry, and only collinear spin-polarization in the s_z-component. Therefore, the terms in the Hamiltonian in the $k_z = 0$ plane read:

$$H^{\alpha\beta}_{\mathbf{k}\sim\mathbf{\Gamma}}(k_x, k_y, k_z = 0) \sim \sigma_z k_i^\alpha k_j^\beta, \quad \alpha + \beta \geq 2 \text{ and even}, \; i, j = x, y, \tag{3.8}$$

where σ_z is a spin Pauli matrix, and a summation over α, β, i, and j is implied. *The inversion symmetry distinguishes this weak altermagnetism, e.g., from relativistic spin-orbit coupling in non-centrosymmetric crystals, which breaks inversion symmetry and allows odd-in-k terms in the Hamiltonian.*

In summary, in the $k_z = 0$ plane, the magnetic group symmetries of MnTe for the easy-axis Néel vector orientation pointing at 30 degrees away from the x-axis (see Fig. 3.3(b)) enforces the weak altermagnetism to be collinear with a spin polarization only in the out-of-plane s_z-component (Eq. (3.6), due to the M_z mirror symmetry), and to be inversion symmetric (Eq. (3.7), due to crystal inversion symmetry $\mathcal{P}$), with only even-in-k terms allowed in the Hamiltonian.

By symmetry, the $m'm'm$ group technically also allows for a net magnetization for the s_z spin component. (To see this, consider the action of M_z on only the spins S_i and not the wavevectors in Eq. (3.6).) Even though a net magnetic moment is allowed for the easy-axis orientation, the net moment has been found to vanish in *ab initio* calculations and experimental magnetometry measurements [113]. We further corroborate this with *(i)* our calculated band structures (Fig. 3.2(a) and in the next section) and *(ii)* the ARPES spectra not being gapped at the $\mathbf{\Gamma}$-point (c.f. Def. 3) [30].

3.1.4 Weak altermagnetic band structure of MnTe

We proceed to compare the *ab initio* band structure calculations of weak altermagnetism in MnTe to angle-resolved photoemission spectroscopy (ARPES) data. We will show that the electronic band structure of MnTe indeed takes *the altermagnetic form* from Def. 3 that we have predicted in the $k_z = 0$ plane in Eq. (3.8), thus providing evidence for altermagnetism in MnTe.

Band structure

We performed the DFT calculations as described in Ch. 2.3.6. We set the Néel vector along the easy-axis direction [166, 113] as illustrated in Fig. 3.3(b). The ARPES experiment was performed at $15\,K$, well below the $310\,K$ critical temperature. The experimental set-up and sample growth allowed for accessing the $k_z = 0$ plane and used a soft X-ray photon energy of 667 eV [30] which is more bulk sensitive than, e.g., lower-energy UV photons [169].

Fig. 3.7 shows the *ab initio* band structures and ARPES spectra [30] in the $k_z = 0$ plane, along k_x ($\mathbf{\Gamma} - \mathbf{K}$) in Fig. 3.7(a) and k_y in ($\mathbf{\Gamma} - \mathbf{M}$) 3.7(b). The ARPES data (top row) have been refined for visual clarity [30].

We compare these data to the corresponding relativistic *ab initio* calculations of the electronic band structure (bottom row). The red and blue colors of the bands

depict the opposite spin polarizations, enforced to be along the z-axis due to the M_z symmetry from Eq. (3.6).

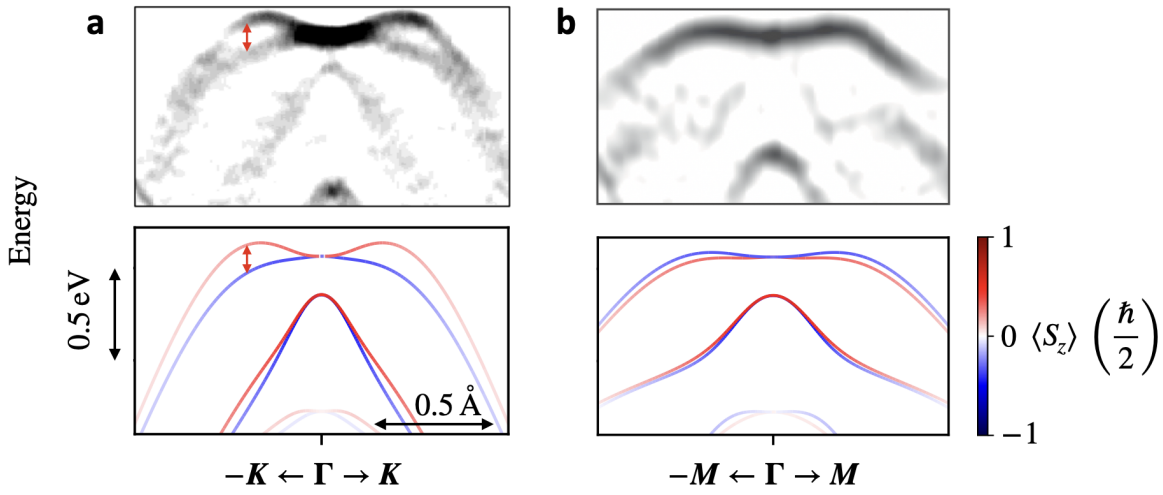

Figure 3.7: Weak altermagnetism of MnTe in the $k_z = 0$ plane. The band structures are shown along (a), $\mathbf{\Gamma} - \mathbf{K}$ and (b), $\mathbf{\Gamma} - \mathbf{M}$ (paths illustrated in Fig. 3.2). The top row shows the ARPES spectra and the bottom row shows the *ab initio*-calculated band structures for the Néel vector along the easy-axis direction [166, 113] shown in Fig. 3.3(b). The red and blue coloring of the latter indicates the spin polarization, which is nonzero in the $s_z = \langle S_z \rangle$ component. The red double arrow highlights the spin-splitting size reaching $\sim 100\,\text{meV}$. Figure adapted from [30], CC BY 4.0.

Consistency with experiment and 100 meV spin splitting. The *ab initio* band structures are remarkably consistent with the ARPES band maps from the experiment in Fig. 3.7. This includes how the bands disperse overall and that the *spin splitting*—where bands with opposite spins meet at $\mathbf{\Gamma}$ and split away from it—along the k_x-axis ($\mathbf{\Gamma} - \mathbf{K}$ path) is larger than along k_y ($\mathbf{\Gamma} - \mathbf{M}$). The double red arrow in Fig. 3.7(a) highlights the spin splitting in the experimental and theoretical band maps. The *ab initio* calculation shows that these two bands have the opposite spin polarization. Remarkably, the spin splitting is of a $\sim 100\,\text{meV}$ scale thanks to the large spin-orbit coupling from Te. Such a large magnitude of the spin splittinis comparable to the large relativistic spin splitting size found in non-centrosymmetric crystals with heavy elements, such as BiTeI [114]. However, unlike in the relativistic case where the bands break inversion symmetry and preserve time-reversal symmetry, in the current case, the bands are centrosymmetric and break time-reversal symmetry.

Altermagnetic form: Inversion symmetry and quadratic band dispersion. The energy bands in Fig. 3.7 take *the altermagnetic form* from Def. 3: The bands meet at the $\mathbf{\Gamma}$-point, are inversion symmetric with a collinear s_z spin polarization, and disperse quadratically, consistent with our predicted weak altermagnetism in the $k_z = 0$ plane from Eq. (3.8).

This quadratic, inversion-symmetric dispersion further highlights the unconventional nature of the weak altermagnetism. The vanishing linear term makes the weak altermagnetism distinct from relativistic spin-orbit coupling in non-centrosymmetric crystals. The inversion symmetry of the spin-polarized bands is a consequence of the inversion symmetry of the MnTe crystal that we showed in Eq. (3.7).

Furthermore, the lowest even term of the band-dispersion around $\mathbf{\Gamma}$ is quadratic and not constant as in the ferromagnetic-like mechanism arising from a net magnetization. The vanishing constant term is thus consistent with the absence of a net magnetic moment in both experiments on epitaxial MnTe thin films and *ab inito* calculations [113]. However, the vanishing net magnetic moment does not prevent the extraordinarily large size of the weak altermagnetic, momentum-dependent spin splitting we see away from $\mathbf{\Gamma}$.

Thus, the absence of linear and constant terms in the spin-split band dispersion distinguishes weak altermagnetic LKSD from the conventional ferromagnetic-like mechanism and the mechanism based on relativistic spin-orbit coupling in non-centrosymmetric crystals.

3.1.5 Domains

We now discuss possible domains in the experiment and their impact on the measured band dispersions. There are six possible orientations of the Néel vector with easy axes pointing along the Mn-Te direction, as shown in Fig. 3.8(a). Moreover, there are two possible crystallographic domains, and the relationship between them, the Néel vector directions, and how it changes the band structure is explained in Fig. 3.8(b). For each possible Néel vector direction, there is an equal number of possible domains with identical spin splitting energy dispersions but opposite spin polarization. That means the spin polarization signal can cancel out in experiments with equally populated domains.

To see the modulation of the band dispersions from the domains, we can study the dependence of the size of the spin splitting on three possible, inequivalent directions of the Néel vector, $\mathbf{N}_1$, $\mathbf{N}_2$, and $\mathbf{N}_3$ ($\mathbf{N}_4$-$\mathbf{N}_6$). (Note that $\mathbf{N}_1$ corresponds to the Néel vector we have considered earlier, shown in Fig. 3.3.) We emulate the averaging as a result of these three directions by calculating the bands for a single domain with Néel vector $\mathbf{N}_1$, along the three $\mathbf{\Gamma} - \mathbf{M}_1$, $\mathbf{\Gamma} - \mathbf{M}_2$, and $\mathbf{\Gamma} - \mathbf{M}_3$ directions shown in Fig. 3.9. That is because the relative orientation between the reciprocal space path and the Néel vector rotates as we do so: bands along $\mathbf{\Gamma} - \mathbf{M}_2$ with Néel vector along $\mathbf{N}_1$ corresponds to bands along $\mathbf{\Gamma} - \mathbf{M}_1$ with Néel vector along $-\mathbf{N}_3$; and bands along $\mathbf{\Gamma} - \mathbf{M}_3$ with Néel vector along $\mathbf{N}_1$ corresponds to $\mathbf{\Gamma} - \mathbf{M}_1$ with Néel vector along $-\mathbf{N}_2$. Fig. 3.10 shows the result: all give rise to a finite spin splitting, and similarly for the $\mathbf{\Gamma} - \mathbf{K}_1$, $\mathbf{\Gamma} - \mathbf{K}_2$, and $\mathbf{\Gamma} - \mathbf{K}_3$ paths.

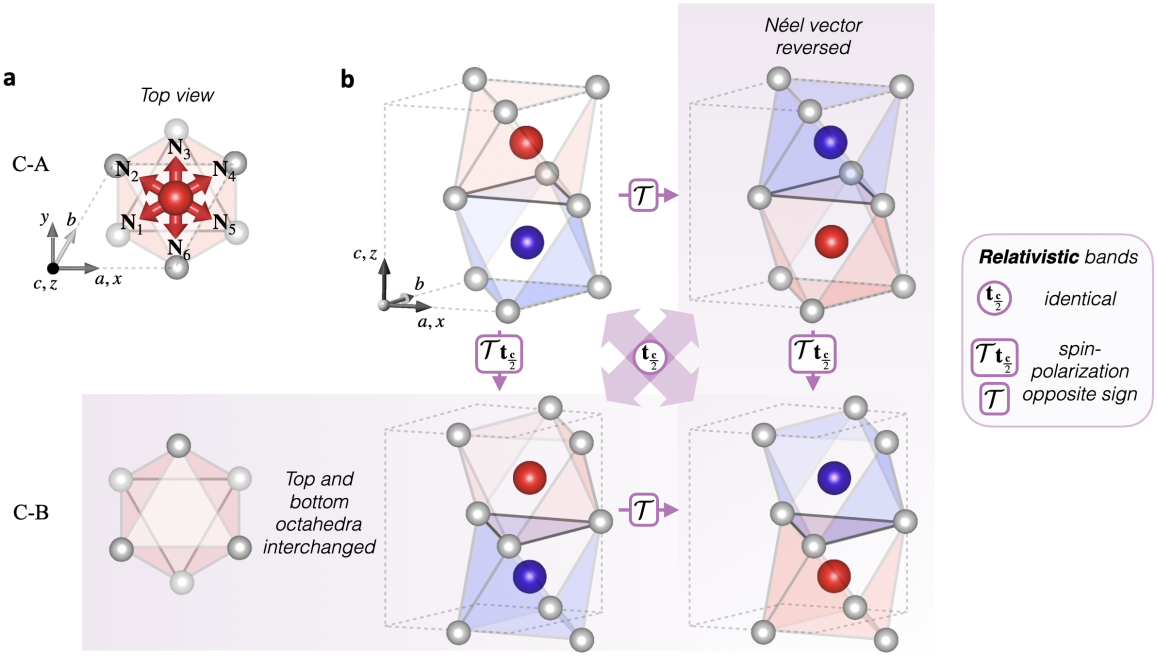

Figure 3.8: Possible MnTe crystals and their impact on the relativistic band structure. (a) Six possible Néel vector orientations, $\mathbf{N}_1$-$\mathbf{N}_6$, along the Mn-Te directions. (b) Top row, left versus right: reversing the Néel vector via a 180-degree rotation (red site becomes blue, the blue site becomes red; from $\mathbf{N}_i$ to $-\mathbf{N}_i$). It is equivalent to applying time-reversal operator $\mathcal{T}$, which reverses the spin polarization of the corresponding energy bands ($\epsilon_{-\mathbf{N}_i}(\sigma,\mathbf{k}) = \epsilon_{\mathbf{N}_i}(-\sigma,-\mathbf{k}) = \epsilon_{\mathbf{N}_i}(-\sigma,\mathbf{k})$ where in the last equality we use the inversion symmetry of the magnetic point group). Bottom row: the second possible crystallinity, C-B, where the Te octahedra have been interchanged compared to the first row with the C-A crystallinity. It is equivalent to applying the time-reversal with vertical half-unit-cell translation, $\mathcal{T}\mathbf{t}_{\frac{c}{2}}$, which therefore also reverses the spin polarization of the bands. Combining it with Néel vector reversal yields the bottom right crystal, which is also equivalent to translating the top left crystal by $t_{\frac{c}{2}}$ (and similarly for the other diagonal, top right versus bottom left). For a given Néel vector $\mathbf{N}_i$, we can combine it with Néel vector reversal and change between C-A and C-B. The corresponding band structure of half of the possibilities will be identical, while the other half will be identical except for a sign change of the spin polarization. Combined there are twelve possible crystals: $\mathbf{N}_1$-$\mathbf{N}_6$ combined with C-A and C-B.

Finally, for two different crystallinities (Fig. 3.8(b), top and bottom rows), the interchanged Te environment would change the sign of the spin polarization of the bands but not its dispersion shape. That means a spin-splitting dispersion would still be visible even for multiple crystallinities in the sample.

To conclude, even with different magnetic domains along six possible easy axes and crystallinities, the spin splitting dispersion in the energy bands would still be visible, in concurrence with the experimental results.

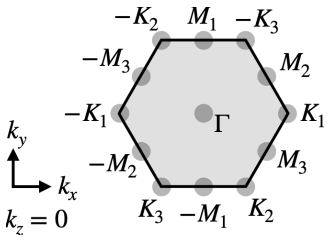

Figure 3.9: Points in the Brillouin zone in the $k_z = 0$ plane, $\mathbf{\Gamma}$, $\mathbf{M}$ and $\mathbf{K}$ points, between which we calculate the electronic band structure.

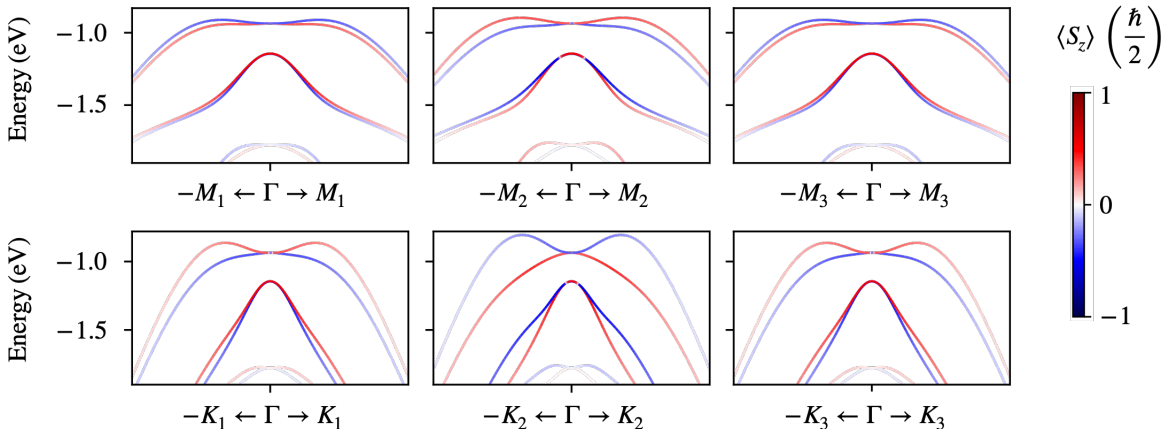

Figure 3.10: Weak altermagnetism along the $\mathbf{\Gamma} - \mathbf{M}$ and $\mathbf{\Gamma} - \mathbf{K}$ paths (Fig. 3.9) for the easy-axis Néel vector along $\mathbf{N}_1$. By considering six-fold-rotated $\mathbf{\Gamma} - \mathbf{M}$ paths, we effectively consider the bands of possible six-fold rotated, easy-axis Néel vectors as described in the main text, and similarly for the $\mathbf{\Gamma} - \mathbf{K}$ paths. Figure adapted from [30], CC BY 4.0.

3.1.6 Weak altermagnetism in the $k_z = 0$ plane

We now demonstrate that the weak altermagnetism in the $k_z = 0$ plane is collinear, even-parity-wave and time-reversal symmetry breaking. To this end, we perform an iso-energy cut calculation at $\sim$ 100 meV below the top of the valence band from Fig. 3.10 along the $\mathbf{\Gamma} - \mathbf{K}_2$ path. We used a 31×31 ($k_x \times k_y$) grid and the same parameters as before, described in Ch. 2.3.6, including the Néel vector being as in Fig. 3.3, i.e., pointing along $\mathbf{N}_1$.

Fig. 3.11 shows the result for the three spin components. It reveals that the spin polarization is only finite in the z-component, thus being collinear. This LKSD is also inversion symmetric, which agrees with the altermagnetic quadratic spin splitting dispersion around the $\mathbf{\Gamma}$-point from Figs. 3.7 and 3.10. The spin polarization being out-of-plane along z (while the Néel vector is in-plane) and the inversion symmetry agrees with the weak *altermagnetic form* for MnTe in Eq. (3.8). In contrast, the spin

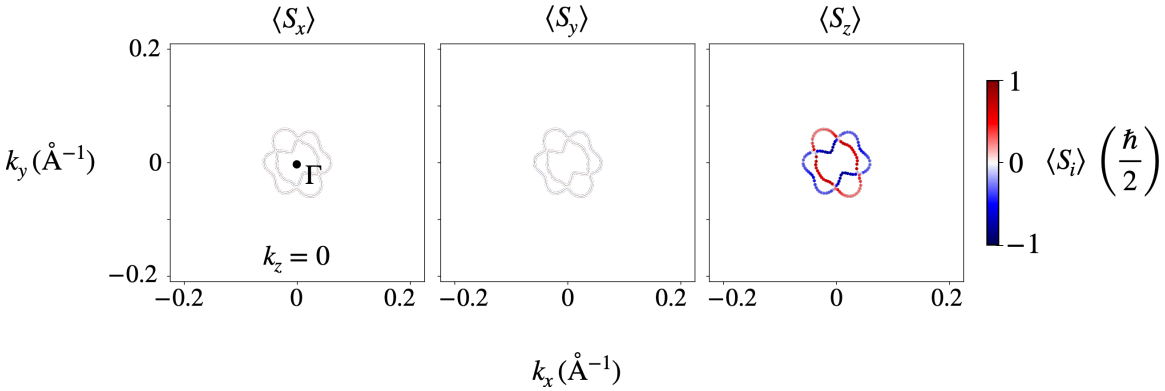

Figure 3.11: Weak altermagnetism in the $k_z = 0$ plane of MnTe for a constant-energy cut of the electronic band structure. The energy cut is $\sim 100\,\text{meV}$ below the top of the valence band shown in Fig. 3.3(b) for the $\mathbf{\Gamma} - \mathbf{K}_2$ path and the Néel vector along the easy-axis orientation. From left to right, we show the x, y, and z components of the spin expectation value. The spin polarization of the bands is collinear out-of-plane, even-parity-wave and time reversal symmetry breaking.

polarization in the strong altermagnetic LKSD (Fig. 3.2(b,top panel)) is along the in-plane easy-axis of the Néel vector.

In summary, distinct strong and weak altermagnetism coexist in MnTe: strong g-wave altermagnetism away from the nonrelativistic nodal planes (Figs. 3.2(b) and 3.5), with an electronic structure with collinear spin polarization along the in-plane easy-axis Néel vector, and weak altermagnetism in the $k_z = 0$ plane, with a collinear, out-of-plane $\langle S_z \rangle$-spin-polarization (e.g., Figs. 3.2(a) and Fig. 3.11) due to M_z symmetry (Eq. (3.6)). Strong and weak altermagnetism both break time-reversal symmetry. They are also even-parity-wave and thus disperse even-in-k (Eqs. (3.1) and (3.8)). The inversion symmetry of the strong LKSD is enforced both due to the collinear spin-only group of the crystal (Eq. (1.19)) and inversion symmetry of the crystal, while the weak LKSD due to inversion symmetry of the crystal (Eq. (3.6)).

3.1.7 Strong altermagnetic band structure of CrSb

CrSb is a predicted g-wave altermagnet belonging to the same spin-point group as MnTe, Eq. (3.2) [25]. As in MnTe, the sublattice-transposing symmetries enforces the g-wave spin-polarization and nodal planes in CrSb [25, 31] as shown earlier in Fig. 3.5. CrSb has a high critical temperature of $700\,K$, higher than that of MnTe, and it is a metal, while MnTe is a semiconductor. These two facts make CrSb a candidate for metallic altermagnetic spintronics research, possibly at room temperature. Its applicability as an altermagnetic metal hinges upon whether spin-splitting of the energy bands is present close to the Fermi energy. In the following, we provide

strong evidence for such a spin splitting with DFT calculations and our experimental collaboration [31].

Magnetic crystal and real-space electronic structure of altermagnetic CrSb

Fig. 3.12 shows the CrSb crystal structure and its altermagnetic order. The lattice parameters are $a = b = 4.103\,\text{Å}$ and $c = 5.463\,\text{Å}$ and the magnetization vectors lie along the z-axis, corresponding to earlier experiment [37, 170]. The spin symmetries of

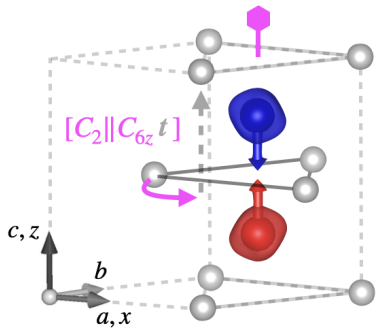

Figure 3.12: Altermagnetic crystal structure of CrSb. The blue and red sites are the Cr atoms with opposite spins along the z axis (red and blue arrows), and the gray sites are the nonmagnetic Sb atoms. The magnetic crystal belongs to the same spin Laue group as MnTe, with the rotational sublattice transposing symmetry highlighted similarly here by the curved magenta arrow. The red and blue surfaces show the anisotropic isosurfaces of the magnetization densities in the collinear case without spin-orbit coupling.

CrSb are identical to those in MnTe, and thus, we refer the reader to spin symmetries shown in Figs. 3.3 and 3.4, which apply analogously to CrSb. Here, we highlight the sublattice-transposing six-fold rotation symmetry by the magenta arrow in Fig. 3.12.

Magnetization densities. We also highlight the real-space electronic structure in terms of magnetization densities calculated from DFT (Eq. (2.43)) in the nonrelativistic limit, shown in Fig. 3.12 by the red and blue shaded isosurfaces. It was calculated in VASP as described in Ch. 2.3.6. As expected for altermagnetism [25, 3], the magnetization densities are anisotropic, where each spin channel breaks the symmetries of the underlying nonmagnetic crystal, recall Fig. 1.7(c), and they obey the symmetries of the spin point group (which equals to the spin Laue group in Eq. (3.2) due to the crystal inversion symmetry present).

Altermagnetic band structure and ARPES spectra of CrSb

We calculated the *ab initio* band structure using the same parameters and convergence criterion as for the above magnetization density calculation, but now with spin-orbit

coupling. We additionally verified that the nonrelativistic bands matched the bands along the $\mathbf{\Gamma} - \mathbf{L}$ path from [25]. We also verified that similarly to MnTe in Fig. 3.2, adding spin-orbit coupling in the calculation only slightly alters the overall band structure compared to the nonrelativistic limit.

We calculated the energy bands along a low-symmetry path from $\frac{\mathbf{M}}{2} - \frac{\mathbf{b}_3}{2}$ to $\frac{\mathbf{M}}{2} + \frac{\mathbf{b}_3}{2}$ shown in Fig. 3.13 (red-blue line), a path that by symmetry should show strong altermagnetism, and which was achieveable in the experimental set-up [31]. Generally,

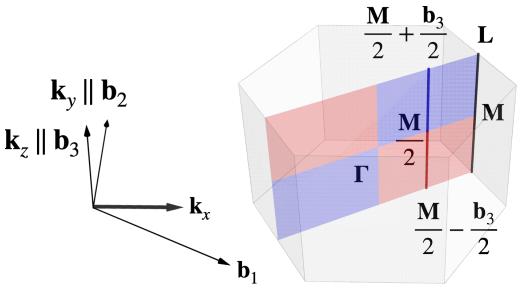

Figure 3.13: Brillouin zone of CrSb. The red-blue line highlights the low-symmetry path where we observe the strong altermagnetic spin splitting of the band structure. Here, $\mathbf{L} = \mathbf{M} + \frac{\mathbf{b}_3}{2}$.

such a cut is promising for observing large spin splittings, as it cuts through regions far from the nonrelativistic nodal planes where strong, nonrelativistic altermagnetism is dominant.

The collaborative experimental spectra were obtained at a $12\,K$, well below the critical temperature, using soft X-ray ARPES. The data was processed by subtracting background data, symmetrized by mirroring and adding the data from opposite sizes of the $k_z = 0$ plane, and the resulting signal was enhanced [31].

Fig. 3.14 shows the energy bands and ARPES band features of CrSb along the above path from $\frac{\mathbf{M}}{2} - \frac{\mathbf{b}_3}{2}$ to $\frac{\mathbf{M}}{2} + \frac{\mathbf{b}_3}{2}$. Fig. 3.14(a) shows the *ab initio* band structure, and Fig. 3.14(b) the ARPES band features.

Both the theoretical and experimental spectra display a strong band splitting, which splits in concurrence with the characteristic even-in-k g-wave *altermagnetic form*, Def. 3, featured in Fig. 3.13: The bands are degenerate at $\frac{\mathbf{M}}{2} \pm \frac{\mathbf{b}_3}{2}$, and split away from these points, with a distinctly present splitting in both theory and experiment highlighted by the double red arrows reaching a $\sim 0.6\,\text{eV}$ scale.

Notably, along this path, the spin splitting is largest approximately in the middle between $\frac{\mathbf{M}}{2}$ and $\frac{\mathbf{M}}{2} \pm \frac{\mathbf{b}_3}{2}$, corresponding to the approximate middle of the blue and red regions in Fig. 3.13. This is concurrent with calculations along $\mathbf{\Gamma} - \mathbf{L}$ [25].

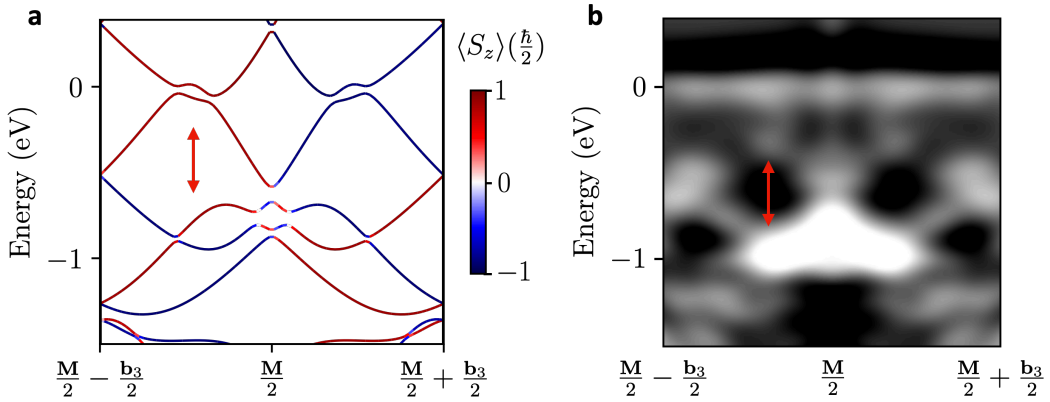

Figure 3.14: Electronic band structure of CrSb. (a) *Ab initio*-calculated, spin-polarized energy bands along the path from $\frac{\mathbf{M}}{2} - \frac{\mathbf{b}_3}{2}$ to $\frac{\mathbf{M}}{2} + \frac{\mathbf{b}_3}{2}$. They display a typical strong altermagnetic spin splitting, closing around the nodal planes (points $\frac{\mathbf{M}}{2} \pm \frac{\mathbf{b}_3}{2}$), and opening with a $\sim 0.6\,\mathrm{eV}$ order spin splitting away from the nodal planes. (b) Filtered and symmetrized X-ray ARPES signal for the same path. It shows the same characteristic closing and opening of the bands in good agreement with our theory. Figure adapted (experimental and theory plots here in separate panels) from [31], the experimental plot provided by Priv.-Doz. Martin Jourdan, CC BY 4.0.

3.1.8 Strong altermagnetic band structure of RuO_2

RuO_2 has been considered a model altermagnetic candidate owing to its rutile crystal structure with the possibility of anisotropic and opposite spin sublattices related by crystal rotations. It is currently heavily discussed under what conditions it is magnetic; e.g., it was suggested that oxygen deficiency [171] and thin film structures [5] stabilize the magnetism. It was one of the first materials that was predicted to be altermagnetic [3, 25], owing to the positions of the oxygen atoms in the crystal causing the breaking of collinear antiferromagnetic sublattice-transposing symmetries, $\mathcal{PT}$ and $\mathcal{T}\mathbf{t}$, inducing anisotropic magnetization densities and an electronic band structure that breaks time-reversal symmetry and spin-polarizes. The electronic structure of RuO_2 was also predicted to give rise to the crystal Hall effect [3]. The effect corresponds to a large transverse Hall current, comparable to in ferromagnets, but originating from the time-reversal symmetry breaking of the altermagnetic band structure, and not a net ferromagnetic moment or noncollinear magnetic order [3]. The altermagnetic anomalous Hall effect (crystal Hall effect) was measured in the altermagnetic candidate MnTe [113], and its possible presence was also indicated in RuO_2 [5, 172] and Mn_5Si_3 [112].

Recently, our experimental collaboration observed time-reversal symmetry breaking more directly in its band structure [38]. Further supporting our observation is a recent report on LKSD and spin-polarized d-wave magnetism [173].

Since the first theory prediction of altermagnetism in RuO_2, there have been

more predictions and experimental evidence of anomalous spintronics phenomena in the material which are unique to altermagnets and unavailable in, e.g., ferromagnets. These effects include the spin-splitter effect [7], experimentally indicated by several groups independently [9, 10, 11], and our predictions of spin-polarized electronic currents and giant magnetoresistance [12], and tunneling magnetoresistance [12, 13] (see Ch. 4).

Here, we discuss the altermagnetic spin symmetries leading to the d-wave altermagnetic and time-reversal symmetry broken band structure of RuO_2, which we used in our works on giant and tunneling magnetoresistance in RuO_2 [12] which we discuss in Ch. 4.

Spin symmetries

Fig. 3.15 shows its crystal structure, where the red and blue-colored Ru atoms (spin up and down) are surrounded by O atoms that form octahedra, as in the discussed compensated collinear magnetic ordering [77, 78, 3].

This magnetic crystal belongs to the tetragonal spin Laue group

$$^{2}4/^{1}m^{2}m^{1}m \tag{3.9}$$

whose generators are illustrated in Fig. 3.15(a). The group has two symmetries that transpose the sublattices, shown by the purple mirror and magenta rotation, and two symmetries that do not, shown by the gray mirrors. We also show the translations in the sublattice-transposing symmetries, $\mathbf{t}_{\frac{1}{2}\pm\frac{1}{2}0}$. For ease of visualization, we illustrate in Fig. 3.15(b) the magnetic sublattices and octahedra environments projected in the $a-b$ plane and the sublattice-transposing mirror and rotation transposing them. Firstly, the $[E||M_x]$ mirror or $[E||C_{4z}]$ rotation transposes the two types of octahedra as illustrated in Fig. 3.15(b), from the octahedron shown on the left to the octahedron shown on the right. The resulting octahedron on the right is then translated, e.g., by $[E||\mathbf{t}_{\frac{1}{2}-\frac{1}{2}0}]$ for the mirror operation as shown by the purple arrow in Fig. 3.15(a), such that it matches the positions of the octahedron around the blue Ru atom (and similarly for the rotation operation, see magenta arrow). Secondly, $[C_2||E]$ rotates the Néel vector by a two-fold rotation, such that the red Ru atom (spin up) changes to blue (spin down).

Spin densities

Given the magnetic crystal in Fig. 3.15, we calculated the spin densities in VASP [165] without spin-orbit coupling as described in Ch. 2.3.6.

Fig. 3.16 shows the spin densities. They obey the same symmetries as the magnetic crystal, e.g., they are related by the rotation and mirror sublattice-transposing

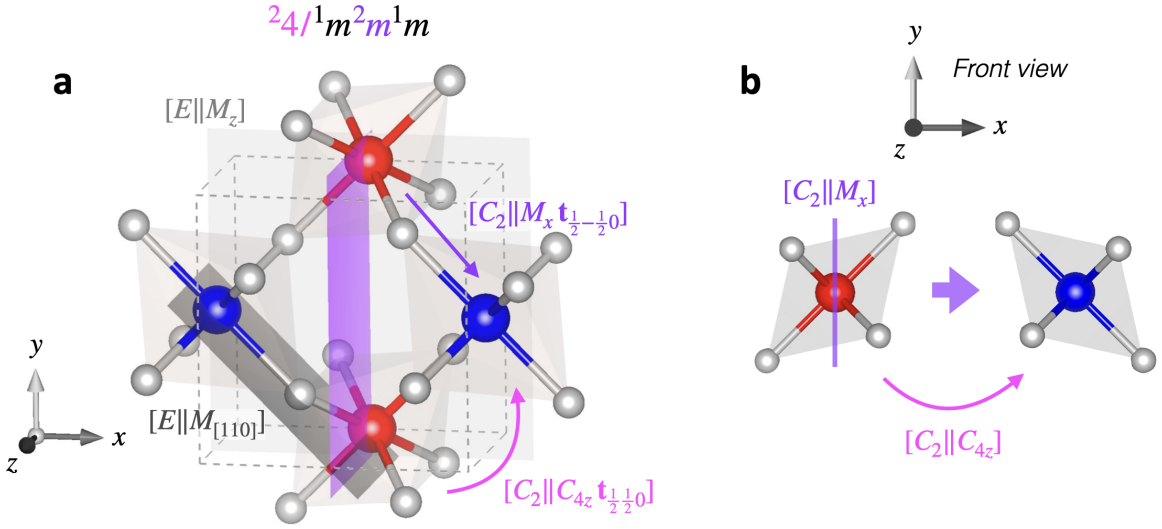

Figure 3.15: The RuO_2 crystal and symmetries in its nontrivial spin Laue group, $^{2}4/^{1}m^{2}m^{1}m$. (a) A three-dimensional view of the tetragonal unit cell (dashed lines), showing the magnetic RuO_2 atoms with opposite spins (red and blue sites) surrounded by octahedra-forming oxygen atoms (gray sites) and associated spin symmetries (planes and arrows). We show the sublattice-transposing symmetries in purple and magenta: e.g., $[C_2||M_x\mathbf{t}_{\frac{1}{2}-\frac{1}{2}0}]$ mirrors around $[E||M_x]$ (purple plane), mirroring the octahedral environments as highlighted in the front view in (b, left and right; differently oriented gray-shaded octahedra). Together with $[C_2||E]$, it transposes also the magnetic sublattice, completing the operation shown in (b) (left red becomes blue right). Lastly, the translation $[E||\mathbf{t}_{\frac{1}{2}-\frac{1}{2}0}]$ (a, purple arrow) shifts to the correct position, completing the symmetry. It works analogously for the sublattice transposing symmetry $[C_2||C_{4z}\mathbf{t}_{\frac{1}{2}\frac{1}{2}0}]$ (magenta curved arrow, a and b). Here, $\mathbf{t}_{\frac{1}{2}\pm\frac{1}{2}0} = (\frac{a}{2}, \pm\frac{b}{2}, 0)$ (lattice vectors $\mathbf{a}\|\mathbf{x}$, $\mathbf{b}\|\mathbf{y}$, and $\mathbf{c}\|\mathbf{z}$). The easy-axis Néel vector orientation is along $\mathbf{z}$ according to experimental and DFT reports [77, 78].

symmetries as shown in Fig. 3.15(b) and obey the spin point group symmetries (equal to the spin Laue group in Eq. (3.9) due to a crystal inversion symmetry).

D-wave-symmetry in reciprocal space

The sublattice-transposing symmetries shown in Fig. 3.15 enforce the electronic band structure to be spin-polarized with a planar d-wave form [3, 25] as illustrated in the Brillouin zone-plot in Fig. 3.17. Contrary to the bulk g-wave symmetry in MnTe and CrSb from Fig. 3.5, the d-wave symmetry has two instead of four nodal surfaces crossing the $\mathbf{\Gamma}$-point. The two nodal planes separating opposite spin-polarization regions both cross constant-$\mathbf{k}_z$-planes–the d-wave planes. Therefore, the d-wave spin-polarization is of the *planar* type, as opposed to a *bulk* d-wave spin-polarization [25], where the d-wave plane is not in the constant-$\mathbf{k}_z$-planes, recall Fig. 1.9.

In the case of this planar d-wave spin polarization in Fig. 3.17, we can first apply

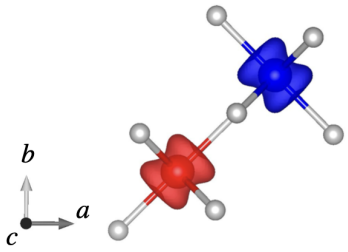

Figure 3.16: RuO2 spin densities, calculated *ab-initio* without spin-orbit coupling. The densities are anisotropic and obey the spin Laue group symmetries (Eq. (3.9)) analogously to the magnetic crystal in Fig. 3.15.

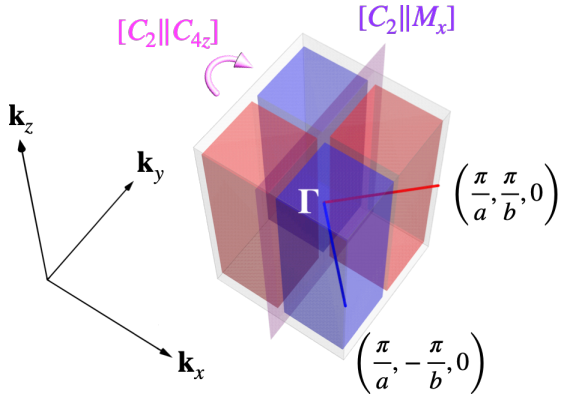

Figure 3.17: Planar d-wave spin polarization in the RuO_2 Brillouin zone. The sublattice-transposing $[C_2||\mathbf{M}_x]$-mirror (purple plane) imposes a nodal plane (in the same purple plane) parallel to the $\mathbf{k}_y$-axis. The sublattice-transposing $[C_2||C_{4z}]$-rotation (magenta arrow) relates it to a second nodal plane parallel to the $\mathbf{k}_k$-axis, and it relates the spin-polarized, strong altermagnetic regions (red and blue spin-polarized volumes) to each other. As a result, the spin-polarization in the Brillouin zone is d-wave, i.e., it has two nodal surfaces between which the spin-polarization alternates, and it is planar, as the two nodal planes cross constant-$\mathbf{k}_z$-planes [25]. Here, $\mathbf{k}_x\|\mathbf{b}_1$, $\mathbf{k}_y\|\mathbf{b}_2$, and $\mathbf{k}_z\|\mathbf{b}_3$, with $\mathbf{b}_1 = \frac{\pi}{a}\hat{\mathbf{k}}_z$ along $\hat{\mathbf{k}}_z$ etc. are the reciprocal lattice vectors. The blue line shows the $\mathbf{\Gamma} - (\frac{\pi}{a} - \frac{\pi}{b})$ path; the red, $\mathbf{\Gamma} - (\frac{\pi}{a}, \frac{\pi}{b}, 0)$.

the mirror $[C_2||M_x]$, shown by the purple plane, to obtain a first nodal plane along the same plane and parallel the $\mathbf{k}_y$-axis. Then, we can apply $[C_2||C_{4z}]$ symmetry to reveal the second, 90-degree-rotated nodal plane, parallel to the $\mathbf{k}_x$-axis. The nodal planes encasing the Brillouin zone can be obtained analogously to before as in Eq. (3.4) [6]. Thus, only two sublattice-transposing symmetries are needed to reveal the entire d-wave spin-polarization in the Brillouin zone here. In general, more symmetries might be needed. For example, mapping the entire *bulk* g-wave spin polarization in Fig. 3.5 requires a minimum of two orthogonal mirror planes and a rotation.

The d-wave symmetry applies to the electronic band structure, which thus breaks $\mathcal{T}$ symmetry—the spin does not invert when inverting the momentum $\mathbf{k}$, Eq. (1.7)–

which is a principle ingredient for, e.g., the crystal and anomalous Hall effects [3].

We point out that also other observables beyond the electronic structure can follow the d-wave altermagnetic symmetry, an example being the altermagnetic d-wave magnons proposed in RuO_2 [116].

Band structure of RuO_2

We now show that, given the magnetic crystal in Fig. 3.15, the band-structure of RuO_2 takes *the altermagnetic form*, Def. 3, concurrent with its d-wave symmetry in Fig. 3.17. We performed *ab initio* calculations with and without spin-orbit coupling, along the $\mathbf{\Gamma} - (\frac{\pi}{a}, \pm\frac{\pi}{b}, 0)$, blue-red path shown in Fig. 3.17. We used the same parameters as above, as described in Ch. 2.3.6. For the calculation with spin-orbit coupling, we set the Néel vector along the easy-axis **z**-direction, consistent with previous Néel vector measurements, transport, and DFT studies [77, 78, 3, 5].

Fig. 3.18(a) shows the band-structure for RuO_2 without spin-orbit coupling. It displays the expected symmetry, as every spin-up band along $\mathbf{\Gamma} - (\frac{\pi}{a}, \frac{\pi}{b}, 0)$ (red line in Fig. 3.17) has an opposite-spin partner band along the four-fold-rotated $\mathbf{\Gamma} - (\frac{\pi}{a}, -\frac{\pi}{b}, 0)$ path (blue line in Fig. 3.17). The bands meet at $\mathbf{\Gamma}$ and $(\frac{\pi}{a}, \pm\frac{\pi}{b}, 0)$, which are points

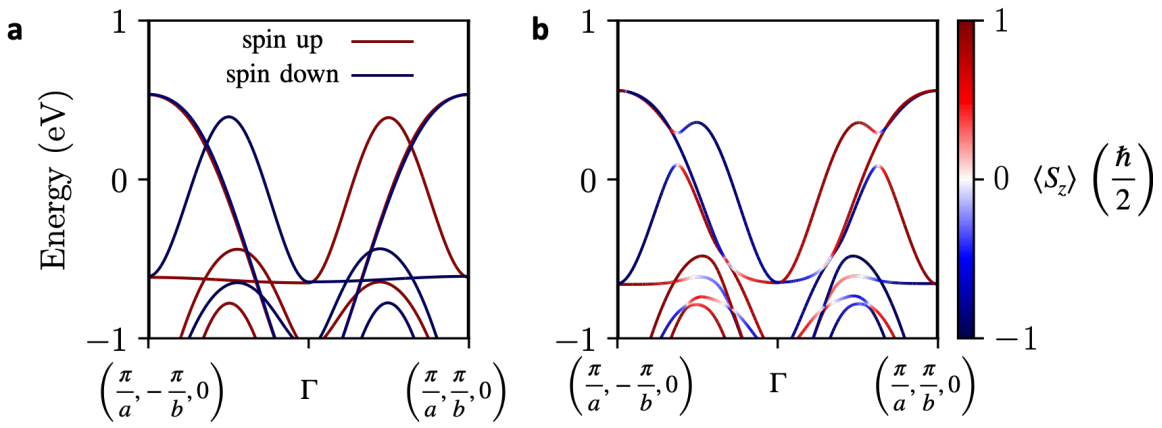

Figure 3.18: Altermagnetic RuO_2 energy bands. (a) Strong altermagnetic band structure (without spin-orbit coupling) along the mutually four-fold-rotated $\mathbf{\Gamma} - (\frac{\pi}{a}, \pm\frac{\pi}{b}, 0)$ paths shown in Fig. 3.17. It displays the expected altermagnetic form of spin splitting (Def. 3): the bands are degenerate when intersecting nodal planes at $\mathbf{\Gamma}$ and $(\frac{\pi}{a}, \pm\frac{\pi}{b}, 0)$, and spin-split away from them with a lowest-order term in the dispersion at $\mathbf{\Gamma}$ being quadratic, and the spin polarization alternates according to, e.g., $[C_2||C_{4z}]$ (relating each spin-up band along $\mathbf{\Gamma} - (\frac{\pi}{a}, \frac{\pi}{b}, 0)$ to a spin-down band along $\mathbf{\Gamma} - (\frac{\pi}{a}, -\frac{\pi}{b}, 0)$). (b) Turning on spin-orbit coupling deforms the energy bands, but strong altermagnetism still dominates the overall band dispersions. Figure adapted from [38], CC BY 4.0.

where two nodal planes meet at the center and edges of the Brillouin zone, respectively, as we recall from Fig. 3.17. They spin-split away from these points, forming

a $\sim 1\,\mathrm{eV}$ spin-splitting, consistent with previous studies [3]. The lowest order term in the dispersion around the $\mathbf{\Gamma}$ point is quadratic, in concurrence with the inversion symmetry due to collinear magnetism. Thus, we have shown that the electronic band structure takes *the altermagnetic form*, Def. 3, on the nonrelativistic level. Notably, the central two bands in this spin splitting fits well with the tight-binding model we developed in Ch. 2.2, see Fig. 2.4(b,d).

We also verify that adding spin-orbit coupling, shown in Fig. 3.18(b), deforms the bands, but the large band separation from the strong altermagnetic spin-splitting remains, as similarly to in MnTe and CrSb, the energy scale of the nonrelativistic, strong altermagnetism is larger than that of the relativistic, weak altermagnetism, even with Ru having a high atomic number of 44.

3.1.9 Discussion

Strong and weak altermagnetism can enrich both fundamental and applied fields in condensed matter physics research, with phenomenology ranging from nonrelativistic spin-polarized currents and giant magnetoresistance effects to Berry phase physics and anomalous Hall currents [12, 7, 9, 10, 11, 3, 174, 2, 112, 5, 172, 113]. Furthermore, strong and weak altermagnetism could be used to develop new device concepts combining advantageous proprieties unique to altermagnets. These properties include magnetic compensation and THz magnetization switching frequencies, typically reserved for antiferromagnets. Collinear antiferromagnets, however, do not possess LKSD on the nonrelativistic level; thus, they only host weak spin responses. Altermagnets combine magnetic compensation with spin responses as strong as those in ferromagnets. For example, spin-polarized currents in altermagnets exerting torques on ferromagnets and crystal anomalous Hall currents, have already been indicated in experiments with altermagnetic candidates RuO_2, MnTe, and Mn_5Si_3 [5, 113, 172, 9, 10, 11]. In ferromagnets, however, the strong spin response is a consequence of a net magnetic moment, while this net moment vanishes in altermagnets, allowing for device miniaturization.

3.2 P-wave (odd-parity-wave) magnetism

With the verification of the existence of even-parity-wave altermagnetism, a natural question to ask is whether we can also achieve odd-parity-wave magnetism shown in Fig. 3.1 by employing spin group theory. In this section, we answer this question in the affirmative: We first describe the symmetries of p-wave magnets and odd-parity-wave magnets generally, which arise from the magnetic order on the crystal. Then, we illustrate it on models and a real material candidate, CeNiAsO.

3.2.1 Spin-symmetry classification of even- and odd-parity-wave magnets on the nonrelativistic level

First, we recall the recent classification of collinear magnets [25] described from Ch. 1 and earlier in this chapter.

Collinear magnets can exhibit only even-parity-wave order. We have seen that all collinear magnets have inversion-symmetric band structures due to their $C_{2\perp}\mathcal{T}$ and SO(2) symmetries in the collinear spin-only group $\mathbf{r}_s^{\text{coll}}$, see Eq. (1.17) and Fig. 1.3. These two symmetries enforce an even-parity, effective inversion symmetry, which the energy bands obey, see Eqs. (1.19) and (1.20). Moreover, ferromagnets and altermagnets break $\mathcal{T}$ symmetry, not only in real space, but also in reciprocal space as shown in Fig. 3.1—the energy bands at opposite wavevectors have the same spin expectation value. Their electronic band structures thus exhibit an even-parity-wave, $\mathcal{T}$-broken spin-polarization.

For collinear magnets, if we write down the k.p Hamiltonian for the nonrelativistic bands around the $\mathbf{\Gamma}$-point, the wavevectors must obey the collinearity-induced inversion symmetry. Thus, only even-in-wavevector terms are allowed on the nonrelativistic level for altermagnets, as shown in Eq. (3.1) [25]. Hence, ferromagnets and altermagnets have even-in-wavevector, nonrelativistic spin-splitting dispersions around the $\mathbf{\Gamma}$-point, as we have demonstrated with altermagnetic models and ab initio calculations in Figs. 2.3, 2.4, and 3.18(a).

We also recall from Ch. 1 that ferromagnets have a net magnetization in real space and a corresponding s-wave-like spin polarization in reciprocal space. They belong to the type-I spin Laue group—$\mathbf{R}_s^{\text{I}}$—from Eq. (1.27) [25]. Altermagnets have d-, g-, and i-wave-modulated magnetization densities in real space corresponding to their crystal symmetries combining the two-fold spin-rotation (C_2) in spin space, with rotations and mirrors ($A\mathbf{H}$) in crystal space. In reciprocal space, the corresponding spin-polarization is d-, g-, or i-wave with 2, 4, and 6 spin-degenerate nodal planes, respectively, as shown in Fig. 1.9 [25, 1, 6]. They belong to the type-III spin Laue group—$\mathbf{R}_s^{\text{III}}$—from Eq. (1.29) [25].

Conventional collinear antiferromagnets also have the effective inversion symmetry in reciprocal space due to collinearity (collinear spin-only group $\mathbf{r}_s^{\text{coll}}$), which, combined with $\mathcal{T}\mathbf{t}$ enforces Kramers spin degeneracy in the entire Brillouin zone unless, e.g., spin-orbit coupling breaks the collinear symmetries, as we showed in Ch. 1.7. Alternatively, suppose an antiferromagnet has $\mathcal{PT}$ symmetry. In that case, both its nonrelativistic and relativistic band structures are Kramers spin degenerate in the entire Brillouin zone [95, 96], as we showed in Ch. 1.6.2.

Odd-parity-wave and p-wave magnets. The odd-parity-wave (p-wave) spin-polarization we are seeking in the electronic band structure breaks inversion symmetry, as exempli-

fied by a p-wave electronic band structure in Fig. 3.1. In contrast, the nonrelativistic electronic structure of ferromagnets and altermagnets preserve it and thus exhibit even-parity-wave order. Moreover, odd-parity-wave (p-wave) magnets preserve $\mathcal{T}$ symmetry in reciprocal space. Ferromagnets and altermagnets break it.

We now explain the symmetry guidelines for odd-parity-wave magnetism in general: *noncollinear spin order in real space, an inversion $\mathcal{P}$ symmetry breaking magnetic crystal, and time-reversal combined with real space translation symmetry $\mathcal{T}\mathbf{t}$. We also show that if additional criteria are satisfied, then we can achieve the long sought-after [39] p-wave-type odd-parity-wave magnetism. These additional criteria are: a spin group supporting a single symmetry-enforced nodal surface for p-wave magnetism, and, remarkably, coplanar real space order yielding a collinear spin polarization in the band structure.*

3.2.2 Symmetry guidelines for p-wave and odd-parity-wave magnetism

The following symmetry guidelines led us to identify p-wave and odd-parity-wave magnetism in general. For clarity, we enumerate each symmetry guideline and illustrate them in Fig. 3.19 on an example of a magnetic crystal and a corresponding electronic structure we seek.

The first three points in the following are our symmetry guidelines for *odd-parity-wave* magnetism in general and, nonrelativistically, enable lifting of the spin degeneracy and a time-reversal-symmetry-even spin polarizatioin $\mathcal{T}\mathbf{t}$-symmetric systems by noncollinear and inversion-breaking magnetic crystals as discussed in Ch. 1.7.

1. *Break inversion symmetry, $\mathcal{P} = [E||\mathcal{P}]$, in the magnetic crystal.* In Fig. 3.19, we show how the magnetic state breaks the inversion symmetry of the nonmagnetic crystal, marked by the black cross. We see in Fig. 3.19(a; 1) that the inverting around the black cross connects two spins that are not related by inversion, thus breaking the crystal's original inversion symmetry. It is necessary in order for the electronic structure we seek, illustrated in Fig. 3.19(b; 1), to break inversion symmetry. This symmetry breaking illustrates that we can achieve the odd-parity wave spin polarisation in an inversion symmetric crystal by breaking the inversion symmetry through phase transition into a magnetic state.

2. *Noncollinear magnetic order in the magnetic crystal*, illustrated in Fig. 3.19(a; 2). It needs to be noncollinear to break the effective inversion symmetry $[E||\mathcal{P}]$, which is present in collinear magnets due to SO(2) and $C_{2\perp}\mathcal{T}$ symmetries in the collinear spin-only-group $\mathbf{r}_s^{\text{coll}}$, as we recall from Fig. 1.3 and Eq. (1.19).
   Points 1 and 2 force the energy bands to break inversion symmetry, which can

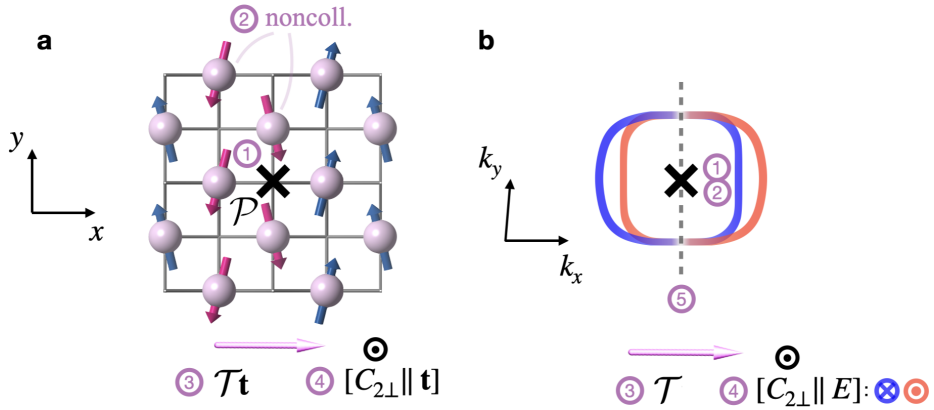

Figure 3.19: Summary of symmetry guidelines for odd-parity-wave and p-wave magnetism. The symmetries are illustrated (a) in real space and (b) in reciprocal space. (a) The red and blue arrows mark spin order in real space. Inversion-symmetry ($\mathcal{P} = [E||\mathcal{P}]$) breaking in the crystal (a; black cross, 1), as well as noncollinear magnetism (a; 2) are necessary to break inversion symmetry in the electronic structure (b; black cross, 1, 2). $\mathcal{T}\mathbf{t}$ symmetry (a; 3), marked by the magenta arrow, ensures $\mathcal{T}$ symmetry in the electronic structure (b; 3). 1-3 are symmetry guidelines for odd-parity-wave magnetism. Further enforcing the magnetic moments to be coplanar, as shown here in (a), the system has $[C_{2\perp}||\mathbf{t}]$ symmetry in real space (a; 4), where the rotation axis of $C_{2\perp}$ points out-of-plane with respect to the coplanar spins (a and b, indicated by the black circled dot). Remarkably, in reciprocal space, this symmetry ($[C_{2\perp}||E]$) enforces a collinear, out-of-plane spin polarization in reciprocal space (b; 4, blue circled cross and red circled dot). Lastly, the crystallographic spin group can enforce a single spin-degenerate nodal surface in reciprocal space, illustrated by the gray dashed line (b; 5).

be expressed as

$$\epsilon(\sigma, \mathbf{k}) \neq \epsilon(\sigma, -\mathbf{k}). \tag{3.10}$$

where σ is a spin index. If, on the contrary, either 1 or 2 is not satisfied, then the bands become inversion symmetric, even-parity-wave. Thus, both 1 and 2 are needed for odd-parity-wave magnetism.

3. *Preserve $\mathcal{T}\mathbf{t}$ symmetry in the magnetic crystal.* $\mathcal{T}$ is time-reversal symmetry acting in both spin and crystal space. $\mathbf{t}$ is a translation illustrated in Fig. 3.19(a; 3) by the magenta arrow, and the combined symmetry with $\mathcal{T}$ relates the red and blue spins. This symmetry allows the electronic band structure to have the necessary $\mathcal{T}$ symmetry indicated in Fig. 3.19(b; 3) by the magenta arrow, enforcing the spin expectation value to be equal and opposite for opposite wavevectors:

$$\epsilon(\sigma, \mathbf{k}) = \epsilon(-\sigma, -\mathbf{k}). \tag{3.11}$$

Note that $\mathcal{T}\mathbf{t}$ can be present in both *coplanar and noncoplanar* systems.

We can further divide odd-parity-wave magnets into coplanar and noncoplanar (in real space) systems. Remarkably, we find that coplanar (in real space) odd-parity-wave magnets have collinear (in reciprocal space) spin-polarized electronic structures due to a particular emerging symmetry:

4. *Preserve* $[C_{2\perp}||\mathbf{t}]$ *spin symmetry in the magnetic crystal* ($C_{2\perp}$ is a two-fold spin-space rotation around an axis oriented perpendicular all spins in the crystal, and $\mathbf{t}$ is a translation in real space). $\mathbf{t}$ is shown by the magenta arrow in Fig. 3.19(a; 4), and the out-of-plane ($\perp$) rotation axis by the black circled dot. $[C_{2\perp}||\mathbf{t}]$ can only be present in *coplanar* (and collinear) systems because the $C_{2\perp}$ rotation axis is perpendicular to all spins in real space (if noncoplanar, such an axis would not exist; recall Fig. 1.6). Remarkably, $[C_{2\perp}||\mathbf{t}]$ yields a collinear spin-polarization in reciprocal space, $\sigma_\perp$, along the rotation axis of $C_{2\perp}$. Now, the corresponding constrain on the energy bands can be expressed as:

$$\epsilon(\sigma_\perp, \mathbf{k}) = \epsilon(-\sigma_\perp, -\mathbf{k}). \tag{3.12}$$

The symmetry rules 1.-3. ensure an inversion-broken, time-reversal symmetric band structure, which can, in general, exhibit an odd number of spin degenerate/unpolarised nodal surfaces. To additionally symmetry-enforce p-wave magnetism with a single spin degenerate/unpolarized nodal surface, the following criterion must be satisfied.

5. *Have a single, symmetry-enforced nodal surface through the* $\mathbf{\Gamma}$*-point (center of the Brillouin zone) where the spin polarization vanishes.* Such a spin-degenerate nodal surface is indicated by the dashed line in Fig. 3.19(b, 5). It can be enforced in the crystallographic spin group by symmetries involving rotations in both spin and crystal space, which can be proper or improper, as described in Ch. 1.8.

We emphasize again that if the magnetic crystal is collinear—it does not satisfy guideline 2.—then its nonrelativistic electronic structure does not break the inversion symmetry $[E||\mathcal{P}]$ enforced by the collinear spin-only group $\mathbf{r}_s^{\text{coll}}$, and will be spin-degenerate in the entire Brillouin zone because the system has both $[E||\mathcal{P}]$ and $\mathcal{T}\mathbf{t}$ symmetries as we recall from Theorem 2. Also note that $\mathcal{PT}$ systems preserve time-reversal symmetry in their electronic band structure, but they are Kramers spin degenerate by Theorem 1 and do not allow the bands to spin-polarize; thus, they do not allow for odd-parity-wave magnetism. We also note that the $\mathcal{T}\mathbf{t}$ and $[C_{2\perp}||\mathbf{t}]$ symmetries ensure zero net magnetization in the system.

In the following, we discuss the symmetry guidelines in more detail and their consequences for the spin-polarization and dispersion of the electronic structure. First, we note that the energy dispersion is odd-in-wavevector in odd-parity-wave magnets. Then, we will show that $[C_{2\perp}||\mathbf{t}]$ symmetry corresponds to a combination of the symmetry $C_{2\perp}\mathcal{T}$ of coplanar systems and $\mathcal{T}\mathbf{t}$ symmetry; how it enforces out-of-plane

collinearity in contrast to altermagnets and ferromagnets on the nonrelativistic level where the collinearity aligns with the real-space collinear spin quantization axis; and why noncoplanar systems break it.

3.2.3 Energy dispersion in odd-parity-wave magnets

The energy bands in our odd-parity-wave magnets and p-wave magnets break inversion symmetry and preserve $\mathcal{T}$, as shown in Eqs. (3.10)-(3.11). Since it breaks inversion symmetry, only odd terms are allowed in a k.p expansion around the $\mathbf{\Gamma}$-point. For example, k can be allowed because inverting k yields $-k$, which breaks inversion as imposed by the inversion-breaking. Even terms are not allowed because, for example, inverting k^2 yields $(-k)^2 = k^2$ which preserves inversion and is thus not allowed. Therefore, the band structure-dispersion around the $\mathbf{\Gamma}$-point is odd in the wavevector in odd-parity-wave magnets, which we can express as follows:

$$H^{\alpha\beta\gamma}_{\mathbf{k}\sim\mathbf{\Gamma}}(k_x,k_y,k_z) \sim \Delta'\mathbf{d}'\cdot\boldsymbol{\sigma}\, k_l^\alpha k_m^\beta k_n^\gamma, \quad \alpha+\beta+\gamma \geq 1 \text{ is an odd integer; } l,m,n = x,y,z \tag{3.13}$$

Here, Δ' parametrizes the size and sign of the spin splitting, $\mathbf{d}'$ is a unit vector along a given spin quantization axis, $\boldsymbol{\sigma}$ is a vector with the spin Pauli matrices, the term is odd in wavevectors $k_l^\alpha k_m^\beta k_n^\gamma$ as $\alpha+\beta+\gamma$ is an odd integer, and summation over the indices is implied. For example, when the spin-split bands disperse linearly $\sim k$ around $\mathbf{\Gamma}$, then $\alpha+\beta+\gamma = 1$ and the bands are thus odd in the wavevector. We will see examples of this later in our models and DFT calculations.

3.2.4 Collinear out-of-plane spin polarization in $[C_{2\perp}||\mathbf{t}]$ systems

$[C_{2\perp}||\mathbf{t}]$ symmetry from guideline 4., combined with crystal inversion breaking and noncollinearity from guidelines 1. and 2., corresponds to odd-parity-wave magnetism in *coplanar in real space* magnetic crystals, hosting a *collinear in reciprocal space* spin-polarized electronic band structure. We will show that $[C_{2\perp}||\mathbf{t}]$ symmetry leads to the collinear spin polarization in the band structure.

Fig. 3.20 shows a generic spin order that obeys $[C_{2\perp}||\mathbf{t}]$ symmetry. For brevity, we have also translated the noncollinear spins into two common origins. The rotation axis of $[C_{2\perp}||E]$ points along the gray out-of-plane arrow with respect to the coplanar spins. Being coplanar, it also preserves $C_{2\perp}\mathcal{T}$ symmetry while it breaks SO(2) symmetry, as we recall from Fig. 1.5.

Note that the spin symmetry $[C_{2\perp}||\mathbf{t}]$ is $[C_{2\perp}||E]$ in momentum space because the translation $[E||\mathbf{t}]$ does not affect the band structure and its spin expectation value.

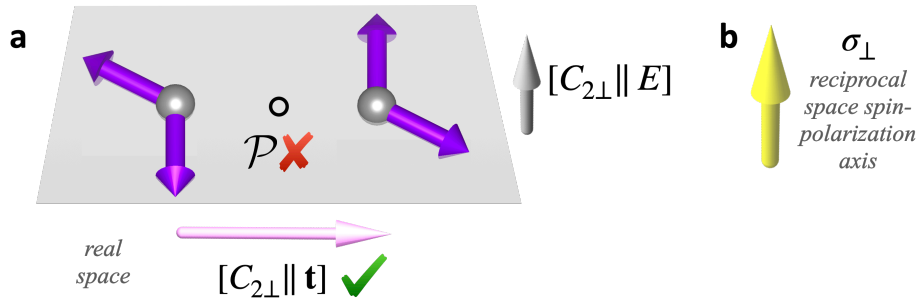

Figure 3.20: General symmetries of coplanar odd-parity-wave magnets, hosting collinear spin polarization in reciprocal space. (a) Generic coplanar set of spins in real space. To keep it general, we do not show the spins on a specific lattice but rather emphasize that they are coplanar and related by the necessary symmetries. We note that the spin order has a minimum of four spins, as shown here, but can also have more spins as long as it obeys the necessary symmetries. This spin order obeys the necessary symmetries from guidelines 1.-4.: It breaks crystal inversion $[E||\mathcal{P}]$ (guideline 1.), as inverting the leftmost spins around the central point, shown by the black circle, brings them onto the rightmost spins, which are not the same. It is noncollinear (guideline 2.). It is coplanar and preserves $[C_{2\perp}||\mathbf{t}]$ symmetry (guideline 4.) indicated by the magenta arrow, relating spins with opposite directions. The gray arrow shows the $[C_{2\perp}||E]$ rotation axis, which is out-of-plane with respect to the coplanar spins lying in the gray plane. Due to the $[C_{2\perp}||\mathbf{t}]$ symmetry, the reciprocal space spin order has a single spin-polarization axis, $\sigma_\perp$, as shown in (b).

In other words, the translation does not affect the momentum-space odd-parity-wave nature of the magnetic order.

We now show that the $[C_{2\perp}||\mathbf{t}]$ symmetry enforces the spin-polarization to be *collinear* in the band structure. We have indicated this collinearity by the out-of-plane spin polarization in Fig. 3.19(b) shown by the blue circled cross and red circled dot, and in Fig. 3.20(b) by the yellow arrow denoted *reciprocal space spin polarization axis* $\sigma_\perp$. To show that the band structure is collinear, let x and y be the axes that are in-plane with the coplanar spins, and let $z = \perp$ be the out-of-plane axis. We now apply $[C_{2\perp}||E] = [C_{2z}||E]$ to spin components with arbitrary values s_x, s_y, and s_z, which yields

$$\begin{aligned} [C_{2\perp}||E]s_z &= s_z \\ [C_{2\perp}||E]s_x &= -s_x = s_x = 0 = s_y. \end{aligned} \tag{3.14}$$

In the last line, we used the fact that $[C_{2\perp}||E]$ is a symmetry in the second equality, and in the last equality, we note that the rotation is analogous for s_x and s_y. We see that the only non-zero component is the out-of-plane s_z component, thus making the spin polarization collinear and pointing parallel or antiparallel to the axis $\sigma_\perp$. This derivation generalizes to an arbitrary orientation of the $[C_{2\perp}||E]$ symmetry, for example, $\perp = x, y$ or any other orientation perpendicular to the coplanar spins.

Unconventional out-of-plane spin-polarization axis in $[C_{2\perp}||\mathbf{t}]$ *systems.* We highlight that the spin-polarization axis here is unconventional, as it is *perpendicular to the real-space spin order* being protected by the effective $[C_{2\perp}||E]$ symmetry in reciprocal space. In altermagnets and ferromagnets, the spin-polarization axis is *parallel to the real-space spin order* on the nonrelativistic level, because it is protected by the SO(2) and $C_{2\perp}\mathcal{T}$ spin-only group symmetries, as we have demonstrated throughout our DFT and model calculations in Chs. 3.1 and 2.2.

We note that it is also possible to have a single spin-polarization axis of reciprocal-space spin textures that arise from a combination of altermagnetism and relativistic spin-orbit coupling in MnTe [30], or from relativistic spin-orbit coupling without spontaneous magnetic real space order [167, 175]. However, in our odd-parity-wave magnets, the spontaneous magnetic crystal order symmetry-protects the spin-polarization axis throughout the Brillouin zone. In contrast, the collinear spin polarization in the weak altermagnetic mechanism is only symmetry-protected in the $k_z = 0$ plane as we showed in Ch. 3.1.3 [30], while the other relativistic spin-orbit coupling mechanisms require fine-tuning spin-orbit-coupling strength parameters [167], or the spin order is approximately collinear only around high symmetry points in the Brillouin zone [175].

In summary, we have shown that coplanar odd-parity-wave magnets with $[C_{2\perp}||\mathbf{t}]$ symmetry have nonrelativistic electronic band structures with spin polarizations that are, unconventionally, *collinear and point perpendicular to the noncollinear-coplanar spin order in real space* due to this symmetry.

3.2.5 Noncollinear spin texture in noncoplanar systems

With our symmetry guidelines, we have established that our coplanar odd-parity-wave magnets have $[C_{2\perp}||\mathbf{t}]$ symmetry, and now we will describe what happens when the system is instead noncoplanar. We illustrate a generic spin order for noncoplanar odd-parity-wave magnetism in Fig. 3.21, similarly to the coplanar-order-illustration in Fig. 3.20, except it is now noncoplanar. Note that, in order to be noncoplanar while obeying $\mathcal{T}\mathbf{t}$ symmetry, the unit cell must have at least six spins, while coplanar odd-parity-wave magnets have at least four.

If we relax the coplanarity condition, the system will be noncoplanar instead. It, therefore, breaks $[C_{2\perp}||\mathbf{t}]$ symmetry, as indicated in Fig. 3.21, and $C_{2\perp}\mathcal{T}$, as we recall from Fig. 1.6(b). Noncoplanar odd-parity-wave magnets thus do not have the corresponding, single out-of-plane spin polarization axis in reciprocal space from $[C_{2\perp}||\mathbf{t}]$ symmetry, and as a result, the reciprocal space spin texture can in general be noncollinear.

The odd-parity-wave, noncollinear spin texture can be viewed as a nonrelativistic counterpart of odd-parity spin textures arising from relativistic spin-orbit coupling.

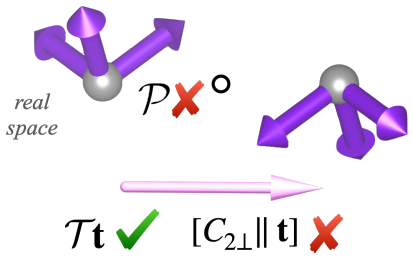

Figure 3.21: General symmetries of noncoplanar odd-parity-wave magnets. It is analogous to in Fig. 3.20 except, now, the real-space spin order is noncoplanar, breaking $[C_{2\perp}||\mathbf{t}]$ symmetry. As a result, $[C_{2\perp}||\mathbf{t}]$ no longer enforces the reciprocal-space spin polarization to be collinear.

However, a significant difference here is that it arises from the Coulomb interaction, and therefore, we generally expect the resulting spin-splittings to be larger, as we discussed in Ch. 1.5. This generally expected larger scale also applies to coplanar odd-parity-wave magnets.

3.2.6 Coplanar and noncoplanar Kagome model of p-wave collinear spin polarization and noncollinear spin texture

We now illustrate the realization of p-wave magnetism for coplanar and noncoplanar models on a Kagome lattice [93, 176]. Fig. 3.22(a) shows our tight-binding model for the coplanar case. Here, the $[C_{2\perp}||\mathbf{t}]$ symmetry, shown by the magenta arrow, doubles the unit cell compared to the conventional nonmagnetic Kagome lattice and magnetic Kagome models without this symmetry. The lattice vectors are therefore $\mathbf{a}_1 = (2, 0)$ and $\mathbf{a}_2 = (1/2, \sqrt{3}/2)$, where $\mathbf{a}_1$ is twice the length of the nonmagnetic Kagome lattice.

This model satisfies the guidelines for coplanar odd-parity-wave magnets. It breaks crystal inversion symmetry $\mathcal{P}$ from guideline 1, highlighted by the inversion-symmetry breaking in the black circled point in Fig. 3.22(a). This point is an inversion center in the nonmagnetic Kagome lattice, but it is here broken by the magnetic order. The magnetic crystal is noncollinear and thus satisfies guideline 2., and it preserves $[C_{2\perp}||\mathbf{t}]$ and thus satisfies guideline 4. Such a Kagome system can be found in real materials, as we will see in Sec. 3.2.8.

The tight-binding Hamiltonian for this structure is

$$H = \sum_i \mathbf{J} \cdot \boldsymbol{\sigma}\, c_i^\dagger c_i + \sum_{<ij>} t\, c_i^\dagger c_j. \tag{3.15}$$

The first term is the local onsite magnetic exchange, where $\mathbf{J}$ parametrizes the size and direction of the exchange, and $\boldsymbol{\sigma} = (\sigma_x, \sigma_y, \sigma_z)$ are the three spin Pauli matrices.

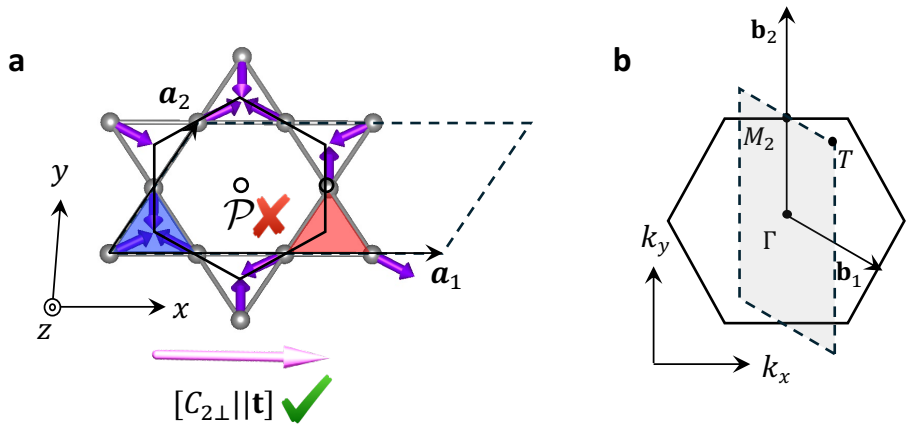

Figure 3.22: Odd-parity-wave model on a Kagome lattice. (a) Here, we show the model with noncollinear-coplanar spins indicated by the purple arrows, where noncollinearity is guideline 2. It breaks crystal inversion $\mathcal{P} = [E||\mathcal{P}]$ from guideline 1. of the corresponding nonmagnetic Kagome lattice. It preserves $[C_{2\perp}||\mathbf{t}]$ symmetry, indicated by the magenta arrow, which relates the spins in the blue triangle to those in the red triangle and doubles the unit cell compared to the nonmagnetic Kagome lattice. Thus, it satisfies guideline 4. The unit cell, shown by dashed lines, is spanned by the lattice vectors $\mathbf{a}_1$ and $\mathbf{a}_2$, shown by black arrows, and is twice the size of the unit cell of the nonmagnetic crystal, shown by the black-lined hexagon. (b) The Brillouin zone of the model, shown by the dashed-bordered gray region, compared to a Brillouin zone without the doubled unit cell, shown by the black-lined hexagon. The figure is adapted from [93], CC BY 4.0.

The second term is a normal hopping connecting nearest neighbors on the lattice, with a hopping amplitude t.

Fig. 3.22(b) shows the first Brillouin zone for the model (dashed parallelogram). It is spanned by the reciprocal vectors $\mathbf{b}_1 = (\pi, -\pi/\sqrt{3})$ and $\mathbf{b}_2 = (0, 4\pi/\sqrt{3})$. For comparison, the hexagon in Fig. 3.22(b) shows the first Brillouin zone of a Kagome lattice that does not have the doubling of the unit cell from $[C_{2\perp}||\mathbf{t}]$ symmetry.

In the following, we use the parameters $J = |t|$, and we implement the model and diagonalize the Hamiltonian numerically using the Pythtb package version 1.7.2 [121].

P-wave collinear spin-polarization in coplanar model

We first consider the coplanar spin configuration for the model from Fig. 3.22(a). Fig. 3.23 shows the corresponding collinear, odd-parity-wave spin-texture in reciprocal space for this coplanar configuration.

Iso-energy cut with collinear p-wave spin polarization. Fig. 3.23(a) shows an iso-energy surface calculated for the energy $-1.65\,t$. As expected from our symmetry analysis from Fig. 3.20 and Eq. (3.14), the spin polarization in reciprocal space obeys

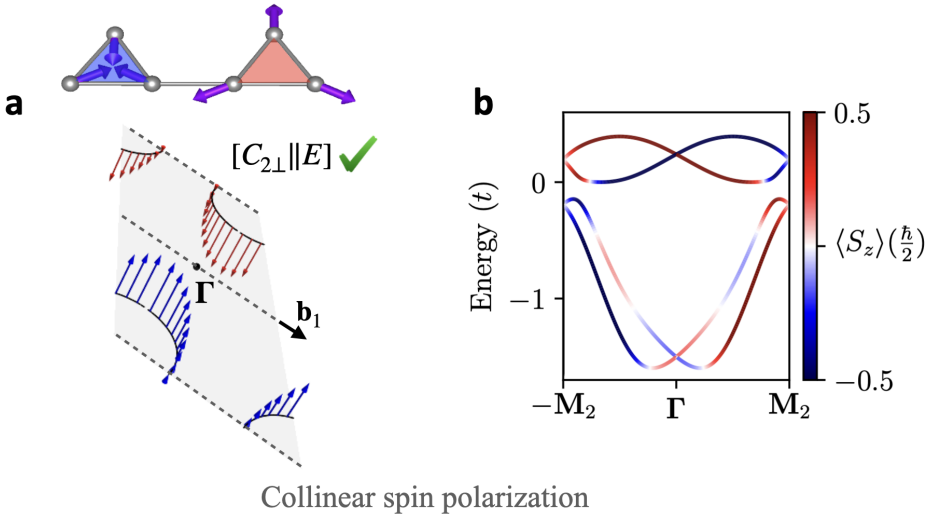

Figure 3.23: P-wave spin polarization in reciprocal space for the coplanar model. It satisfies the symmetry guidelines for p-wave magnetism. Being coplanar, it preserves the effective $[C_{2\perp}||E]$ symmetry in spin and reciprocal space from guideline 4. This symmetry ensures the spin polarization is collinear and out-of-plane, as is evident from the iso-energy cut in (a) and from the energy bands in (b) where $\langle S_z\rangle$ is the only non-zero spin component. The iso-energy cut in (a) hosts nodal lines parallel to the $\mathbf{b}_1$-vector at the edges of the Brillouin zone, shown by the top and bottom dashed lines, and through $\mathbf{\Gamma}$, the middle dashed line, thus it is p-wave. The bands disperse linearly around the $\mathbf{\Gamma}$-point, as is expected due to the crystal inversion symmetry breaking from guideline 1. and Eq. (3.13). The figure is adapted from [93], CC BY 4.0.

the effective $[C_{2\perp}||E]$ symmetry and is thus collinear along an axis out-of-plane with respect to the coplanar, real-space spin order.

This spin polarization starkly contrasts altermagnets and ferromagnets. Firstly, it preserves $\mathcal{T}$ and breaks inversion. We can see this by bringing each point with red spin on the iso-energy surface in Fig. 3.23(a) onto a point of opposite wavevector, and see that the spin changes sign to a blue spin according to $\epsilon_n(\sigma_\perp, \mathbf{k}) = \epsilon_n(-\sigma_\perp, -\mathbf{k})$ as in Eq. (3.12). By contrast, the iso-energy cuts in altermagnets and ferromagnets always break $\mathcal{T}$ and preserve inversion, so opposite-wavevector spins are identical according to $\epsilon_n(\sigma_\parallel, \mathbf{k}) = \epsilon_n(\sigma_\parallel, -\mathbf{k})$as in Eq. (1.20), where $\sigma_\parallel$ is aligned with the collinear Néel vector axis on the nonrelativistic level. Secondly, the size of the spin-polarization varies along the iso-energy cut, while in collinear magnets, it does not, since spin is a good quantum number in collinear systems in the nonrelativistic limit as discussed in Ch. 1.1.1.

Inspecting the iso-energy cut in Fig. 3.23(a), it is evident that it has nodes at the edges of the Brillouin zone parallel to the $\mathbf{b}_1$-vector where the spin expectation value goes to zero and changes sign between red and blue on opposite sides of these edges. However, it does not have nodes at the other edges parallel to the $\mathbf{b}_2$-vector, because

the spin expectation value there is finite and does not change sign. As we show in Appendix D, a spin symmetry enforces a nodal line along the $\mathbf{b}_1$-vector crossing the $\mathbf{\Gamma}$-point, and combined with the periodicity of the Brillouin zone, it also enforces nodal lines at the Brillouin zone edges that are parallel to the $\mathbf{b}_1$-vector. The model is, therefore, p-wave: a single nodal line goes through $\mathbf{\Gamma}$.

Odd-parity-wave electronic band structure. Fig. 3.23(b) shows the corresponding energy bands for the model. We can see that the bands preserve $\mathcal{T}$ symmetry for every energy because $\langle S_z \rangle$ changes sign if we invert a wavevector around $\mathbf{\Gamma}$. Secondly, the energy bands disperse linearly around $\mathbf{\Gamma}$ and is thus odd in the wavevector. This is concurrent with the breaking of crystal inversion symmetry as described in Eq. (3.13) with $\sim k$.

P-wave spin texture in noncoplanar model

We now consider the same model, but where the spin configuration is made noncoplanar. Fig. 3.24 shows the noncoplanar spin order (Fig. 3.24(a,inset)) and corresponding spin texture of the electronic band structure.

Iso-energy cut with coplanar, p-wave spin texture. Similarly to the coplanar order, this noncoplanar order fulfills the symmetry guidelines 1.-3. for odd-parity-wave magnetism, but it breaks the $[C_{2\perp}||\mathbf{t}]$ symmetry. Due to this symmetry-breaking, the iso-energy cuts in Fig. 3.24(a) have a noncollinear spin texture, e.g., as shown in Fig. 3.24(a) around $\mathbf{\Gamma}$ for the energy $-1.39\,t$ (a, left) and around a time-reversal invariant momentum $\mathbf{T}$ for the energy $0.65\,t$ (a, right). The spin texture preserves $\mathcal{T}$ for all wavevectors, similarly to the coplanar model.

Fig. 3.24(a, left) shows that the spin-texture is p-wave: As evident from the central band cut around the $\mathbf{\Gamma}$-point, the spin polarization winds once and has two nodes with zero spin expectation value. We also see a winding around the $\mathbf{T}$ point at the Brillouin zone edge in Fig. 3.24(a, right), but no nodes where the spin expectation value goes to zero.

The spin texture winding once is similar to Rashba and Dresselhaus spin-orbit coupling. However, it is different as it is not helically locked. For example, if we trace the spins along the iso-energy cuts in Fig. 3.24, the spin directions change clockwise and anti-clockwise, and the phase and magnitude vary, making the bands more anisotropic. This makes our odd-parity-wave spin texture different from, e.g., Rashba spin-orbit coupling, not only because the latter is relativistic and the former originates from magnetic exchange but also in terms of the spin texture in reciprocal space. For comparison, we show a helically locked Rashba spin texture in Fig. 3.25.

Note that our p-wave spin texture here is coplanar, even though the real-space spin texture is noncoplanar, due to an additional symmetry in the system, which we will now describe.

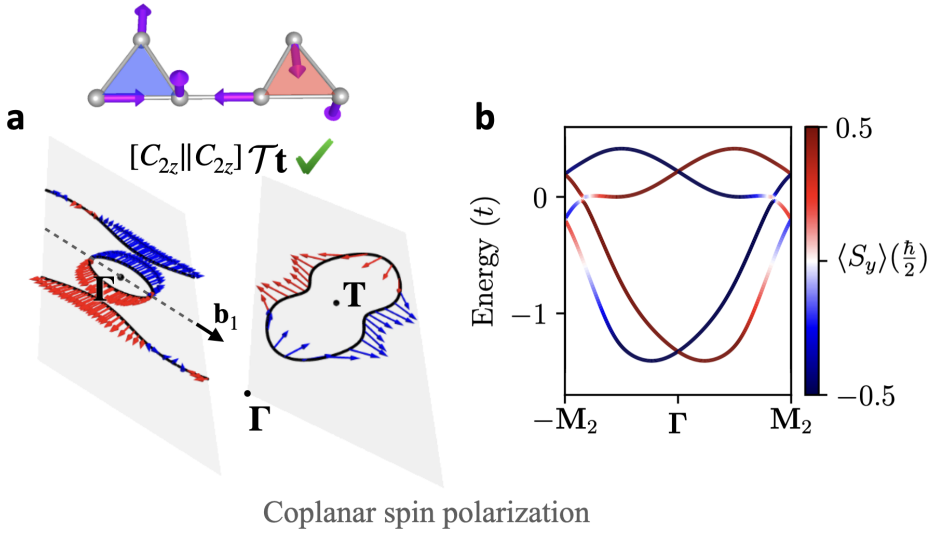

Figure 3.24: P-wave spin polarization in reciprocal space for the noncoplanar model. Similarly to the coplanar model, it satisfies the p-wave symmetry guidelines. (a) Being noncollinear-noncoplanar as shown in the inset in (a), it breaks the effective $[C_{2\perp}||E]$ symmetry in spin and reciprocal space otherwise present in coplanar odd-parity-wave magnets. Thus, the spin texture here is not collinear as in the coplanar model. However, it preserves $\mathcal{T}\mathbf{t}$ from guideline 3. and an additional $[C_{2z}||C_{2z}]$ symmetry, which combined enforce the *reciprocal space spin texture to be coplanar*, as shown in the iso-energy cuts where now the out-of-plane component $\langle S_z\rangle = 0$. The iso-energy cut shows a p-wave form, winding once around $\mathbf{\Gamma}$ and with two nodes where the spin polarization is zero. (b) Similarly to the coplanar model, the bands disperse linearly around the $\mathbf{\Gamma}$-point, as expected from the crystal inversion symmetry breaking from guideline 1. Figure adapted from [93], CC BY 4.0.

Symmetry-protection of the coplanar spin texture in our model. The symmetry that protects the coplanarity of the momentum-space spin texture in our model is the combined symmetry

$$[C_{2z}||C_{2z}]\,\mathcal{T}\mathbf{t} \tag{3.16}$$

where $[C_{2z}||E]$ is a spin-rotation around the out-of-plane z-axis. Note that here, this symmetry is particular to our model, while the $[C_{2\perp}||\mathbf{t}]$ symmetry protecting collinear spin polarization discussed above applies to all our coplanar odd-parity-wave magnets.

Before we show why the symmetry in Eq. (3.16) implies coplanarity, we first show in Fig. 3.26 that $[C_{2z}||C_{2z}]$ itself is a symmetry.

The $[C_{2z}||C_{2z}]$ symmetry. First, $[C_{2z}||E]$ rotates every in-plane spin in Fig. 3.26(a), which are parallel to the x and y axes, while the out-of-plane spins along the z axis are unchanged. This results in the spin order in Fig. 3.26(b). Then, the $[E||C_{2z}]$ crystal rotation around the gray rotation axis shown in Fig. 3.26(b) rotates the magnetic crystal site positions (and not the spins themselves), as indicated by the curved gray arrow. This rotation reverts the crystal to its original form in Fig. 3.26(a). Thus,

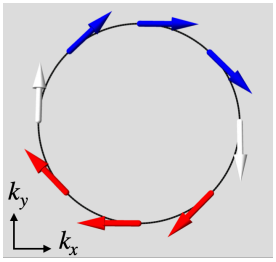

Figure 3.25: Relativistic Rashba spin texture. It is helically locked, in contrast to our odd-parity-wave spin texture, which is not.

$[C_{2z}||C_{2z}]$ is a symmetry.

Symmetry-enforced coplanarity. Now, we show that the combination of this $[C_{2z}||C_{2z}]$ symmetry with $\mathcal{T}\mathbf{t}$ symmetry protects the coplanarity of the reciprocal-space spin texture. We can show this by applying them to the wavevectors and spins as follows:

$$\begin{aligned}(k_x, k_y, s_x, s_y, s_z) &= [C_{2z}||C_{2z}](k_x, k_y, s_x, s_y, s_z) \\ &= (-k_x, -k_y, -s_x, -s_y, s_z) \\ &\overset{\mathcal{T}\mathbf{t}}{=} (k_x, k_y, s_x, s_y, -s_z),\end{aligned} \tag{3.17}$$

where, in the last equality, we applied $\mathcal{T}\mathbf{t}$ and used that $\mathcal{T}\mathbf{t} \sim \mathcal{T}$ in reciprocal space. Comparing the first and last expressions, we see that $s_z = 0$, and thus, the spin texture is coplanar in reciprocal space.

Energy bands of collinear model with $\mathcal{T}\mathbf{t}$ symmetry is spin degenerate

We also verify that a collinear spin texture with $\mathcal{T}\mathbf{t}$ is spin degenerate as shown in Fig. 3.27. The reason for the spin degeneracy is that the collinear model shown in Fig. 3.27(a) only satisfies crystal inversion symmetry breaking from guideline 1. and $\mathcal{T}\mathbf{t}$ symmetry from guideline 3., while it does not satisfy guideline 2., which is noncollinearity. Being collinear, it preserves the effective $[E||\mathcal{P}]$ crystal inversion symmetry induced by the collinear spin-only group symmetry $C_{2\perp}\mathcal{T} \times \mathrm{SO}(2) \in \mathbf{r}_s^{\mathrm{coll}}$ as we recall from Eq. (1.19). Thus, the system preserves the combined $C_{2\perp}\mathcal{T} \times \mathrm{SO}(2) \times \mathcal{T}\mathbf{t}$ symmetry, which by Theorem 2 enforces spin degeneracy of the energy bands as we showed in Ch. 1.7. In simple terms, the only way in which the energy bands in Fig. 3.27(b) can preserve time-reversal $\mathcal{T}$ and inversion $[E||\mathcal{P}]$ symmetries simultaneously is by being doubly spin-degenerate, which they are.

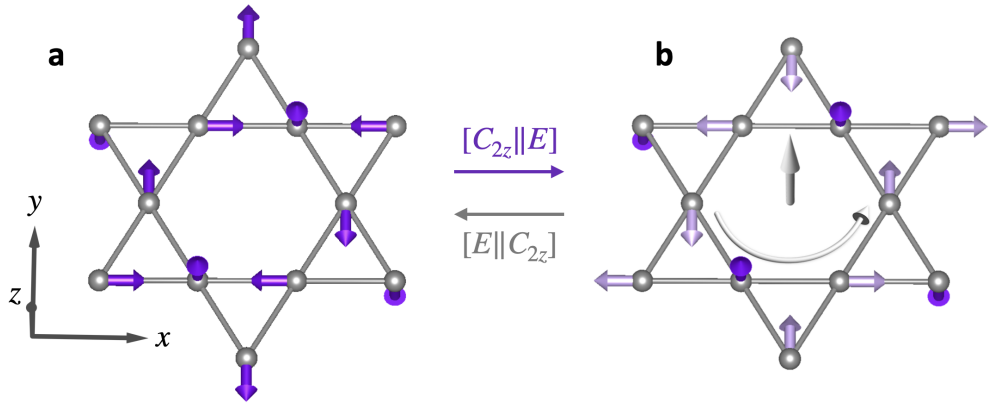

Figure 3.26: $[C_{2z}||C_{2z}]$ is a symmetry of the noncoplanar, odd-parity-wave model. (a) Original spin order. (b) Spin order after $[C_{2z}||E]$. $[C_{2z}||E]$ rotates all in-plane moments by a two-fold rotation, resulting in the light purple colored spins. The gray out-of-plane arrow is the rotation axis for the crystal rotation, $[E||C_{2z}]$, which rotates the crystal sites but not the spins. For example, the curved gray arrow shows that the left spin, pointing along $-y$, ends up on the site on the right when rotating by $[E||C_{2z}]$, thus reverting it to its original spin configuration from (a). Repeating this, we see that all sites and accompanying spins revert to their original configuration in (a), thus showing that $[C_{2z}||C_{2z}]$ is a symmetry.

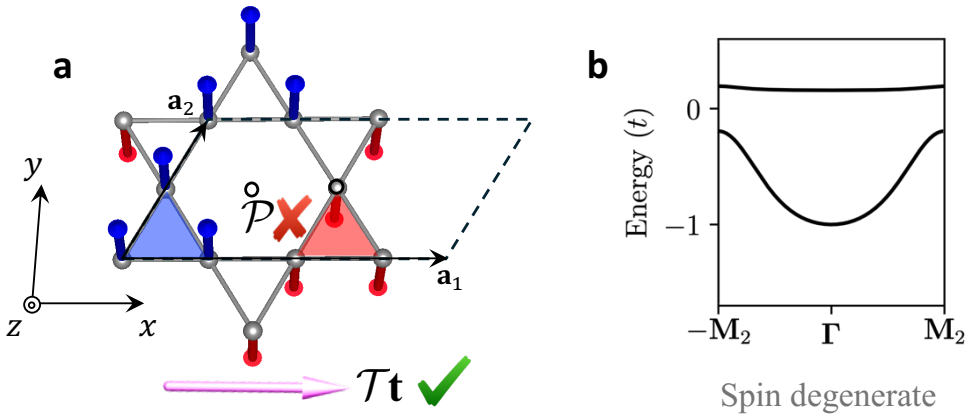

Figure 3.27: Collinear model with $\mathcal{T}\mathbf{t}$ symmetry has spin-degenerate energy bands. It does not satisfy all symmetry guidelines for odd-parity-wave magnetism. (a) The model preserves $\mathcal{T}\mathbf{t}$ symmetry from guideline 3. and breaks crystal inversion symmetry $\mathcal{P}$ from guideline 1. However, it is collinear and, therefore, it does not satisfy guideline 2. As a result, it preserves collinearity-induced $[E||\mathcal{P}]$ inversion symmetry of the energy bands, which together with $\mathcal{T}\mathbf{t}$ symmetry enforces spin degeneracy of the energy bands, as shown in (b), as we recall from Theorem 2. Figure adapted from [93], CC BY 4.0.

3.2.7 P-wave material candidate CeNiAsO

Using symmetry analysis and density functional theory, we now demonstrate collinear p-wave spin polarization and giant spin-split energy bands manifesting in a coplanar p-wave material candidate, CeNiAsO.

Magnetic crystal structure

The magnetic crystal structure of CeNiAsO is shown here in Fig. 3.28, which correspond to its experimentally reported magnetic crystal below $7.6\,K$ [44]. Its lattice parameters are $a = 8.124\,\text{Å}$, $b = 4.062\,\text{Å}$, and $c = 8.106\,\text{Å}$ [44]. It can be considered as quasi-two-dimensional Ce-O and As-Ni layers that stack on top of each other along the z direction, as shown in Fig. 3.28(a). The magnetic unit cell shown in Fig. 3.28(b) is double that of the corresponding nonmagnetic unit cell shown in the inset, thanks to the $[C_{2\perp}||\mathbf{t}]$ symmetry indicated by the black straight arrow. $[C_{2\perp}||\mathbf{t}]$ relates sites with opposite sublattice magnetizations, as indicated by red versus blue magnetization arrows. The magnetic moments are coplanar and lie in the xy-plane, which means CeNiAsO preserves $[C_{2z}||\mathbf{t}]$ symmetry with $C_{2\perp} = C_{2z}$, where the $\perp = z$ rotation axis points out-of-plane as indicated by the black circled dot in Fig. 3.28(b). Lastly, the magnetic crystal breaks inversion symmetry, $[E||\mathcal{P}]$, as highlighted in Fig. 3.28(b) by the black cross. Thus, it satisfies all the symmetry guidelines 1. through 4., making it a candidate material for hosting odd-parity, collinear spin polarization in reciprocal space.

In addition, to be p-wave, the electronic structure must have a single symmetry-enforced nodal surface by guideline 5. To determine this surface, we write down the spin space group for the material. By following the algorithm in [171, 86], we obtain the following symmetry elements of the nontrivial spin group: $[E||E]$, $[E||M_y\boldsymbol{t}_{0.5b}]$, $[C_{2z}||\boldsymbol{t}_{0.5a}]$, $[C_{2z}||M_y\boldsymbol{t}_{0.5a+0.5b}]$, $[C_{2x}||C_{2y}\boldsymbol{t}_{0.5b}]$, $[C_{2y}||C_{2y}\boldsymbol{t}_{0.5a+0.5b}]$, $[C_{2x}||P]$, $[C_{2y}||P\boldsymbol{t}_{0.5a}]$. We note that $[C_{2z}||\boldsymbol{t}_{0.5a}]$ is the symmetry shown by the black arrow in Fig. 3.28(b). The spin and reciprocal space symmetry $[C_{2y}||C_{2y}]$ enforces a single spin-degenerate nodal surface that intersects along the entire the k_y-axis ($k_x = k_z = 0$), because

$$[C_{2y}\|C_{2y}]\,E(k_x, k_y, k_z, 0, 0, s_z) = E(-k_x, k_y, -k_z,\, 0, 0, -s_z). \tag{3.18}$$

It implies that $s_z = 0$ for $k_x = k_z = 0$, which is the k_y-axis. Analogously, the $[C_{2x}\|C_{2y}]$ symmetry enforces the same nodal surface.

We also note that the nontrivial spin group does not contain the four-fold rotation symmetry of the nonmagnetic crystal $[E||C_{4z}]$ shown in the inset in Fig. 3.28(b). The noncollinear spin order breaks this four-fold rotation symmetry. This symmetry-breaking also manifests in the spin densities, shown by gray iso-surfaces in Fig. 3.28(b)

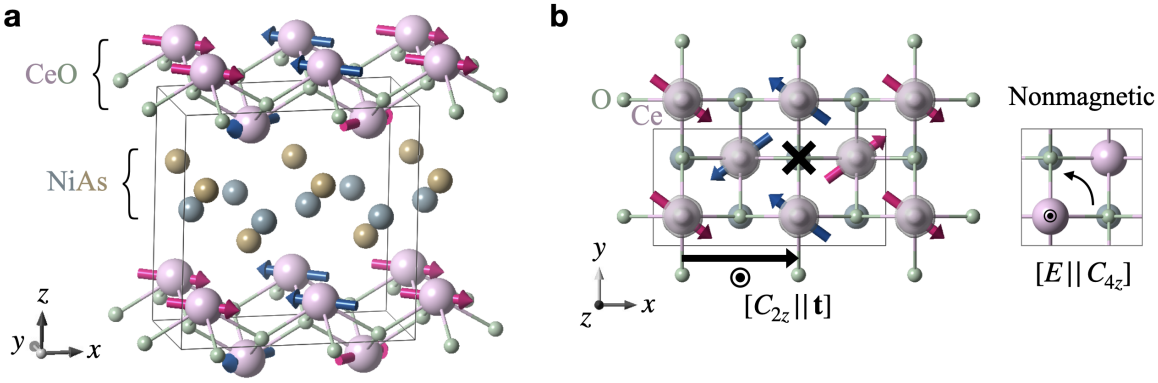

Figure 3.28: The magnetic crystal structure of CeNiAsO: (a) side-view and (b) top view. The magnetic crystal obeys $[C_{2z}||\mathbf{t}]$ symmetry, with $C_{2\perp} = C_{2z}$ and $\mathbf{t} = \boldsymbol{t}_{0.5a}$, as indicated by the black arrow in (b) relating the red- and blue-colored spins. The rectangles show the magnetic unit cell, which is doubled compared to the nonmagnetic unit cell (inset in b) due to the $[C_{2z}||\mathbf{t}]$ symmetry. The magnetic order breaks the four-fold $[E||C_{4z}]$ rotation of the nonmagnetic crystal. The spin densities, shown in for the x-component of the spin by the gray iso-surfaces in (b), also break this four-fold rotation symmetry. The magnetic unit cell is orthorhombic, and the nonmagnetic one is tetragonal in this material. Figure adapted from [93], CC BY 4.0.

for the x-component of the spin, as they have an anisotropic shape that breaks this four-fold symmetry. We performed these spin density calculations without spin-orbit coupling as described in Ch. 2.3.6.

We now investigate the electronic structure of CeNiAsO using DFT.

P-wave electronic band structure of CeNiAsO

We now show the p-wave spin polarization and spin split energy bands in CeNiAsO obtained from our *ab initio* calculations. We performed the DFT calculations as described in Ch. 2.3.6. Recall from Fig. 3.28(b) that it has $[C_{2z}||\mathbf{t}]$ symmetry, where $\perp = z$ is oriented out-of-plane with respect to the coplanar spin order in real space. The $[C_{2z}||\mathbf{t}]$ symmetry effectively acts as $[C_{2\perp}||E]$ on the electronic band structure due to Eq. (3.14). Thus, we expect the spin polarization to be collinear and finite only for the out-of-plane z-component $\langle S_z \rangle$. Moreover, we expect iso-energy cuts and energy bands to preserve $\mathcal{T}$ and break $[E||\mathcal{P}]$, thus obeying Eq. (3.12), and to display the spin-degenerate nodal surface we predicted to cross along the entire k_y-axis in Eq. (3.18).

P-wave Fermi surface. Fig. 3.29 shows the Fermi surface cut for nonmagnetic and magnetic calculations, where the magnetic case displays the p-wave spin polarization. The cut is in the $k_x k_y$-plane. In Fig. 3.29(a), the Fermi surface satisfies the four-fold rotation symmetry $[E||C_{4z}]$ of the nonmagnetic crystal from Fig.3.28(b, inset).

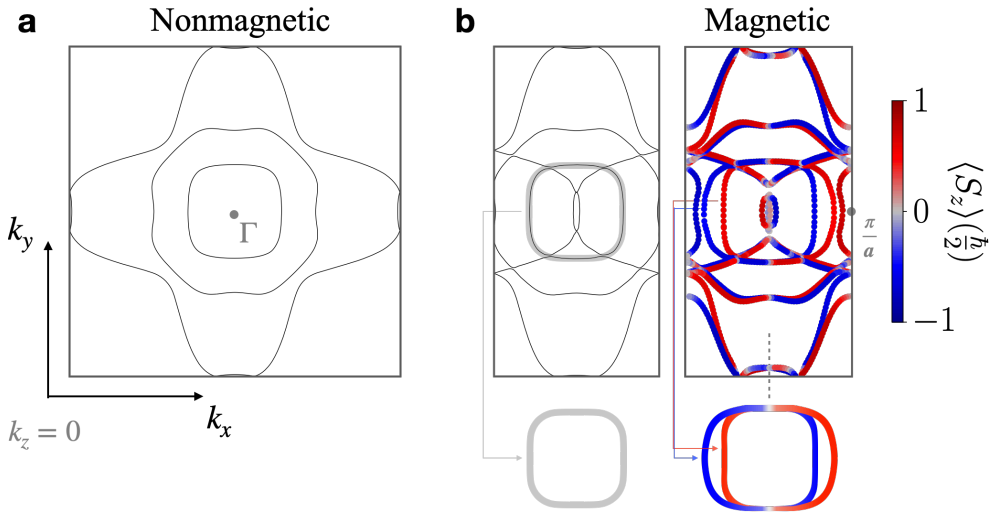

Figure 3.29: P-wave Fermi surface cut of CeNiAsO in the $k_z = 0$ plane. (a) Fermi surface for the nonmagnetic case. (b) P-wave Fermi surface in the magnetic case. For comparison, we show on the left the nonmagnetic case calculated with the magnetic unit cell to illustrate that the $[C_{2z}||\mathbf{t}]$ symmetry halves the Brillouin zone along the k_x-direction, thus folding the bands. Adding magnetism, the band sheets for positive and negative spin polarizations (red versus blue band sheets) shift in opposite directions away from the $\mathbf{\Gamma}$-point, and their shapes distort, thus breaking symmetries of the nonmagnetic crystal. The insets highlight this for the central band sheets in the nonmagnetic case (gray square-like shape on the left) transforming into the p-wave form (red and blue shifted and distorted sheets on the right). The gray dashed line in (b, right) shows the symmetry-enforced spin-degenerate nodal line along the k_y-axis with $k_x = k_z = 0$. Figure adapted from [93], CC BY 4.0.

Adding magnetism gives rise to a p-wave Fermi surface shown in Fig. 3.29(b). Firstly, the unit cell doubles due to the $[C_{2z}||\mathbf{t}_{0.5a}]$ symmetry, and the corresponding Brillouin zone halves in size along the corresponding $\mathbf{k}_x$-direction, folding the bands. In the left panel in Fig. 3.29(b), we illustrate this band-folding in a nonmagnetic calculation with the magnetic unit cell. We highlight the central, unfolded, doubly-degenerate band sheet by the gray square-like shape Fig. 3.29(b, left inset), which obeys the four-fold rotation symmetry $[E||C_{4z}]$ of the nonmagnetic crystal

Secondly, the magnetic order distorts the shape of the band sheet for each opposite spin polarization, the blue sheets comprising one spin polarization with $\langle S_z \rangle < 0$, the red the other spin polarization with $\langle S_z \rangle > 0$. The previously gray-highlighted band sheets in the central region, Fig. 3.29(b, left inset), now correspond to the pairs of spin-split blue- and red-highlighted band sheets Fig. 3.29(b, right inset). Each of them is distorted, breaking the symmetries otherwise present for the nonmagnetic case such as the four-fold $[E||C_{4z}]$ rotation.

Third, the band sheets are mutually shifted away from the origin in opposite

directions for opposite spin polarizations.

Lastly, the magnetic Fermi surface has a single symmetry-enforced nodal surface crossing the entire k_y-axis, highlighted by the gray dashed arrow in Fig. 3.29(b), as predicted in Eq. (3.18).

The magnetic Fermi surface displays p-wave magnetism: it is odd-parity-wave, breaks inversion, preserves $\mathcal{T}$, has a single symmetry-enforced nodal surface, and breaks original lattice symmetries such as $[E||C_{4z}]$. We additionally calculated the isoenergy cuts for energies between $-0.3\,\text{eV}$ and $0.1\,\text{eV}$, and confirmed that these symmetries hold for all the calculated energies.

Collinear p-wave electronic band structure with giant spin splittings. We now show that the electronic band structure hosts collinear spin polarization, disperses linearly around the $\mathbf{\Gamma}$-point, and displays giant spin splittings. Fig. 3.30 shows the calculated energy bands along the $-\frac{\pi}{a}\Gamma\frac{\pi}{a}$ path, which lies along the k_x-axis with $k_y = k_z = 0$. Firstly, it confirms that the spin polarization is collinear and out-of-plane with respect to the coplanar spins in real space because only the z-component of the spin, $\langle S_z\rangle$, is finite. This is what we predicted from the $[C_{2z}||\mathbf{t}_{0.5a}]$ symmetry in Eq. (3.14). Secondly, analogously to the isoenergy-cut, the spin polarization obeys the odd-parity-

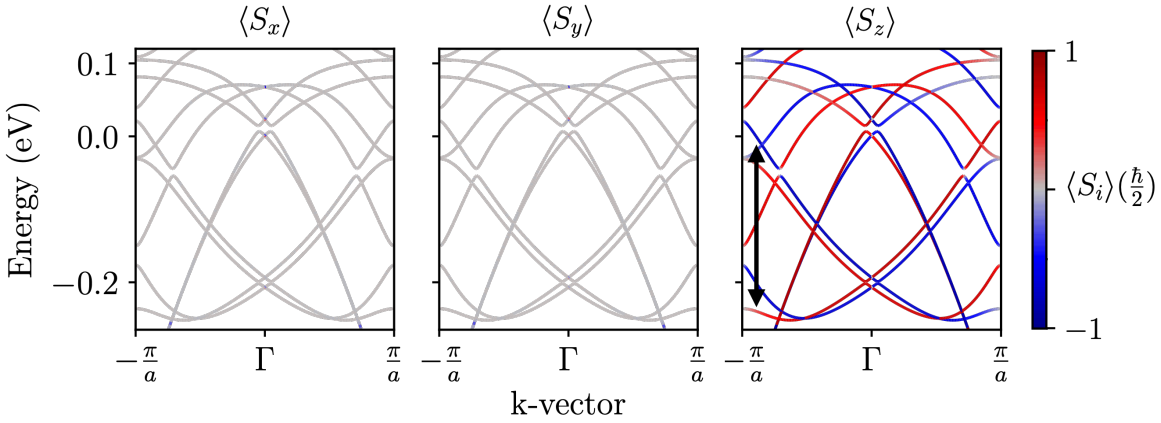

Figure 3.30: Collinear, nonrelativistically spin-split, odd-parity-wave energy bands of p-wave CeNiAsO. The path is $-\frac{\pi}{a}\Gamma\frac{\pi}{a}$, which lies along the k_x-axis (the path coincides with the Fermi surface cut in Fig. 3.29). The band structure is fully spin-polarized along the z-axis ($\langle S_z\rangle$, right panel), while the x and y spin polarizations are zero ($\langle S_x\rangle = \langle S_y\rangle = 0$, left and middle panels). The spin splitting reaches a giant $\sim 200\,\text{meV}$ indicated by the double black arrows. Figure adapted from [93], CC BY 4.0.

wave symmetries by breaking inversion and preserving $\mathcal{T}$. Thirdly, the spin splitting disperses linearly around the $\mathbf{\Gamma}$-point, which, similarly to the models, concurs with CeNiAsO breaking crystal inversion symmetry from guideline 1., thus leaving only odd-in-momentum terms in the k.p Hamiltonian as in Eq. (3.13).

The bands reach a *spin splitting*—which we recall is where two bands of opposite spin meet at $\mathbf{\Gamma}$ and spin-split away from it—of a giant $\sim 200\,\mathrm{meV}$, highlighted by the black double arrows. The giant size is reasonable as the spin splitting originates from magnetic exchange, typically associated with larger energy scales than relativistic spin-orbit coupling.

In summary, using spin symmetry analysis and DFT, we have shown that CeNiAsO is a candidate p-wave material whose electronic band structure breaks inversion symmetry, thus dispersing linearly around the $\mathbf{\Gamma}$-point, preserves time-reversal symmetry, and has a single spin-degenerate nodal surface crossing $\mathbf{\Gamma}$ enforced by spin symmetry. The band structure hosts a spin polarization that is collinear and out-of-plane with respect to the coplanar spin order in real space, as well as giant, nonrelativistic $\sim 200\,\mathrm{meV}$ spin splittings.

3.2.8 Material candidates search

In our paper [93], we searched the Magndata database [177] for experimentally reported magnetic materials and their magnetic crystal order. Analyzing their symmetries using our symmetry guidelines, we identified 73 odd-parity-wave material candidates with noncentrosymmetric, coplanar magnetic crystals featuring $[C_{2\perp}||\mathbf{t}]$ symmetry. Of these, 43 are p-wave candidates with a single spin-unpolarized nodal surface [93], similar to CeNiAsO.

We note that a noncoplanar candidate includes Ce_3InN—a tetragonal system which, remarkably, has a Kagome structure in its (201) plane, analogously to our model Fig. 3.22. Another noncoplanar material is the low atomic number compound Mn_5Si_3—Mn has an atomic number of 25, Si 14—in its bulk, low-temperature AF1 phase [47, 48, 178]. Their odd-parity-wave band structure may contribute to unconventional anisotropic transport [130, 93].

3.2.9 Experimental signatures

Our odd-parity-wave magnetism is robust due to its origin and symmetry protection from the spontaneous magnetic crystal order. Similarly to altermagnets, this makes them well-suited for experimental detection through photoemission spectroscopy and for applications in insulating and metallic device physics. For example, we have proposed [93] an experimentally available anisotropy of the resistivity in p-wave magnets, owing to the anisotropic spin polarization that each breaks symmetries of the underlying nonmagnetic crystal, as for instance highlighted for the Fermi surface of CeNiAsO in Fig. 3.29(b). For example, suppose we measure resistivity in the xy-plane for R_{xx} and R_{yy} of CeNiAsO. In that case, we expect the signal for the nonmagnetic case above the critical temperature to be four-fold symmetric and thus not show

anisotropic transport $R_{xx} - R_{yy}$. However, as the p-wave Fermi surface breaks the four-fold symmetry, we expect a finite anisotropy $R_{xx} - R_{yy}$ below the critical temperature, as we have demonstrated with models and in collaborative simulations [93]. Being a nonrelativistic effect arising from highly anisotropic spin polarizated energy bands, symmetry-protected by the crystal itself and spin-split by strong magnetic exchange, it lends itself to be sizeable even in materials with light elements such as Mn_5Si_3.

3.2.10 Discussion

The symmetry guidelines and materials we have identified here have been missed in previous studies [179, 110, 21] due to the common belief [179, 110, 21, 180] that nonrelativistic spin-splitting is impossible in magnets with $\mathcal{T}\mathbf{t}$ symmetry, which are magnets belonging to type-IV magnetic space groups. As we have shown here, spin-splitting is only impossible in the subset of $\mathcal{T}\mathbf{t}$-symmetric magnets that are collinear: $\mathcal{T}\mathbf{t}$ *combined with collinearity* imposes the spin-degeneracy as we showed in Ch. 1.7 and discussed in our symmetry guideline 2, because collinear magnets have centrosymmetric electronic energy band structures. These observations being largely overlooked in existing literature may be one reason why p-wave magnetism has not been realized, or was impossible to realize, in the past [39, 41, 42].

We emphasize that our odd-parity-wave magnetism differs from anomalous Hall antiferromagnets such as Mn_3X (X=Sn, Ga, Ge, Pt, Ir) [181, 2, 119], multipolar orders [20, 182, 183], and other noncollinear magnets [180, 184, 185], as their magnetic crystals break $\mathcal{T}\mathbf{t}$ and $[C_{2\perp}||\mathbf{t}]$ symmetry and/or preserve crystal inversion symmetry. Thus, their band structures are even-parity-wave and break $\mathcal{T}$ symmetry. In contrast, our odd-parity-wave magnets preserve $\mathcal{T}\mathbf{t}$ and/or $[C_{2\perp}||\mathbf{t}]$ symmetry and break crystal inversion symmetry, and their resulting band structures preserve $\mathcal{T}$. The $\mathcal{T}$ symmetry in the electronic band structure, or its absence, has significant consequences for the measurable transport properties of the materials. For example, noncollinear magnets whose electronic band structures break $\mathcal{T}$ symmetry can host the anomalous Hall effect [2]; our odd-parity-wave magnets preserve $\mathcal{T}$ and cannot.

Our odd-parity-wave spin polarization and textures arise already on a single quasiparticle level of density functional theory and are symmetry-protected. It does not require strong correlations to be realized, making it conceptually different from previous and, so far, unsuccessful attempts at realizing p-wave magnetism with strong correlations [39, 41, 42]. Moreover, it is as robust as the magnetic order of the crystal itself, contrary to other proposals for relativistic p-wave spin polarization [167] that require fine-tuning relativistic spin-order-coupling parameters. Further contrasting relativistic counterparts is that our p-wave magnetism manifests on the nonrelativistic level, which, in principle, allows it to be realized using light element materials.

Conclusion. In conclusion, we have identified the—for decades elusive [39, 40, 43]—p-wave magnetism arising from magnetic exchange, as well as odd-parity-wave magnetism generally. Our p-wave and odd-parity-wave magnetism displays attractive physical properties, such as giant nonrelativistically spin-split, strongly anisotropic energy bands, and collinear spin polarization in reciprocal space. We note that nonrelativistic odd-parity-wave order has been anticipated to host, for instance, spin currents in analogy to its relativistic counterpart [40], which can now be studied with our odd-parity-wave magnets [93]. In our other work, we have also predicted a large nonrelativistic Edelstein effect in coplanar p-wave magnets [176], i.e., a nonequilibrium spin density accumulation arising due to an applied electric field, typically in noncentrosymmetric systems with particular spin-momentum-lockings in the electronic band structure that, traditionally, have a relativistic origin [186]. Furthermore, on the nonrelativistic level, our odd-parity-wave magnets can host anisotropic resistivities in analogy to anisotropic magnetoresistance [93]. The linear dispersion around the $\mathbf{\Gamma}$-point could be further studied in the context of topological quasiparticles [80, 187].

Chapter 4

Spin-dependent transport in altermagnets

In ferromagnets, the nonrelativistic electronic band structure is time-reversal symmetry broken and spin-split, giving rise to spin-dependent transport, which is utilized in of spintronics effects including giant and tunneling magnetoresistance (GMR and TMR). These effects can be used for reading out information stored in mangetic tunnel junctions [51].

GMR and TMR effects can be realized in junctions with two ferromagnetic electrodes separated by a spacer shown in Fig. 4.1. In real space, the magnetization of the free layer FM_2 can be parallel or antiparallel to that of the pinned layer FM_1. In the figure, we also show the corresponding Zeeman-split electronic energy bands in momentum space, where the color of the bands corresponds to their spin expectation value. This spin polarization changes sign when the free layer magnetization is reversed, shown by the blue-colored band changing to red, and the red-colored band to blue. The spin-split energy bands in ferromagnets have a majority spin channel that is more occupied with a higher density of states than the minority channel at a given Fermi energy [51].

In this setup, the spacer can be metallic or insulating, leading to different types of transport. If the spacer is insulating, it acts as a tunneling barrier for the electrons. This tunneling is suppressed in the antiparallel configuration compared to the parallel one because there are fewer available states with matching spin to tunnel into in the adjacent ferromagnet [51].

If the spacer is metallic, the transport proceeds via conduction, and the changes in the resistance of the heterostructure are referred to as the GMR effect. We now review the conductivity description of the structures.

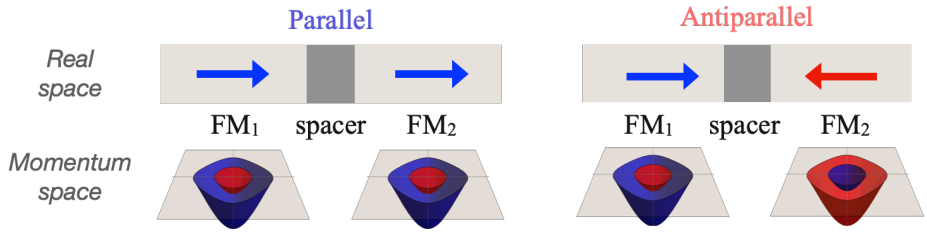

Figure 4.1: Trilayer setup with two ferromagnets separated by a spacer. The spacer is a metal in the case of GMR and a tunneling barrier for TMR. For the two ferromagnets FM_1 and FM_2, we show parallel and antiparallel configurations of the magnetization in real space, shown by the red and blue arrows, and illustrations of corresponding Zeeman-split energy bands momentum space.

Conductivity tensor in linear response. Recall that applying a static electric field in a crystal results in a current density to linear order in the field, expressed by [188]

$$j_\alpha = \sigma_{\alpha\beta} E_\beta. \tag{4.1}$$

Here, α and β are cartesian coordinate indices $\{x, y, z\}$, a summation is implied over the β index, E_β is the electric field applied along β, and j_α is the resulting current density along α. The quantity relating j_α and E_β is the conductivity $\sigma_{\alpha\beta}$, which are elements of the *conductivity tensor*, σ, given by

$$\sigma = \begin{pmatrix} \sigma_{xx} & \sigma_{xy} & \sigma_{xz} \\ \sigma_{yx} & \sigma_{yy} & \sigma_{yz} \\ \sigma_{zx} & \sigma_{zy} & \sigma_{zz} \end{pmatrix}. \tag{4.2}$$

The diagonal elements of σ correspond to *longitudinal* conductivity components along the electric field. Off-diagonal elements correspond to *transverse* components, perpendicular to the electric field [188]. This tensor and its elements correspond to *charge conductivities*. In the Mott model [189, 190] in the nonrelativistic approximation neglecting spin-orbit coupling, the charge conductivity is expressed as the sum of the conductivities in the two spin channels [7, 52]:

$$\sigma = \sigma^{\uparrow} + \sigma^{\downarrow}. \tag{4.3}$$

Within this model [189], we can also define the *spin conductivity tensor* by taking the difference between the conductivities in the two spin channels, which is [7]

$$\sigma^s = \sigma^{\uparrow} - \sigma^{\downarrow}. \tag{4.4}$$

In systems with finite spin conductivities, or *spin-polarized* conductivities, electrons carry a spin current that flows in the material in response to the electric field.

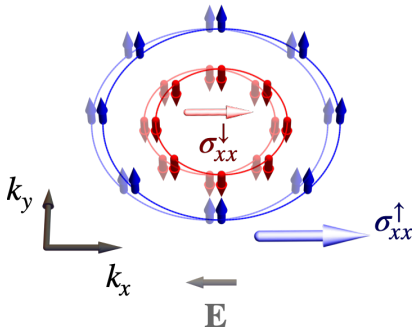

Figure 4.2: Illustration of ferromagnetic Fermi surface giving rise to a finite spin conductivity in linear response to an electric field **E**. The electric field shifts the Fermi surface from left to right, generating a larger conductivity $\sigma_{xx}^{\uparrow}$ for the blue spin channel than $\sigma_{xx}^{\downarrow}$ in the red spin channel, and thus an overall spin conductivity $\sigma_{xx}^{\uparrow} - \sigma_{xx}^{\downarrow}$.

Spin currents, GMR and TMR in ferromagnets. The electric current in ferromagnets can be spin-polarized, as illustrated in Fig. 4.2. The Fermi surface shifts in response to an electric field, where the majority spin channel shown in blue generates a larger conductivity $\sigma_{xx}^{\uparrow}$ than the minority spin channel shown in red, $\sigma_{xx}^{\downarrow}$, thus generating an overall spin current. For instance, this can be modeled by Boltzmann theory applied to each spin channel [52]. The theory applies to diffusive transport, where there is scattering, but a net electron flow can still occur. Characteristically, the mean free path is much smaller than the system size and much larger than the lattice constant [52]. It describes the conductivity resulting from the change in an assumed distribution function as a result of external fields, such as an electric field; diffusion, the tendency of the electrons to move from areas of higher to lower electron density [191]; and scattering, for example from occupied to unoccupied electron states, with other quasiparticles, or off impurities [52, 192].

For GMR, consider the system where a metal separates the two ferromagnetic electrodes. When the magnetizations of the two ferromagnetic electrodes are parallel, as shown in Fig. 4.1, electrons in the red spin-down channel can travel through the system almost without scattering [51]. When the magnetizations are antiparallel, electrons in both spin channels undergo collisions in the electrodes, giving rise to an overall higher resistance than in the parallel configuration [51]. The difference between the two resistances for the parallel and antiparallel configurations quantifies the GMR [51].

For TMR, consider the system where an insulating tunneling barrier separates the two ferromagnets. In response to a higher chemical potential in one of the leads, electrons may tunnel into the adjacent lead [53, 52]. The tunneling depends on the availability of transport channels in the adjacent lead into which the electrons can tunnel; for the antiparallel configuration, there are fewer available states to tunnel

into that are associated with the same spin than in the parallel case [52, 51]. As a result, the tunneling current in the antiparallel case is suppressed compared to the parallel case, and this difference in tunneling current quantifies the TMR [53, 52, 51].

Since the resistance depends on the relative magnetization of the two layers, TMR and GMR are used to read the magnetic state of the free layer [51]. Moreover, spin currents can enable efficient magnetization switching through spin transfer torque (STT) in ferromagnets [54, 55, 56]. STT is combined with TMR and GMR to create memory devices used in information technologies [193].

Spin-dependent transport in collinear, compensated magnets. As GMR and TMR rely on the presence of net magnetization, realizing counterpart effects in compensated magnets has been considered challenging. This conventional view has been based on the assumption that all collinear compensated magnets are antiferromagnets with spin-degenerate electronic bands in the entire Brillouin zone on the nonrelativistic level. As we have seen in Ch. 1.3, collinear compensated magnets belonging to the nontrivial spin group is $\mathbf{R}_s^{\mathrm{II}} = [E\|\mathbf{G}] + [C_2\|\mathbf{G}]$ (Eq. (1.28)), collinear antiferromagnets, are indeed Kramers spin degenerate on the nonrelativistic level, and only a specific subset of them with $\mathcal{T}\mathbf{t}$ symmetry can lift the spin degeneracy via spin-orbit coupling, but only weakly, thus hosting correspondingly weak spin responses (see Ch. 1.6) [25, 1]. Therefore, contrary to TMR and GMR in ferromagnets, any TMR or GMR mechanism in collinear antiferromagnets cannot arise from strongly, nonrelativistically spin-polarized electronic band structures.

However, several alternative mechanisms for TMR have been proposed in collinear antiferromagnets [57, 59]. One mechanism relies on sending a staggered spin polarized wave from one antiferromagnet into another [57]. It is a delicate quantum interference effect relying on the antiferromagnets being perfectly commensurate and epitaxial [57, 58]. It can be challenging to fabricate such perfect antiferromagnetic domains and interfaces, which may explain why it has yet to be experimentally viable to realize TMR in collinear antiferromagnets [58]. Another mechanism arises from the termination of the antiferromagnet at the insulator interface, which can produce local ferromagnetic moments in real space [59]. These effects arise from staggered or localized magnetization in real space, not spin-orbit coupling.

Instead, the antiferromagnetic spintronics field has turned its focus to relativistic spin-orbit interaction to circumvent the challenge of functionalizing antiferromagnets. The field has successfully demonstrated control of the antiferromagnetic order [67, 69, 70, 64, 65]. Owing to their magnetic compensation, antiferromagnets can be insensitive to external magnetic fields [64]. Moreover, their magnetic order can be switched faster (due to their THz spin dynamics and in contrast to GHz spin dynamics of ferromagnets) and more efficiently than ferromagnets [72, 71], thus showing that compensated magnetic order can be superior to ferromagnetic order for miniaturiza-

tion and fast, energy-efficient manipulation. However, realizing the nonrelativistic GMR, TMR, and STT counterparts to ferromagnets using conserved, robust spin currents has remained elusive.

Spin-dependent transport in altermagnets. Both theory predictions show, and recent experiments provide evidence that altermagnets produce strongly exchange-split and spin-polarized electronic structures that break time-reversal symmetry [25, 3, 30, 31, 38, 32, 194, 195, 196, 197, 198]. Such a spin-polarized electronic band structure could support TMR and GMR effects akin to those effects in ferromagnets described above.

In this chapter, we develop spin-dependent transport concepts for GMR and TMR in altermagnets. Based on spin symmetry analysis and altermagnetic electronic structures, we will explain how altermagnets can host these effects, show that altermagnets can host spin-polarized conductivities in the nonrelativistic limit, and discuss what types of altermagnetic spin polarizations, or spin splittings, in the band structure are favorable for these spin-dependent transport effects to be large. Our mechanisms of spin currents are allowed by nonrelativistically spin-split band structures of altermagnets and are thus different from previously considered mechanisms in conventional collinear antiferromagnets. Our mechanisms also share the nonrelativistic spin-splitting origin with mechanisms known from ferromagnets. We can thus expect large signals, as we will show that our model and DFT calculations confirm [12].

4.1 Spin-dependent currents in altermagnets

We now develop our spin currents and giant and tunneling magnetoresistance concepts in altermagnets. We will link the concepts to two main types of *spin polarizations*, or spin-splittings, of the nonrelativistic energy bands in altermagnets that are possible by symmetry: the *anisotropic* and the *valley spin polarizations*. In our publication [12], we have shown that despite the absence of net magnetization in altermagnets:

- Anisotropic spin polarizations can produce different spin conductivities for the two spin channels and, therefore, is a favorable band structure feature for GMR.

- Valley spin polarizations allow for valley- and spin-dependent tunneling with well-defined momentum and spin channel separation and, therefore, is a favorable band structure feature for TMR.

In the following, we focus on the pristine forms of these polarizations, meaning they take the precise form of our described k.p models. We note that both can coexist in general nonrelativistic band structures.

4.1.1 Spin conductivity and giant magnetoresistance from anisotropic spin polarization

Fig. 4.3(a) shows the GMR concept for altermagnetism based on the anisotropic spin polarization. The anisotropic spin polarization shown in Fig. 4.3(b) has a character-

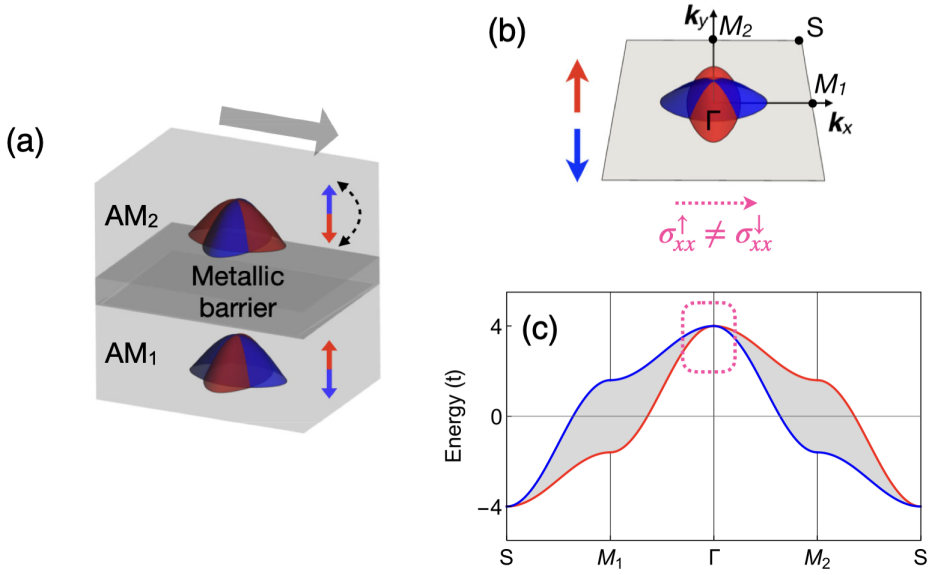

Figure 4.3: Archetype model mechanism for GMR in altermagnets. Spin polarization up and down are shown in red and blue, respectively. (a) GMR junction with two altermagnets in the antiparallel configuration, separated by a metal spacer in a *current-in-plane geometry* (the current travels parallel to the plane of the interface). Red-blue double arrows indicate the Néel vector. Here, the top layer is the free layer where the Néel vector is free to switch (indicated by black dashed double-arrows). (b) The anisotropic bands around the **Γ** point in the Brillouin zone give rise to different longitudinal conductivities for the spin up and down channels. (c) Energy band dispersions for the tight-binding model describing the anisotropic splitting. The rectangle highlights the region around **Γ** with mainly the anisotropic type of splitting. Figure adapted from [12], CC BY 4.0.

istic band anisotropy

$$\frac{\partial^2 E_s(\mathbf{k})}{\partial k_x^2} \neq \frac{\partial^2 E_s(\mathbf{k})}{\partial k_y^2} \tag{4.5}$$

for each spin channel s (red versus blue bands) as a function of momentum $\mathbf{k} = (k_x, k_y)$, localized around the **Γ**-point. In each spin channel s, the anisotropic spin polarization takes the form

$$E_s(\mathbf{k}) \sim \alpha^s k_x^2 + \beta^s k_y^2. \tag{4.6}$$

Note that Eq. (4.6) is even-in-momentum in concurrence with the *altermagnetic form of spin splitting*, owing to the effective inversion symmetry imposed by collinear magnetism (see, e.g., Def. 3). $\alpha^s \neq \beta^s$ signifies the anisotropy and thus *highly anisotropic*

bands would have $|\alpha^s| \gg |\beta^s|$ or vice versa. In turn, the group velocities of each spin channel are also anisotropic, satisfying:

$$[\partial E_\uparrow(\mathbf{k})/\partial k_i] \neq [\partial E_\downarrow(\mathbf{k})/\partial k_i]\,. \tag{4.7}$$

Anisotropic spin polarization in tight-binding model. Fig. 4.3(c) shows a tight-binding model hosting the anisotropic spin polarization, highlighted by the magenta rectangle around the $\mathbf{\Gamma}$-point. It is the model we derived in Eq. (2.31) and showed in Fig. 2.4(a, c), consisting of a nearest-neighbor altermagnetic hopping term $H_{\mathrm{AM}}^{\mathrm{NN}}$ plus a normal hopping term $H_{\mathrm{N}}^{\mathrm{NN}}$ on a square lattice.

We obtain the anisotropic spin polarization in this model by approximating the bands in Eq. (2.32) with a $\mathbf{k}\cdot\mathbf{p}$ expansion around the $\mathbf{\Gamma}$-point,

$$E_\pm(\mathbf{k}) = 4t - (t \pm t_J)\, k_x^2 - (t \mp t_J)\, k_y^2, \tag{4.8}$$

with $t > 0$ and $t_J = 0.4t$ and where $E_\pm$ denotes the energy in the two spin channels. It takes a form analogous to our general expression for anisotropic spin polarization in Eq. (4.6).

Spin conductivity and GMR. Due to sublattice-transposing symmetries such as $[\overset{\text{spin}}{C_2}||\overset{\text{crystal}}{C_{4z}}]$ in this case, the opposite spin channels are equally populated and related by a four-fold crystal rotation. Further sublattice-transposing symmetries discussed in Ch. 2.2 imposes the d-wave symmetry shown in Fig. 4.3(b). This d-wave symmetry implies that the two spin channels host different longitudinal spin conductivities along the same direction in real space,

$$\sigma_{xx}^{\uparrow} \neq \sigma_{xx}^{\downarrow},\ \sigma_{yy}^{\uparrow} \neq \sigma_{yy}^{\downarrow} \tag{4.9}$$

as indicated in Fig. 4.3(b). We can express the four-fold symmetry relating the spin channels in this case as

$$\sigma_{xx}^{\uparrow} = \sigma_{yy}^{\downarrow}, \quad \sigma_{xx}^{\downarrow} = \sigma_{yy}^{\uparrow}. \tag{4.10}$$

Fig. 4.4(a) shows a diagram for the linear response, analogously to the ferromagnetic diagram (Fig. 4.1), with the anisotropic spin polarization. The Fermi surface area shifted in the red (spin up) channel is greater than that of the blue (spin down) channel, in concurrence with Eq. (4.9), producing a finite spin conductivity $\sigma_{xx}^{\uparrow} - \sigma_{xx}^{\downarrow}$.

With different spin conductivities for the two spin channels, we can model the system with a two-resistance model [128]. The ratio of these conductivities,

$$R_\sigma = \frac{\sigma_{xx}^{\uparrow}}{\sigma_{xx}^{\downarrow}} = \frac{\sigma_{xx}^{\uparrow}}{\sigma_{yy}^{\uparrow}} = \frac{\sigma_{yy}^{\downarrow}}{\sigma_{xx}^{\downarrow}} \tag{4.11}$$

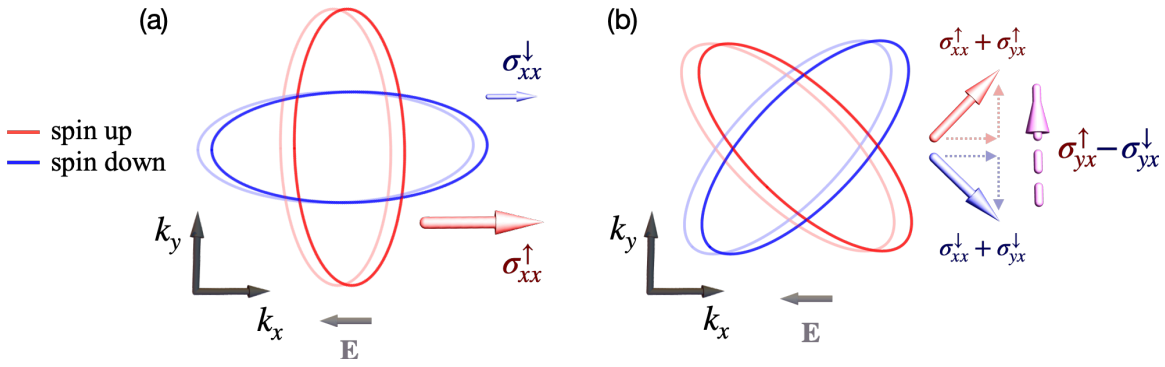

Figure 4.4: Spin-polarised conductivities in altermagnets. The conductivities (red and blue arrows) result from the linear response of the anisotropic spin polarization in the band structure to an electric field **E** around the Fermi energy. The direction and size of the red and blue arrows illustrate the direction and size of the conductivities. The color of the arrows and the Fermi surfaces indicate the spin channel (red is spin up, ↑, blue spin down, ↓). In (a), the electric field is oriented along the most anisotropic axis in each spin channel. It produces a larger longitudinal current in the red spin channel ($\sigma_{xx}^{\uparrow}$, larger red arrow) than the blue ($\sigma_{xx}^{\downarrow}$, smaller blue arrow) because the Fermi surface area shifted in the red spin channel is larger, and thus a spin-polarized longitudinal charge current $\sigma_{xx}^{\uparrow} - \sigma_{xx}^{\downarrow} > 0$. In (b), the electric field lies along the spin-degenerate nodal line of the Fermi surface. In the transverse direction, the net response is a pure spin current $\sigma_{yx}^{\uparrow} - \sigma_{yx}^{\downarrow} \neq 0$ shown by the magenta dashed arrow. Dashed red and blue arrows indicate the longitudinal and transverse components of the red and blue arrow.

can be used to estimate the GMR depicted in Fig. 4.3(a), analogously to the two-current model adopted for ferromagnets [51]:

$$\mathrm{GMR} = \frac{1}{4}\left(R_\sigma + \frac{1}{R_\sigma} - 2\right). \tag{4.12}$$

This function has a minimum for $R_\sigma = 1$ and increases monotonically towards infinity for $R_\sigma \to 0$ or ∞. Therefore, the GMR in Eq. (4.12) is larger the more the conductivities in the two different spin channels differ from each other, which in altermagnets can manifest from band features being more anisotropic.

For comparison, we also illustrate the *spin-splitter effect* [7] in Fig. 4.4(b). The plane with the d-wave magnetism is rotated compared to the Fermi surface in Fig. 4.4(a) and with respect to the applied electric field **E**. As indicated by the red and blue arrows in Fig. 4.4(b), the linear response to the field produces not only a longitudinal component in the conductivities for each spin channel (e.g., $\sigma_{xx}^{\uparrow}$ for the red arrow for the spin up channel), but also a transverse component (e.g., $\sigma_{yx}^{\uparrow}$ for the red arrow). The magenta dashed arrow shows the corresponding *spin conductivity* (Eq. (4.4)), $\sigma_{xx}^{\uparrow} + \sigma_{yx}^{\uparrow} - (\sigma_{xx}^{\downarrow} + \sigma_{yx}^{\downarrow}) = \sigma_{yx}^{\uparrow} - \sigma_{yx}^{\downarrow}$. It is a pure spin conductivity [7] as can be seen by the transverse component of the red and blue solid arrows (shown by vertical

dashed arrows) being equal and in opposite directions. Thus, the spin conductivity is $\sigma^{\uparrow}_{yx} - \sigma^{\downarrow}_{yx} \neq 0$, and the charge conductivity is $\sigma^{\uparrow}_{yx} + \sigma^{\downarrow}_{yx} = 0$. Analogously, the longitudinal component is a pure charge current because spin up and down components (shown by horizontal dashed arrows) are equal and in the same direction. In contrast to the spin Hall effect, this pure spin conductivity or *spin-splitter effect* is of nonrelativistic origin and is odd under time-reversal [7].

4.1.2 General symmetry criteria for the conductivity tensor in altermagnets

We now describe the general method for deriving which elements of the spin conductivity tensor are allowed by spin symmetries in altermagnets in the nonrelativistic limit. Our steps correspond to the symmetry analysis in [25] and [199]. We will focus on nonrelativistic spin currents [12, 7] that are *symmetric*, i.e., $\sigma^{s}_{\alpha\beta} = \sigma^{s}_{\beta\alpha}$ with $\alpha, \beta = x, y, z$, because, in altermagnets, they tend to be larger than the relativistic, antisymmetric counterpart [7]. For example, the spin-splitter effect, which per definition originates from the symmetric part of the conductivity tensor, was shown to be orders of magnitude larger than the spin Hall effect in the same material [7], conventionally [7] defined from the antisymmetric part [200]. Moreover, adding spin-orbit coupling tends not to affect the spin current significantly [7]. These symmetric spin conductivities originate from the nonrelativistic spin polarization, which can be highly anisotropic and thus produce large spin currents, as we discussed in the last section.

General method for symmetry-constraining the conductivity tensor, and a d-wave example

Here, we will formulate three steps for applying symmetry elements of the spin group of an altermagnet to obtain the conductivity response. Recall from Ch. 1.3.1 that the spin channels are de-coupled in the nonrelativistic limit. Therefore, analogously to the Hamiltonian, we can apply the symmetry elements h of the halving subgroup $\mathbf{H}$ to each spin channel separately [25]. This application in each spin channel forms the first step of the general recipe to determine which elements of the spin conductivity tensor are allowed by symmetry.

Step 1. The conductivity tensor obeys the symmetries of the halving subgroup $\mathbf{H}$ in each spin channel:

$$\sigma^{\uparrow} = h\sigma^{\uparrow}h^{-1} \quad \text{for } h \text{ in the halving subgroup } \mathbf{H} \tag{4.13}$$

and similarly for $\sigma^{\downarrow}$. We may reduce the number of elements in the tensor by comparing the left- and right-hand sides of this equation. For example, for the $\mathbf{R}^{\mathrm{III}}_{s} = {}^{2}2/{}^{2}m$

spin Laue group from Ch. 1, $\mathbf{H} = \{E, \mathcal{P}\}$ does not impose restrictions on $\sigma^{\uparrow}$ and $\sigma^{\downarrow}$ because $\mathcal{P}\sigma^{\uparrow}\mathcal{P}^{-1} = -\mathcal{P}\sigma^{\uparrow} = \sigma^{\uparrow}$ and $E\sigma^{\uparrow}E^{-1} = \sigma^{\uparrow}$. Moving on to the next step, we use the updated tensor with possibly fewer elements.

Step 2. The transposing symmetry, A, relates the spin channels [25] [1]. We can express this by

$$\sigma^{\uparrow} = A\sigma^{\downarrow}A^{-1} \quad \text{for the transposing symmetry } A. \tag{4.14}$$

In our example, we can insert for $A = C_{2y}$ and obtain

$$\sigma^{\downarrow} = C_{2y}\sigma^{\uparrow}C_{2y}^{-1} = \begin{pmatrix} \sigma^{\uparrow}_{xx} & -\sigma^{\uparrow}_{xy} & \sigma^{\uparrow}_{xz} \\ -\sigma^{\uparrow}_{yx} & \sigma^{\uparrow}_{yy} & -\sigma^{\uparrow}_{yz} \\ \sigma^{\uparrow}_{zx} & -\sigma^{\uparrow}_{zy} & \sigma^{\uparrow}_{zz} \end{pmatrix} \tag{4.15}$$

Step 3. Finally, the spin conductivity tensor is given by Eq. (4.4). In our example, we insert for Eq. (4.15) and obtain the following symmetric spin conductivity:

$$\begin{aligned} \sigma^{\text{symm},s} &= \text{symm}\left[\sigma^{\uparrow} - \sigma^{\downarrow}\right] \\ &= \text{symm}\left[\begin{pmatrix} \sigma^{\uparrow}_{xx} & \sigma^{\uparrow}_{xy} & \sigma^{\uparrow}_{xz} \\ \sigma^{\uparrow}_{yx} & \sigma^{\uparrow}_{yy} & \sigma^{\uparrow}_{yz} \\ \sigma^{\uparrow}_{zx} & \sigma^{\uparrow}_{zy} & \sigma^{\uparrow}_{zz} \end{pmatrix} - \begin{pmatrix} \sigma^{\uparrow}_{xx} & -\sigma^{\uparrow}_{xy} & \sigma^{\uparrow}_{xz} \\ -\sigma^{\uparrow}_{yx} & \sigma^{\uparrow}_{yy} & -\sigma^{\uparrow}_{yz} \\ \sigma^{\uparrow}_{zx} & -\sigma^{\uparrow}_{zy} & \sigma^{\uparrow}_{zz} \end{pmatrix}\right] \\ &= 2\begin{pmatrix} 0 & \sigma^{\uparrow}_{xy} & 0 \\ \sigma^{\uparrow}_{xy} & 0 & \sigma^{\uparrow}_{yz} \\ 0 & \sigma^{\uparrow}_{yz} & 0 \end{pmatrix} \end{aligned} \tag{4.16}$$

This expression shows that the ${}^{2}2/{}^{2}m$ spin Laue group allows for non-zero symmetric spin conductivities [12].

G-wave example

We now derive the symmetric spin conductivity tensor in a g-wave spin Laue group, showing that its elements are zero in the nonrelativistic limit, in contrast to the above d-wave example. We consider the spin Laue group $\mathbf{R}_s^{\text{III}} = {}^{1}4/{}^{1}m^{2}m^{2}m$, with $\mathbf{H} = 4/m$ and $A = C_{2x}$ which describes, e.g., $KMnF_3$ [25]. The generators of $\mathbf{H}$ are [201, 202]

$$\mathcal{P},\ C_{2z},\ \text{and } C^{+}_{4,001} = \begin{pmatrix} 0 & -1 & 0 \\ 1 & 0 & 0 \\ 0 & 0 & 1 \end{pmatrix}. \tag{4.17}$$

[1] Analogously, it relates the diagonal blocks of the Hamiltonian, $H_{\uparrow}$ and $H_{\downarrow}$, from Ch. 1.3.1.

Step 1. Applying these generators of **H** using Eq. (4.13) constrains the conductivity tensor to take the following form [203] in the spin-up channel

$$\sigma^{\uparrow} = \begin{pmatrix} \sigma^{\uparrow}_{xx} & \sigma^{\uparrow}_{xy} & 0 \\ -\sigma^{\uparrow}_{xy} & \sigma^{\uparrow}_{xx} & 0 \\ 0 & 0 & \sigma^{\uparrow}_{zz} \end{pmatrix}, \tag{4.18}$$

and analogously in the spin-down channel.

Step 2. Applying Eq. (4.14) with $A = C_{2x} = \mathrm{diag}(1, -1, -1)$ yields

$$\sigma^{\downarrow} = C_{2x}\sigma^{\uparrow}C_{2x}^{-1} = \begin{pmatrix} \sigma^{\uparrow}_{xx} & -\sigma^{\uparrow}_{xy} & 0 \\ \sigma^{\uparrow}_{xy} & \sigma^{\uparrow}_{xx} & 0 \\ 0 & 0 & \sigma^{\uparrow}_{zz} \end{pmatrix} \tag{4.19}$$

Step 3. The symmetric spin conductivity tensor is then

$$\begin{aligned} \sigma^{\mathrm{symm},s} &= \mathrm{symm}\left[\sigma^{\uparrow} - \sigma^{\downarrow}\right] \\ &= \mathrm{symm}\left[\begin{pmatrix} \sigma^{\uparrow}_{xx} & \sigma^{\uparrow}_{xy} & 0 \\ -\sigma^{\uparrow}_{xy} & \sigma^{\uparrow}_{xx} & 0 \\ 0 & 0 & \sigma^{\uparrow}_{zz} \end{pmatrix} - \begin{pmatrix} \sigma^{\uparrow}_{xx} & -\sigma^{\uparrow}_{xy} & 0 \\ \sigma^{\uparrow}_{xy} & \sigma^{\uparrow}_{xx} & 0 \\ 0 & 0 & \sigma^{\uparrow}_{zz} \end{pmatrix}\right] \\ &= \begin{pmatrix} 0 & 0 & 0 \\ 0 & 0 & 0 \\ 0 & 0 & 0 \end{pmatrix}. \end{aligned} \tag{4.20}$$

This example shows that this g-wave spin Laue group does not allow for any symmetric spin currents.

Summary. We have shown with examples that a d-wave spin Laue group allows for symmetric spin conductivities, while a g-wave spin Laue group does not, in the nonrelativistic limit.

Analogously, we can repeat this exercise for all eleven altermagnetic spin Laue groups. In conclusion, we find that the symmetric spin conductivity persists in all d-wave altermagnets but that it is zero in g- and i-wave altermagnets [12].

4.1.3 Spin-dependent tunneling and tunneling magnetoresistance from valley spin polarization

Fig. 4.5(a) shows the TMR concept based on the *valley spin polarization*, shown by red and blue iso-energy cuts, in altermagnets. A tunnel barrier separates the altermagnetic electrodes. In the top panel in Fig. 4.5(a), the Néel vectors of the two altermagnets, shown by double blue-red arrows, are aligned parallel to each other in

a *parallel configuration*. In the bottom panel, they are antialigned in an *antiparallel configuration*. The magnitude of the tunneling, indicated by curved red arrows in the red spin channel, is suppressed in the antiparallel configuration because there are fewer available states to tunnel into in the adjacent altermagnet in the same spin channel, as the adjacent valley is of opposite, blue spin. The difference between the tunneling currents for the two different Néel vectors quantifies the TMR.

Valley spin polarization. Altermagnetic symmetries allow for localized, isotropic spin polarizations that form valleys in the nonrelativistic electronic structure, illustrated by an example in Fig. 4.5(b). On the nonrelativistic level, the valleys must form away from the sublattice-transposing symmetry-enforced nodal planes and the nodal $\mathbf{\Gamma}$-point, e.g., illustrated in Fig. 1.9, thus separating the valleys reciprocal space as indicated in Fig. 4.5(b) by the separation Δ shown by the black double arrow. In this example, the separation of the valleys corresponds to the four-fold crystal rotation $[E||C_{4z}]$ in the sublattice-transposing symmetry $[C_2||C_{4z}]$.

In each spin channel s, we can express the localized isotropic spin polarization as

$$E_s(\mathbf{k}) \sim \alpha \left(k_x^2 + k_y^2\right). \tag{4.21}$$

Compared to the anisotropic spin polarization in Eq. (4.6), this has no anisotropy as it corresponds to $\alpha = \beta$, which demonstrates that, unlike the GMR, the anisotropy is not needed for TMR. A general sublattice-transposing symmetry $[C_2||A]$ dictates that the opposite spin channels are related by

$$E_\uparrow(\mathbf{M}_1) = [C_2||A]E_\downarrow(\mathbf{M}_2) \tag{4.22}$$

with $A = C_4$ in our example.

The valley spin polarization corresponds to spin-polarized eigenstates whose eigenenergies often form band extrema:

$$\left.\frac{\partial E_s(\mathbf{k})}{\partial \mathbf{k}}\right|_{\mathbf{k}\to\mathbf{M}_\nu} = 0 \tag{4.23}$$

where $\mathbf{M}_\nu$ represents the momentum of the valley and ν denotes the valley index.

Recall that altermagnets have inversion-symmetric electronic energy bands enforced by their collinear spin-only group (Eq. (1.20)). This inversion symmetry relates the valleys as follows:

$$E_s(\mathbf{M}_\nu) = E_s(-\mathbf{M}_\nu) \tag{4.24}$$

Notably, this differs from valleys commonly induced by relativistic spin-orbit coupling in noncentrosymmetric systems [73]. For example, a Rashba spin-orbit coupling term (see Eq. (2.34)) results in spin polarizations that are odd under inversion, denoted as $E^R_{\langle\sigma_i\rangle}(\mathbf{k}) = E^R_{-\langle\sigma_i\rangle}(-\mathbf{k})$, where $\langle\sigma_i\rangle$ represents the expectation value of each spin component i, and σ_i represents a spin Pauli matrix.

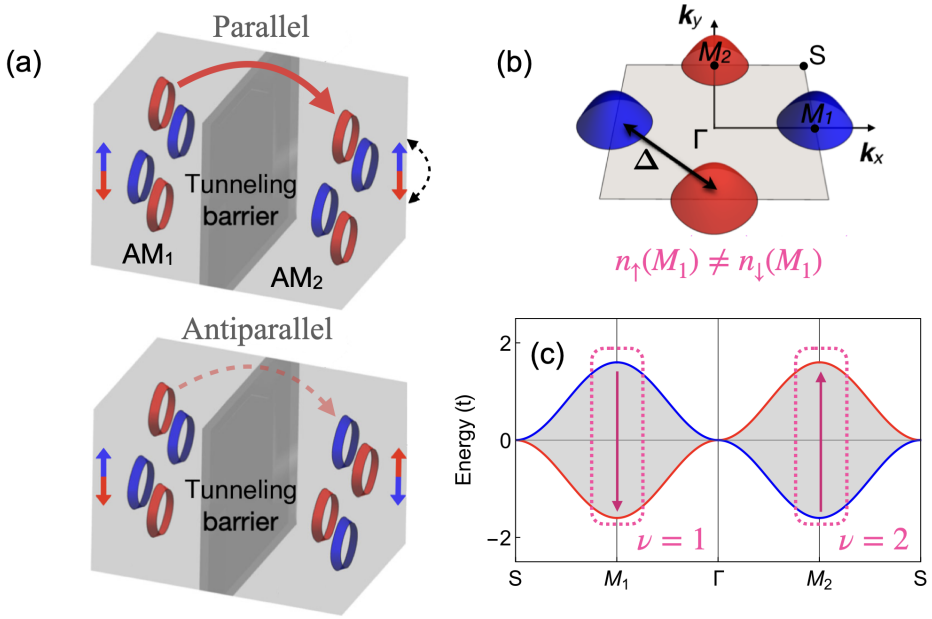

Figure 4.5: Archetype model mechanism for TMR in altermagnets. (a) TMR junction with two altermagnets in the parallel configuration, separated by an insulating spacer (out-of-plane tunneling geometry with respect to the d-wave plane). Red and blue insets show band cuts of the valley spin polarization of the energy bands. The tunneling current between adjacent valleys is indicated by the curved red arrows for parallel (top panel) and antiparallel (bottom panel) orientations of the Néel vectors (blue-red double arrows). It is suppressed in the antiparallel case because there are fewer states in the same spin channel in the adjacent valley compared to the parallel case. (b) The valley spin polarization, with valleys around $\mathbf{M}_1$ and $\mathbf{M}_2$, giving rise to spin- (s) and valley- (ν) dependent densities of states $n_s(M_\nu)$. The momentum Δ separates the valleys well in the Brillouin zone. Symmetries of the altermagnetic crystal enforce this separation. (c) Band dispersions of an altermagnetic model highlighting the spin splitting, which is opposite for the two valleys (model from Fig. 2.3(a, c)). Figure adapted from [12], CC BY 4.0.

Density of states for valley spin polarization. Each valley ν has an associated density of states in each spin channel, $n_s(\mathbf{M}_\nu)$. For example, we see in Fig. 4.5(b) that the density of states at the $\mathbf{M}_1$-valley is different for the two spin channels (it is large in the blue spin channel and small in the red channel), and thus

$$n_\uparrow(\mathbf{M}_1) \neq n_\downarrow(\mathbf{M}_1) \tag{4.25}$$

and similarly for the other valleys.

Valley spin polarization in tight-binding model. Fig. 4.5(c) shows the energy bands of a tight-binding model that hosts the valley spin polarization in Fig. 4.5(b). The dashed rectangles in Fig. 4.5(c) highlight the valleys. The model is $H_{\mathrm{AM}}^{\mathrm{NN}}$ from Fig. 2.3(a, c) and Eq. (2.26) with $t_J = 0.4\,t$.

We can derive the expression of the valleys by expanding the model (Eq. (2.26)) around $\mathbf{M}_1$ and $\mathbf{M}_2$. With $t = 0$ and $t_J > 0$, we get

$$\begin{aligned} E_{\pm}(\mathbf{M}_1, \mathbf{k}) &= \pm t_J \left(4 - k^2\right) \\ E_{\pm}(\mathbf{M}_2, \mathbf{k}) &= \mp t_J \left(4 - k^2\right), \end{aligned} \tag{4.26}$$

where $k = \sqrt{k_x^2 + k_y^2}$. These equations are analogous to our general expression for isotropic valley spin polarization in Eq. (4.21).

TMR for valley-conserved tunneling. In analogy to ferromagnets, the valleys have a magnetic exchange-induced spin splitting, as highlighted by the magenta arrows in Fig. 4.5(c). Tunneling that conserves the valley index ν thus follows a two-current model [190] where the two spin channels are de-coupled, in analogy to TMR in ferromagnets [12]. Therefore, for valley-conserving tunneling, we can apply Jullière's formula for TMR for each valley separately,

$$\mathrm{TMR} = \frac{1}{2}\left(R_n + \frac{1}{R_n} - 2\right), \tag{4.27}$$

where

$$R_n = \frac{n_{\uparrow}(\mathbf{M}_{\nu})}{n_{\downarrow}(\mathbf{M}_{\nu})} \tag{4.28}$$

is the ratio of the density of states of the two spin channels for the valley ν. From Eq. (4.27), we see that the TMR is finite if the density of states is different for the two spin channels for the same valley. As we have established, these densities of states are indeed different (see Eq. (4.25) and Fig. 4.5(b)), thus allowing for a finite TMR according to Eq. (4.27). This equation reflects the archetype mechanism illustrated in Fig. 4.5(a): for each valley, the tunneling current is different for parallel and antiparallel orientations of the Néel vectors, giving rise to TMR.

We also note that, similarly to the valleys themselves, the densities of states of the valleys are related by the sublattice transposing symmetries of the altermagnet. Thus, we can relate the densities of states of different valleys and spin channels analogously to in Eq. (4.22), yielding in our example $n_{\uparrow}(\mathbf{M}_1) = n_{\downarrow}(\mathbf{M}_2)$ and $n_{\downarrow}(\mathbf{M}_1) = n_{\uparrow}(\mathbf{M}_2)$, which we can alternatively insert in the expression for R_n above.

We note that the pristine form of the valley polarization in Eq. (4.21) is entirely isotropic, so the Fermi surface of each valley is circular. As a result, isotropic valley spin polarizations themselves do not produce net spin conductivities and, therefore, not GMR.

TMR allowed in all altermagnets. In principle, all d-, g-, and i-wave altermagnets allow for TMR due to their spin-polarized electronic band structure. Their band dispersions typically have some degree of *valley-character* (dispersing similar to

Eq. (4.21) and being separate in momentum-space from similarly dispersing bands, as in Fig. 4.5(b)), which we will demonstrate enhances TMR in our simulations in Sec. 4.2.

4.1.4 Landauer-Büttiker formalism

To quantify the tunneling magnetoresistance in altermagnets, we can calculate the differential conductance for the parallel and antiparallel configurations shown in Fig. 4.5. Differential conductance refers to the change in current from a voltage drop across a device, $G = dI/dV$, where I is the current and V is the voltage.

Here, we will focus on whether tunneling magnetoresistance is present in altermagnetic models in single-domain systems with pristine interfaces. With pristine interfaces in the clean limit, we are in a regime where the momentum parallel to the interface is conserved. This regime contrasts the dirty regime with rough interfaces, where the momenta are not conserved, and the relevant quantity is instead the density of states, as considered in the Jullière formalism [204].

We will use the Kwant package [205] to perform the calculations, which implements the Landauer-Büttiker formalism. In the following, we review this formalism and show an example of differential conductance calculated with Kwant for an altermagnetic wire, compared to a ferromagnetic one, and which serves as a reference to compare to the TMR calculation in the next section.

Nature of the transport. In the Landauer-Büttiker formalism, one considers a voltage drop across a ballistic system that arises from a difference in chemical potential $\delta\mu$, or electron density ($\delta n = \delta\mu\,\rho(E_F)$, with ρ the density of states), as illustrated in Fig. 4.6 [206, 207, 208]. The ballistic region is considered to be an *ideal waveguide* [209,

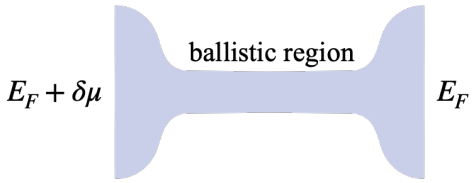

Figure 4.6: Transport of a ballistic region, shown in the middle, in the Landauer-Büttiker formalism. It arises from a voltage drop V due to a difference in chemical potential, $\delta\mu = eV$, or electron density, across the reservoirs shown by the wide regions on the left and right [206, 207, 208, 209].

210], where electrons are injected from the reservoirs into the central region without reflecting back into the reservoirs [206, 208]. Therefore, right-moving electrons are occupied up to the chemical potential of the left lead, $E_F + \delta\mu$, and left-moving ones up to that of the right lead, E_F.

With current technology, it is possible to fabricate nanoelectronic devices that are smaller than the *mean-free path* of electrons, a distance over which the momentum of the electrons is conserved [191]. Such nano-systems have been widely studied with semiconductors, for instance, with Si with a mean-free path of the order of 100 nm and GaAs where it can reach the order of μm [206]. Thus, ballistic transport is often realistic in today's nanoelectronics [191, 206].

Landauer-Büttiker formalism. In the Landauer-Büttiker formalism, the central ballistic region, or scattering region, can be attached to ballistic leads that act as waveguides, bringing plane waves to and from the scattering region [205, 209, 210, 208]. These leads act as the contacts in the experiment [205, 209, 208]. This formalism can describe systems with any number of terminals. Moreover, it has been used to describe phenomena beyond semiconducting transport [191, 206, 209, 210], including, but not limited to, transport in topological [209], superconducting [211], and magnetic systems [124]. The formalism can also be extended to include quantum interference and thus noncoherent transport [191, 206, 209, 208, 210], but this is beyond our scope, as we will consider coherent transport where the coherence length of electrons is larger than the system.

Kwant transport simulation. Kwant is a simulation package that utilizes the Landauer-Büttiker formalism, describes ballistic transport, and can treat infinite systems [205]. It implements the Hamiltonians in the leads and scattering region as tight-binding Hamiltonians, where the scattering region is finite, and the leads are semi-infinite, meaning they are infinite in the direction not attached to the scattering region [205]. The key output from Kwant which we will use is the *scattering matrix*, which describes reflection and transmission probabilities for transverse modes passing in and out of the scattering region [205, 136, 191, 206].

In the following, we provide a derivation for the Landauer formula for differential conductance, which is given in terms of the scattering matrix and which we will use to calculate tunneling magnetoresistance in altermagnetic models.

Derivation of the Landauer formula

Two-terminal setup. The system we will consider has two (altermagnetic) leads, or terminals, as illustrated in Fig. 4.7(a). In general, a two-terminal system consists of five regions: the left reservoir, left lead, scattering region, right lead, and right reservoir. Adding leads between the reservoirs allows for a well-defined scattering problem [208, 209]. Each lead, labeled by $\alpha = L, R$, are translationally invariant and is associated with transverse modes $\phi^{\pm}_{\alpha nE}$, labeled by n at a specific *energy of incident electrons*, E [136, 209, 205], as illustrated in Fig. 4.7(b). These modes propagate either to the right ($\phi^{+}_{\alpha nE}$) or to the left ($\phi^{-}_{\alpha nE}$).

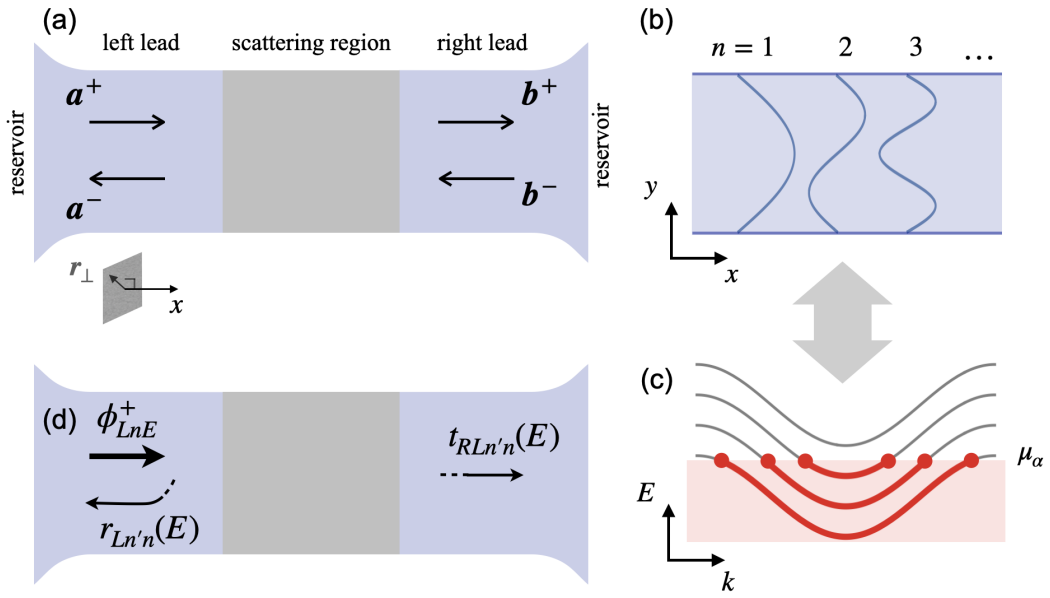

Figure 4.7: Two-terminal setup and transport quantities in the Landauer-Büttiker formalism. (a) Two-terminal setup of a scattering region connected to two leads and reservoirs. $\mathbf{a}^\pm$ and $\mathbf{b}^\pm$ are vectors containing wavefunction-coefficients for the eigenstates (comprised of linear combinations of transverse modes) in the leads, incident ($\mathbf{a}^+$, $\mathbf{b}^-$) and outgoing ($\mathbf{a}^-$, $\mathbf{b}^+$), moving to the right ($\mathbf{a}^+$, $\mathbf{b}^+$) or left ($\mathbf{a}^-$, $\mathbf{b}^-$). The inset shows $\mathbf{r}_\perp$, a vector in a cross-section perpendicular to the longitudinal position, x. (b) Illustration of three lowest-order transverse modes ($n = 1, 2, 3$). (c) The number of transverse modes equals the number of filled bands, which depends on the chemical potential μ_α of the lead ($\alpha = L, R$, left or right lead). (d) Illustration of a scattering state from an incident transverse mode in the left lead, $\psi_{LnE}(x, \mathbf{r}_\perp)$. It reflects into the same lead with the wavefunction-coefficient $r_{Ln'n}(E)$ and transmits into the adjacent lead with the wavefunction-coefficient $t_{RLn'n}(E)$. The absolute-squared of these coefficients yields the probability of reflecting and transmitting.

The energy bands within a lead are filled by electronic states up to a chemical potential μ_α of the reservoirs [207]. The number of filled bands in the lead, as shown in Fig. 4.7(c), corresponds to the total number of transverse modes, N_α, or *channels* [136, 209] in the lead. For example, the filling of three bands shown in Fig. 4.7(c) corresponds to $N_\alpha = 3$ transverse modes. We emphasize two key assumptions in this formalism:

Remark 2. *The contacts between the reservoirs and leads are assumed to be reflectionless (electrons enter the leads without being reflected) and the leads are treated as ideal waveguides (right-moving states all originate from the left reservoir, and left-moving ones only from the right reservoir) [191, 206, 136, 191, 208, 209].*

Therefore, right-moving electrons are occupied up to μ_L, and left-moving ones up to μ_R.

Scattering matrix. The eigenstates in the leads are given by the linear combination of transverse modes propagating to the left and right [209, 136], which can be expressed as [136]:

$$\psi_{eig,E}(x,\mathbf{r}_\perp) = \begin{cases} \sum_n^{N_L} a_n^+ \phi_{LnE}^+(x,\mathbf{r}_\perp) + \sum_n^{N_L} a_n^- \phi_{LnE}^-(x,\mathbf{r}_\perp), & (x,\mathbf{r}_\perp) \in L, \\ \psi_{M,E}(x,\mathbf{r}_\perp), & (x,\mathbf{r}_\perp) \in M, \\ \sum_n^{N_R} b_n^+ \phi_{RnE}^+(x,\mathbf{r}_\perp) + \sum_n^{N_R} b_n^- \phi_{RnE}^-(x,\mathbf{r}_\perp), & (x,\mathbf{r}_\perp) \in R. \end{cases} \quad (4.29)$$

Here, $(x,\mathbf{r}_\perp)$ are the spatial coordinates shown in the inset of Fig. 4.7(a). x is the longitudinal direction and indicates whether the position is within the left lead (L), the scattering region (M), or the right lead (R). $\mathbf{r}_\perp$ is a coordinate in the transverse direction (in a plane parallel to the interface). We denote the eigenfunction within the scattering region by $\psi_{M,E}(x,\mathbf{r}_\perp)$, which we can obtain by solving the eigenvalue problem associated with the Hamiltonian in the scattering region. It is, in general, a complicated function that we do not need to describe transport in the leads [136, 210]. The sum is over all transverse modes available for the given chemical potential in each lead (N_L and N_R modes).

The coefficients in the linear combination are associated with different transverse modes. As shown in Fig. 4.7(a), $\mathbf{a}^+ = (a_1^+, a_2^+, \ldots, a_n^+, \ldots, a_{N_L}^+)$ is associated with incident modes in the left lead moving to the right, while $\mathbf{b}^- = (b_1^-, b_2^-, \ldots, b_n^-, \ldots, b_{N_R}^-)$ with incident modes in the right lead moving to the left. Outgoing modes are given similarly by $\mathbf{a}^-$ and $\mathbf{b}^+$. The coefficients for incoming and outgoing modes can be collected in vectors $\mathbf{c}_{\text{in}} = (\mathbf{a}^+, \mathbf{b}^-)$ and $\mathbf{c}_{\text{out}} = (\mathbf{a}^-, \mathbf{b}^+)$.

We can equate the incoming and outgoing coefficients via a block matrix [136],

$$\mathbf{c}_{\text{out}} = \begin{pmatrix} \mathbf{a}^- \\ \mathbf{b}^+ \end{pmatrix} = \begin{pmatrix} r_L(E) & t_{LR}(E) \\ t_{RL}(E) & r_R(E) \end{pmatrix} \begin{pmatrix} \mathbf{a}^+ \\ \mathbf{b}^- \end{pmatrix} \equiv \mathbf{S} \begin{pmatrix} \mathbf{a}^+ \\ \mathbf{b}^- \end{pmatrix} = \mathbf{S}\mathbf{c}_{\text{in}}. \quad (4.30)$$

This block matrix,

$$S(E) = \begin{pmatrix} r_L(E) & t_{LR}(E) \\ t_{RL}(E) & r_R(E) \end{pmatrix}, \quad (4.31)$$

is the *scattering matrix* [136, 207, 212, 208, 209]. For a given energy of incident electrons, E, the scattering matrix contains the *reflection* and *transmission matrices* r_α and $t_{\bar{\alpha}\alpha}$ ($\alpha, \bar{\alpha} = L, R$, $\alpha \neq \bar{\alpha}$) that contain individual reflection and transmission probability coefficients relating the channels in the same and adjacent leads, respectively [191, 136, 212, 210]. We note that the matrices r_α and $t_{\bar{\alpha}\alpha}$ are $N_{Ch} \times N_{Ch}$ dimensional, where we define N_{Ch} as the total number of (effective) *channels* [136, 212, 209]. N_{Ch} can be different from N_L and N_R. For example, say the right lead has no available modes, but the left lead does. Then, $N_R = 0$, while the effective number of channels is $N_{Ch} = N_L$.

Scattering states. Scattering states are nonlocal wavefunctions that account for incident, transmitted, and reflected wavefunctions [136, 212, 210], and can be used to derive the expression for the total current and the conductance. At a given energy of incident electrons E, they, $\psi_{\alpha nE}$, constitute an incident state n in the lead α, reflected into the same lead in a state n' with a reflection coefficient $r_{\alpha n'n}(E)$, and transmitted into the other lead with the transmission coefficient $t_{\bar{\alpha}\alpha n'n}(E)$. For example, for a state incident in the left lead, $\phi^{+}_{LnE}(x, \mathbf{r}_\perp)$, the scattering state is therefore [136, 210]

$$\psi_{LnE}(x, \mathbf{r}_\perp) = \begin{cases} \phi^{+}_{LnE}(x, \mathbf{r}_\perp) + \sum_{n'}^{N_{Ch}} r_{Ln'n}(E)\, \phi^{-}_{Ln'E}(x, \mathbf{r}_\perp), & (x, \mathbf{r}_\perp) \in L \\ \psi_{M,E}(x, \mathbf{r}_\perp), & (x, \mathbf{r}_\perp) \in M \\ \sum_{n'}^{N_{Ch}} t_{RLn'n}(E)\, \phi^{+}_{Rn'E}(x, \mathbf{r}_\perp), & (x, \mathbf{r}_\perp) \in R \end{cases} \tag{4.32}$$

Fig. 4.7(d) illustrates this scattering state. It reflects from state n to n' in the left (with a probability $r_{Ln'n}$, first line in Eq. (4.32)) and transmits from state n to n' to the right lead (with a probability $t_{RLn'n}$, last line in Eq. (4.32)). We can obtain an analogous expression for ψ_{RnE}, the scattering state originating from an incident state ϕ^{-}_{RnE} in the right lead.

Landauer formula. The Landauer formula relates the differential conductance, which we will use for our TMR calculations, to the scattering matrix. The differential conductance is defined as the infinitesimal change in electric current resulting from an applied voltage, V_{RL}, between the two leads [136]:

$$C_{RL}(E) = \frac{dI(E)}{dV_{RL}}, \tag{4.33}$$

The electric current is given by [136] $I_e(x) = -e \int_{\tilde{\Omega}} d\mathbf{r}_\perp \Psi^*(x, \mathbf{r}_\perp) \hat{J}_x \Psi(x, \mathbf{r}_\perp)$, the expectation value of the current operator $\hat{J}_x$ for a given eigenstate $\Psi(x, \mathbf{r}_\perp)$ at a given energy of incident electrons E, through a cross-section $\tilde{\Omega}$ (inset in Fig. 4.7(a)) of the system. For example, if we consider the left lead ($(x, \mathbf{r}_\perp) \in L$), we obtain the corresponding probability current $I_L = I_e(x)/(-e)$ by inserting for the explicit form of the eigenstate $\psi_{eig,E}$ from Eq. (4.29) as follows:

$$I_L = \int_{\tilde{\Omega}} d\mathbf{r}_\perp \left(\mathbf{a}^{+} \cdot \phi^{+}_{L,E} + \mathbf{a}^{-} \cdot \phi^{-}_{L,E}\right)^* \hat{J}_x \left(\mathbf{a}^{+} \cdot \phi^{+}_{L,E} + \mathbf{a}^{-} \cdot \phi^{-}_{L,E}\right). \tag{4.34}$$

Here, we have written the sum over n in Eq. (4.29) as a dot product between the vectors $\mathbf{a}^{+}$ and $\phi_{L,E} = (\phi_{L0E}, \phi_{L1E}, \ldots, \phi_{LnE}, \ldots \phi_{LN_LE})$.

We use the following observations to derive the Landauer formula for differential conductance. The first two points follow from the above assumptions that the contacts are *reflectionless* and the leads are *ideal waveguides* (Remark 2).

Remark 3.

(i) Every incident electron in lead α follows the Fermi-Dirac distribution of the corresponding reservoir, $f_\alpha(\epsilon) = n_F(\epsilon - \mu_\alpha)$, where ϵ is energy and μ_α the chemical potential [208].

(ii) In the basis of scattering states, the incident coefficient $\mathbf{b}^- = 0$ in the left lead, and the incident coefficient $\mathbf{a}^+ = 0$ in the right lead [136].

(iii) The system conserves probability current, or equivalently, the scattering matrix is unitary ($S^\dagger S = \mathbf{1}_{2N_{Ch}\times 2N_{Ch}}$), resulting in relations such as [212, 136, 209, 210] $\mathbf{1}_{N_{Ch}\times N_{Ch}} = r_L^\dagger r_L + t_{RL}^\dagger t_{RL}$ and $\mathrm{Tr}[t_{LR}^\dagger t_{LR}] = \mathrm{Tr}[t_{RL}^\dagger t_{RL}]$, where the trace is over all N_{Ch} channels.

Due to *(i)*, the total charge current, I_e, is the sum of the probability currents, $I_{\alpha nE}$, originating from the scattering states of each lead, weighed by the occupancy at the incident energy, $f_\alpha(E)$ [191, 136, 207]:

$$I_e = -e \sum_{nE} I_{LnE} f_L(E) + I_{RnE} f_R(E) \tag{4.35}$$

Due to *(ii)*, the probability current, $I_{\alpha nE}$, of a scattering state in, for example, the left lead from Eq. (4.34) is given by [136]

$$I_{LnE} \propto 1 - \left(r_L^\dagger(E)\, r_L(E) \right)_{nn} \tag{4.36}$$

in the scattering state basis. We obtain this by first inserting in Eq. (4.34) for $\mathbf{a}^- = r_L \mathbf{a}^+ + t_{LR}\mathbf{b}^-$ from Eq. (4.30), then using *(ii)* that $\mathbf{b}^- = 0$ in the left lead. The proportionality constant corresponds to a normalization factor of the probability current of the wavefunctions $\phi_{LnE}^\pm$ through a given cross-section [136].

We can now insert in the total current in Eq. (4.35), first Eq. (4.36) and the analogous expression obtained for the right lead, $I_{RnE} \propto -1 + (r_R^\dagger(E)\, r_R(E))_{nn}$, and then use the unitarity relations in *(iii)* to obtain an expression only in terms of transmission probabilities, thus obtaining the Landauer formula given by [136]:

$$I_e = \frac{e}{h} \int_{-\infty}^{\infty} T(E) \left[f_L(E) - f_R(E) \right] dE. \tag{4.37}$$

Here, we have converted the energy-sum into an integral and the n-sum into a trace over transmission matrices, with [212, 136, 210]

$$T(E) = \sum_{n=1}^{N_{Ch}} T_n(E) = \mathrm{Tr}[t_{RL}^\dagger(E)\, t_{RL}(E)]. \tag{4.38}$$

$T(E)$ is the total transmission probability across the junction for a given energy of incident electrons. $f_\alpha = f(E-\mu_\alpha)$, are the Fermi distribution functions, $\mu_\alpha = \mu - eV_\alpha$, and h is Planck's constant. The voltage V can shift the chemical potential from its equilibrium value of μ. Notably, thus far, there is no linear response assumption.

Linear response in the zero-temperature limit

We now derive the Landauer formula for linear response in a two-terminal device at zero temperature. First, we will show that the transport takes place between μ_L and μ_R, thus changing the limits of the integral of the Landauer formula in Eq. (4.37) to this range. We can do linear response for small differences $\delta\mu = \mu_L - \mu_R$.

Zero-temperature limit. For a general two-terminal device, the left and right leads may have different electronic dispersions and chemical potentials as illustrated in Fig. 4.8(a,b). In the zero-temperature limit, Fermi distributions are step functions

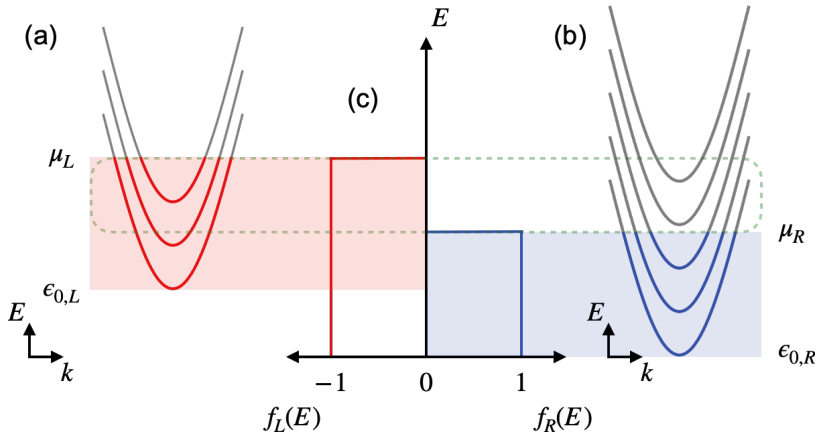

Figure 4.8: Band-filling and Fermi distributions for a two-terminal device in the zero-temperature limit. (a,b) The energy bands in the left and right leads are filled up to the chemical potentials μ_L and μ_R. (c) Shows the corresponding Fermi distribution functions $f_L(E)$ and $f_R(E)$ at zero temperature forming step-functions. The red and blue areas in (a-c) highlight the energy ranges for which electronic transport can place in each lead on their own ($\epsilon_{0,L}$ to μ_L in the left lead and $\epsilon_{0,R}$ to μ_R in the right lead). When the leads are part of the two-terminal system, transport can take place in the energy range between μ_L and μ_R (green dashed rectangle).

$f_\alpha = \Theta(E-\mu_\alpha)$, shown in Fig. 4.8(c). For the left lead, $\epsilon_{0,L}$ is the lowest available energy in the energy bands that a transverse mode can occupy, and for the right lead, it is $\epsilon_{0,R}$. Similarly, the highest available energies are μ_L and μ_R.

Let us consider the current through a cross-section in the left lead. The current through a cross-section in the right lead will be the same because there are only two

terminals. Inserting for the Fermi distributions at zero temperature shown in Fig. 4.8, the Landauer formula (Eq. (4.37)) for current in the left lead simplifies as follows:

$$I_e = \frac{e}{h}\left[\int_{\epsilon_{0,L}}^{\mu_L} T(E)\,dE + \int_{\mu_R}^{\epsilon_{0,R}} T(E)\,dE\right] = \frac{e}{h}\int_{\mu_R}^{\mu_L} T(E)dE. \tag{4.39}$$

In the first equality, we have inserted the step-functions $f_\alpha(E)$ and reversed the sign and integration limits in the second term. As is evident from Fig. 4.8, there are no available states in the left lead between $\epsilon_{0,R}$ and $\epsilon_{0,L}$, and therefore $\int_{\mu_R}^{\epsilon_{0,R}} T(E)\,dE = \int_{\mu_R}^{\epsilon_{0,L}} T(E)\,dE$ for current in the left lead, which is what we are considering here, thus yielding the second equality.

Eq. (4.39) shows that the relevant energy range for transport is between μ_L and μ_R. When μ_L is larger than μ_R, the sign of the current is positive, flowing from left to right, from a region of higher electron density in the left lead to a region with lower electron density in the right lead. Eq. (4.39) holds in general: performing an analogous derivation for the case where, instead, $\epsilon_{0,L}$ is lower than $\epsilon_{0,R}$, also yields the same result; and if $\mu_R > \mu_L$, Eq. (4.39) yields the expected sign-change of the current so that the current flows from right to left, from the region of higher to the one of lower electron density.

Linear response. A small voltage $\delta V = V_L - V_R$ can be applied between the two leads, inducing a small difference in chemical potential $\mu_L - \mu_R \equiv e\,\delta V$. The above integral, Eq. (4.39), then reduces to

$$\lim_{(\mu_L-\mu_R)\to 0} I_e = \frac{e}{h}\,T(\mu)(\mu_L - \mu_R) = \frac{e^2}{h}\,T(\mu)\delta V \tag{4.40}$$

which is notably linear in δV. In the linear response limit, $\delta V \to dV$, and thus the differential conductance is [191, 136]

$$C(E) = \frac{e^2}{h}T(E). \tag{4.41}$$

We have now derived the Landauer formula for differential conductance in the zero-temperature, linear response limit, which is notably proportional to the transmission.

Ferromagnetic and altermagnetic quantum wire calculation

We now apply the Landauer-Büttiker formalism to a quantum wire system with a ferromagnet and an altermagnet using Kwant. As discussed in the summary at the end of this section, we will use this quantum wire calculation as a reference when we later compute tunneling through a central barrier.

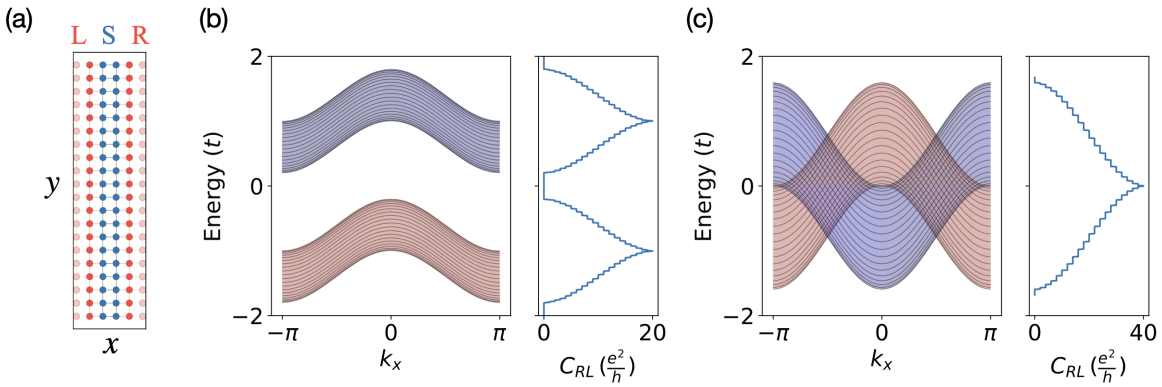

Figure 4.9: Differential conductance through a ferromagnetic and altermagnetic quantum wire model. (a) Set-up with a left lead L, scattering region S, and right lead R. The tight-binding Hamiltonian is identical in all three regions; thus, it is a quantum wire. (b) Energy bands of the ferromagnetic leads are shown in the left panel by red- and blue-colored spin up- and down-polarized bands. The right panel shows the differential conductance C_{RL} as a function of the chemical potential or energy of incident electrons. (c) Same for the altermagnetic model.

Quantum wire. Consider the quantum wire setup in Fig. 4.9(a) made using Kwant [205]. The system is two-terminal, with two leads shown by red and blue regions marked L and R and a scattering region shown by the blue central region marked S. The leads and the scattering region consist of the same Hamiltonian, and the leads are translationally invariant in the direction away from the scattering region, so this system is an infinite quantum wire.

Figs. 4.9(b) and 4.9(c) show the energy bands of the ferromagnetic and altermagnetic leads, respectively, computed with Kwant [205]. The ferromagnetic model is given by the real-space Hamiltonian $H_{\rm FM} = t_{\rm FM}\sum_{\langle ij\rangle} c_i^\dagger c_j + J_{\rm FM}\sum_i c_i^\dagger c_i \sigma_z$ with nearest-neighbor hoppings $t_{\rm FM}$ and onsite spin-dependent Zeeman term $J_{\rm FM}\sigma_z$. We set $t_{FM} = 0.2\,t$ and $J_{\rm FM} = -0.5\,t$. The altermagnetic model is given by $H_{\rm AM}^{\rm NN}$ from Eqs. (2.21) and (2.26), and Fig. 2.3(a,c), which we showed hosted the valley spin-polarization in Fig. 4.5(c). We set $t_J = -0.4\,t$.

The bands here are, in effect, projected onto the longitudinal k_x-axis, as the leads are finite along the transverse y-direction (for the altermagnet, we can see this by comparing, e.g., to the bulk altermagnetic bands in Fig. 2.3(c)). Because there are twenty sites along y and two possible spins, both models have forty projected energy bands in total. Analogous to Fig. 4.7, the number of possible transport channels at any given chemical potential μ, or energy of incident electrons E on the y-axes here in Figs. 4.9(b) and 4.9(c), depends on the particular energy dispersion. For example, the ferromagnetic model has twenty channels at the energy $E = t$, while the altermagnetic model has forty channels at $E = 0\,t$.

We calculated the transmission $T(E)$ in Eq. (4.41) using Kwant. The right panel in Figs. 4.9(b) and 4.9(c) shows the resulting conductance through the wire. As the energy of the incident electrons increases from $-2\,t$, new bands become occupied, opening new transport channels and thereby producing steps in the differential conductance. In the ferromagnet, the conductance reaches a maximum at $20\,\frac{e^2}{h}$ at the energy t, corresponding to the perfect transmission through the wire with a $\frac{e^2}{h}$ contribution per channel. In the altermagent, the conductance reaches its maximum of $40\,\frac{e^2}{h}$ at the energy $0\,t$, also corresponding to perfect transmission.

Summary. This conductance calculation shows that, in a quantum wire without a central barrier, the differential conductance in Eq. (4.41) changes step-wise in the transmission $T(E)$, each transport channel produces a $\frac{e^2}{h}$ conductance signal, and the conductance is symmetric with respect to the energy of incident electrons, E, for the two models.

We will see in the next section that, when replacing the scattering region by a tunneling barrier in the altermagnetic model, the step-wise signal smoothens out, each transport channel produces $< \frac{e^2}{h}$ conductance, and the conductance is no longer symmetric, but rather, it tends to be larger for higher energies of incident electrons because they can more easily tunnel across the barrier.

4.2 Tunneling magnetoresistance simulation with altermagnetic models

By performing simulations, we now demonstrate a large tunneling magnetoresistance (TMR) in our altermagnetic d-wave models. Furthermore, we will show that the valley spin polarization of the energy bands enhances TMR, demonstrate with three-dimensional models that TMR is present with differently oriented d-wave planes, and that adding spin-orbit coupling does not significantly change the TMR signal.

4.2.1 Quasi-two-dimensional simulations

Model and differential conductance calculation. We use the Landauer-Büttiker formalism and Kwant and the quasi-two-dimensional[2] altermagnetic models considered in previous sections. Fig. 4.10 shows the model and numerical tunneling magnetoresistance results.

Fig. 4.10(a) shows the model setup. We implement the left and right altermagnetic leads (AM_1 and AM_2) as the tight-binding model $H_{\mathrm{AM}}^{\mathrm{NN}}$ from Eq. (2.21)

[2] *Quasi* because the spins can be out-of-plane with respect to the two-dimensional crystal.

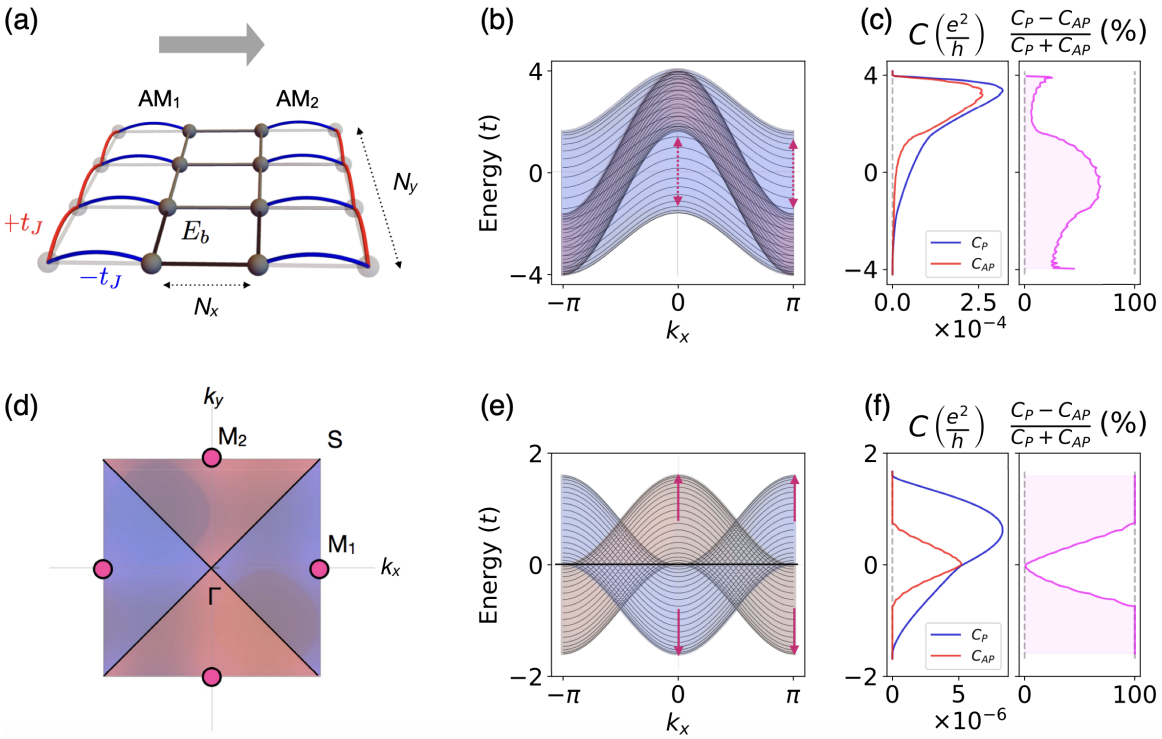

Figure 4.10: Transport calculation for an altermagnetic tunnel junction model. (a) Schematic of the model consisting of two altermagnetic leads, AM_1 and AM_2, separated by a spacer shown by the gray scattering region. For a description of the parameters used, see the main text. (b) Projected spin up (red) and spin down (blue) polarized band structure as a function of the longitudinal wavevector k_x. The Hamiltonian parameters correspond to the first case described in the text and to Fig. 4.3(c). (c) Differential conductance for the parallel (C_P) and antiparallel (C_{AP}) configurations of the Néel vectors of the altermagnetic leads, and their relative difference $\frac{C_P - C_{AP}}{C_P + C_{AP}}$. (d) The altermagnetic band structure in the first Brillouin zone and viewed from above for the second set of parameters described in the text and corresponding to Fig. 4.5(c). The magenta circles mark the valleys. (e, f) The same as (b, c) but for the second set of parameters. The magenta arrows in (b) and (e) mark the energy ranges with pronounced valley spin polarizations, where spin-up and down channels de-couple. Figure adapted from [12], CC BY 4.0.

(Fig. 4.10(a), red and blue hoppings) plus the normal hopping term $H_{\mathrm{N}}^{\mathrm{NN}}$ from Eq. (2.30) (Fig. 4.10(a), gray hoppings). Thus, the bulk model is given by

$$H_{\mathrm{AM}}^{\mathrm{NN}} + H_{\mathrm{N}}^{\mathrm{NN}} = 2t_J \left[\cos k_y - \cos k_x\right] \boldsymbol{d} \cdot \boldsymbol{\sigma} + 2t \left(\cos k_x + \cos k_y\right) \mathbf{1}, \tag{4.42}$$

with a corresponding bulk band structure shown from a top view in 4.10(d). We implement the altermagnetic model for two illustrative cases, namely with and without the added normal hopping term $H_{\mathrm{N}}^{\mathrm{NN}}$ (last term in Eq. (4.42)).

In the first case, shown in Figs. 4.10(b) and 4.10(c), we have added the normal hopping term. We use the paramters $t_J = t_J^L = 0.4\,t$, where t_J^L denotes the hopping

in the lead. This case corresponds to the model we used to explain the GMR concept in Fig. 4.3(c).

In the second case, shown in Fig. 4.10(e) and 4.10(f), there is no normal hopping term in the leads. We used the parameters $t_J = t_J^L$. This case corresponds to the model we used to explain the TMR concept in Fig. 4.5(c) and used to simulate transport through an altermagnetic wire in Fig. 4.9.

The nonmagnetic spacer is the same for both cases, $H_{\mathrm{N}}^{\mathrm{NN}}$, with $t = t^B = 0.025\, t_J^L$, where t^B denotes the hopping in the barrier. In order for the spacer to constitute a barrier where electrons must tunnel to get through, we add an onsite energy term to it, $\mathcal{H}_{\mathrm{onsite}}(\mathbf{k}) = E_B\mathbf{1}$, were we use $E_B = 10\, t_J^L$. We use an $N_x = 2$ number of sites for the barrier length along the longitudinal direction and $N_y = 20$ sites for the width of the system, the same width as in our wire calculation in Fig. 4.9.

We calculate the conductance for Néel vectors in the leads being parallel ($\boldsymbol{d} = \boldsymbol{d}^{\mathrm{AM}_1} = \boldsymbol{d}^{\mathrm{AM}_2}$, where $\boldsymbol{d}$ is the Néel vector in Eq. (4.42)) and antiparallel ($\boldsymbol{d}^{\mathrm{AM}_1} = -\boldsymbol{d}^{\mathrm{AM}_2}$).

As expected from the discussion of the valley polarization in Sec. 4.1.3, the conductivity for the parallel case C_P is larger than for the antiparallel case, C_{AP}. Additionally, compared to the perfect transmission calculation in Fig. 4.9(c), the presence of the barrier induces an energy-dependent asymmetry in the conductance in Fig. 4.10(c) and 4.10(f), because the electrons that have higher energy can more easily tunnel over the barrier. The barrier also reduces the conductance magnitude and smoothens the previously sharp conductance steps in Fig. 4.9(c).

Tunneling magnetoresistance. Figs. 4.10(c) and (f) show the differential conductance for the parallel case, C_P plotted in blue, and antiparallel case, C_{AP} plotted in red. The difference

$$R = \frac{C_P - C_{AP}}{C_P + C_{AP}} \tag{4.43}$$

plotted by the magenta line quantifies the TMR and can be understood by analyzing the band structures of the leads shown to the left, in Figs. 4.10(b) and (e). From our qualitative analysis in Sec. 4.1.3, we expect the ratio $R \sim 100\%$ for energies where the band structure has the pristine valley polarization because the transport channels for opposite spins up and down are separated in momentum space, de-coupling them.

Valley spin polarization enhances the tunneling magnetoresistance. We observe this maximized TMR for the second set of parameters in Fig. 4.10(f) for the energies $E \gtrsim 0.8\, t$ and $E \lesssim -0.8\, t$ highlighted by magenta arrows in Fig. 4.10(e). It manifests in a zero conductance for the antiparallel case $C_{AP} = 0$ because there is a complete mismatch in the spin and momentum in the available lead eigenstates in such a way that the scattering state has a probability 0 of transmitting into the opposite lead, thus closing the transport channels. In the parallel case, there are available states

in the same spin channel in the opposite lead for all the incident energies, and thus, electrons tunnel over the barrier, yielding a finite C_P.

For $E \sim 0\,t$, the tunneling magnetoresistance R is suppressed because the spin up and down bands are degenerate, forming a nodal line highlighted by the black lines in figures 4.10(d) and 4.10(e).

The spin-up and spin-down bands partially overlap for the first set of parameters. This overlap couples the channels. However, valley splittings are present, highlighted by the magenta dashed arrows in Fig. 4.10(b), and for these energies, R is indeed the largest (bump in magenta signal in Fig. 4.10(c)).

For both models, the tunneling magnetoresistance is most prominent for energies with corresponding, pronounced spin-polarized valleys separated from other energy bands in momentum and energy (large degree of *valley-character*), thus de-coupling the transport channels of opposite spins. Therefore, the model simulation corroborates our qualitative analysis in Sec. 4.1.3.

4.2.2 Three-dimensional simulations with in- and out-of-plane d-wave models

In the previous section, we looked at a quasi-two-dimensional altermagnetic system. Now, we will show that large tunneling magnetoresistance ratios $\frac{C_P - C_{AP}}{C_P + C_{AP}} \sim 100\%$ are also present in three-dimensional systems, and with various orientations of the d-wave plane and positions of the valleys relative to the interface.

Set-up and orientations of the d-wave planes. We have investigated junctions with spacer dimensions $N_x \times N_y \times N_z$ and N_i between 2 and 20. One such representative junction is shown in Fig. 4.11(a), with $N_x = N_y = 10$ and $N_z = 2$, which we focus on next.

With the 3D models described in Sec. 2.2 and Fig. 2.5, the *d-wave plane*—where two nodal lines cross $\mathbf{\Gamma}$, or, planes parallel to it—can be oriented in-plane or out-of-plane with respect to the interface between the leads and the tunnel barrier. Without loss of generality, let the interface be in the xy-plane as in Fig. 4.11(a). Then, we recall that the altermagnetic exchange Hamiltonians from Fig. 2.5 with nearest-neighbor or next-nearest neighbor hoppings in the xy-plane (the NN_{xy} and NNN_{xy} models) correspond to the d-wave magnetism being in-the-xy-plane, i.e., in-plane with respect to the interface. Similarly, with nearest-neighbor exchange terms in the zy-plane (the NN_{zy} model), the d-wave plane is out-of-plane with respect to the interface.

Fig. 4.12(a-c) shows the corresponding bulk band structures along the paths in Fig. 4.11(b,c). They all exhibit valley spin polarizations corresponding to the insets from Fig. 2.5. For example, for the NN_{zy} model in 4.1(b), the top right valley corresponds to the iso-energy cut in Fig. 2.5(b). Since the d-wave magnetism lies in

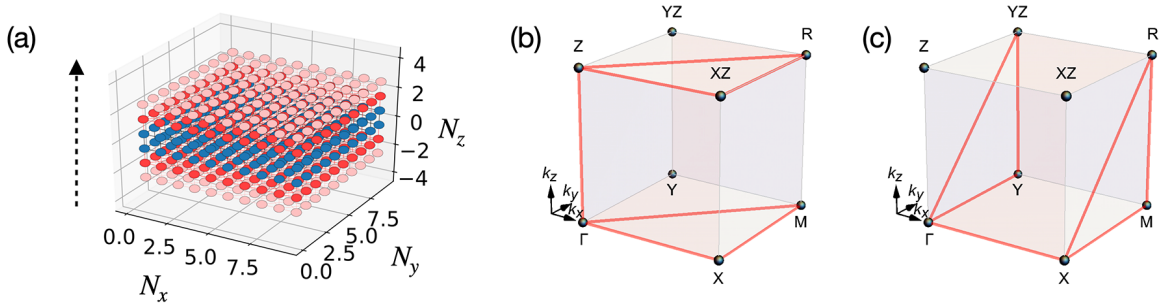

Figure 4.11: Three-dimensional tunnel junction and Brillouin zone. (a) Set-up for a three-dimensional tunnel junction. The altermagnetic leads are shown with red sites and the $10 \times 10 \times 2$-dimensional spacer with blue sites. The dashed arrow marks the transport direction used for all calculations here, z, the out-of-plane direction of the interface plane xy. (b, c) The Brillouin zone notation with two different paths marked by red lines. Figure adapted from [12], CC BY 4.0.

the yz-plane, the bands are spin-split along, e.g., $\Gamma - Y$ and $\Gamma - Z$ but not along $\Gamma - X$. On the left in Fig. 4.1(b), the path is the same as in Fig. 4.1(a, c).

Tunneling magnetoresistance results. In Fig. 4.12(a,a1), we calculate the TMR for the in-plane NN_{xy} model, where the d-wave plane is in-plane with the interface, analogous to our concept illustration for TMR in Fig. 4.5(a). As in the quasi-2D system, the magnetoresistance is maximized for the energy regions with spin-polarized valleys that separate well in momentum space, $E > 2\,t$ and $E < -2\,t$ here.

In Fig. 4.12(b,b1) is the calculation for the out-of-plane NNN_{zy} model. In addition to the maximized signals around the valleys at higher and lower energies, there is an enhanced signal around zero energy for both the parallel and antiparallel orientations of the altermagnetic leads, which was absent in the in-plane simulation in (a,a1). The spin splitting around the $\mathbf{\Gamma}$-point is responsible for the enhancement.

In Fig. 4.12(b,b2), we show that lowering the barrier height and increasing the system size does not significantly alter the substantial tunneling magnetoresistance signal. However, lowering the barrier height alone makes the individual conductance signals more asymmetric than with higher barriers because the relative difference in the transmission of electrons at higher and lower incident energies becomes more significant when the barrier is lower.

In Fig. 4.12(c,c2), we show the result for the NNN_{xy} model. The number of valleys doubles compared to the NN_{xy} model in the first Brillouin zone for a given Fermi surface, as we saw explicitly in Fig. 2.5. The location of the valleys also changes. However, the plateau in the tunneling magnetoresistance does not change compared to Fig. 4.12(a1). This model could be used to approximate valleys in altermagnetic RuO_2 from Fig. 3.18(a) and their contribution to tunneling magnetoresistance, as the valleys for both are centered at the same locations.

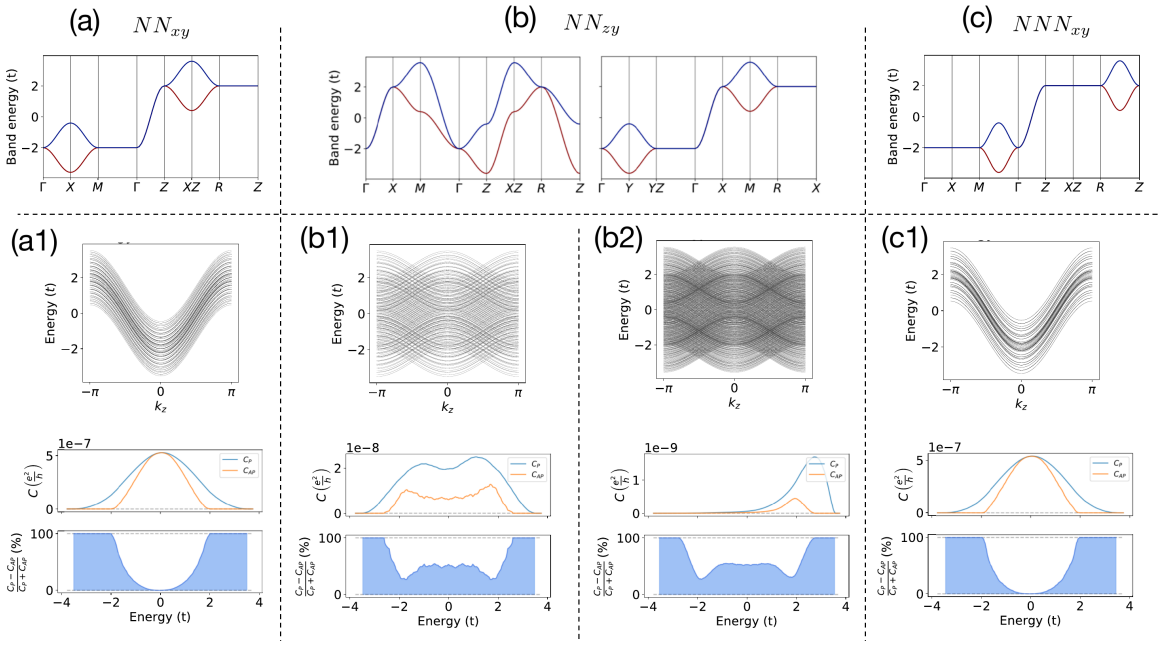

Figure 4.12: Tunneling magnetoresistance simulations for three-dimensional model systems with altermagnetic leads. The first row is bulk energy bands, where the coloring labels the band index. The second row shows the energy bands for the leads (top) and the conductances for parallel and antiparallel geometries and their relative difference (bottom). The system size is $10 \times 10 \times 2$ and the onsite barrier energy is $E_b = 60\,t$ in (a1), (b1) and (c1). In (b2), they are $20 \times 20 \times 4$ and $E_b = 6\,t$. In all the calculations, the planes with the d-wave magnetic hoppings have no additional normal hopping, while the direction out-of-the-d-wave plane has normal hopping t. Similarly to the two-dimensional model, the normal hopping in the spacer is ten times smaller than in the leads ($t_b = t/10$), and we use $t_J = 0.4\,t$ for all the calculations. Figure adapted from the supplementary information of [12], CC BY 4.0.

Adding relativistic spin-orbit coupling. We now study the effect of adding a weak Rashba spin-orbit coupling term, $\lambda\,(\sigma_y \sin k_x - \sigma_x \sin k_y)$, on the TMR. Here, $\lambda = 0.04\,t = t_J/10$ represents the upper limit for the spin-orbit interaction strength in the materials discussed in this chapter. In Fig. 4.13, we show the NNN_{xy} model with the added spin-orbit coupling term in panel (a) and the tunneling magnetoresistance ratio in panel (b). Comparing it to the system without spin-orbit coupling in Fig. 4.12(c,c1), we see that the effect on the tunneling magnetoresistance is insignificant.

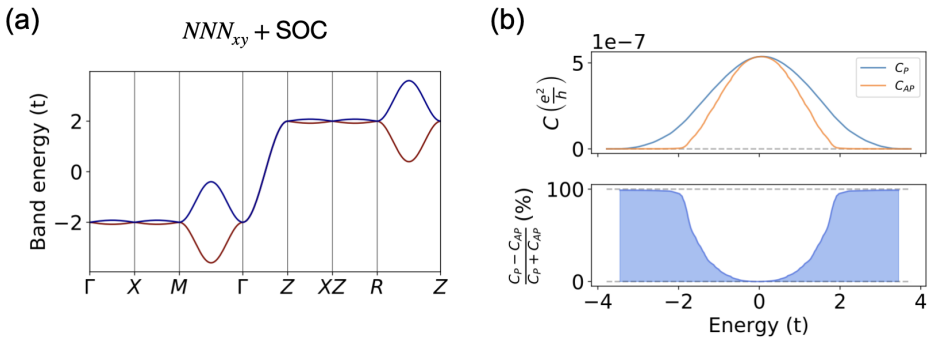

Figure 4.13: Effect of adding spin-orbit coupling to model. (a) Bulk energy bands with the spin-orbit coupling term added to the NNN_{xy} model (the coloring marks the band index). (b) The calculated conductances (top) and their relative difference (bottom). Apart from the spin-orbit coupling term, all parameters are identical to those in Fig. 4.12(c,c1).

4.3 Spin conductivity and giant magnetoresistance in RuO_2

In this section, we show our collaborative density functional theory calculation of the spin conductivity and giant magnetoresistance (GMR) [12] for the altermagnetic candidate RuO_2. Fig. 4.14(a) shows the crystal structure of RuO_2 in the altermagnetic case discussed in Ch. 3.1.8, where we highlight its altermagnetic sublattice-transposing symmetry $[C_2||C_{4z}\boldsymbol{t}]$. For details about this symmetry, see the previous discussion in Fig. 3.15(a). We recall that the nonmagnetic Oxygen atoms, shown by black sites here, break the translation and inversion sublattice-transposing symmetries that would otherwise be present in collinear antiferromagnets and type-II spin Laue groups [3, 25].

In our collaborative work [12], we calculated the electronic band structure and conductivities of RuO_2 with VASP and Wannier90 as described in Ch. 2.3.6. We further confirmed the following results [12] with the WannierBerri code [213].

Fig. 4.14(b-e) shows the spin-polarized band structure, longitudinal charge conductivity for the two spin channels, and GMR for RuO_2. The spin polarization highlighted by the dashed rectangles in panel (c) is of the anisotropic type discussed in Sec. 4.1.1. The group velocities are plotted on the Fermi surface in panel (b), which are anisotropic and differently oriented in the two spin channels shown in the left and right panels (the two channels are related by $[C_2||C_{4z}]$). Panel (d) shows the Boltzmann equation determined longitudinal charge conductivities for the two spin channels. They differ, as predicted from our symmetry analysis. This difference gives rise to a finite GMR, shown by the magenta line in panel (e), calculated from the conductivities in the two spin channels and Eq. (4.12) [12]. The GMR maximizes

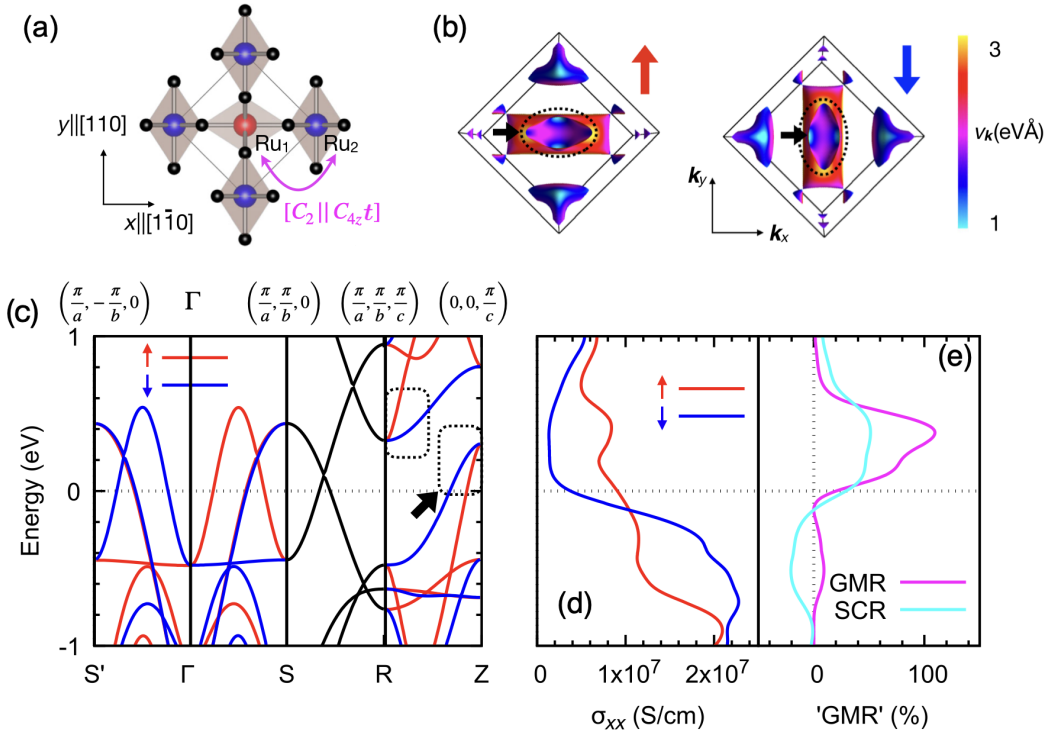

Figure 4.14: First-principles calculation of GMR in RuO_2. (a) Crystal structure of RuO_2. Magnetic sublattices with opposite spins, Ru_1 and Ru_2, are marked by red and blue sites. The magenta arrow highlights the symmetry $[C_2||C_{4z}]$ relating the sublattices. (b) Anisotropic group velocities shown on the Fermi surface. (c) The nonrelativistic electronic band structure with spin-up and spin-down polarized bands marked in red and blue. We identify the anisotropic spin polarization highlighted by the dashed rectangles (and correspondingly for the group velocities, marked by dashed ovals in (b)). The anisotropy leads to (d) large differences in longitudinal charge conductivities for the two spin channels and, hence, (e) GMR shown by the magenta line. For comparison, we also calculated the spin-splitter conductivity shown by the cyan line (SCR) in (e). Figure adapted from [12], CC BY 4.0.

when the Fermi level coincides with the regions of highly anisotropic spin-polarized bands around $\sim 0.4\,\mathrm{eV}$ highlighted by dashed rectangles in panel (c), as expected from our qualitative analysis. In this region, the GMR reaches a scale of $\sim 100\%$.

We note that the size of the GMR signal correlates with the spin-splitter conductivity [7], shown by the cyan line in Fig. 4.14(e). We calculated this conductivity by $(\sigma_{x'y',\uparrow} - \sigma_{x'y',\downarrow})/\sigma_{x'x'}$, c.f. Fig. 4.4(b), where the directions are $x' \parallel [100]$, and $y' \parallel [010]$ shown in Fig. 4.14(a).

4.4 Altermagnetic material design for tunneling magnetoresistance

Here, we discuss the valley spin polarization in the context of searching for altermagnetic candidate materials with large TMR.

For example, in our collaborative work, we studied the electronic structure of a candidate altermagnetic spin order in Mn_5Si_3 [12]. Mn and Si are abundant and light elements (Mn has atomic number 25, Si 11) compared to, e.g., RuO_2 (Ru has atomic number 44), and can be grown epitaxially Si(111) substrates [112, 214]. We took the magnetization to be concentrated on the same two-fifths of Mn sites as reported in several experiments [50, 49, 215] and as suggested by previous DFT calculations [216]. Their symmetry is assumed to be d-wave altermagnetic, belonging to a spin Laue group ${}^2m^2m^1m$ in agreement with the experimentally observed crystal anomalous Hall effect and Nernst effect in thin-films [112, 129]. We performed DFT calculations with collinear VASP without spin-orbit coupling as described in Ch. 2.3.6.

Fig. 4.15(a) shows the calculated spin densities of Mn_5Si_3, concentrated on the abovementioned Mn sites in the altermagnetic order. We also show the sublattice-transposing mirror symmetries from the spin Laue group by magenta lines. Fig. 4.15(b,c) shows the corresponding Brillouin zone and collaboratively calculated spin-polarized band structure [112]. The band structure displays the anticipated valley spin polar-

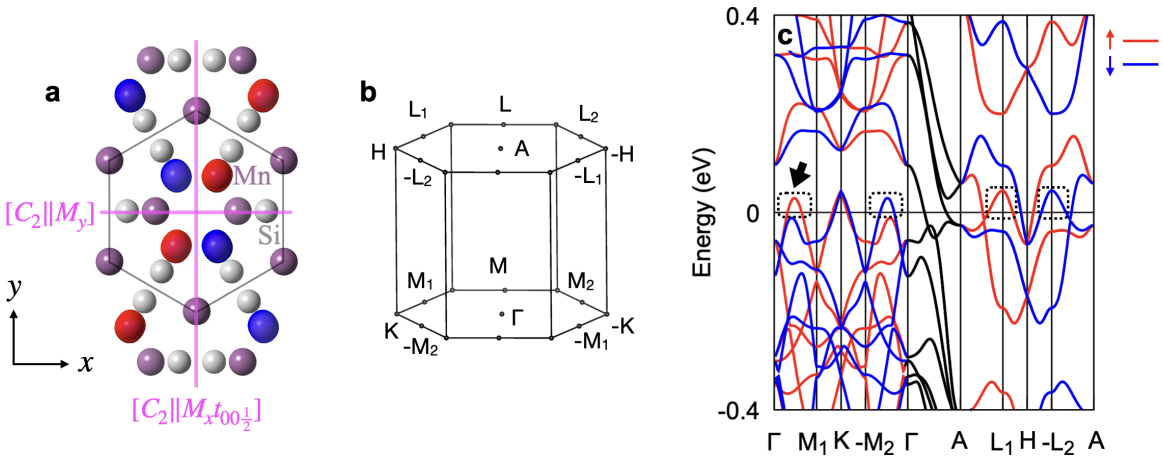

Figure 4.15: Example of valley spin polarization in an altermagnetic candidate material Mn_5Si_3. (a) Magnetization densities (red and blue for spin up and down), mirror sublattice-transposing symmetries (magenta lines indicate the mirror planes), and the unit cell (black lined hexagon). (b) The first Brillouin zone. (c) Spin-polarized energy bands (red and blue denote opposite spin polarizations). The energy bands host valleys with alternating spin polarizations separated in momentum space, which can produce high TMR in altermagnets. Figure (b) and (c) adapted from [112], CC BY 4.0.

ization at the Fermi energy, as highlighted by the dashed rectangles in Fig. 4.15(c). We note that the valleys come in pairs related by the sublattice-transposing symmetries, the mirrors shown in Fig. 4.15(a), in analogy to the valleys seen earlier in Figs. 4.5 and 4.10.

Guiding principles in material search for high TMR in altermagnets. From our analysis, if we want to search for altermagnetic materials with potentially large TMR, we need materials where the valleys are *(i)* close to the Fermi level and *(ii)* well-separated in momentum space. Point *(ii)* de-couples the spin channels and maximizes TMR in analogy to the model in, e.g., Fig. 4.10(e,f). For example, the valleys highlighted in Fig. 4.15(c) satisfy these conditions: they are at the Fermi level, and the mirror sublattice-transposing symmetries in Fig. 4.15(a) relates the opposite-spin valleys at well-separated wavevectors, e.g., L_1 and $-L_2$ shown here.

Fortunately, since sublattice-transposing symmetries relate valleys by rotations and mirrors, they enforce the symmetry-related valleys with opposite spins to be separated in reciprocal space. Regarding the separation of these symmetry-related valleys, we note that d-wave altermagnets, due to their lower number of nodal surfaces than higher-order g- and i-wave altermagnets [25] (see, e.g., Fig. 1.9), on a general level tend to have a larger separation between these symmetry-related valleys. This tendency for larger separation potentially makes d-wave magnets more suitable candidates for searching for TMR. We will further discuss the robustness of TMR and GMR with altermagnets in Sec. 4.5.

4.5 Discussion

General symmetry criteria

TMR. In principle, all altermagnets allow for TMR because the altermagnetic energy bands are spin-polarized. We have additionally demonstrated that TMR is enhanced around the valley spin polarization features of the altermagnetic band structure. These valleys can form around both high-symmetry and low-symmetry points in reciprocal space. For example, Mn_5Si_3 has valleys at the high-symmetry points $\mathbf{M}_1$ and $\mathbf{M}_2$, while RuO_2 has valleys along the low symmetry line $\mathbf{\Gamma} - \mathbf{S}$. However, TMR can also be enhanced away from the band extrema of these valleys, provided that the spin polarized bands are separated enough in reciprocal space to sufficiently de-couple the transport channels for opposite spins. More systematic and detailed analysis is beyond the scope of our work.

GMR. By symmetry, we have found that in-plane GMR is allowed in d-wave altermagnets from symmetric spin-polarized currents, see Sec. 4.1.2. The symmetric spin

currents cancel in g- and i-wave altermagnets within linear response in the nonrelativistic limit [12]. We recall that the d-wave spin point groups are ${}^2m{}^2m{}^1m$, ${}^24/{}^1\mathrm{m}$, ${}^24/{}^1m{}^2m{}^1m$, and ${}^22/{}^2m$ [25].

In contrast to magnetic symmetries, spin symmetries do not depend on the Néel vector orientation. Therefore, these general symmetry criteria for GMR and TMR also do not depend on the Néel-vector orientation.

Robustness

Nonrelativistic spin-splittings. Regarding robustness, we emphasize that strong altermagnetism has nonrelativistic origins. The magnetic exchange and crystal fields determine the strength of the strong altermagnetic spin splittings, and the *spin splitting in the altermagnetic form*, see Def. 3, is moreover protected by the spin symmetries of the magnetic crystal [25, 1]. Typically, strong altermagnetism [30] determines the overall form of the band structure. In contrast, spin-orbit coupling and weak altermagnetism [30] often constitute comparatively weaker relativistic corrections. See for instance Fig. 3.2 and discussions in Ch. 3.1. Spin-orbit coupling usually plays a minor role in the resulting transport we have studied here and does not destroy the transport effects, as exemplified in both our Landauer-Büttiker transport simulation in Sec. 4.2.2 and Boltzmann transport calculations in [7].

Scattering. The spin polarization of electrons can decohere because of scattering, such as from interactions between electrons or from disorder. Scattering can lead to a finite length for which an electron can travel before the direction of its spin changes due to scattering, referred to as the spin-scattering length [204]. We have found band structures in our models, RuO_2, and Mn_5Si_3 with well-separated valley polarizations in momentum space. Similar to conventional valleytronics with two-dimensional materials [73], this significant momentum separation can suppress intervalley scattering. Studying the scattering effect in more detail is beyond the scope of our work

Difference to TMR in antiferromagnets

In antiferromagnets, earlier studies have shown that TMR can originate from quantum interference effects [57], requiring pristine interfaces [58], or an interfacial ferromagnetic moment forming due to the specific termination at the interfaces with the spacer [59].

With our altermagnetic TMR and GMR concepts [12] described in this chapter, however, we have shown that TMR and GMR in altermangets originate from their bulk, spin-polarized band structures with valley and anisotropic spin polarization features [12]. Hence, TMR in altermagnets should be less sensitive to interfacial disorder

than TMR in collinear antiferromagnets—in collinear antiferromagnets, such disorder would tend to suppress the effects proposed in the earlier studies [58]. Our TMR concept [12] indeed agrees with an independently conducted study of a $RuO_2/TiO_2/RuO_2$ tunnel junction, which showed that the TMR in this system (with the *d-wave plane* in a distinct in-plane orientation with the interface, in a so-called spin neutral current mechanism) was nearly independent of the interface termination [12, 13].

Difference to the Anomalous Hall effect for detecting the Néel vector

We now compare GMR and TMR to a different mechanism that can detect Néel vector-reversal, namely the anomalous Hall effect (AHE). Altermagnetism and crystallographic spin group theory can explain the time-reversal symmetry breaking necessary for the AHE, e.g., in RuO_2, Mn_5Si_3, and MnTe [3, 112, 5, 2, 113]. However, for the AHE, additional spin-orbit coupling is needed to translate this time-reversal symmetry breaking from the spin into the orbital sector in order to produce a transverse Hall current [3, 112, 5, 2, 113]. Therefore, the symmetry criteria for AHE differ from the ones for GMR and TMR on a fundamental level.

For the AHE, the symmetry criteria are additionally formulated using magnetic symmetries, which couple spin and crystal space and depend on the Néel vector orientation. In order for the magnetic material to exhibit the AHE, these magnetic symmetries need to allow for a pseudovector which is odd under time-reversal, also known as the anomalous Hall vector [3, 112, 5, 2, 113].

These magnetic symmetries differ from the nonrelativistic crystallographic spin groups classifying altermagnets, as we saw in Ch. 1.4. For example, the d-wave symmetry of RuO_2 is independent of the Néel vector orientation. The magnetic group for RuO_2, however, changes [3]: when the Néel vector is along the [100] axis, the AHE is prohibited, while in the (001)-plane, the AHE is allowed [3]. In contrast to the AHE, the TMR and GMR effects originate from longitudinal, nonrelativistic currents due to nonrelativistic, strong altermagnetism, and thus the crystallographic spin group formalism alone can be used to predict the presence of the spin currents.

Conclusion

In this thesis, we have studied the electronic structure of unconventional magnetic systems. Despite being compensated, these unconventional magnets show spin-polarized order in momentum space even without spin-orbit coupling, contrasting conventional antiferromagnets, which show no nonrelativistic spin-polarised order in momentum space. We have focused on several materials of even-parity-wave altermagnetism (with time-reversal symmetry broken electronic structures), and we have proposed a new class of odd-parity-wave unconventional magnets (with time-reversal symmetric electronic structures).

Tab. 4.1 summarizes the symmetries of the electronic structure and magnetic order in real and crystal space for altermagnets and p-wave magnets, as well as other more conventional magnetic orderings and materials with spin-textures due to spin-orbit coupling. Already on the nonrelativistic level, each opposite-spin channel of the magnetic crystal structure of altermagnets breaks half of the symmetries of the underlying nonmagnetic crystal [25]. Moreover, rotation or mirror symmetries, possibly combined with translations, relate opposite spin channels by bringing one magnetic sublattice onto another, see the *Symmetry* column in Tab. 4.1. These symmetries, together with the symmetry-breaking in each spin channel and collinearity, give rise to spin-polarized, spin-split, collinear electronic band structures in even-parity-wave, d-, g-, and i-wave forms from Fig. 1.9, as described by crystallographic spin group theory [25]. Therefore, the nonrelativistic altermagnetic bands spin-split in the distinct *altermagnetic form* from Def. 3. They disperse even-in-momentum around $\mathbf{\Gamma}$, for instance, $\sim k^2$ as shown in the *Spin-splitting* column in Tab. 4.1, and are therefore distinct from ferromagnets (constant and even-in-momentum Zeeman splitting $\propto k^0$ at $\mathbf{\Gamma}$ shown in the fifth row of the table), and relativistic spin-orbit coupling in noncentrosymmetric systems (odd and linear-in-momentum spin splitting $\sim k$ around $\mathbf{\Gamma}$ shown in the fourth row of the table) [25].

This thesis has built on the crystallographic spin symmetry classification of altermagnets [25] to explore altermagnets and odd-parity-wave magnets and spintronics concepts in them. In Ch. 1 on symmetries of magnetic crystals, we showed that magnetic systems with time-reversal combined with translation symmetry do not have

to be Kramers spin degenerate [93], as previously commonly believed [21, 179, 217]. In Ch. 2 on electronic structure theory, we derived altermagnetic tight-binding models guided by spin symmetries of altermagnetism [12]. We also discussed how to constrain magnetic moments in noncollinear density functional theory (DFT) calculations to make the solution adhere to experimentally observed magnetic structures with symmetries of interest [93].

In Ch. 3.1 on strong (nonrelativistic) and weak (relativistic) altermagnetism, we contributed to confirmations of the existence of altermagnetism for the first time, in collaboration with three experimental groups. We calculated the electronic structures of the selected altermagnets, which were confirmed in photoemission experiments, with excellent agreement in MnTe [30] and very good agreement in CrSb[31].

In Ch. 4 on spin-dependent response, we developed TMR and GMR concepts based on how different types of altermagnetic spin-polarization features in the energy bands de-couple the spin channels and give rise to tunneling current and longitudinal spin-polarized charge current, without requiring net magnetic moments or spin-orbit coupling [12].

In Ch. 3.2, we have predicted unconventional odd-parity-wave magnetism using the crystallographic spin group formalism. We formulated general symmetry guidelines to predict this type of magnetism arising from the magnetic order of magnetic crystals, which has been commonly believed to be impossible in existing literature due to the abovementioned time-reversal combined with crystal translation symmetry. Our symmetry guidelines enabled us to predict p-wave and odd-parity-wave magnetism in numerous material candidates (more than 70 so far), to demonstrate the p-wave electronic structure with DFT calculations of realistic material candidates, to formulate minimal models, and to predict nonrelativistic anisotropic transport as a result of p-wave magnetism [93].

The altermagnetism and odd-parity-wave magnetism we have explored (Tab. 4.1, second and third rows) can potentially have superior properties over conventional ferromagnetic and spin-orbit coupled systems (Tab. 4.1, fourth and fifth rows), for example, due to being magnetically compensated and exhibiting large spin splittings of nonrelativistic origin. Using ferromagnets for TMR and GMR poses a limit on miniaturization due to their net magnetic moment, and the magnetization is slower to switch and may require more energy to switch faster compared to compensated magnets [71, 72]. Moreover, relativistic spin-orbit coupling is often weak and requires heavy, rare, and sometimes toxic elements to be sizeable, which may not be feasible for applications.

P-wave and odd-parity-wave magnetism, like relativistic spin-orbit coupling in noncentrosymmetric systems, breaks inversion symmetry, preserves $\mathcal{T}$ due to the sublattice-transposing symmetry $\mathcal{T}\mathbf{t}$, and disperses odd-in-wavevector around the $\mathbf{\Gamma}$-point, for

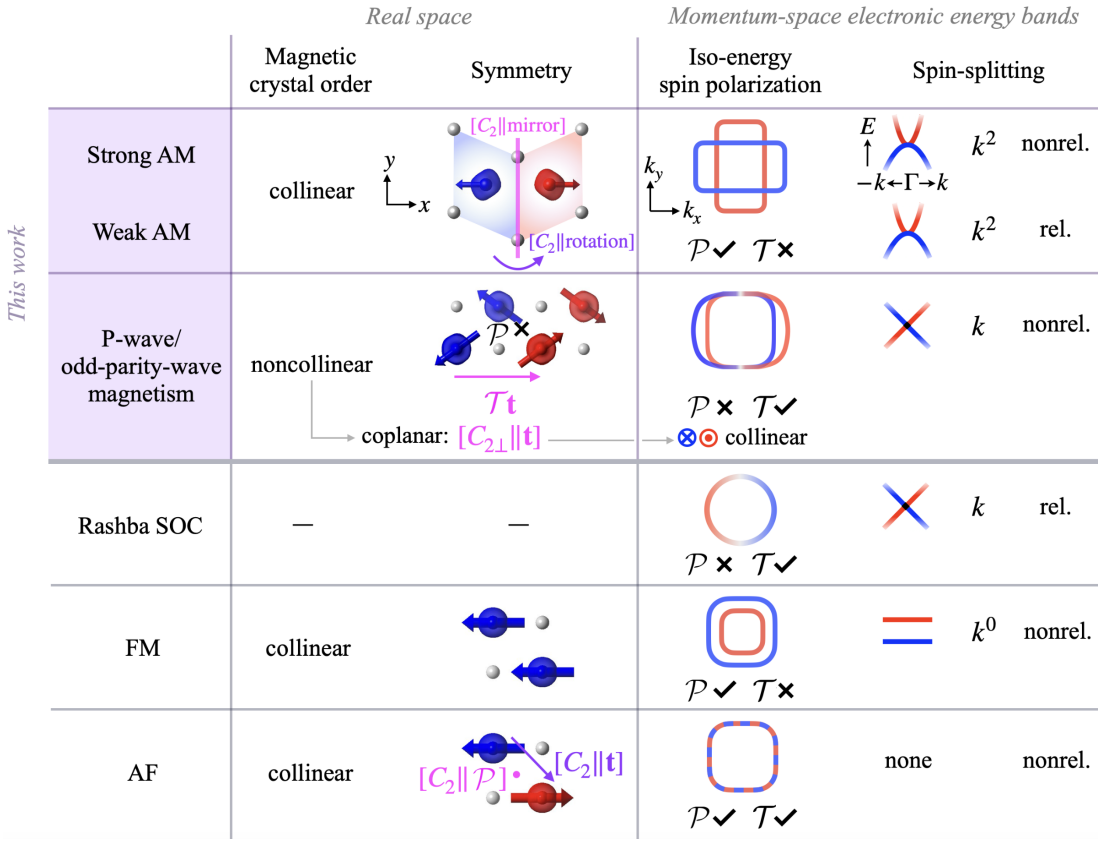

Table 4.1: Symmetries of altermagnets and odd-parity-wave magnets explored in this thesis (first two magenta rows) compared to conventional magnets and spin-orbit coupling typically used for spintronics (Rashba spin-orbit coupling, SOC, ferromagnetism, and collinear antiferromagnetism; last three rows). The middle columns—*Real space*—show the magnetic crystals (colored magnetic and gray nonmagnetic sites and arrows showing the magnetic moments) and representative spin-polarized electronic structures in real space, or spin densities (red-blue shapes around magnetic atoms). We highlight their distinct sublattice-transposing symmetries (magenta and purple annotated lines, arrows, and points; bracketed annotations use the crystallographic spin symmetry notation) and that our odd-parity-wave magnets must break crystal inversion $\mathcal{P} = [E||\mathcal{P}]$ (black cross). The right columns—*Momentum-space electronic energy bands*—illustrate the electronic energy band structures resulting from the symmetry constraints of the real space magnetic orders. On the left are iso-energy cuts (red-blue colors are opposite spin expectation values along a given spin quantization axis) with even- or odd-parity-wave spin polarizations. We highlight their breaking/preserving $\mathcal{P}$ and time-reversal $\mathcal{T}$, and the out-of-plane collinearity for coplanar odd-parity-wave magnets. On the right are spin-split energy dispersions around $\mathbf{\Gamma}$. They are even-in-wavevector k (e.g., $\sim k^2$) for strong altermagnetism from collinearity and weak altermagnetism when crystal inversion symmetric; odd-in-k (e.g., $\sim k$) for odd-parity-wave magnets from noncollinearity and crystal inversion breaking; odd-in-k for Rashba SOC from crystal inversion breaking, and constant for ferromagnets ($\propto k^0$ at $\mathbf{\Gamma}$) from net magnetism.

instance $\sim k$ as illustrated in Tab. 4.1 (for more details, see Eq. (3.13)). However, unlike their relativistic counterparts, odd-parity-wave and p-wave magnetism originates from magnetic exchange, not relativistic spin-orbit coupling. We moreover elucidate that coplanar odd-parity-wave magnets host nonrelativistic, collinear spin polarizations protected by $[C_{2\perp}||\mathbf{t}]$ symmetry of their magnetic crystal [93], and not, e.g., from fine-tuning relativistic spin-orbit coupling parameters [167]. Due to their crystalline protection, our odd-parity-wave magnets lend themselves to spectroscopic verification and device physics. To address the latter, we have predicted nonrelativistic anisotropic transport as a consequence of p-wave magnetism [93].

Given the recent, broad, and immediate impact that even-parity d- and g-wave altermagnetism has had across several contemporary research fields, including, but not limited to [1, 218, 45] fundamental magnetism research [30, 33, 34, 32, 31, 197, 198, 196, 219], spintronics [12, 7, 9, 10, 11, 3, 174, 2, 112, 5, 172, 113], optical effects [174, 220, 221, 92, 222, 223], and superconducting or topological insulator hybrid systems [224, 87, 225, 226, 227, 228, 229, 230], our present identification of odd-parity-wave and p-wave magnets could allow similar research directions utilizing odd-parity-wave magnetism instead. Since odd-parity-wave magnetism does not require heavy elements, and the spin-splitting-size can be orders of magnitude larger than from spin-orbit coupling in the same material, it may open possibilities for research areas where the physics so far relies on strong spin-orbit coupling systems – from topology research to efficient charge-to-spin conversion research [93].

Altermagnetism and odd-parity-wave magnetism are distinct. Altermagnetism and our odd-parity-wave magnetism constitute distinct and complementary forms of magnetism, as shown in Tab. 4.1. The latter is noncollinear and odd-parity, and their spin-polarized band structure preserves $\mathcal{T}$ symmetry; in contrast, altermagnetism is collinear and even-parity with its d-, g-, and i-wave spin polarizations, and breaks $\mathcal{T}$ symmetry, akin to ferromagnets—see the right column in Tab. 4.1. This robust $\mathcal{T}$ breaking from the magnetic order in altermagnets is not present in p-wave and odd-parity-wave magnetism (Tab. 4.1, third row), relativistic spin-orbit coupling (fourth row), and collinear antiferromagnetism (last row).

The spin density ordering in real space is the original culprit distinguishing these types of magnetism. The central columns in Tab. 4.1 illustrate these distinct symmetries. The shaded regions represent spin densities around atoms, and the colored arrows indicate the direction of the magnetic moments. In ferromagnets and antiferromagnets, each spin channel obeys all symmetries of the underlying crystal, represented by rounder-shaped spin densities. In contrast, in altermagnets and odd-parity-wave magnets, they do not, represented by anisotropic-shaped spin densities. Moreover, in altermagnets and odd-parity-wave magnets, the spin channels are related by distinct sublattice-transposing symmetries of the spin Laue groups, shown by purple

and magenta annotations. These symmetries impose spin-degenerate or zero spin-expectation value nodal surfaces in the electronic band structures, here only in these magnets.

We also emphasize that due to their distinct symmetries, altermagnets and our p-wave and odd-parity-wave magnets differ from other noncollinear compensated magnets [181, 2, 119], multipolar orders in noncollinear magnets [20, 182, 183], and further noncollinear magnets [180, 184, 185], as they are noncollinear, contrary to altermagnets, and their magnetic crystals break $\mathcal{T}\mathbf{t}$ and $[C_{2\perp}||\mathbf{t}]$ symmetry or preserve crystal inversion symmetry, or both, contrary to our p-wave and odd-parity-wave magnets.

Strong altermagnetism arises from magnetic exchange on the nonrelativistic level, and thus, it typically manifests as considerable spin-splittings away from the symmetry-imposed, nonrelativistic nodal surfaces. It reaches values of an $\sim$ eV scale in the candidate materials MnTe, CrSb, and RuO_2 we have studied here [30, 31, 38].

Weak altermagnetism arises along the nonrelativistic spin-degenerate nodal surfaces where the spin-degeneracy lifts when adding spin-orbit coupling [30, 6]. In MnTe, these splittings are inversion symmetric due to the inversion symmetry of the magnetic MnTe crystal. In both theory and the collaborative experiment, this relativistic spin spitting disperses quadratically around the $\mathbf{\Gamma}$-point, in concurrence with the crystal inversion symmetry. Constant or linear terms vanish around the Γ-point. This weak altermagnetic form of the spin splitting is highlighted in the *Weak AM* column of Tab. 4.1.

Vanishing net moment. In the altermagnetic and odd-parity-wave magnetic candidates we have studied here [30, 31, 38, 93, 12, 112, 129, 130], the presence of only even terms in altermagnets, or odd terms in odd-parity-wave magnets, shows that any net magnetic moment is vanishing, as a net moment leads to a constant term and band-splitting at the Γ-point as illustrated in the row marked *FM* in Tab. 4.1. The vanishing of a net magnetic moment agrees with previous *ab initio* and experimental studies of MnTe [113], RuO_2 [77, 5], CrSb [35, 37], Mn_5Si_3 [50, 49, 231, 215], and CeNiAsO [44]. The vanishing of linear terms in altermagnets is in contrast to Rashba and our odd-parity-wave magnetism, which all disperse linearly or odd in k around $\mathbf{\Gamma}$ as shown in Tab. 4.1 [30, 93].

Hierarchy of energy scales and coexistence of strong and weak altermagnetism. The weak altermagnetic splittings in MnTe, remarkably, reach a $\sim 100\,\mathrm{meV}$ energy scale in both experiment and *ab initio* calculations along the $\Gamma - K$ path [30]. The high atomic number of Te (52) explains this large spin splitting size, which is comparable to the large spin splittings found in noncentrosymmetric materials with heavy elements, such as BiTeI [114], where Bi has a higher atomic number (83).

Notably, the spin splitting due to strong altermagnetism is larger than that of the weak altermagnetic spin-splittings we studied, e.g., in MnTe, which is reasonable

because the origin of strong altermagnetism is nonrelativistic, arising from magnetic exchange. The strong altermagnetic spin splitting in MnTe and CrSb reaches the scale of half an eV in both theory and experiment along the paths we have studied (in MnTe: $\bar{\mathbf{\Gamma}} - \bar{\mathbf{M}}$ shifted along $+k_z$ away from the $\mathbf{\Gamma} - \mathbf{M}$ path, where $\mathbf{M} = \frac{\mathbf{b_1}}{2} + \frac{\mathbf{b_2}}{2}$; in CrSb: $\frac{\mathbf{M}}{2} - (\frac{\mathbf{M}}{2} + \frac{\mathbf{b}_3}{2})$) [30, 31]. Similar results for MnTe were also reported in [32, 33]. The strong altermagnetic splitting can be even larger along other paths, such as $\mathbf{\Gamma} - \mathbf{L}$ in MnTe and CrSb ($\mathbf{L} = \mathbf{M} + \frac{\mathbf{b}_3}{2}$) [25]. For example, experimental spectroscopic data of MnTe along paths intersecting with the $\mathbf{\Gamma} - \mathbf{L}$ path agrees well with theory [34]. Further reports of altermagnetic band splittings have also appeared in CrSb [198, 197, 196].

We also show with *ab inito* calculations that MnTe simultaneously hosts strong g-wave altermagnetism, as well as weak altermagnetism in the $k_z = 0$ plane that is collinear: in the $k_z = 0$ plane, the spin expectation values for the weak altermagnetism point out-of-plane along z, contrary to the strong altermagnetism, where it points along the in-plane Néel vector. These two types of strong and weak altermagnetism coexist in the system in the presence of relativistic spin-orbit coupling [30].

The agreement between our *ab initio* calculated band structures and ARPES experiments shows that altermagnetism can directly arise from the symmetries of the magnetic crystal, as predicted in [25, 1]. Since altermagnetism is mathematically rigorously described by distinct symmetries of their magnetic crystal, it is an elementary phase of matter, as phases of matter are in general distinguished by their symmetries (the Landau paradigm) and topology [26]. Remarkably, it has been omitted from band theory in solid-state physics for nearly a century. Our work highlights the strength of the crystallographic spin group theory classification: we can use this classification to unravel new magnetic phases and their rich phenomenology, for which there is a hierarchy of energy scales and numerous potential applications [30].

Materials design for spintronics. The above-described features of altermagnetism and p-wave and odd-parity-wave magnetism lead to strong spintronics effects that could be superior to their conventional counterparts in several aspects, in addition to the prospects of miniaturization and orders of magnitude faster devices of compensated magnets. We can here produce large $\sim$ eV scale spin splittings that either break or preserve time-reversal symmetry, thus allowing for spin-dependent transport protected by the magnetic crystal [12, 93], dissipationless currents [112], or the possibility of spin-orbit coupling-like physics, without requiring the use of heavy elements [93]. Additionally, the spin polarization is collinear in the electronic band structures for both the strong and weak altermagnetism we studied [30, 31, 38, 12, 112, 129], and coplanar odd-parity-wave magnets [93], which has so far not been available in noncollinear compensated magnets [2, 119].

In altermagnets and our p-wave and odd-parity-wave magnets, contrary to rela-

tivistic spin-orbit coupling, we principally do not rely on including heavy elements to reach large spin splittings because they arise from magnetic exchange. Thus, the materials design approach for identifying materials with large spin splittings in these magnets can be based on identifying materials with significant exchange and crystal fields [25, 1]. Seeking to maximize the size of the spin splitting could allow for larger and more robust spin-polarized currents and magnetoresistive effects by helping to decouple or enhance the anisotropy of different spin channels, as we demonstrated with our TMR and GMR concepts.

TMR, GMR, and spin-polarized currents. In analogy to ferromagnets, the strong spin-split, spin-polarized energy bands are responsible for TMR and GMR effects in altermagnets. In contrast to ferromagnets, however, our GMR and TMR concepts in altermagnets rely on the valley and anisotropic spin-polarizations unique to altermagnets and not present in ferromagnets.

The altermagnetic valley spin polarization forms isotropic valleys that break symmetries of the underlying crystal in each spin channel and which are related by $[C_2||A]$ symmetry (A is a rotation or mirror) in reciprocal space. It is allowed in every altermagnet away from the $\mathbf{\Gamma}$-point and nodal planes on the nonrelativistic level. This valley spin polarization allows for electrons to tunnel between valleys of the same spin polarization when the Néel vector for the two altermagnetic electrodes in a TMR set-up are parallel, allowing an overall current to run between the electrodes. When the two Néel vectors are antiparallel, the spin polarization is opposite for matching-wavevector valleys, suppressing the overall tunneling current. The difference in current between the electrodes for the parallel and antiparallel orientations of the Néel vector quantifies the TMR. In our model Landauer-Büttiker simulations and collaboratively in altermagnetic material candidates RuO_2 and Mn_5Si_3, the simulated TMR and GMR values, with TMR being $R = \frac{C_P - C_{AP}}{C_P + C_{AP}}$ in our model, and TMR $= \frac{1}{2}(R_n + \frac{1}{R_n} - 2)$ and GMR $= \frac{1}{4}(R_\sigma + \frac{1}{R_\sigma} - 2)$ in the DFT, see Eqs. (4.43), (4.27) and (4.12) for details, reached an order of $\sim 100\%$.

The anisotropic spin-polarization forms around the $\mathbf{\Gamma}$-point. It is also enforced by $[C_2||A]$ symmetries and each spin channel breaking symmetries of the underlying crystal. It exists in all altermagnets by symmetry, but, also by symmetry, only d-wave magnets produce longitudinal, symmetric spin-polarized charge current (predicted to be significantly larger than the antisymmetric component [7]) due to the anisotropic spin-polarization. Due to these spin-polarized charge currents, altermagnets can also host GMR, in analogy to ferromagnets. However, we stress that the anisotropic spin-polarization giving rise to the spin-polarized currents is unique to altermagnets due to their above-described symmetries and being overall magnetically compensated.

From a materials design perspective, spin-polarized currents are generally larger the more anisotropic the spin polarization, which generally may accompany materials

with larger spin-splittings. The valley spin polarizations may generally also separate more from other energy bands with larger spin splittings and in d-wave altermagnets over g- and i-wave altermagnets, resulting in a larger separation of the opposite spin channels.

Our nonrelativistic TMR and GMR mechanisms are based on strong, nonrelativistic altermagnetism. They are thus unavailable in collinear antiferromagnets, as they are Kramers spin degenerate, while compensated magnetism is unavailable in ferromagnets with their net magnetization. Thus, with our TMR and GMR concepts, altermagnetism can, in principle, combine superior properties of collinear antiferromagnets and ferromagnets: compensated magnetism and strong nonrelativistic spin-dependent transport.

Summary. Our work has implications ranging from the fundamental understanding of magnetic quantum matter to functionalizing compensated magnets for spintronics. Altermagnetism, p-wave magnetism, and odd-parity-wave magnetism can principally host spin-splittings of the $\sim$ eV scale that robustly follows from their magnetic crystal structures without being accompanied by net magnetization and without requiring heavy elements. Moreover, our work highlights the strength of crystallographic spin group theory as we delineate the subtle coexistence of quadratically dispersing strong and weak altermagnetism and the hierarchy of their energy scales. We have also used it to propose the existence of our p-wave and odd-parity-wave magnetism generally. Our identification and corroboration of spin splittings in altermagnets, p-wave, and odd-parity-wave magnets break with previously held notions that spin-split energy bands in collinear magnets could only arise from net magnetization in real space or relativistic spin-orbit coupling, as well as the notion that materials belonging to type-IV magnetic groups do not host spin splittings [21, 179, 217].

Our identification of spin polarizations and their symmetries in altermagnets and p-wave and odd-parity-wave magnets, and the magnetoresistive and anisotropic transport that follow, redefines what has been thought to be possible in spintronics with compensated magnets and spin-orbit coupling-dependent physics. For example, it overcomes the inherent challenges with functionalizing Kramers spin degenerate antiferromagnets for spintronics. In these antiferromagnets (if allowed by symmetry), the relativistic spin-orbit coupling has been necessary to spin-split the energy bands and achieve spin polarizations useful for functionalization in spintronics, bringing the additional challenge that relativistic spin-orbit coupling is weak for common elements and is significant only in heavy, rare elements. However, altermagnets and our odd-parity-wave magnets can principally overcome such functionalization challenges. Firstly, altermagnets can potentially have applications for computing hardware using magnetoresistance effects with faster magnetization switching and lower energy consumption than ferromagnets [1]. Secondly, our p-wave and odd-parity-wave mag-

netism has the potential to overcome the challenge of relativistic spin-orbit coupling requiring heavy elements. Due to their time-reversal-preserving, inversion-breaking spin polarizations and textures, they provide an alternative avenue for exploring spin-orbit coupling-like physics, using light elements instead of heavy ones, combined with large $\sim$ eV scale spin splittings, with potential ramifications ranging from fundamental physics such as topological materials to the more applied, such as charge to spin conversion [93], e.g., a sizeable nonrelativistic Edelstein effect, i.e., a spin density accumulation due to an applied electric field [176].

Appendices

A Anti-unitarity of the time-reversal operator

Here, we verify that time-reversal $\mathcal{T}$ is *antiunitary*, i.e., that it obeys Eqs. (1.3) and (1.4). We first note that it can be written as a product of a unitary operator U and complex conjugation K [94]:

$$\mathcal{T} = UK \tag{44}$$

To show Eq. (1.3) holds for the time-reversal operator, we start by showing how time-reversal acts on a state, $|\tilde{\alpha}\rangle = \mathcal{T}|\alpha\rangle$. Note that we can expand the eigenstates in the basis kets as $|\alpha\rangle = \sum_{a'} |a'\rangle\langle a'|\alpha\rangle$ and that the basis kets, given by

$$|a'\rangle = (0, 0, \ldots, 1, \ldots 0) \tag{45}$$

are not affected by complex conjugation K. We thus have

$$|\tilde{\alpha}\rangle = \mathcal{T}|\alpha\rangle = UK \sum_{a'} |a'\rangle\langle a'|\alpha\rangle = \sum_{a'} \langle a'|\alpha\rangle^* U|a'\rangle = \sum_{a'} \langle\alpha|a'\rangle U|a'\rangle, \tag{46}$$

where we have inserted for a complete basis set $1 = \sum_{a'} |a'\rangle\langle a'|$ (second equality) and performed the complex conjugation (third equality). Similarly, for $|\tilde{\beta}\rangle$:

$$|\tilde{\beta}\rangle = \sum_{a'} \langle\beta|a'\rangle U|a'\rangle \longleftrightarrow \langle\tilde{\beta}| = \sum_{a'} \langle a'|\beta\rangle U^\dagger|a'\rangle. \tag{47}$$

Inserting these expressions (Eqs. (46) and (47)), we have

$$\langle\tilde{\beta}|\tilde{\alpha}\rangle = \sum_{aa''} \left[\langle a''|\beta\rangle U^\dagger|a''\rangle\right] \left[\langle\alpha|a'\rangle U|a'\rangle\right] = \sum_{a'} \langle a'|\beta\rangle\langle\alpha|a'\rangle = \langle\alpha|\beta\rangle = \langle\beta|\alpha\rangle^* \tag{48}$$

Here, we have used unitarity $U^\dagger U = \mathbf{1}$, and the orthogonality $\langle a''|a\rangle = \delta_{a'a''}$ to perform the first summation (second equality), and then removed the complete set (third equality). We have thus shown that when we apply $\mathcal{T}$ to the kets $|\alpha\rangle$ and $|\beta\rangle$, the transformed kets $|\tilde{\alpha}\rangle$ and $|\tilde{\beta}\rangle$ obey Eq. (1.3) [94].

To show that $\mathcal{T}$ is antiunitary, it now remains to show that it obeys Eq. (1.4) (that it is antilinear). To show this, we apply complex conjugation to the complex constants c_1 and c_2 and then move them to the left as follows:

$$UK(c_1|\alpha\rangle + c_2|\beta\rangle) = Uc_1^* K|\alpha\rangle + Uc_2^* K|\beta\rangle = c_1^* UK|\alpha\rangle + c_2^* UK|\beta\rangle. \tag{49}$$

We now have the desired relation in Eq. (1.4), with $UK = \Theta$.

In summary, we have shown that the time-reversal operator is antiunitary: it obeys Eq. (1.3) and is antilinear (Eq. (1.4)) [94].

B Basis for spin-half systems

Note that even though K does not affect the basis kets, $|a'\rangle$, its action on the eigenvectors, $|\alpha\rangle$, is affected by the choice of basis. For example, a spin-half $S_y = \frac{\hbar}{2}\sigma_y$ eigenket (σ_i being spin Pauli matrices) in the S_z basis reads [94]

$$\frac{1}{\sqrt{2}}|\uparrow\rangle \pm \frac{i}{\sqrt{2}}|\downarrow\rangle \tag{50}$$

and changes under the action of K due to the complex factor i. But if we use the S_y eigenkets themselves as basis kets, the eigenkets do not change because $K|\uparrow\rangle = |\uparrow\rangle$, as was the case with the basis ket in Eq. (45).

C Coset decomposition of the crystallographic group G

Firstly, note that we can decompose any group $\mathbf{G}$ into two parts or cosets. These two cosets' sum, or union, must contain all elements of $\mathbf{G}$. The two cosets are always disjoint, with no elements in common, and form sets with an equal number of elements. Formally, cosets are defined as follows[232].

Definition 4. *If g is an element of the group $\mathbf{G}$ and $\mathcal{B}$ is a subgroup of $\mathbf{G}$, then the left coset of $\mathcal{B}$ is $g\mathcal{B} = \{gE, gB_2, gB_3, \dots\}$, where $B_2, B_3, \dots$ are elements of $\mathcal{B}$.*

The two cosets of $\mathbf{G}$ are,

$$\mathbf{G} = \mathbf{H} + (\mathbf{G} - \mathbf{H}) \tag{51}$$

The first part, $\mathbf{H}$, is the halving subgroup of $\mathbf{G}$. $\mathbf{H}$ contains half the elements of $\mathbf{G}$, namely $\{E, h_2, \dots\}$, and it is itself a group according to the conditions in Def. 1. Since $\mathbf{H}$ is a group, it must contain the identity element. The second part, $\mathbf{G}-\mathbf{H}$, contains the rest of the elements of $\mathbf{G}$, after subtracting the halving subgroup $\mathbf{H}$, namely the elements $\{A, \mathcal{G}_2, \dots\}$. This second part is not a group because subtracting $\mathbf{H}$ removes the identity element.

The second coset can be further expressed as,

$$\mathbf{G} - \mathbf{H} = A\mathbf{H} \tag{52}$$

where A is an arbitrary element of $\mathbf{G}-\mathbf{H}$. This way of writing the coset will be useful later. For example, if $\mathbf{G}$ is the Laue group in Eq. (1.14), then we can choose $\mathbf{H}$ to be the first two elements, $\{E, P\}$ and $\mathbf{G} - \mathbf{H}$ the last two elements, $\{C_{2y}, M_y\}$. A can be either C_{2y} or M_y, and with either choice of A, Eq. (52) holds: $A\mathbf{H} = C_{2y}\{E, P\} =$

$\{C_{2y}, M_y\} = \mathbf{G} - \mathbf{H}$ and $A\mathbf{H} = M_z\{E, P\} = \{M_y, C_{2y}\} = \mathbf{G} - \mathbf{H}$, where we used $C_{2y}P = M_y$ and $M_yP = C_{2y}$ (see the multiplication table in Eq. (1.15)).

Now, we provide a general proof for Eq. (52). Because $\mathbf{H}$ contains half the elements of $\mathbf{G}$, using $\mathbf{H}$, there are two possible cosets of $\mathbf{G}$, namely $\mathbf{H}$ itself and $g\mathbf{H}$, where g is any element of $\mathbf{G}$. Per construction, $\mathbf{G}$ is the sum over, or union of, all left cosets of $\mathbf{G}$, expressed as

$$\mathbf{G} = \mathbf{H} + g\mathbf{H}$$

But $\mathbf{G}$ is also the sum over, or union of, $\mathbf{H}$ with $\mathbf{G} - \mathbf{H}$:

$$\mathbf{G} = \mathbf{H} + (\mathbf{G} - \mathbf{H})$$

Comparing these two forms of $\mathbf{G}$, we see that $g\mathbf{H} = \mathbf{G} - \mathbf{H}$ for any element g of $\mathbf{G}$. We can further restrict ourselves to the case where $g = A$, an element of $\mathbf{G} - \mathbf{H}$, because all elements of $\mathbf{G} - \mathbf{H}$ are elements of $\mathbf{G}$. Therefore, $\mathbf{G} - \mathbf{H} = A\mathbf{H}$.

With this alternative form of the second coset, we can write $\mathbf{G}$ in terms of its coset decomposition,

$$\mathbf{G} = \mathbf{H} + A\mathbf{H} \tag{53}$$

To summarize, we have seen that with Eq. (51), we can decompose a space or point group $\mathbf{G}$ into two cosets. With Eq. (53), the second coset is expressed as a product between the halving subgroup $\mathbf{H}$ and an arbitrary element of $\mathbf{G} - \mathbf{H}$. From the form $A\mathbf{H}$, we can already anticipate that if A is a rotation or a mirror operation, and if there are further translation operators in $\mathbf{H}$, then there are also rotations or mirrors combined with translations in $\mathbf{G} - \mathbf{H}$. If elements of $\mathbf{G} - \mathbf{H}$ are exclusively rotations or mirrors (possibly combined with translations), we can construct altermagnetic crystallographic spin groups with it, which are mutually exclusive from ferromagnetic and antiferromagnetic ones (Eqs. (1.27)-(1.29)) [25].

D Nodal lines in coplanar p-wave Kagome model

Here, we derive the nodal lines parallel to the $\mathbf{b}_1$-axis in the coplanar p-wave Kagome model from Fig. 3.23(a). Fig. S1 shows the symmetry $[C_{2x'}||M_{\mathbf{a}_2}]$ enforcing the nodal lines. The symmetry comprises a mirror $M_{\mathbf{a}_2}$ in real space, marked by the magenta thick line in Fig. S1, and the two-fold spin-space rotation $C_{2x'}$ around the marked x'-axis. The mirror $[E||M_{\mathbf{a}_2}]$ lies parallel to the x' axis, which is -30 degrees rotated from the x-axis, or, in reciprocal space, it points parallel to the $\mathbf{b}_1$-vector, shown in Fig. 3.22 in the main text, and crosses the $\mathbf{\Gamma}$-point. Let $k_{x'}$ be a wavevector-component along the $\mathbf{b}_1$-vector and $k_{\perp x'}$ be a wavevector-component that is perpendicular to the $\mathbf{b}_1$-vector. Then, the symmetry acts as follows on the energy bands:

$$\epsilon(k_{x'}, k_{\perp x'}, 0, 0, s_z) = [C_{2x'}||M_{\mathbf{a}_2}]\epsilon(k_{x'}, k_{\perp x'}, 0, 0, s_z) = \epsilon(k_{x'}, -k_{\perp x'}, 0, 0, -s_z). \tag{54}$$

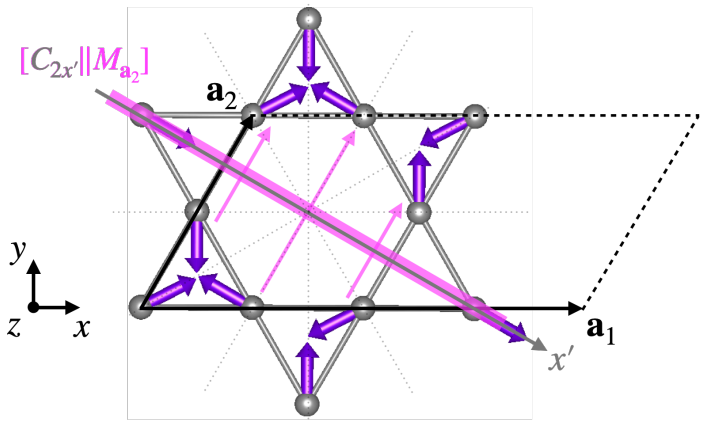

Figure S1: Symmetry $[C_{2x'}||M_{\mathbf{a}_2}]$ of the coplanar p-wave Kagome model. The mirror $[E||M_{\mathbf{a}_2}]$ is shown by the thick magenta line. It mirrors pairs of sites as indicated by the magenta arrows. Combined with the spin-space rotation $[C_{2x'}||E]$ around the rotation axis x' (gray arrow), $[C_{2x'}||M_{\mathbf{a}_2}]$ transposes the differently oriented spins, or, magnetic sublattices. All other mirror symmetries of the nonmagnetic crystal (dotted gray lines) are not associated with spin symmetries of the magnetic crystal.

This equation implies that $s_z = 0$ for $k_{\perp x'} = 0$, which corresponds to the line along $\mathbf{b}_1$ crossing the $\mathbf{\Gamma}$-point. Therefore, $[C_{2x'}||M_{\mathbf{a}_2}]$ imposes the nodal line, with zero spin expectation value, parallel to the $\mathbf{b}_1$-vector and crossing $\mathbf{\Gamma}$.

By combining this symmetry with the periodicity of the Brillouin zone, analogously to in Eq. (3.4), we see that also the Brillouin zone edges parallel to the $\mathbf{b}_1$-axis are nodal lines, concurrent with Fig. 3.23(a). These are the only nodal lines as further mirrors that are symmetries of the nonmagnetic crystal (dotted gray lines in Fig. S1) are not associated with spin symmetries of the magnetic crystal.

Bibliography

[1] Libor Šmejkal, Jairo Sinova, and Tomas Jungwirth. Emerging Research Landscape of Altermagnetism. *Physical Review X*, 12(4):040501, dec 2022.

[2] Libor Šmejkal, A. H. MacDonald, Jairo Sinova, Satoru Nakatsuji, and Tomas Jungwirth. Anomalous Hall antiferromagnets. *Nature Reviews Materials*, 7(6):482–496, mar 2022.

[3] Libor Šmejkal, Rafael González-Hernández, Tomáš Jungwirth, and Jairo Sinova. Crystal time-reversal symmetry breaking and spontaneous Hall effect in collinear antiferromagnets. *arXiv:1901.00445, Science Advances*, 6(23):eaaz8809, jun 2020.

[4] Makoto Naka, Satoru Hayami, Hiroaki Kusunose, Yuki Yanagi, Yukitoshi Motome, and Hitoshi Seo. Spin current generation in organic antiferromagnets. *arXiv:1902.02506, Nature Communications*, 10(1):4305, dec 2019.

[5] Zexin Feng, Xiaorong Zhou, Libor Šmejkal, Lei Wu, Zengwei Zhu, Huixin Guo, Rafael González-Hernández, Xiaoning Wang, Han Yan, Peixin Qin, Xin Zhang, Haojiang Wu, Hongyu Chen, Ziang Meng, Li Liu, Zhengcai Xia, Jairo Sinova, Tomáš Jungwirth, and Zhiqi Liu. An anomalous Hall effect in altermagnetic ruthenium dioxide. *Nature Electronics*, 5(11):735–743, nov 2022.

[6] Igor I. Mazin, Klaus Koepernik, Michelle D. Johannes, Rafael González-Hernández, and Libor Šmejkal. Prediction of unconventional magnetism in doped FeSb 2. *Proceedings of the National Academy of Sciences*, 118(42):e2108924118, oct 2021.

[7] Rafael González-Hernández, Libor Šmejkal, Karel Výborný, Yuta Yahagi, Jairo Sinova, Tomáš Jungwirth, and Jakub Železný. Efficient Electrical Spin Splitter Based on Nonrelativistic Collinear Antiferromagnetism. *Physical Review Letters*, 126(12):127701, mar 2021.

[8] Makoto Naka, Yukitoshi Motome, and Hitoshi Seo. Perovskite as a spin current generator. *Physical Review B*, 103(12):125114, nov 2021.

[9] Arnab Bose, Nathaniel J. Schreiber, Rakshit Jain, Ding-Fu Shao, Hari P. Nair, Jiaxin Sun, Xiyue S. Zhang, David A. Muller, Evgeny Y. Tsymbal, Darrell G. Schlom, and Daniel C. Ralph. Tilted spin current generated by the collinear antiferromagnet ruthenium dioxide. *Nature Electronics*, 5(5):267–274, may 2022.

[10] Hua Bai, Lei Han, X. Y. Feng, Y. J. Zhou, R. X. Su, Qian Wang, L. Y. Liao, W. X. Zhu, X. Z. Chen, Feng Pan, X. L. Fan, and Cheng Song. Observation of Spin Splitting Torque in a Collinear Antiferromagnet RuO2. *Physical Review Letters*, 128(19):197202, may 2022.

[11] Shutaro Karube, Takahiro Tanaka, Daichi Sugawara, Naohiro Kadoguchi, Makoto Kohda, and Junsaku Nitta. Observation of Spin-Splitter Torque in Collinear Antiferromagnetic RuO2. *Physical Review Letters*, 129(13):137201, sep 2022.

[12] Libor Šmejkal, Anna Birk Hellenes, Rafael González-Hernández, Jairo Sinova, and Tomas Jungwirth. Giant and Tunneling Magnetoresistance in Unconventional Collinear Antiferromagnets with Nonrelativistic Spin-Momentum Coupling. *Physical Review X*, 12(1):011028, feb 2022.

[13] Ding-Fu Shao, Shu-Hui Zhang, Ming Li, Chang-Beom Eom, and Evgeny Y. Tsymbal. Spin-neutral currents for spintronics. *Nature Communications*, 12(1):7061, dec 2021.

[14] Hai-Yang Ma, Mengli Hu, Nana Li, Jianpeng Liu, Wang Yao, Jin-Feng Jia, and Junwei Liu. Multifunctional antiferromagnetic materials with giant piezomagnetism and noncollinear spin current. *Nature Communications*, 12(1):2846, dec 2021.

[15] S. López-Moreno, A. H. Romero, J. Mejía-López, A. Muñoz, and Igor V. Roshchin. First-principles study of electronic, vibrational, elastic, and magnetic properties of FeF2 as a function of pressure. *Physical Review B*, 85(13):134110, apr 2012.

[16] Yusuke Noda, Kaoru Ohno, and Shinichiro Nakamura. Momentum-dependent band spin splitting in semiconducting MnO2 : a density functional calculation. *Physical Chemistry Chemical Physics*, 18(19):13294–13303, 2016.

[17] Kyo-Hoon Ahn, Atsushi Hariki, Kwan-Woo Lee, and Jan Kuneš. Antiferromagnetism in RuO2 as d-wave Pomeranchuk instability. *Physical Review B*, 99(18):184432, may 2019.

[18] Satoru Hayami, Yuki Yanagi, and Hiroaki Kusunose. Momentum-Dependent Spin Splitting by Collinear Antiferromagnetic Ordering. *Journal of the Physical Society of Japan*, 88(12):123702, dec 2019.

[19] Lin-Ding Yuan, Zhi Wang, Jun-Wei Luo, Emmanuel I Rashba, and Alex Zunger. Giant momentum-dependent spin splitting in centrosymmetric low-Z antiferromagnets. *Physical Review B*, 102(1):014422, jul 2020.

[20] Satoru Hayami, Yuki Yanagi, and Hiroaki Kusunose. Bottom-up design of spin-split and reshaped electronic band structures in antiferromagnets without spin-orbit coupling: Procedure on the basis of augmented multipoles. *Physical Review B*, 102:144441, 2020.

[21] Lin-Ding Yuan, Zhi Wang, Jun-Wei Luo, and Alex Zunger. Prediction of low-Z collinear and noncollinear antiferromagnetic compounds having momentum-dependent spin splitting even without spin-orbit coupling. *Physical Review Materials*, 5(1):014409, jan 2021.

[22] Sergei A. Egorov and Robert A. Evarestov. Colossal Spin Splitting in the Monolayer of the Collinear Antiferromagnet MnF2. *The Journal of Physical Chemistry Letters*, 12(9):2363–2369, mar 2021.

[23] Pengfei Liu, Jiayu Li, Jingzhi Han, Xiangang Wan, and Qihang Liu. Spin-Group Symmetry in Magnetic Materials with Negligible Spin-Orbit Coupling. *Physical Review X*, 12(2):21016, apr 2022.

[24] Jian Yang, Zheng-Xin Liu, and Chen Fang. Symmetry Invariants of Spin Space Groups in Magnetic Materials. may 2021.

[25] Libor Šmejkal, Jairo Sinova, and Tomas Jungwirth. Beyond Conventional Ferromagnetism and Antiferromagnetism: A Phase with Nonrelativistic Spin and Crystal Rotation Symmetry. *Physical Review X*, 12(3):031042, sep 2022.

[26] M. Zahid Hasan and Joel E. Moore. Three-Dimensional Topological Insulators. *Annual Review of Condensed Matter Physics*, 2(1):55–78, mar 2011.

[27] LD Landau and EM Lifshitz. *Electrodynamics of Continuous Media, vol. 8 of Course of Theoretical Physics*. Pergamon Press, Oxford, 2nd edition, may 1965.

[28] S. J. Blundell. *Magnetism in condensed matter*. Oxford University Press, 2001.

[29] R. Winkler. *Spin—Orbit Coupling Effects in Two-Dimensional Electron and Hole Systems*, volume 191 of *Springer Tracts in Modern Physics*. Springer Berlin Heidelberg, Berlin, Heidelberg, 2003.

[30] J Krempaský, L Šmejkal, S. W. D'Souza, M Hajlaoui, G Springholz, K Uhlířová, F Alarab, P C Constantinou, V. Strocov, D Usanov, W R Pudelko, R González-Hernández, A. Birk Hellenes, Z Jansa, H Reichlová, Z Šobáň, R. D. Gonzalez Betancourt, P Wadley, Jairo Sinova, D Kriegner, J Minár, J H Dil, and T Jungwirth. Altermagnetic lifting of Kramers spin degeneracy. *Nature*, 626(7999):517–522, feb 2024.

[31] Sonka Reimers, Lukas Odenbreit, Libor Šmejkal, Vladimir N. Strocov, Procopios Constantinou, Anna B. Hellenes, Rodrigo Jaeschke Ubiergo, Warlley H. Campos, Venkata K. Bharadwaj, Atasi Chakraborty, Thibaud Denneulin, Wen Shi, Rafal E. Dunin-Borkowski, Suvadip Das, Mathias Kläui, Jairo Sinova, and Martin Jourdan. Direct observation of altermagnetic band splitting in CrSb thin films. *Nature Communications*, 15(1):2116, mar 2024.

[32] Mahdi Hajlaoui, Sunil Wilfred D'Souza, Libor Šmejkal, Dominik Kriegner, Gauthier Krizman, Tetiana Zakusylo, Natalia Olszowska, Ondřej Caha, Jan Michalička, Jaime Sánchez-Barriga, Alberto Marmodoro, Karel Výborný, Arthur Ernst, Mirko Cinchetti, Jan Minar, Tomas Jungwirth, and Gunther Springholz. Temperature Dependence of Relativistic Valence Band Splitting Induced by an Altermagnetic Phase Transition. *Advanced Materials*, 36(31):2314076, aug 2024.

[33] Suyoung Lee, Sangjae Lee, Saegyeol Jung, Jiwon Jung, Donghan Kim, Yeonjae Lee, Byeongjun Seok, Jaeyoung Kim, Byeong Gyu Park, Libor Šmejkal, Chang-Jong Kang, and Changyoung Kim. Broken Kramers Degeneracy in Altermagnetic MnTe. *Physical Review Letters*, 132(3):036702, jan 2024.

[34] T. Osumi, S. Souma, T. Aoyama, K. Yamauchi, A. Honma, K. Nakayama, T. Takahashi, K. Ohgushi, and T. Sato. Observation of a giant band splitting in altermagnetic MnTe. *Physical Review B*, 109(11):115102, mar 2024.

[35] W. J. Takei, D E Cox, and G. Shirane. Magnetic Structures in the MnSb-CrSb System. *Physical Review*, 129(5):2008–2018, mar 1963.

[36] Nobuhiko Kunitomi, Yoshikazu Hamaguchi, and Shuichiro Anzai. Neutron diffraction study on manganese telluride. *Journal de Physique*, 25(5):568–574, 1964.

[37] Jibao Yuan, Yuzhu Song, Xianran Xing, and Jun Chen. Magnetic structure and uniaxial negative thermal expansion in antiferromagnetic CrSb. *Dalton Transactions*, 49(48):17605–17611, dec 2020.

[38] Olena Fedchenko, J. Minar, Akashdeep Akashdeep, S. W. D'Souza, Dmitry Vasilyev, Olena Tkach, Lukas Odenbreit, Q. L. Nguyen, Dmytro Kutnyakhov, Nils

Wind, Lukas Wenthaus, Markus Scholz, Kai Rossnagel, Moritz Hoesch, Martin Aeschlimann, B. Stadtmueller, M. Klaeui, G. Schoenhense, Gerhard Jakob, Tomas Jungwirth, L. Smejkal, Jairo Sinova, and H. J. Elmers. Observation of time-reversal symmetry breaking in the band structure of altermagnetic RuO2. *Science Advances*, 10(5):31, feb 2024.

[39] J. E. Hirsch. Spin-split states in metals. *Physical Review B*, 41(10):6820–6827, apr 1990.

[40] Congjun Wu and Shou-Cheng Zhang. Dynamic Generation of Spin-Orbit Coupling. *Physical Review Letters*, 93(3):036403, jul 2004.

[41] Egor I. Kiselev, Mathias S. Scheurer, Peter Wölfle, and Jörg Schmalian. Limits on dynamically generated spin-orbit coupling: Absence of l=1 Pomeranchuk instabilities in metals. *Physical Review B*, 95(12):125122, mar 2017.

[42] Yi-Ming Wu, Avraham Klein, and Andrey V. Chubukov. Conditions for l=1 Pomeranchuk instability in a Fermi liquid. *Physical Review B*, 97(16):165101, apr 2018.

[43] Congjun Wu, Kai Sun, Eduardo Fradkin, and Shou-Cheng Zhang. Fermi liquid instabilities in the spin channel. *Physical Review B*, 75(11):115103, mar 2007.

[44] Shan Wu, W. A. Phelan, L Liu, J. R. Morey, J. A. Tutmaher, J. C. Neuefeind, Ashfia Huq, Matthew B Stone, M Feygenson, David W Tam, Benjamin A Frandsen, Benjamin Trump, Cheng Wan, S. R. Dunsiger, T. M. McQueen, Y. J. Uemura, and C. L. Broholm. Incommensurate Magnetism Near Quantum Criticality in CeNiAsO. *Physical Review Letters*, 122(19):197203, may 2019.

[45] Tomas Jungwirth, Rafael M Fernandes, Jairo Sinova, and Liboř Smejkal. Altermagnets and beyond: Nodal magnetically-ordered phases. *ArXiv 2409.10034v1*, 2024.

[46] VP Mineev, K Samokhin, and LD Landau. *Introduction to unconventional superconductivity*. Gordon and Breach Science Publishers, Amsterdam, 1999.

[47] P J Brownt, J B Forsythl, V Nunezt, and F Lhssett lnslilut hue Langevin. The low-temperature antiferromagnetic structure of Mn5Si3 revised in the light of neutron polarimetry. *J. Phys.: Condens. Matter*, 4:1–5, 1992.

[48] N. Biniskos, F. J. Dos Santos, K. Schmalzl, S. Raymond, M. Dos Santos Dias, J. Persson, N. Marzari, S. Blügel, S. Lounis, and T. Brückel. Complex magnetic structure and spin waves of the noncollinear antiferromagnet Mn5Si3. *Physical Review B*, 105(10):104404, mar 2022.

[49] Michael Gottschilch, Olivier Gourdon, Joerg Persson, Clarina de la Cruz, Vaclav Petricek, and Thomas Brueckel. Study of the antiferromagnetism of Mn5Si3: an inverse magnetocaloric effect material. *Journal of Materials Chemistry*, 22(30):15275, jul 2012.

[50] P J Brown and J B Forsyth. Journal of Physics: Condensed Matter. Technical report, 1995.

[51] Claude Chappert, Albert Fert, and Frédéric Nguyen Van Dau. The emergence of spin electronics in data storage. *Nature Materials*, 6(11):813–823, may 2007.

[52] Sadamichi Maekawa and Teruya Shinjo. *Spin dependent transport in magnetic nanostructures*. CRC press, 2002.

[53] M. Julliere. Tunneling between ferromagnetic films. *Physics Letters A*, 54(3):225–226, sep 1975.

[54] D. C. Ralph and M. D. Stiles. Spin transfer torques. *Journal of Magnetism and Magnetic Materials*, 320(7):1190–1216, may 2008.

[55] J.C. Slonczewski. Current-driven excitation of magnetic multilayers. *Journal of Magnetism and Magnetic Materials*, 159(1-2):L1–L7, jun 1996.

[56] L. Berger. Emission of spin waves by a magnetic multilayer traversed by a current. *Physical Review B*, 54(13):9353–9358, may 1996.

[57] A. S. Núñez, R. A. Duine, Paul Haney, and A. H. MacDonald. Theory of spin torques and giant magnetoresistance in antiferromagnetic metals. *Physical Review B*, 73(21):214426, may 2006.

[58] A. H. MacDonald and M. Tsoi. Antiferromagnetic metal spintronics. *Philosophical Transactions of the Royal Society A: Mathematical, Physical and Engineering Sciences*, 369(1948):3098–3114, may 2011.

[59] Maria Stamenova, Razie Mohebbi, Jamileh Seyed-Yazdi, Ivan Rungger, and Stefano Sanvito. First-principles spin-transfer torque in CuMnAs—GaP—CuMnAs junctions. *Physical Review B*, 95(6):060403, feb 2017.

[60] A. B. Shick, Sergii Khmelevskyi, O. N. Mryasov, J. Wunderlich, and T. Jungwirth. Spin-orbit coupling induced anisotropy effects in bimetallic antiferromagnets: A route towards antiferromagnetic spintronics. *Physical Review B*, 81(21):212409, jun 2010.

[61] B. G. Park, J. Wunderlich, X. Martí, V. Holý, Y. Kurosaki, M. Yamada, H. Yamamoto, A. Nishide, J. Hayakawa, H. Takahashi, A. B. Shick, and T. Jungwirth. A spin-valve-like magnetoresistance of an antiferromagnet-based tunnel junction. *Nature Materials*, 10(5):347–351, may 2011.

[62] X. Marti, I. Fina, C. Frontera, Jian Liu, P. Wadley, Q. He, R. J. Paull, J. D. Clarkson, J. Kudrnovský, I. Turek, J. Kuneš, D. Yi, J-H. Chu, C. T. Nelson, L. You, E. Arenholz, S. Salahuddin, J. Fontcuberta, T. Jungwirth, and R. Ramesh. Room-temperature antiferromagnetic memory resistor. *Nature Materials*, 13(4):367–374, apr 2014.

[63] J. Železný, H. Gao, K. Výborný, J. Zemen, J. Mašek, Aurélien Manchon, J. Wunderlich, Jairo Sinova, and T. Jungwirth. Relativistic Néel-order fields induced by electrical current in antiferromagnets. *Physical Review Letters*, 113(15):157201, may 2014.

[64] P. Wadley, B. Howells, J. Železný, C. Andrews, V. Hills, R. P. Campion, V. Novák, K. Olejník, F. Maccherozzi, S. S. Dhesi, S. Y. Martin, T. Wagner, J. Wunderlich, F. Freimuth, Y. Mokrousov, J. Kuneš, J. S. Chauhan, M. J. Grzybowski, A. W. Rushforth, Kw Edmond, B. L. Gallagher, and T. Jungwirth. Electrical switching of an antiferromagnet. *Science*, 351(6273):587–590, may 2016.

[65] T. Jungwirth, X. Marti, P. Wadley, and J. Wunderlich. Antiferromagnetic spintronics. *Nature Nanotechnology*, 11(3):231–241, mar 2016.

[66] Peter Wadley, Sonka Reimers, Michal J. Grzybowski, Carl Andrews, Mu Wang, Jasbinder S. Chauhan, Bryan L. Gallagher, Richard P. Campion, Kevin W. Edmonds, Sarnjeet S. Dhesi, Francesco Maccherozzi, Vit Novak, Joerg Wunderlich, and Tomas Jungwirth. Current polarity-dependent manipulation of antiferromagnetic domains. *Nature Nanotechnology*, 13(5):362–365, may 2018.

[67] Hua Chen, Qian Niu, and A. H. Macdonald. Anomalous hall effect arising from noncollinear antiferromagnetism. *Physical Review Letters*, 112(1):017205, may 2014.

[68] J. Kübler and C. Felser. Non-collinear antiferromagnets and the anomalous Hall effect. *Epl*, 108(6):67001, may 2014.

[69] Satoru Nakatsuji, Naoki Kiyohara, and Tomoya Higo. Large anomalous Hall effect in a non-collinear antiferromagnet at room temperature. *Nature*, 527(7577):212–215, nov 2015.

[70] Ajaya K. Nayak, Julia Erika Fischer, Yan Sun, Binghai Yan, Julie Karel, Alexander C. Komarek, Chandra Shekhar, Nitesh Kumar, Walter Schnelle, Jürgen Kübler, Claudia Felser, and Stuart S.P. Parkin. Large anomalous Hall effect driven by a nonvanishing Berry curvature in the noncolinear antiferromagnet Mn3Ge. *Science Advances*, 2(4):e1501870–e1501870, may 2016.

[71] Kamil Olejník, Tom Seifert, Zdeněk Kašpar, Vít Novák, Peter Wadley, Richard P. Campion, Manuel Baumgartner, Pietro Gambardella, Petr Němec, Joerg Wunderlich, Jairo Sinova, Petr Kužel, Melanie Müller, Tobias Kampfrath, and Tomas Jungwirth. Terahertz electrical writing speed in an antiferromagnetic memory. *Science Advances*, 4(3):eaar3566, mar 2018.

[72] O. Gomonay, V. Baltz, A. Brataas, and Y. Tserkovnyak. Antiferromagnetic spin textures and dynamics. *Nature Physics*, 14(3):213–216, mar 2018.

[73] John R. Schaibley, Hongyi Yu, Genevieve Clark, Pasqual Rivera, Jason S. Ross, Kyle L. Seyler, Wang Yao, and Xiaodong Xu. Valleytronics in 2D materials. *Nature Reviews Materials*, 1(11):16055, nov 2016.

[74] Xianzhe Chen, Tomoya Higo, Katsuhiro Tanaka, Takuya Nomoto, Hanshen Tsai, Hiroshi Idzuchi, Masanobu Shiga, Shoya Sakamoto, Ryoya Ando, Hidetoshi Kosaki, Takumi Matsuo, Daisuke Nishio-Hamane, Ryotaro Arita, Shinji Miwa, and Satoru Nakatsuji. Octupole-driven magnetoresistance in an antiferromagnetic tunnel junction. *490 — Nature —*, 613, 2023.

[75] Peixin Qin, Han Yan, Xiaoning Wang, Hongyu Chen, Ziang Meng, Jianting Dong, Meng Zhu, Jialin Cai, Zexin Feng, Xiaorong Zhou, Li Liu, Tianli Zhang, Zhongming Zeng, Jia Zhang, Chengbao Jiang, and Zhiqi Liu. Room-temperature magnetoresistance in an all-antiferromagnetic tunnel junction. *Nature*, 613(7944):485–489, jan 2023.

[76] Louis Néel. Magnetism and Local Molecular Field. *Science*, 174(4013):985–992, dec 1971.

[77] T. Berlijn, P. C. Snijders, O. Delaire, H.-D. Zhou, T. A. Maier, H.-B. Cao, S.-X. Chi, M. Matsuda, Y. Wang, M. R. Koehler, P. R. C. Kent, and H. H. Weitering. Itinerant Antiferromagnetism in RuO2. *Physical Review Letters*, 118(7):077201, feb 2017.

[78] Z. H. Zhu, J. Strempfer, R. R. Rao, C. A. Occhialini, J. Pelliciari, Y. Choi, T. Kawaguchi, H. You, J. F. Mitchell, Y. Shao-Horn, and R. Comin. Anomalous Antiferromagnetism in Metallic RuO2 Determined by Resonant X-ray Scattering. *Physical Review Letters*, 122(1):017202, jan 2019.

[79] C. J. Bradley and A. P. Cracknell. *The Mathematical Theory of Symmetry in Solids*. Oxford Univeristy Press, 1972.

[80] Libor Šmejkal, Yuriy Mokrousov, Binghai Yan, and A. H. MacDonald. Topological antiferromagnetic spintronics. *Nature Physics*, 14(3):242–251, mar 2018.

[81] Martin Leijnse and Karsten Flensberg. Introduction to topological superconductivity and Majorana fermions. *Semiconductor Science and Technology*, 27(12):124003, dec 2012.

[82] A. Kitz. Über die Symmetriegruppen von Spinverteilungen. *physica status solidi (b)*, 10(2):455–466, 1965.

[83] D.B. B Litvin and W. Opechowski. Spin groups. *Physica*, 76(3):538–554, sep 1974.

[84] Hana Schiff, Alberto Corticelli, Afonso Guerreiro, Judit Romhányi, and Paul McClarty. The Spin Point Groups and their Representations. *ArXiv 2307.12784*, jul 2023.

[85] Hikaru Watanabe, Kohei Shinohara, Takuya Nomoto, Atsushi Togo, and Ryotaro Arita. Symmetry Analysis with Spin Crystallographic Groups: Disentangling Spin-Orbit-Free Effects in Emergent Electromagnetism. pages 1–58, 2023.

[86] Kohei Shinohara, Atsushi Togo, Hikaru Watanabe, Takuya Nomoto, Isao Tanaka, and Ryotaro Arita. Algorithm for spin symmetry operation search. *Acta Crystallographica Section A Foundations and Advances*, 80(1):94–103, jan 2024.

[87] C. W. J. Beenakker and T. Vakhtel. Phase-shifted Andreev levels in an altermagnet Josephson junction. *Physical Review B*, 108(7):075425, aug 2023.

[88] Valentin Leeb, Alexander Mook, Libor Smejkal, Johannes Knolle, Valentin Leeb, Alexander Mook, Libor Šmejkal, and Johannes Knolle. Spontaneous Formation of Altermagnetism from Orbital Ordering. *Arxiv Preprint*, 2023.

[89] Charles R. W. Steward, Rafael M. Fernandes, and Joerg Schmalian. Dynamic paramagnon-polarons in altermagnets. jul 2023.

[90] Sayantika Bhowal and Nicola A. Spaldin. Ferroically Ordered Magnetic Octupoles in <math display="inline"> <mi>d</mi> </math> -Wave Altermagnets. *Physical Review X*, 14(1):011019, feb 2024.

[91] Purnendu Das, Valentin Leeb, Johannes Knolle, and Michael Knap. Realizing Altermagnetism in Fermi-Hubbard Models with Ultracold Atoms. *Physical Review Letters*, 132(26):263402, jun 2024.

[92] O. J. Amin, A. Dal Din, E. Golias, Y. Niu, A. Zakharov, S. C. Fromage, C. J. B. Fields, S. L. Heywood, R. B. Cousins, J. Krempasky, J. H. Dil, D. Kriegner, B. Kiraly, R. P. Campion, A. W. Rushforth, K. W. Edmonds, S. S. Dhesi, L. Šmejkal, T. Jungwirth, and P. Wadley. Nanoscale imaging and control of altermagnetism in MnTe. *Nature*, in press, may.

[93] Anna Birk Hellenes, Tomáš Jungwirth, Rodrigo Jaeschke-Ubiergo, Atasi Chakraborty, Jairo Sinova, and Libor Šmejkal. P-wave magnets. *ArXiv 2309.01607*, sep 2023.

[94] J. J. Sakurai. *Advanced Quantum Mechanics*. Addison-Wesley, may 2018.

[95] Peizhe Tang, Quan Zhou, Gang Xu, and Shou-Cheng Zhang. Dirac fermions in an antiferromagnetic semimetal. *Nature Physics*, 12(12):1100–1104, dec 2016.

[96] Libor Šmejkal, J. Železný, Jairo Sinova, and T. Jungwirth. Electric Control of Dirac Quasiparticles by Spin-Orbit Torque in an Antiferromagnet. *Physical Review Letters*, 118(10):106402, mar 2017.

[97] Charles Kittel. *Introduction to Solid State Physics*. John Wiley & Sons, 8 edition, 2004.

[98] Neil W. Ashcroft and N. David Mermin. *Solid State Physics*. Saunders College Publishing, Philadelphia, 2nd edition, 1976.

[99] Mildred S. Dresselhaus, Gene Dresselhaus, and Ado Jorio. *Group Theory*. Springer Berlin Heidelberg, Berlin, Heidelberg, 2008.

[100] D. B. Litvin. Spin point groups. *Acta Crystallographica Section A*, 33(2):279–287, mar 1977.

[101] Schwarzenbach. *Crystallography*. Wiley, United Kingdom, 1996.

[102] M.-T. Suzuki, T. Koretsune, M. Ochi, and R. Arita. Cluster multipole theory for anomalous Hall effect in antiferromagnets. *Physical Review B*, 95(9):094406, mar 2017.

[103] P Weinberger. All you need to know about the Dirac equation. *Philosophical Magazine*, 88(18-20):2585–2601, jun 2008.

[104] M. Z. Hasan and C. L. Kane. Colloquium: Topological insulators. *Reviews of Modern Physics*, 82(4):3045–3067, nov 2010.

[105] Xiao-Liang Qi and Shou-Cheng Zhang. Topological insulators and superconductors. *Reviews of Modern Physics*, 83(4):1057–1110, oct 2011.

[106] Naoto Nagaosa, Jairo Sinova, Shigeki Onoda, A. H. MacDonald, and N. P. Ong. Anomalous Hall effect. *Reviews of Modern Physics*, 82(2):1539–1592, may 2010.

[107] Olena Fedchenko, L. Šmejkal, Michael Kallmayer, Yarina Lytvynenko, Katerina Medjanik, Sergey Babenkov, Dmitry Vasilyev, M. Kläui, Jure Demsar, G. Schönhense, Martin Jourdan, Jairo Sinova, and H. J. Elmers. Direct observation of antiferromagnetic parity violation in the electronic structure of Mn 2 Au. *Journal of Physics: Condensed Matter*, 34(42):425501, oct 2022.

[108] K V Shanavas, Z S Popović, and S Satpathy. Theoretical model for Rashba spin-orbit interaction in d electrons. *Physical Review B*, 90(16):165108, oct 2014.

[109] Matthias Greber. *Metrics for Spin Splittings in Altermagnets*. Bachelor thesis, Johannes Gutenberg University Mainz, 2023.

[110] Yaqian Guo, Hui Liu, Oleg Janson, Ion Cosma Fulga, Jeroen van den Brink, and Jorge I. Facio. Spin-split collinear antiferromagnets: A large-scale ab-initio study. *Materials Today Physics*, 32:100991, mar 2023.

[111] Helena Reichlová, Rafael Lopes Seeger, Rafael González-Hernández, Ismaila Kounta, Richard Schlitz, Dominik Kriegner, Philipp Ritzinger, Michaela Lammel, Miina Leiviskä, Václav Petříček, Petr Doležal, Eva Schmoranzerová, Antonín Bad'ura, Andy Thomas, Vincent Baltz, Lisa Michez, Jairo Sinova, Sebastian T. B. Goennenwein, Tomáš Jungwirth, and Libor Šmejkal. Macroscopic time reversal symmetry breaking by staggered spin-momentum interaction. *Arxiv Preprint*, dec 2020.

[112] Helena Reichlova, Rafael Lopes Seeger, Rafael González-Hernández, Ismaila Kounta, Richard Schlitz, Dominik Kriegner, Philipp Ritzinger, Michaela Lammel, Miina Leiviskä, Anna Birk Hellenes, Kamil Olejník, Vaclav Petříček, Petr Doležal, Lukas Horak, Eva Schmoranzerova, Antonín Badura, Sylvain Bertaina, Andy Thomas, Vincent Baltz, Lisa Michez, Jairo Sinova, Sebastian T. B. Goennenwein, Tomáš Jungwirth, and Libor Šmejkal. Observation of a spontaneous anomalous Hall response in the Mn5Si3 d-wave altermagnet candidate. *Nature Communications*, 15(1):4961, jun 2024.

[113] R. D. Gonzalez Betancourt, J. Zubáč, R. Gonzalez-Hernandez, K. Geishendorf, Z. Šobáň, G. Springholz, K. Olejník, L. Šmejkal, Jairo Sinova, T. Jungwirth, S. T. B. Goennenwein, A. Thomas, H. Reichlová, J. Železný, and D. Kriegner. Spontaneous Anomalous Hall Effect Arising from an Unconventional Compensated Magnetic Phase in a Semiconductor. *Physical Review Letters*, 130(3):036702, jan 2023.

[114] K. Ishizaka, Mohammad Saeed Bahramy, H. Murakawa, M. Sakano, T. Shimojima, T. Sonobe, K. Koizumi, S. Shin, H. Miyahara, A. Kimura, K. Miyamoto, T. Okuda, H. Namatame, M. Taniguchi, R. Arita, N. Nagaosa, K. Kobayashi, Y. Murakami, R. Kumai, Y. Kaneko, Y. Onose, and Y. Tokura. Giant Rashba-type spin splitting in bulk BiTeI. *Nature Materials*, 10(7):521–526, jul 2011.

[115] Valentin Leeb, Alexander Mook, Libor Šmejkal, and Johannes Knolle. Spontaneous Formation of Altermagnetism from Orbital Ordering. *Physical Review Letters*, 132(23):236701, jun 2024.

[116] Libor Šmejkal, Alberto Marmodoro, Kyo-Hoon Ahn, Rafael González-Hernández, Ilja Turek, Sergiy Mankovsky, Hubert Ebert, Sunil W. D'Souza, Ondřej Šipr, Jairo Sinova, and Tomáš Jungwirth. Chiral magnons in altermagnetic RuO2. *Physical Review Letters*, 131(25):256703, dec 2023.

[117] Libor Šmejkal. *Topological band theory of relativistic spintronics in antiferromagnets*. PhD thesis, apr 2019.

[118] A. Dal Din, O. J. Amin, P. Wadley, and K. W. Edmonds. Antiferromagnetic spintronics and beyond. *npj Spintronics 2024 2:1*, 2(1):1–8, jul 2024.

[119] Berthold H. Rimmler, Banabir Pal, and Stuart S. P. Parkin. Non-collinear antiferromagnetic spintronics. *Nature Reviews Materials*, pages 1–19, aug 2024.

[120] Yang Zhang, Yan Sun, Hao Yang, Jakub Železný, Stuart P.P. Parkin, Claudia Felser, and Binghai Yan. Strong anisotropic anomalous Hall effect and spin Hall effect in the chiral antiferromagnetic compounds Mn3X (X=Ge, Sn, Ga, Ir, Rh, and Pt). *Physical Review B*, 95(7):075128, may 2017.

[121] David Vanderbilt. *Berry Phases in Electronic Structure Theory*. Cambridge University Press, oct 2018.

[122] Walter A Harrison. Bond-Orbital Model and the Properties of Tetrahedrally Coordinated Solids. *Physical Review B*, 8(10):4487–4498, nov 1973.

[123] P. Vogl, Harold P. Hjalmarson, and John D. Dow. A Semi-empirical tight-binding theory of the electronic structure of semiconductors†. *Journal of Physics and Chemistry of Solids*, 44(5):365–378, jan 1983.

[124] Søren Smidstrup, Troels Markussen, Pieter Vancraeyveld, Jess Wellendorff, Julian Schneider, Tue Gunst, Brecht Verstichel, Daniele Stradi, Petr A. Khomyakov, Ulrik G. Vej-Hansen, Maeng-Eun Lee, Samuel T. Chill, Filip Rasmussen, Gabriele Penazzi, Fabiano Corsetti, Ari Ojanperä, Kristian Jensen, Mattias L. N. Palsgaard, Umberto Martinez, Anders Blom, Mads Brandbyge, and Kurt Stokbro. QuantumATK: an integrated platform of electronic and atomic-scale modelling tools. *Journal of Physics: Condensed Matter*, 32(1):015901, jan 2020.

[125] Gen Yin, Jie-Xiang Yu, Yizhou Liu, Roger K Lake, Jiadong Zang, and Kang L Wang. Planar Hall Effect in Antiferromagnetic MnTe Thin Films. *Physical Review Letters*, 122, 2019.

[126] Mercè Roig, Andreas Kreisel, Yue Yu, Brian M. Andersen, and Daniel F. Agterberg. Minimal Models for Altermagnetism. feb 2024.

[127] June Gunn Lee. *Computational Materials Science*. CRC Press, 2 edition, nov 2016.

[128] Institut für Festkörperforschung (Jülich). *Computing Solids. Models, ab-initio methods and supercomputing. Lecture Notes of the 45th IFF Spring School*. Forschungszentrum Jülich GmbH, Jülich, 2014.

[129] Antonin Badura, Warlley H. Campos, Venkata K. Bharadwaj, Ismaïla Kounta, Lisa Michez, Matthieu Petit, Javier Rial, Miina Leiviskä, Vincent Baltz, Filip Krizek, Dominik Kriegner, Jan Zemen, Sjoerd Telkamp, Sebastian Sailler, Michaela Lammel, Rodrigo Jaeschke Ubiergo, Anna Birk Hellenes, Rafael González-Hernández, Jairo Sinova, Tomáš Jungwirth, Sebastian T. B. Goennenwein, Libor Šmejkal, and Helena Reichlova. Observation of the anomalous Nernst effect in altermagnetic candidate Mn5Si3. *ArXiv 2403.12929*, mar 2024.

[130] Christoph Sürgers, Gerda Fischer, Warlley H. Campos, Anna Birk Hellenes, Libor Šmejkal, Jairo Sinova, Michael Merz, Thomas Wolf, and Wolfgang Wernsdorfer. Anomalous Nernst effect in the noncollinear antiferromagnet Mn\textsubscript{5}Si\textsubscript{3}. *Communications Materials*, 5(1):176, aug 2024.

[131] Igor Mazin, Rafael González-Hernández, and Libor Šmejkal. Induced Monolayer Altermagnetism in MnP(S,Se)$_3$ and FeSe. 2:1–11, 2023.

[132] Rafael M. Fernandes, Vanuildo S. de Carvalho, Turan Birol, and Rodrigo G. Pereira. Topological transition from nodal to nodeless Zeeman splitting in altermagnets. *Physical Review B*, 109(2):024404, jan 2024.

[133] Yu. A. Bychkov and E. I. Rashba. Properties of a 2D electron gas with lifted spectral degeneracy. *JETP Letters*, 39:78–81, may 1984.

[134] A. Manchon, H. C. Koo, J. Nitta, S. M. Frolov, and R. A. Duine. New perspectives for Rashba spin–orbit coupling. *Nature Materials*, 14(9):871–882, sep 2015.

[135] Jürgen Kübler. *Theory of Itinerant Electron Magnetism*. Oxford University Press, Oxford, 2nd editio edition, sep 2021.

[136] Henrik Bruus and Karsten Flensberg. *Many-Body Quantum Theory in Condensed Matter Physics: An Introduction (Oxford Graduate Texts)*. Number August. Oxford University Press, 2016 edition, 2004.

[137] Michael A Nielsen and Isaac L Chuang. *Quantum Computation and Quantum Information*. Cambridge University Press, Cambridge, 10th anniv edition, 2010.

[138] Douglas Rayner Hartree. *The Calculation of Atomic Structures*. J. Wiley, 1957.

[139] P. Hohenberg and W. Kohn. Inhomogeneous Electron Gas. *Physical Review*, 136(3B):B864–B871, nov 1964.

[140] W. Kohn and L. J. Sham. Self-Consistent Equations Including Exchange and Correlation Effects. *Physical Review*, 140(4A):A1133–A1138, nov 1965.

[141] U von Barth and L. Hedin. A local exchange-correlation potential for the spin polarized case. i. *Journal of Physics C: Solid State Physics*, 5(13):1629–1642, jul 1972.

[142] John P. Perdew, Kieron Burke, and Matthias Ernzerhof. Generalized Gradient Approximation Made Simple. *Physical Review Letters*, 77(18):3865–3868, oct 1996.

[143] J. Paier, M. Marsman, K. Hummer, G. Kresse, I. C. Gerber, and J. G. Angyán. Screened hybrid density functionals applied to solids. *Journal of Chemical Physics*, 124(15):154709, apr 2006.

[144] J. Paier, M. Marsman, K. Hummer, G. Kresse, I. C. Gerber, and J. G. Angyán. Erratum: Screened hybrid density functionals applied to solids (Journal of Chemical Physics (2006) 124 (154709)). *Journal of Chemical Physics*, 125(23):249901, dec 2006.

[145] J. Hubbard. Electron correlations in narrow energy bands. *Proceedings of the Royal Society of London. Series A. Mathematical and Physical Sciences*, 276(1365):238–257, nov 1963.

[146] S. L. Dudarev, G. A. Botton, S. Y. Savrasov, C. J. Humphreys, and A. P. Sutton. Electron-energy-loss spectra and the structural stability of nickel oxide: An LSDA+U study. *Physical Review B*, 57(3):1505–1509, jan 1998.

[147] V. I. Anisimov, J. Zaanen, and O. K. Andersen. Band theory and Mott insulators: Hubbard U instead of Stoner I. *Physical Review B*, 44(3):943–954, jul 1991.

[148] A. I. Liechtenstein, V. I. Anisimov, and J. Zaanen. Density-functional theory and strong interactions: Orbital ordering in Mott-Hubbard insulators. *Physical Review B*, 52(8):R5467–R5470, aug 1995.

[149] M. T. Czyyk and G. A. Sawatzky. Local-density functional and on-site correlations: The electronic structure of La2CuO4 and LaCuO3. *Physical Review B*, 49(20):14211–14228, may 1994.

[150] A. Rohrbach, J. Hafner, and G. Kresse. Electronic correlation effects in transition-metal sulfides. *Journal of Physics: Condensed Matter*, 15(6):979–996, feb 2003.

[151] P. E. Blöchl. Projector augmented-wave method. *Physical Review B*, 50(24):17953–17979, dec 1994.

[152] David Vanderbilt. Soft self-consistent pseudopotentials in a generalized eigenvalue formalism. *Physical Review B*, 41(11):7892–7895, apr 1990.

[153] E. van Lenthe, E. J. Baerends, and J. G. Snijders. Relativistic regular two component Hamiltonians. *The Journal of Chemical Physics*, 99(6):4597–4610, may 1993.

[154] S. Steiner, S. Khmelevskyi, M. Marsmann, and G. Kresse. Calculation of the magnetic anisotropy with projected-augmented-wave methodology and the case study of disordered Fe 1-x Co x alloys. *Physical Review B*, 93(22):224425, jun 2016.

[155] Georg Kresse and Daniel Joubert. From ultrasoft pseudopotentials to the projector augmented-wave method. *Physical Review B*, 59(3):1758–1775, jan 1999.

[156] D. R. Hamann, M. Schlüter, and C. Chiang. Norm-Conserving Pseudopotentials. *Physical Review Letters*, 43(20):1494, nov 1979.

[157] N. Troullier and José Luriaas Martins. Efficient pseudopotentials for plane-wave calculations. *Physical Review B*, 43(3):1993, jan 1991.

[158] David J. Griffiths. *Introduction to Electrodynamics*. Prentice-Hall, New Jersey, 3rd edition, 1999.

[159] ISYM, VASP manual.

[160] I_CONSTRAINED_M, VASP manual.

[161] Pui Wai Ma and S L Dudarev. Constrained density functional for noncollinear magnetism. *Physical Review B*, 91(5):054420, feb 2015.

[162] Vei Wang, Nan Xu, Jin-Cheng Liu, Gang Tang, and Wen-Tong Geng. VASPKIT: A user-friendly interface facilitating high-throughput computing and analysis using VASP code. *Computer Physics Communications*, 267:108033, 2021.

[163] Koichi Momma and Fujio Izumi. VESTA3 for three-dimensional visualization of crystal, volumetric and morphology data. *Journal of Applied Crystallography*, 44(6):1272–1276, dec 2011.

[164] Uthpala Herath, Pedram Tavadze, Xu He, Eric Bousquet, Sobhit Singh, Francisco Muñoz, and Aldo H Romero. PyProcar: A Python library for electronic structure pre/post-processing. *Computer Physics Communications*, 251:107080, jun 2020.

[165] G. Kresse and J. Furthmüller. Efficient iterative schemes for ab initio total-energy calculations using a plane-wave basis set. *Physical Review B*, 54(16):11169–11186, may 1996.

[166] D. Kriegner, H. Reichlova, J. Grenzer, W. Schmidt, E. Ressouche, J. Godinho, T. Wagner, S. Y. Martin, A. B. Shick, V. V. Volobuev, G. Springholz, V. Holý, J. Wunderlich, T. Jungwirth, and K. Výborný. Magnetic anisotropy in antiferromagnetic hexagonal MnTe. *Physical Review B*, 96(21):214418, dec 2017.

[167] B. Andrei Bernevig, J. Orenstein, and Shou Cheng Zhang. Exact SU(2) symmetry and persistent spin helix in a spin-orbit coupled system. *Physical Review Letters*, 97(23):236601, may 2006.

[168] J. Krempaský, L. Šmejkal, S. W. D'Souza, M. Hajlaoui, G. Springholz, K. Uhlířová, F. Alarab, P. C. Constantinou, V. Strokov, D. Usanov, W. R. Pudelko, R. González-Hernández, A. Birk Hellenes, Z. Jansa, H. Reichlová, Z. Šobáň, R. D. Gonzalez Betancourt, P. Wadley, Jairo Sinova, D. Kriegner,

J. Minár, J. H. Dil, and T. Jungwirth. Altermagnetic lifting of Kramers spin degeneracy. *Arxiv Preprint*, aug 2023.

[169] Shigemasa Suga, Akira Sekiyama, and Christian Tusche. *Photoelectron Spectroscopy – Bulk and Surface Electronic Structures*. Springer Series in Surface Sciences. Springer, Berlin, 2nd edition, 2021.

[170] MAGNDATA - Collection of Magnetic Structures.

[171] Andriy Smolyanyuk, Igor I. Mazin, Laura Garcia-Gassull, and Roser Valentí. Fragility of the magnetic order in the prototypical altermagnet RuO2. *Physical Review B*, 109(13):134424, apr 2024.

[172] Teresa Tschirner, Philipp Keßler, Ruben Dario Gonzalez Betancourt, Tommy Kotte, Dominik Kriegner, Bernd Büchner, Joseph Dufouleur, Martin Kamp, Vedran Jovic, Libor Smejkal, Jairo Sinova, Ralph Claessen, Tomas Jungwirth, Simon Moser, Helena Reichlova, and Louis Veyrat. Saturation of the anomalous Hall effect at high magnetic fields in altermagnetic RuO2. *APL Materials*, 11(10):101103, oct 2023.

[173] Zihan Lin, Dong Chen, Wenlong Lu, Xin Liang, Shiyu Feng, Kohei Yamagami, Jacek Osiecki, Mats Leandersson, Balasubramanian Thiagarajan, Junwei Liu, Claudia Felser, and Junzhang Ma. Observation of Giant Spin Splitting and d-wave Spin Texture in Room Temperature Altermagnet RuO2. feb 2024.

[174] Kartik Samanta, Marjana Ležaić, Maximilian Merte, Frank Freimuth, Stefan Blügel, and Yuriy Mokrousov. Crystal Hall and crystal magneto-optical effect in thin films of SrRuO3. *Journal of Applied Physics*, 127(21):213904, jun 2020.

[175] L. L. Tao and Evgeny Y. Tsymbal. Persistent spin texture enforced by symmetry. *Nature Communications*, 9(1):2763, jul 2018.

[176] Atasi Chakraborty, Anna Birk Hellenes, Rodrigo Jaeschke-Ubiergo, Tomas Jungwirth, Libor Šmejkal, and Jairo Sinova. Highly Efficient Non-relativistic Edelstein effect in p-wave magnets. *ArXiv 2411.16378*, 2024.

[177] Samuel V Gallego, J Manuel Perez-Mato, Luis Elcoro, Emre S Tasci, Robert M Hanson, Koichi Momma, Mois I Aroyo, and Gotzon Madariaga. MAGNDATA: towards a database of magnetic structures. I. The commensurate case. *J. Appl. Cryst*, 49:1750–1776, 2016.

[178] Christoph Sürgers, Gerda Fischer, Patrick Winkel, and Hilbert V. Löhneysen. Large topological Hall effect in the non-collinear phase of an antiferromagnet. *Nature Communications*, 5(1):3400, may 2014.

[179] Sergei A Egorov, Daniel B Litvin, and Robert A Evarestov. Antiferromagnetism-Induced Spin Splitting in Systems Described by Magnetic Layer Groups. *The Journal of Physical Chemistry C*, page acs.jpcc.1c02653, jul 2021.

[180] Yu-Peng Zhu, Xiaobing Chen, Xiang-Rui Liu, Yuntian Liu, Pengfei Liu, Heming Zha, Gexing Qu, Caiyun Hong, Jiayu Li, Zhicheng Jiang, Xiao-Ming Ma, Yu-Jie Hao, Ming-Yuan Zhu, Wenjing Liu, Meng Zeng, Sreehari Jayaram, Malik Lenger, Jianyang Ding, Shu Mo, Kiyohisa Tanaka, Masashi Arita, Zhengtai Liu, Mao Ye, Dawei Shen, Jörg Wrachtrup, Yaobo Huang, Rui-Hua He, Shan Qiao, Qihang Liu, and Chang Liu. Observation of plaid-like spin splitting in a noncoplanar antiferromagnet. *Nature*, 626(7999):523–528, feb 2024.

[181] Jakub Železný, Yang Zhang, Claudia Felser, and Binghai Yan. Spin-Polarized Current in Noncollinear Antiferromagnets. *Physical Review Letters*, 119(18):187204, nov 2017.

[182] Satoru Hayami, Yuki Yanagi, and Hiroaki Kusunose. Spontaneous antisymmetric spin splitting in noncollinear antiferromagnets without spin-orbit coupling. *Physical Review B*, 101(22):220403, 2020.

[183] Satoru Hayami. Mechanism of antisymmetric spin polarization in centrosymmetric multiple- Q magnets based on effective chiral bilinear and biquadratic spin cross products. *Physical Review B*, 105(2):024413, jan 2022.

[184] Ryuichi Shindou and Naoto Nagaosa. Orbital Ferromagnetism and Anomalous Hall Effect in Antiferromagnets on the Distorted fcc Lattice. *Physical Review Letters*, 87(11):116801, aug 2001.

[185] Wanxiang Feng, Jan-Philipp Hanke, Xiaodong Zhou, Guang-Yu Guo, Stefan Blügel, Yuriy Mokrousov, and Yugui Yao. Topological magneto-optical effects and their quantization in noncoplanar antiferromagnets. *Nature Communications*, 11(1):118, dec 2020.

[186] V. M. Edelstein. Spin polarization of conduction electrons induced by electric current in two-dimensional asymmetric electron systems. *Solid State Communications*, 73(3):233–235, may 1990.

[187] B. Andrei Bernevig, Claudia Felser, and Haim Beidenkopf. Progress and prospects in magnetic topological materials. *Nature*, 603(7899):41–51, mar 2022.

[188] Stepan Tsirkin and Ivo Souza. On the separation of Hall and Ohmic nonlinear responses. *SciPost Physics Core*, 5(3):039, aug 2022.

[189] T. Jungwirth, J. Wunderlich, V. Novák, K. Olejník, B. L. Gallagher, R. P. Campion, K. W. Edmonds, A. W. Rushforth, A. J. Ferguson, and P. Němec. Spin-dependent phenomena and device concepts explored in (Ga,Mn)As. *Reviews of Modern Physics*, 86(3):855–896, jul 2014.

[190] N. F. Mott. The Electrical Conductivity of Transition Metals. *Proceedings of the Royal Society A: Mathematical, Physical and Engineering Sciences*, 153(880):699–717, may 1936.

[191] Supriyo Datta. *Electronic Transport in Mesoscopic Systems*. Cambridge University Press, Cambridge, may 1995.

[192] M P Marder. *Condensed Matter Physics, 2nd Edition*. Wiley, 2nd edition, 2010.

[193] Arne Brataas, Andrew D. Kent, and Hideo Ohno. Current-induced torques in magnetic materials. *Nature Materials*, 11(5):372–381, may 2012.

[194] Suyoung Lee, Sangjae Lee, Saegyeol Jung, Jiwon Jung, Donghan Kim, Yeonjae Lee, Byeongjun Seok, Jaeyoung Kim, Byeong Gyu Park, Libor Šmejkal, Chang-Jong Kang, and Changyoung Kim. Broken Kramers' degeneracy in altermagnetic MnTe. *Arxiv Preprint*, aug 2023.

[195] T. Osumi, S. Souma, T. Aoyama, K. Yamauchi, A. Honma, K. Nakayama, T. Takahashi, K. Ohgushi, and T. Sato. Observation of Giant Band Splitting in Altermagnetic MnTe. *Arxiv Preprint*, aug 2023.

[196] Wenlong Lu, Shiyu Feng, Yuzhi Wang, Dong Chen, Zihan Lin, Xin Liang, Siyuan Liu, Wanxiang Feng, Kohei Yamagami, Junwei Liu, Claudia Felser, Quansheng Wu, and Junzhang Ma. Observation of surface Fermi arcs in altermagnetic Weyl semimetal CrSb. *ArXiv 2407.13497*, jul 2024.

[197] Meng Zeng, Ming-Yuan Zhu, Yu-Peng Zhu, Xiang-Rui Liu, Xiao-Ming Ma, Yu-Jie Hao, Pengfei Liu, Gexing Qu, Yichen Yang, Zhicheng Jiang, Kohei Yamagami, Masashi Arita, Xiaoqian Zhang, Tian-Hao Shao, Yue Dai, Kenya Shimada, Zhengtai Liu, Mao Ye, Yaobo Huang, Qihang Liu, and Chang Liu. Observation of Spin Splitting in Room-Temperature Metallic Antiferromagnet CrSb. *Advanced Science*, 11(43):2406529, nov 2024.

[198] Guowei Yang, Zhanghuan Li, Sai Yang, Jiyuan Li, Hao Zheng, Weifan Zhu, Saizheng Cao, Wenxuan Zhao, Jiawen Zhang, Mao Ye, Yu Song, Lun-Hui Hu, Lexian Yang, Ming Shi, Huiqiu Yuan, Yongjun Zhang, Yuanfeng Xu, and Yang Liu. Three-dimensional mapping and electronic origin of large altermagnetic splitting near Fermi level in CrSb. *ArXiv 2405.12575*, may 2024.

[199] Ilja Turek. Altermagnetism and magnetic groups with pseudoscalar electron spin. *Physical Review B*, 106(9):094432, sep 2022.

[200] Jairo Sinova, Sergio O. Valenzuela, J. Wunderlich, C. H. Back, and T. Jungwirth. Spin Hall effects. *Reviews of Modern Physics*, 87(4):1213–1260, oct 2015.

[201] Mois I. Aroyo, Asen Kirov, Cesar Capillas, J. M. Perez-Mato, and Hans Wondratschek. Bilbao Crystallographic Server. II. Representations of crystallographic point groups and space groups. *Acta Crystallographica Section A Foundations of Crystallography*, 62(2):115–128, mar 2006.

[202] Mois Ilia Aroyo, Juan Manuel Perez-Mato, Cesar Capillas, Eli Kroumova, Svetoslav Ivantchev, Gotzon Madariaga, Asen Kirov, and Hans Wondratschek. Bilbao Crystallographic Server: I. Databases and crystallographic computing programs. *Zeitschrift fur Kristallographie*, 221(1):15–27, jan 2006.

[203] M. Seemann, D. Ködderitzsch, S. Wimmer, and H. Ebert. Symmetry-imposed shape of linear response tensors. *Physical Review B*, 92(15):155138, oct 2015.

[204] Institut für Festkörperforschung (Jülich). *Spintronics - from GMR to quantum information: lecture notes of the 40th spring school 2009*, volume 10 of *Schriften des Forschungszentrums Jülich. Reihe Schlüsseltechnologien / key technologies*. Forschungszentrum Jülich GmbH, Jülich, 2009.

[205] Christoph W. Groth, Michael Wimmer, Anton R. Akhmerov, and Xavier Waintal. Kwant: a software package for quantum transport. *New Journal of Physics*, 16(6):063065, jun 2014.

[206] C.W.J. Beenakker and H. van Houten. Quantum Transport in Semiconductor Nanostructures. In *Solid State Physics*, volume 44 of *Solid State Physics*, pages 1–228. Elsevier, dec 1991.

[207] Rolf Landauer. Can a length of perfect conductor have a resistance? *Physics Letters A*, 85(2):91–93, sep 1981.

[208] R. Landauer. Spatial variation of currents and fields due to localized scatterers in metallic conduction. *IBM Journal of Research and Development*, 32(3):306–316, may 1988.

[209] M. Büttiker. Voltage fluctuations in small conductors. *Physical Review B*, 35(8):4123–4126, mar 1987.

[210] M. Büttiker. Absence of backscattering in the quantum Hall effect in multiprobe conductors. *Physical Review B*, 38(14):9375–9389, nov 1988.

[211] Jeroen Danon, Anna Birk Hellenes, Esben Bork Hansen, Lucas Casparis, Andrew P. Higginbotham, and Karsten Flensberg. Nonlocal Conductance Spectroscopy of Andreev Bound States: Symmetry Relations and BCS Charges. *Physical Review Letters*, 124(3):036801, jan 2020.

[212] Yoseph Imry. *Physics of mesoscopic systems*, pages 101–163. World Scientific, 1 edition, aug 1986.

[213] Stepan S. Tsirkin. High performance Wannier interpolation of Berry curvature and related quantities with WannierBerri code. *npj Computational Materials*, 7(1):33, feb 2021.

[214] Ismaïla Kounta, Helena Reichlova, Dominik Kriegner, Rafael Lopes Seeger, Antonin Bad'ura, Miina Leiviska, Amine Boussadi, Vasile Heresanu, Sylvain Bertaina, Matthieu Petit, Eva Schmoranzerova, Libor Smejkal, Jairo Sinova, Tomas Jungwirth, Vincent Baltz, Sebastian T. B. Goennenwein, and Lisa Michez. Competitive actions of MnSi in the epitaxial growth of Mn5Si3 thin films on Si(111). *Physical Review Materials*, 7(2):024416, feb 2023.

[215] F. J. dos Santos, N. Biniskos, S. Raymond, K. Schmalzl, M. dos Santos Dias, P. Steffens, J. Persson, S. Blügel, S. Lounis, and T. Brückel. Spin waves in the collinear antiferromagnetic phase of Mn5Si3. *Physical Review B*, 103(2):024407, jan 2021.

[216] N. Biniskos, K. Schmalzl, S. Raymond, S. Petit, P. Steffens, J. Persson, and T. Brückel. Spin Fluctuations Drive the Inverse Magnetocaloric Effect in Mn5Si3. *Physical Review Letters*, 120(25):257205, 2018.

[217] Peng-Jie Guo, Yuhao Gu, Ze-Feng Gao, and Zhong-Yi Lu. Altermagnetic ferroelectric LiFe2F6 and spin-triplet excitonic insulator phase. dec 2023.

[218] Ling Bai, Wanxiang Feng, Siyuan Liu, Libor Šmejkal, Yuriy Mokrousov, and Yugui Yao. Altermagnetism: Exploring New Frontiers in Magnetism and Spintronics. *Advanced Functional Materials*, pages 1–49, sep 2024.

[219] Paul A. McClarty and Jeffrey G. Rau. Landau Theory of Altermagnetism. *Physical Review Letters*, 132(17):176702, apr 2024.

[220] Xiaodong Zhou, Wanxiang Feng, Xiuxian Yang, Guang Yu Guo, and Yugui Yao. Crystal chirality magneto-optical effects in collinear antiferromagnets. *Physical Review B*, 104(2):1–8, 2021.

[221] A. Hariki, A. Dal Din, O. J. Amin, T. Yamaguchi, A. Badura, D. Kriegner, K. W. Edmonds, R. P. Campion, P. Wadley, D. Backes, L. S. I. Veiga, S. S. Dhesi, G. Springholz, L. Šmejkal, K. Výborný, T. Jungwirth, and J. Kuneš. X-Ray Magnetic Circular Dichroism in Altermagnetic α -MnTe. *Physical Review Letters*, 132(17):176701, apr 2024.

[222] Theodoros Adamantopoulos, Maximilian Merte, Frank Freimuth, Dongwook Go, Lishu Zhang, Marjana Ležaić, Wanxiang Feng, Yugui Yao, Jairo Sinova, Libor Šmejkal, Stefan Blügel, and Yuriy Mokrousov. Spin and orbital magnetism by light in rutile altermagnets. *npj Spintronics*, 2(1):46, sep 2024.

[223] Peng Rao, Alexander Mook, and Johannes Knolle. Tunable band topology and optical conductivity in altermagnets. mar 2024.

[224] Jabir Ali Ouassou, Arne Brataas, and Jacob Linder. dc Josephson Effect in Altermagnets. *Physical Review Letters*, 131(7):076003, aug 2023.

[225] Qiang Cheng and Qing-Feng Sun. Orientation-dependent Josephson effect in spin-singlet superconductor/altermagnet/spin-triplet superconductor junctions. *Physical Review B*, 109(2):024517, jan 2024.

[226] Chi Sun, Arne Brataas, and Jacob Linder. Andreev reflection in altermagnets. mar 2023.

[227] Michał Papaj. Andreev reflection at the altermagnet-superconductor interface. *Physical Review B*, 108(6):1–7, 2023.

[228] Sayed Ali Akbar Ghorashi, Taylor L. Hughes, and Jennifer Cano. Altermagnetic Routes to Majorana Modes in Zero Net Magnetization. jun 2023.

[229] Di Zhu, Zheng-Yang Zhuang, Zhigang Wu, and Zhongbo Yan. Topological Superconductivity in Two-Dimensional Altermagnetic Metals. may 2023.

[230] Yu-Xuan Li and Cheng-Cheng Liu. Majorana corner modes and tunable patterns in an altermagnet heterostructure. *Physical Review B*, 108(20):205410, nov 2023.

[231] Christoph Sürgers, Wolfram Kittler, Thomas Wolf, and Hilbert V. Löhneysen. Anomalous Hall effect in the noncollinear antiferromagnet Mn5Si3. *AIP Advances*, 6(5):055604, may 2016.

[232] Mildred S. Dresselhaus. *Group Theory: Application to the Physics of Condensed Matter - Mildred S. Dresselhaus, Gene Dresselhaus, Ado Jorio.*